Transparent transducers and fast electronics for next-generation ultrasound and photoacoustic imaging

by

Afshin Kashani Ilkhechi

A thesis submitted in partial fulfillment of the requirements for the degree of

Doctor of Philosophy

in

Microsystems and Nanodevices

Department of Electrical and Computer Engineering

University of Alberta

©Afshin Kashani Ilkhechi, 2022

Abstract

Most ultrasound transducers are opaque. Transparent transducers could lead to novel applications, including combined optical and ultrasound imaging, photoacoustic imaging and other multi-modality systems. This thesis introduces transparent capacitive micromachined ultrasound transducers and demonstrates their use for some of these novel applications. Our long-term objective is to develop 2D row-column arrays for 3D ultrasound, photoacoustic, and optical imaging. The achievement of this long-term objective requires stepwise innovation. We first demonstrate 1D array transparent CMUTs, then overcome optical and electrical material property challenges to fabricate the first-ever transparent linear arrays. We demonstrate these arrays for photoacoustic imaging and combined ultrasound and optical imaging. We additionally take steps toward mitigation of dielectric charging problems in these CMUTs using novel thin-film processes. As a step towards 3D & 4D imaging with row-column arrays, we first design and fabricate needed fast bias-switching electronics and demonstrate their use with non-transparent row-column arrays. Finally, we outline a roadmap for achieving transparent 2D arrays and postulate their future utility for next-generation 3D multi-modal imaging.

Preface

This thesis is a combination of original and previously published works by Afshin Kashani Ilkhechi. Sections of Chapters 3, Chapter 4, Chapter 5, and Chapter 7 consist of peer-reviewed research publications by Afshin Kashani Ilkhechi et al. Chapters in this thesis contain minor modifications of the originally published papers to accommodate the thesis layout.

Chapter 3 and Chapter 4 have been published as Afshin Kashani Ilkhechi et al. "Transparent capacitive micromachined ultrasonic transducer (CMUT) arrays for real-time photoacoustic applications." Optics express 28.9 (2020): 13750-13760. Afshin Kashani Ilkhechi and Roger Zemp introduced the fabrication processes discussed in Chapter three. I was responsible for design, fabrication, characterization, and manuscript composition. C. Ceroici helped with photoacoustic setup and data acquisition, Z. Li helped with fabrication process development, and R. J. Zemp was the supervisory author and involved with manuscript composition.

Chapter 5 of this thesis has been published as Afshin Kashani Ilkhechi et al. "Transparent capacitive micromachined ultrasound transducer linear arrays for combined realtime optical and ultrasonic imaging." Optics Letters 46.7 (2021): 1542-1545. I was responsible for design, fabrication, and characterization of the transparent CMUT arrays, setting up the imaging system, data collection, and manuscript composition. C. Ceroici designed the interfacing electronic for ultrasound imaging, E. Dew helped with acoustic characterization of the transducers, and R. J. Zemp was the supervisory author and involved with manuscript composition.

Chapter 6 of this thesis has been partially presented in Afshin Kashani Ilkhechi et al. "Fast bias-switching electronics for ultrafast volumetric imaging with bias-encodedrow-column 2D arrays,"IEEE International Ultrasonics Symposium, 2021. Afshin Kashani Ilkhechi was the primary designer of the biasing electronics, and R. J. Zemp was the supervisory author and was involved with the concept formation.

Chapter 7 of this thesis discusses fabricating charging free-CMUTs and is currently under review for publication with the title "Fabricating charging-free capacitive micromachined ultrasound transducers (CMUTs) with high contact resistance semiconductors." I was responsible for design, fabrication, and characterization of the CMUT devices, data collection, and manuscript composition. C. Ceroici helped with the data acquisition, E. Rafie Borujeny, T. Muneshwar performed the semiconductor depositions, M. Ghavami helped with the data acquisition, D. Barlage, and K. Cadien was involved with the concept formation, and R. J. Zemp was the supervisory author and was involved with the concept formation and manuscript composition.

Acknowledgments

I owe my deepest gratitude to my supervisor Prof. Roger Zemp for offering me the opportunity to work on exciting projects and his guidance throughout this research project. I greatly appreciate the help of my lab colleagues, specifically Chris Ceroici, for his assistance with my research. I am also grateful to the staff of the University of Alberta nanoFAB for fabrication advice and support. I would like to acknowledge the scholarship support from the University of Alberta. This research work has been supported by funding from NSERC (STPGP 494293-16, RGPIN-2018-05788, I2IPJ 536752-19), CIHR (PS 153067), and the Canadian Cancer Society (IG 706275). I am grateful to CMC Microsystems for access to the design tools used in this work. Finally, I appreciate my family for their unique love. They always supported and encouraged me to explore new directions in life and seek my dreams.

Contents

Abstract . . . . **ii**

Preface . . . . **iii**

Acknowledgments . . . . **v**

List of Tables . . . . **ix**

List of Figures . . . . **x**

Chapter 1: Introduction **1**
Objective: 1
1.1.1 Transparent ultrasound transducer arrays: 2
1.1.2 Device through-illumination photoacoustic imaging 2
1.1.3 Combined optical-ultrasound imaging 3
1.1.4 Ultra-fast biasing electronics for bias-encoded ultrasound, and photoacoustic imaging systems 4
1.1.5 Charging-free CMUT transducers 4
1.2 Main contributions 6
1.2.1 Novel fabrication techniques for fabricating 1D and 2D transparent CMUT devices and their unique applications for multi-modality imaging systems. 6
1.2.2 Ultra-fast high-voltage biasing electronic for next generation of fast volumetric ultrasound imaging systems 7
1.3 Published work 8
1.4 Thesis layout 9

Chapter 2: Background **10**
2.1 Ultrasound imaging 10
2.2 Photoacoustic imaging 11
2.3 Image resolution 15
2.4 Signal-to-noise ratio 16
2.5 Synthetic aperture imaging 16
2.6 Ultrasound transducers 18
2.6.1 Piezoelectric transducers 18
2.6.2 Capacitive micromachined ultrasound transducers (CMUTs) 20
2.6.3 Transparent transducers 22
2.6.4 2D transducers with TOBE wiring 27
2.6.5 Bias sensitivity of ultrasound transducers 30

Chapter 3: Design and fabrication of transparent CMUT transducers . . . **34**
Objective 34
3.1 Introduction 35
3.2 One-dimensional transparent CMUT arrays with wafer bonding technique . . 36
3.2.1 Material selection and design considerations 36
3.2.2 Fabrication overview for 1D transparent CMUTs 37

Chapter 4: Transparent CMUT linear arrays for device-through illumination photoacoustic imaging **41**
Objective 41
4.1 Introduction 42
4.2 Design and simulation 45
4.3 Characterization 46
4.3.1 Transducer structure and dimensions 46
4.3.2 Transducer transparency 48
4.3.3 Device receive sensitivity 49

4.3.4 B-scan PA imaging . . . 50
4.3.5 Durability test . . . 53
Conclusion . . . 53

Chapter 5:Transparent CMUTs for combined optical-ultrasound endoscopy systems . . . 55
Objective . . . 55
5.1 Introduction . . . 56
5.2 Methods . . . 58
5.3 Results . . . 60
Conclusion and future work . . . 65

Chapter 6: High-speed bias switching electronics for fast 3D and 4D ultrasound imaging . . . 66
Objective . . . 66
6.1 Introduction . . . 67
6.2 High voltage high speed biasing electronics requirements . . . 69
6.3 High voltage bias electronics design . . . 72
6.3.1 Interface board . . . 72
6.3.2 πCards . . . 75
6.3.3 Central control unit (CCU) . . . 79
6.3.4 CCU app . . . 80
6.4 Live cross-plane FORCES imaging . . . 84
6.5 Cross-plane power Doppler imaging . . . 86
Conclusion and future work . . . 88

Chapter 7: Charging-free CMUT transducers . . . 89
Objective . . . 89
7.1 Motivation . . . 90
7.2 Alternative semiconducting isolation layers and their electrical properties . . . 93
7.3 Fabrication process . . . 95
7.4 Device characterization . . . 96
7.5 Discussion . . . 99
Conclusion and future work . . . 100

Chapter 8: Conclusion . . . 101

References . . . 106

Appendix A: Ultra-fast deformable mirrors for laser pulse modulations . . . 117
Objective . . . 117
A.1 Introduction . . . 118
A.2 Principle of operation and simulations . . . 121
A.3 Device fabrication . . . 125
A.4 Device characterization . . . 128
A.4.1 Surface quality . . . 128
A.4.2 Static characterization . . . 130
A.4.3 Dynamic characterization . . . 132
A.5 Focus control demonstration . . . 134
A.6 Discussion . . . 138
Conclusions . . . 139

Appendix B: CCU code . . . 141

Appendix C: Matlab script for imaging with CCU . . . 152

Appendix D: Schematics . . . 171

Appendix E: Fabrication processes for fabricating transparent TOBE arrays183

E.1 Fabrication process for 2D transparent CMUT transducers 183
E.2 Transparent TOBE CMUT transducers with sacrificial release process 187

List of Tables

1 Comparesion between OR-PAM and AR-PAM imaging systems 14
2 Design parameters of the transparent CMUT arrays 46
3 Transparent CMUT arrays' structural dimensions. 48
4 B-scan results comparison for Transparent CMUT for various DC bias voltages and laser powers 53
5 Experimental data for contact and sheet resistances of ALD ZnO and Ga_2O_3 thin films 94

List of Figures

1 Photoacoustic imaging. (left) OR-PAM imaging using an objective lens with a single-element ultrasound transducer. PA images are formed by mechanically scanning. (right) AR-PAM imaging using diffused laser pulses with an ultrasound transducer array. 12
2 A comparison between photoacoustic imaging modes. (left) OR-PAM of cortical vasculature in a living mouse. For this experiment, the scalp was removed, but the skull remained intact. Figure taken from [1]. (right) AR-PAM of cortical vasculature in a living mouse where scalp and skull remained intact. Figure taken from [2]. 13
3 Synthetic aperture ultrasound imaging method. Figure taken from [3] 17
4 (Left) Piezoelectric and reverse piezoelectric effect (Right) Schematic drawing of a single element piezoelectric transducer. 19
5 A cross-sectional drawing a circular CMUT cell, where the membrane is deflected under ultrasonic pressures. 21
6 (a) Single element LiNbO3 substrate-coated with ITO (b) LiNbO3 transparent transducer integrated with an optical fiber for PA imaging. Figure taken from [4] 23
7 (a) Front side of the fabricated focused transparent transducer mounted on a 3D-printed fixture (b) Test setup diagram (c) PA image of the black leaf skeleton. Figure taken from [5] 24
8 (a) Layer strucutre of the transparent ultrasound transducer (b) Assembled transparent ultrasound transducer (c) Imaging results of the quadruple imging system. Figure taken from [6] 25
9 (a) Receive beamforming used in ultrasound imaging scanners. The time delays applied are proportional to the distance between the region of interest (ROI) and the probe elements. An apodization can be used to reduce sidelobes or control energy. (b) PA raw channel data of a 20 μm gold wire illuminated by 532 nm laser (c) Beamformed image of the collected PA data. 27
10 ADS simulation results of the sensitivity of the channels with and without biasing. The graph illustrates the i_c of every single element normalized to 20 pA. The active channel is biased with 100 V biased and is contributing to the 99% of the received signal. 32
11 Bias polarity sensitivity test of an electrostrictive relaxor array. (a) schematic of the test setup, where one channel of the transducer is connected to a biasing electronics and imaging system through a bias tee. The transducer is placed in a water tank, and a hydrophone is suspended over the transducer to record the generated ultrasound pressures. (b) illustrates the test results for positive and negative bias voltages with positive and negative transmit pulse polarity. Based on our results, pressures generated in the medium experienced 180-degree phase shit compared to transmit polarity when positive bias voltages are applied. 33
12 Fabrication process flow of transparent CMUTs arrays. 38
13 Photos of the Fabricated CMUT. (a) Wire bonded 64 Channel transparent CMUT die on a PCB board for testing (b) A 3D drawing of a transparent CMUT Chip. 39
14 ADS simulation of the frequency response of the proposed transparent CMUT arrays. Simulation parameters are presented in Table 2 45

15 Images of a fabricated transparent CMUT array with 64 channels (a) A photo of the array, where the University of Alberta's logo can be seen through the device. (b) Microscope image of the die showing membranes within elements, along with their associated dimensions. The die has a pitch of 204 μm and a kerf of 26 μm. The pitch is close to the center frequency wavelength. (c) Helium ion microscope image of the cross-sectional structure and the thicknesses of the layers. 47
16 Transparency measured by spectrophotometer of the fabricated transparent CMUT arrays with 64 channels 49
17 Results of receive sensitivity test of the transparent CMUT array. (a) Receive Senstivity v.s. bias voltage of a single element of the array (b) Frequency response 50
18 (a) Drawing of the experimental PA setup with laser delivered through the transparent tank on a gold wire phantom. Wires are positioned orthogonal to the CMUT arrays and placed with 5 mm spacing in the Z-axis. (b) Drawing of the experimental PA setup with laser passing through the transparent CMUT array and 20 μm gold wire phantoms. (c) A camera image of the imaging setup with the transparent CMUTs with a laser passing through the tank. (d) A camera photo of the PA setup with a laser delivery to the targets by passing through the transparent CMUT arrays (e) Beamformed image of the PA test guiding laser through the tank. (f) Beamformed image of the collected PA data of laser-illuminated through the transducer. All four wires are detected with the transducer. 52
19 (Left) Cross-sectional drawing of the CMUT structure (Right) A photo of transparent CMUT over University of Alberta logo demonstrating the device transparency. 58
20 Diagram of our combined ultrasound-optical imaging system using transparent linear array CMUT transducers 59
21 Ultrasound transparent array evaluation setup. (a) A cross-sectional view of the setup, (b) Side photo of the setup illustrating the phantom wire targets and the ultrasound sensor, (c) Top view of the the setup, showing the camera position under the CMUT die. 60
22 Combined optical-ultrasound imaging test results. (a) Camera shot of the wire phantom through transducer, (b) Beamformed image of the wire phantom targets with 10 mm spacing. For ultrasound imaging, plane-wave imaging is performed with a bias voltage of 100 VDC on all elements, and transmit signal amplitude is set to 30 V_{pp}. A full-length video recording of realtime optical-ultrasound imaging is provided as supplementary material (see Visualization 1). 61
23 a) Photo of ex-vivo experimental setup, b) Camera image of tissue with needle, c) ultrasound image using the transparent CMUT array. 62
24 Optical and ultrasound characterization of the setup (a) Camera resolution test with USAF 1951 target without attaching the transparent CMUT. (b) Camera resolution test through CMUT. (c) Time-varying acoustic pressure generated with a single element of the transparent CMUT due to a transmit pulse with 100 μJ energy under various bias voltages. (d) The frequency response of the transmit sensitivity. The central operating frequency is determined to be 9 MHz with a fractional bandwidth of 150%. 63
25 Block diagram of bias controlled ultrasound imaging system 71

26 Interface board to connect πCards and Verasonics. a) Interface board without the connection. The board has 256 individual bias-tees to support up to 256 imaging channels. b) Ultrasound imaging setup. A TOBE array with 128 $\times$ 128 attached to a separate PCB board is plugged into the designated area at the center of the interface board. Four πCards are plugged into the interface board for providing the bias voltages. Verasonics Vantage ultrasound imaging System is attached to the board through APEX connectors. 73
27 μIBs for handheld scanner a) μIB PCBs, each consisting of 64 channels. b) A μIB board with the AC and DC connections, a πCard is connected through a flexPCB and Vantage Verasonics is connected through APEX connectors. c) Handheld design concept using four μIBs in a housing 74
28 Block Diagram of a single high-voltage high-speed switching channel 76
29 Block Diagram of the VPP switching block 76
30 a) Block diagram of a single element of TOBE array biased with πCards. In this example, an electrostrictive TOBE array is connected to πCards, where a column is biased with VPP and a row is biased GND. b) Transitioning the output of a single channel from VNN to VPP. Blue sginal is the traigger generated with the imaging system, and yellow line is the voltage transion at the output of the channel switching from -175V to +175V during a 648 nS time period. 77
31 Assembled πCards a) Logic side, consisting low voltage electronics and logic controls, b) High voltge side, consisting high voltage MOSFETs, and gate drivers. 79
32 Central Contol Unit (CCU), the main hub of the imaging system. CCU can connect to power supplies, ultrasound imaging system, πCards, lasers, photodiodes, and a computer to synchronize all units for ultrasound and photoacoustic imaging. 80
33 Screenshot of CCU app. This software can program the CCU and πCards with a single matlab command and monitor them live during the imaging. . 81
34 Bit Sequence Viewer app. (a) sequence 1 of the biasing pattern mentioned in the text, (b) the second sequence 83
35 Cross-plane live FORCES imaging. (a) Imaging setup, where an electrostrictive TOBE array is connected to the interfacing board and πCards and Verasonics Vantage Ultrasound System are connected to the interfacing board. A spring-shaped wire target is suspended in the water tack attached to the TOBE array as a target. The wire target is rotated clockwise for the cross-plane imaging, and a video file is generated of the moving target. (b) Frame 3 of the live cross-plane FORCES imaging video, illustrating cross-plane FORCES imaging the spring in a 90-degree orientation. (c) Frame 7 of the live cross-plane FORCES imaging video, illustrating cross-plane FORCES imaging the spring in a 45-degree orientation and (d) Frame 14 of the live cross-plane FORCES imaging video, illustrating cross-plane FORCES imaging a spring in a 0-degree orientation. 85
36 Cross-plane Doppler imaging with electrostrictive TOBE array. (a) Schematic of the imaging setup, a tube with a flowing corn starch solution is used to mimic blood flow in a vessel (b) A picture of the setup with the tube and a 128x128 electrostrictive TOBE array connected to our bias-encoded ultrasound imaging setup (c) Cross-plane Doppler imaging with FORCES imaging scheme. To obtain cross-plane images, transmit, receive, and biasing channels are electronically switched between rows and columns. 87
37 Fabrication process flow of the charging free CMUT transducers. 95

38 (a) Fabricated CMUts (b) Cross-sectional view of the structure of a single CMUT cell (c) Helium ion microscopy image of the CMUTs. A cut is made with a FIB to reveal the CMUT structure (d) A close view of the layers with their relative thicknesses. 97
39 (a) Capacitance versus voltage measured for ZnO CMUTs with a Keithley 4200-Semiconductor Characterization System. (b) Membrane deflection versus bias voltage measured by ZYGO optical profilometer (c) Capacitance versus voltage measured for Ga_2O_3 CMUTs with Keithley 4200-Semiconductor Characterization System. 98
40 (a) Capacitance versus voltage measured with a Keithley 4200-Semiconductor Characterization System of the CMUTs fabricated with a silicon dioxide layer. (b) Charging effect on the operation of the CMUT cells. Charged CMUT cells exhibit an unrestorable membrane snapdown due to the build up charge in the dielectric layer 99
41 Illustration showing the principle of fast optical focusing with a Capacitive Micromachined Optical Focusing (CMOF) deformable MEMS mirror (a) non deflected CMOF mirror (b) deflected CMOF mirror. 122
42 MATLAB Calculations (a) Optical power of a CMOF for various membrane sizes and deflection (b) focal length shift of a laser beam after refocusing with a CMOF for various membrane sizes and deflections (c) focal spot size change of a laser beam after refocusing with a CMOF for various membrane sizes and deflections (d) focal spot shift of a laser beam after a lens relay with $f = 3\ mm$. 124
43 Fabrication process flow (a) dry thermal oxidation to grow 340 nm oxide, (b) etching the gap spacing with BOE (c) bonded a SOI wafer on the prime wafer, the backside of the prime wafer is protected with PECVD Oxide (d) Handle and BOX layers of the silicon wafer are selectively etched and the device layer is exposed (e) the membrane of the deformable mirror is formed by selectively etching the silicon layer (f) the bottom pad is exposed by selectively etching the oxide layer and (g) the metal coating is deposited and etched to form the reflective coating and the electrical pads. 126
44 Fabricated CMOF-MEMS deformable mirrors. (a) a full wafer view of the fabricated dies (b) Helium Ion Microscopy image of a CMOF-MEMS cell with 20 μm radius (c) AFM surface profile of a CMOF-MEMS mirror at the center of the mirror (d) 3D reconstructed image taken by ZYGO optical profilometer of a CMOF cell with 30 μm radius and 100 nm central deflection. 129
45 Static tests (a) Deflection versus voltage changes measured by an optical profilometer (b) Capacitive versus voltage changes measured with a Semiconductor Characterization System. Both graphs are normalized to the snapdown voltage of the CMOF mirror which is 29.6 V 131
46 Sample laser Doppler vibrometry measurements. (a) 2-D scan showing the membrane displacement for a given frequency. (b) Single point measurement using an 8 V AC signal. The peak shows the first fundamental frequency of the membrane. (c) Single point time domain measurement of the membrane displacement for a step-function input with 22V amplitude. 133
47 3D drawing of the optical setup for testing the CMOFs. Camera taken picture of the focused laser on a CMOF is showing a 16 μm laser spot on a 30 μm radius CMOF. 135

48 Focal Point shifts recorded for a laser beam in the presented optical setup. The measurements are performed with a Shack-Hartman wavefront sensor and the distance between the focus point and camera CCD is removed in the graphs. (a) The graph shows measurements for a 30 μm radius membrane (b) Magnified focal point shift with a $f = 50\ mm$ lens for 30 μm membrane size. (c) Beam profile intensity recorded with the SWF sensor for membrane at 100 nm deflection. Pixelation of the figure is due to the lens array of the SWF sensor. . . . 137
49 πCards' single channel schematic . . . 171
50 πCards' eight channels with shift registers . . . 172
51 πCards' all channels' connections . . . 173
52 πCards' main card controller . . . 174
53 πCards' power control schematic . . . 175
54 CCUs' main controller . . . 176
55 CCUs' delay generator . . . 177
56 CCUs' πCard interface . . . 178
57 CCUs' power controller . . . 179
58 CCUs' power supply port . . . 180
59 CCUs' high voltage sampler . . . 181
60 CCUs' trigger receiving electronics . . . 182
61 Fabrication process flow for TOBE CMUT arrays with BCB wafer bonding technique. . . . 184
62 (a) Before performing the undercut (b) Proper undercut (c) Excess undercut. . . . 185
63 Top view and cross-sectional views of the transparent CMUTs with BCB bonding technique. . . . 186
64 Sacrificial release fabrication process flow for fabricating high-frequency transparent TOBE arrays. The process involves a silicon dioxide layer as a sacrificial layer and a silicon nitride layer as the membrane materials. (a) Etching thin trenches in the fused silica substrate. (b) Metal deposited in the trenches (c) ITO deposition and formation into the channels for the bottom electrodes. (d) Deposition of PECVD nitride for protecting the ITO layer. (e) Silicon dioxide deposition and formation as a sacrificial release layer. (f) LPCVD nitride deposition as a membrane material. (g) RIE nitride etching to open the etch holes for releasing the membrane. (h) Vapour HF etching the sacrificial layer. (i) PECVD dioxide deposition to seal the etch holes and formation into the plugs. (j) ITO deposition and formation into top electrodes (k) Metal strip deposition to improve the channel conductivity. . . . 189

Chapter 1: Introduction

Objective:

The majority of the ultrasound transducers designed today are based on the piezoelectric effect with 2D imaging systems. The high sensitivity and reliability of the piezoelectric materials and well-developed 2D imaging algorithms are some of the compelling properties that make these systems a favourite diagnostic candidate. This thesis is mainly focused on improving and advancing ultrasound and photoacoustic imaging technology from various perspectives. One of the main drawbacks of the current transducers is their lack of transparency. Transparent ultrasound transducers could lead to novel applications, including optical and photoacoustic imaging systems. This thesis addresses this limitation by introducing novel techniques to design and fabricate transparent transducers with capacitive micromachined ultrasound transducer (CMUT) technology and utilizes them in multi-modality imaging systems. This thesis also investigates new fabrications techniques for fabricating 2D ultrasound transducers for 3D ultrasound imaging and introduces ultra-fast electronic designs for high resolution and high signal-to-noise 3D & 4D ultrasound imaging systems. Finally, this thesis introduces high contact resistance materials for fabricating CMUT transducers to mitigate their charging problem.

1.1.1 Transparent ultrasound transducer arrays:

This thesis mainly focuses on the design, fabrication and characterization of transparent ultrasound transducer arrays with CMUT technology. CMUT devices are designed and fabricated with microelectromechanical systems' technology and have some advantages over piezoelectric transducers. For example, CMUTs offer a higher transmit and receive bandwidth which results in higher resolution ultrasound images. Also, they can be fabricated in different structures with a large selection of materials. Therefore, CMUT devices can be precisely designed and manufactured for every specific application to meet the requirements and constraints.

This thesis focuses on developing a novel fabrication process for fabricating highly transparent transducers. Initially, a wafer bonding process is developed and modified to fabricate transparent CMUT arrays for the first time. Then, to expand the arrays into 2D structures, two new fabrication processes based on the wafer bonding technique and sacrificial release process are invented, proposed, and developed.

1.1.2 Device through-illumination photoacoustic imaging

Photoacoustic imaging has shown great potential for non-invasive high-resolution deep-tissue imaging. In this technique, a laser pulse is illuminated on the target tissue. Absorbed optical energy creates localized heat, and as a result, the tissue experiences a sudden expansion due to optical absorption. The expansion generates acoustic pressure and propagates in the tissue, and is detected by an ultrasound transducer. Minimizing the optical and acoustic paths for excitation and detection could significantly increase the signal-to-noise ratio. This

could be accomplished by transparent ultrasound transducers permitting through transducer illumination.

This thesis will investigate the transparent array architectures, applications and explore the advantages of device-through illumination. Through-illumination imaging can potentially improve the signal-to-noise (SNR) ratio of the photoacoustic images and lead to advanced photoacoustic scanners.

1.1.3 Combined optical-ultrasound imaging

Endoscopy makes it possible to inspect and diagnose the gastrointestinal tract [7] and is a tool for interventional and surgical procedures. Superficial visualization is a limitation of camera endoscopy, making it hard and sometimes impossible to detect more profound disorders. To address this, endoscopic ultrasound imaging technology can be used to reveal depth-related information beyond the surface [8], which may include visualization of lungs, gall bladder, pancreas, and liver without the need for surgical exposure [9, 10]. However, the main limitation of such multi-modality scanners is their size and lack of flexibility. This is due to the use of non-transparent transducers in the structure of the ultrasound-endoscopy probes.

This thesis investigates the possibility of designing highly compact endoscopy ultrasound probes with the help of transparent transducer technology, where the optical camera can be placed behind the transducer array. This technology may enable one to visually see what is being scanned and scan what one sees without co-registration errors. Future applications could include multi-modality probes for interventional and surgical procedures.

1.1.4 Ultra-fast biasing electronics for bias-encoded ultrasound, and photoacoustic imaging systems

The majority of the ultrasound systems are only capable of producing 2D images. 3D and 4D ultrasound imaging require 2D ultrasound arrays and, due to a large number of the elements on these transducers, designing large fully wired 2D ultrasound arrays is impractical. Utilizing a row-column wiring approach can significantly reduce the number of channels required. However, to fully exercise the advantages of these types of transducers, fast bias switching electronics with the possibility of providing bi-polar voltages are needed. Such an electronic system can enable emerging novel imaging schemes that can provide high image quality.

This thesis investigates novel ultrasound biasing techniques and develops ultra-fast bi-polar biasing electronics for performing cross-plane bias-coded ultrasound images. Furthermore, ultrasound and photoacoustic imaging with 2D row-column arrays are investigated with the help of the presented biasing electronics.

1.1.5 Charging-free CMUT transducers

The main drawback of CMUT devices is their dielectric charging problem. The dielectric layer charging is mainly attributed to electron injection during snapdown events [11]. However, other mechanisms such as operating temperature can also affect the charging process, accelerating or decelerating the charging independent from the actuation mechanism. Charging can cause an unreliable transducer operation and reduced sensitivity. In addition, it may cause early device failure and membrane breakdown for CMUT devices.

This thesis addresses this problem by introducing a novel fabrication technique in order to fabricate CMUT transducers with non-isolating materials such as Zinc Oxide and Gallium Oxide. Semiconductor materials mentioned can present high contact resistances, which is a problem for semiconductor industries, but if they are implemented in the CMUT structure, their high contact resistance can prevent short-circuiting in snapdown events, and their low sheet resistance can dissipate any trapped charges in the dielectric.

1.2 Main contributions

Chapters three to seven of this thesis consist of original research, some of which are published or under-review in peer-reviewed scientific journals. The followings discuss the main contributions for chapters three to seven.

1.2.1 Novel fabrication techniques for fabricating 1D and 2D transparent CMUT devices and their unique applications for multi-modality imaging systems.

Transparent transducer arrays can provide a unique opportunity for emerging novel multi-modality imaging systems. However, fabricating them is not simple and requires a precise material selection and optimized fabrication process flows. The main constraint with the current fabrication process flows is their incompatibility to make ultrasound transducer arrays with optically transparent materials. There are limited reports of single-element transparent transducers, but there was no report of transparent transducer arrays made for visible wavelengths at the time of writing this thesis. This thesis introduces novel fabrication processes to fabricate transparent ultrasound transducers into large arrays for the first time. Initially, a fabrication technique based on photosensitive polymer called Benzocyclobutene (BCB) is introduced for fabricating transparent transducers arrays into 1D arrays. Then the process is expanded into fabricating 2D transparent transducer arrays with TOBE wiring.

In order to experimentally test the transparent transducer arrays for ultrasound, photoacoustic and multi-modality systems, custom-designed PCBs are made enabling device through illumination. Then, photoacoustic imaging was performed by passing laser pulses through the transducer. To our knowledge, this was the first time performing a device

through photoacoustic imaging by employing a transparent transducer array.

Multi-modality applications of the transparent transducer arrays are also demonstrated by performing a device through optical imaging combined with ultrasound imaging simultaneously for endoscopy applications. Ex-vivo imaging of rat heart revealed the unique advantage of the transparent transducer arrays where optical imaging provided visual and ultrasound provided depth information of the target.

1.2.2 Ultra-fast high-voltage biasing electronic for next generation of fast volumetric ultrasound imaging systems

Our novel fabrication processes introduced in Chapter three allow for fabricating ultra-transparent TOBE CMUT arrays, which can be used for high-resolution multi-modality 3D imaging systems. However, a significant bottleneck for employing TOBE arrays is their row-column addressing, limiting direct access to the elements. One way to achieve single element addressing in TOBE arrays is to use bias sensitive transducers such as CMUTs or electrostrictive materials. Bias sensitivity in TOBE arrays provides extra control where elements can be electronically activated by applying bias voltages on the corresponding row and columns. However, generating high voltage bi-polar biasing sequences requires a high-speed, high-voltage electronic design that is currently unavailable. Here, we addressed this problem by designing special electronics to perform bias-encoded imaging with TOBE arrays. The electronics developed for this purpose are optimized for rapid bipolar high-voltage switching and tested by performing high frame rate cross-plane ultrasound imaging.

1.3 Published work

Research regarding the fabrication of transparent ultrasound transducer arrays is published in the OSA Optics Express journal [12] as well as presented in three conferences [13–15]. The publication and presentation discussed the design and fabrication of linear transparent ultrasound transducer arrays for a device through illumination photoacoustic imaging. Furthermore, a comparison between device through and side illumination photoacoustic imaging is presented, emphasizing the SNR improvements.

Work related to multi-modality imaging systems is published in OSA Optics Letters [16] as well as presented in [17]. The publication and the presentation presented the results and advancements of utilizing optically transparent transducer arrays combined with endoscopy probes.

The use of fast-biasing electronics with TOBE arrays for 3D and 4D ultrasound systems is presented in [18] and is currently in preparation for a journal publication. The work demonstrates the results of bias-encoded live 3D and 4D ultrasound imaging moving wire-target. 3D imaging was previously performed with TOBE arrays, but they suffered from low SNR and slow imaging acquisition speed. We demonstrated 3D imaging with 20 Vol/sec and dynamic range of -40 dB.

Research regarding mitigating the charging problem in CMUT transducers is also presented in [19] and is currently under preparation for a journal publication. The presented results exhibit an improvement over the charging characteristics of the CMUT devices and promise an extended reliable operation for the transducers.

1.4 Thesis layout

Chapter 2 of this thesis will provide background information on ultrasound imaging, CMUT technology, transparent transducer and their applications.

Chapter 3 of this thesis will describe a novel fabrication technique for fabricating transparent transducer arrays.

Chapter 4 of this thesis will present the advantages of transparent transducer arrays for photoacoustic imaging with the device through illumination.

Chapter 5 of this thesis will present the application of transparent transducers for multimodality imaging systems capable of performing optical and ultrasound imaging simultaneously.

Chapter 6 of this thesis will describe the design and development of fast biasing electronics for rapid 3D and 4D ultrasound imaging.

Chapter 7 of this thesis will address the CMUT transducers' charging problem by introducing a new fabrication process flow.

Chapter 8 of this thesis will conclude and will provide a summary of the research presented.

Chapter 2: Background

2.1 Ultrasound imaging

Ultrasound imaging has a well-established place in medical diagnostics. In the last four decades, ultrasound technology has seen a steep pace in development, and innovation [20]. Some of the compelling properties of ultrasound imaging that had an undeniable effect on its popularity for research and development are its non-ionizing radiation, live imaging, and affordable installation cost.

Ultrasound imaging relies on the pulse-echo technique to map inside the body. This is done by transmitting sound waves into the tissue and listening to the backscattered waves. Then, a depth-related image can be generated by recording the intensity of the reflected pulses as a time series [21]. The propagation of the ultrasounds in tissue is non-linear [22], which can be used to perform harmonic imaging, but for most imaging applications, the propagation of the sound waves is approximately linear. The acoustic impedance of tissues is related to the density and the speed of the sound in the tissue. Since various tissues in the body have different densities, ultrasound waves will experience diverse reflection and penetration ratios in the boundaries of tissues and scattering from microstructures, which will determine the image contrast in an ultrasound scan [22].

2.2 Photoacoustic imaging

Ultrasound imaging has had a tremendous effect on diagnostic applications and works by mapping the acoustic mismatches in tissues. However, living tissues are biologically active and determining the biological state of tissues is essential for diagnostic purposes.

On the other hand, photoacoustic (PA) imaging is a relatively new modality that works based on the tissue's photoacoustic effect and maps the optical absorption contrast to form photoacoustic images [23]. In this imaging modality, non-ionizing laser pulses are delivered into biological tissues where some of the optical energy is absorbed by biomolecules such as hemoglobin, and then converted into localized heat. As a result of the sudden heating, the tissue experiences immediate pressure changes due to thermal expansion and generates ultrasound pressures. These pressures then travel to the surface of the tissue, where they can be detected by an ultrasound transducer and converted into PA images.

PA imaging can be categorized into optical-resolution photoacoustic microscopy (OR-PAM), and acoustic resolution photoacoustic microscopy (AR-PAM) [23].

OR-PAM employs optical focusing and works by focusing laser pulses on a tight spot on the tissue and recording the generated photoacoustic pressures. Every excitation point generates an A-line scan (providing depth information in Z-axis). Thus, mechanically scanning of the probe will result in 2D and 3D photoacoustic images. Thanks to optical waves having much higher frequencies than acoustic waves, performing optical focusing enables a significantly tight focusing spot; therefore, OR-PAM can provide a superior special resolution compared to AR-PAM. Fig. 1 (left) illustrates OR-PAM imaging techniques. As seen in the figure, OR-PAM imaging is a combination of an objective lens and a single element

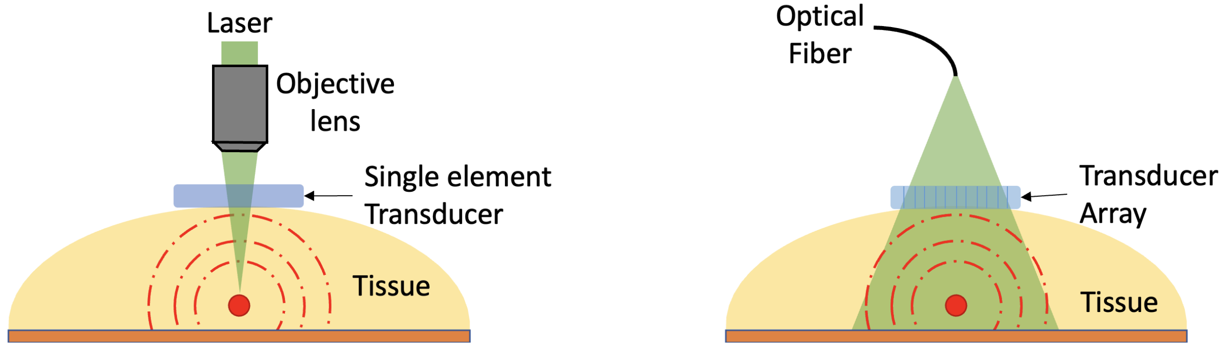

Fig. 1: Photoacoustic imaging. (left) OR-PAM imaging using an objective lens with a single-element ultrasound transducer. PA images are formed by mechanically scanning. (right) AR-PAM imaging using diffused laser pulses with an ultrasound transducer array.

transducer (which may or may not allow device-through illumination). The main constraint of OR-PAM imaging is its limited imaging depth due to the optical diffusion limit [24].

AR-PAM, on the other hand, utilizes ultrasound focusing to generate photoacoustic images [25]. With the sacrifice of the spatial resolution compared to OR-PAM, this technique can generate PA images much deeper in the tissue with higher depth-to-resolution ratios and perform fast 2D and 3D imaging without mechanical scanning. Fig. 1 (right) illustrates a diagram of an AR-PAM imaging system employing a transparent transducer for a device-through illumination. A diffuser would also help to diffuse the laser pulses for a wider field of view.

For a better compression between the two systems in respect to achievable image resolutions and depths, Fig. 2 is prepared, where both modalities are used for imaging a mouse brain [1, 2].

Fig. 2(left) shows cortical vasculature in a living mouse taken with OR-PAM. Thanks to the optical diffraction limit of light, OR-PAM has a micron-scale resolution. However, due to the depth limitation of OR-PAM, the scalp of the brain had to be removed to make

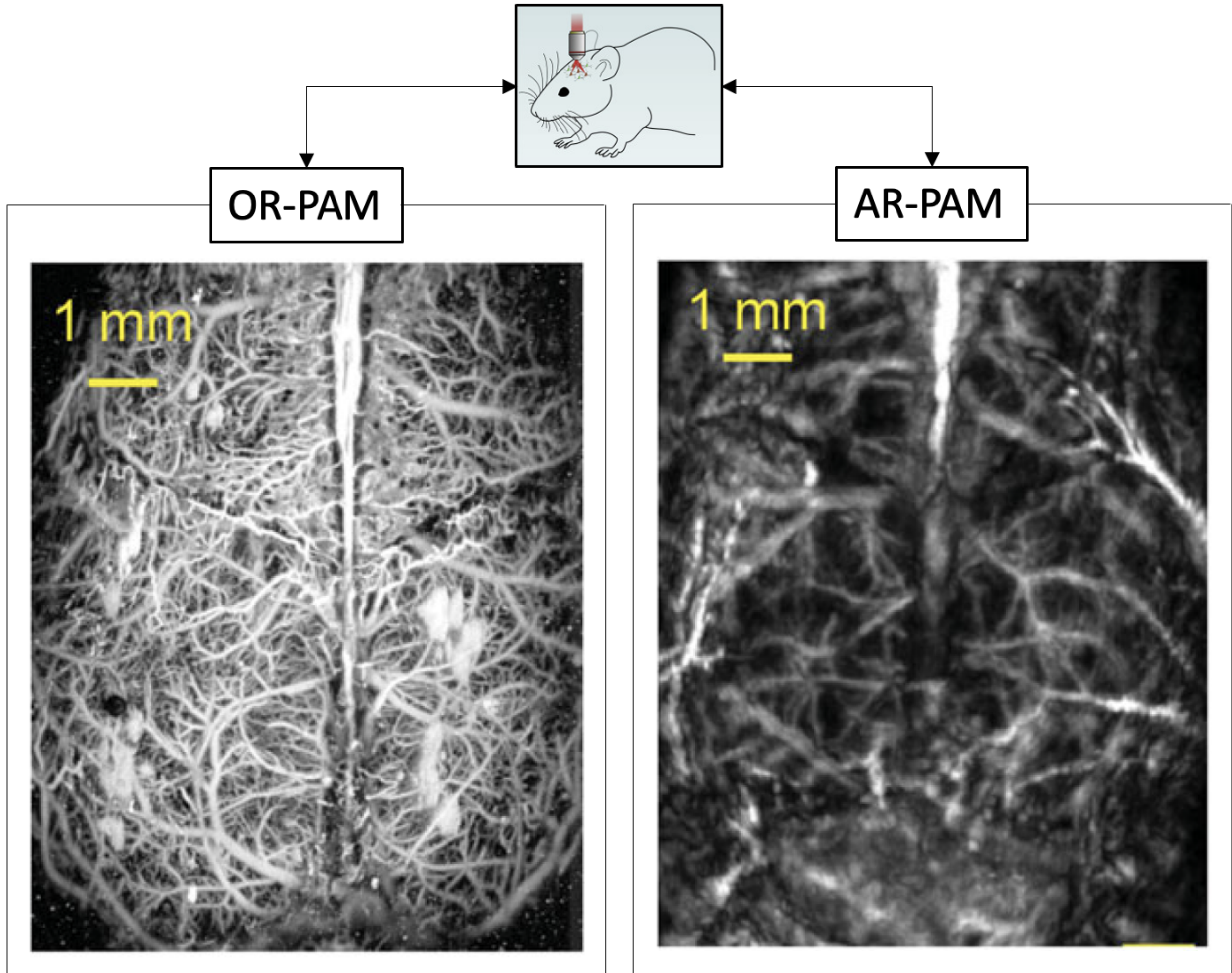

Fig. 2: A comparison between photoacoustic imaging modes. (left) OR-PAM of cortical vasculature in a living mouse. For this experiment, the scalp was removed, but the skull remained intact. Figure taken from [1]. (right) AR-PAM of cortical vasculature in a living mouse where scalp and skull remained intact. Figure taken from [2].

the imaging possible. In contrast, Fig. 2(right) illustrate the same brain imaging using the AR-PAM imaging technique, where the scalp and skull of the brain remained intact. A detailed comparison between the two modalities is provided in Table 1.

The lateral resolution of OR-PAM systems is mainly determined by the imaging optical wavelength, and the objective lens's numerical aperture (NA) [26], where tighter laser focusing can be achieved with larger NAs and shorter optical wavelengths. AR-PAM has a

Table 1: Comparesion between OR-PAM and AR-PAM imaging systems

Parameter	OR-PAM	AR-PAM
Lateral resolution	$0.51\frac{\lambda_0}{NA_o}$	$0.71\frac{Co_1}{NA.f} = 1.42\lambda\frac{a}{D}$
Axial resolution	$0.88\frac{Co_1}{\Delta f_a}$	
Imaging depth	≤ 1 mm	≈ 5 cm
Image acquiring speed	Slow (scanning)	Fast (single laser shot)

similar definition for lateral resolution, where the f-number of the transducer and ultrasound wavelength determines the lateral resolution. Therefore, OR-PAM can provide micron-scale resolutions, and AR-PAM can reach sub-millimetre resolutions [23]. The axial resolution of both systems is similar and is related to the bandwidth of the transducer.

2.3 Image resolution

Resolution is one of the main factors determining the quality of an ultrasound image and can be characterized into axial, lateral and azimuthal resolutions. The resolution of an ultrasound system is defined as the minimum detectable distance between two scatters [22]. The resolution is sometimes measured using a full-width-at-half-maximum (FWHM) of a measured point-spread function (PSF). The FWHM for lateral resolution can also be calculated with the following equation [22]:

$$FWHM = 1.4\lambda \frac{focallength}{Aperture} = 1.4\lambda f\# \quad (1)$$

Where λ is the wavelength of the transducer, which is calculated based on the frequency and the speed of sound in the medium, $F\#$ is the f-number of the transducer. This is calculated as the ratio of the focal point and the aperture size of the transducer. In the case of array systems, the focus can be adjusted electronically.

The axial resolution of a linear array ultrasound transducer has an inverse relation to the receive bandwidth, where transducers with larger bandwidths can provide higher axial resolution. For a 50% fractional bandwidth linear piezoelectric transducer, the axial resolution is approximately twice the wavelength [22].

Elevaltional resolution is mainly defined for 3D imaging systems. Depending on the method 3D images are made, elevational resolution can significantly vary. For 2D transducers with similar elements in the rows and columns, elevational resolution can be identical to azimuthal (lateral) resolution.

2.4 Signal-to-noise ratio

The SNR values can be used to determine the maximum imageable depth of an ultrasound system. Noise in an ultrasound system can arise from sources including but not limited to transducers, operational preamplifiers, electronic noise, thermal noise, and the random nature of the background medium causing speckles. If the received signal amplitude falls below a certain threshold, the signal might get buried under the noise and become undetectable. SNR is defined as below [22]:

$$SNR = \frac{MaximumIntensityReceivedSignalPower}{NoisePower} \tag{2}$$

The transducer and electronic systems mainly determine noise power in an ultrasound system. If speckles are neglected, the noise power remains independent from the imaging power and transmit intensity; therefore, by increasing the transmit power or transmit duration (following the safety limits), higher SNR values can be achieved.

2.5 Synthetic aperture imaging

One of the imaging schemes we will use in this thesis leverages coded aperture synthetic aperture imaging. Thus, it is important to provide some background about synthetic aperture ultrasound imaging. This imaging method was initially used in radar systems but eventually was adapted to biomedical ultrasound imaging [27]. The first implementation of synthetic aperture imaging was the monostatic synthetic aperture imaging done by Bennett et al. [28]. In the mono-static method, only a single element is used for transmitting, and all elements are used for the reception to create a low resolution, low SNR image. After firing from all the

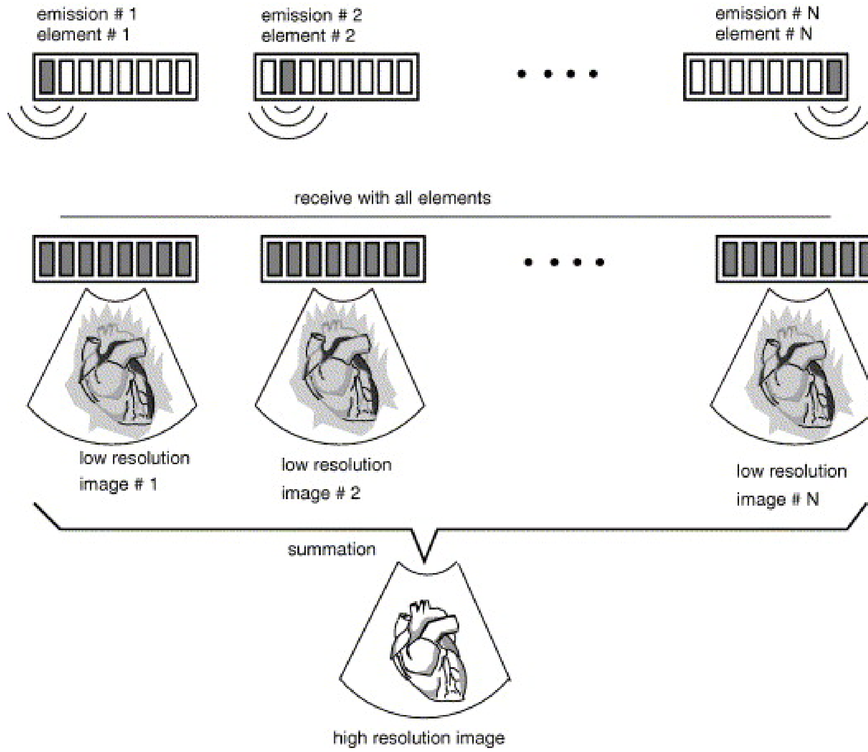

Fig. 3: Synthetic aperture ultrasound imaging method. Figure taken from [3]

elements and acquiring receive signals, a high-resolution image can be made by coherently compounding the low-resolution image as shown in Fig. 3.

However, using a single element for emission will result in weak transmit signals and eventually result in low SNR and low image quality. Another drawback is the amount of transmit events required to generate a single beamformed image. A different approach would be using sparse elements for transmitting and reducing the number of transmit events with the cost of even lower SNR images. Several transmitters can be used as a group to transmit more powerful signals to address the low transmit power problem.

Unlike focused steered beams or walking beam methods, synthetic aperture imaging enables transmit- and receive-focusing everywhere in the image [27]. When using synthetic transmit focusing, a virtual transmit aperture is synthesized. Transmit focusing can be

done by steering the transmit beam, translating transmit aperture and the location of the transmitting elements, or a combination of them both. Receive focusing is achieved by using dynamic receive beamforming (DRBF) [29, 30], which performs receive focusing all over the ultrasound field of view.

Using aperture coding for synthetic aperture imaging can provide exceptionally high SNR ultrasound images. For example, the Hadamard matrix can be used to code every frame of the synthetic ultrasound imaging, and the inverse Hadamard matrix can decode the received data [31, 32]. However, performing coding requires high-speed electronics that can provide high-speed bias voltage and polarity switching for transmitting and receiving elements. Since CMUTs and electrostrictive materials are biased sensitive, their sensitivity can be manipulated with a bias voltage. Bias-sensitivity and bias coded imaging are further discussed in Chapter 5.

2.6 Ultrasound transducers

Some of the most common ultrasound transducers include piezoelectric transducers and capacitive transducers. The following subsections will describe each type in detail.

2.6.1 Piezoelectric transducers

Piezoelectric transducer operation is based on the piezoelectric and inverse piezoelectric effects where electrical signals and mechanical pressures are converted one into another [33]. As shown in Fig. 4a mechanical force displaces electrical charges in a material with asymmetric crystal structure and causing electrical energy storage, which can be sensed by using electrodes (Fig. 4b). The figure illustrates a simplified lattice structure of a single

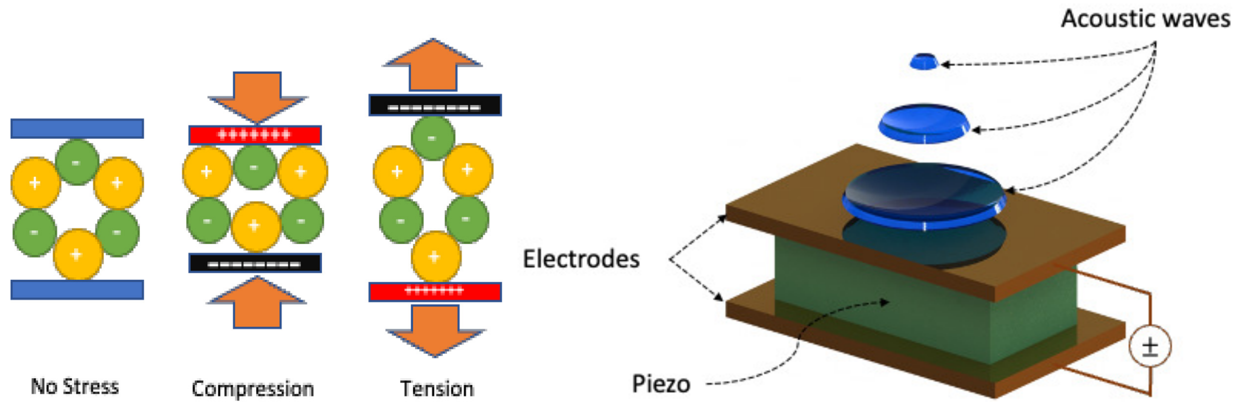

Fig. 4: (Left) Piezoelectric and reverse piezoelectric effect (Right) Schematic drawing of a single element piezoelectric transducer.

crystal piezoelectric material, where yellow circles represent ions with a positive charge and green circles represent ions with a negative charge. The charge generated by the material is due to compulsive or tension pressures resulting from the displacement of the ions. The opposite can also happen when an electric pulse is applied, and the displacement of the ions in the crystal structure causes a physical displacement in the materials. Thus, ultrasound pressures can be generated in the medium.

Electrostrictive materials are also used to build ultrasound transducers [34, 35]. The main advantage of electrostrictive relaxor arrays compared to piezoelectric transducers is their dependency on an external electric field to exhibit an inverse piezoelectric effect [36]. Briefly, applying an electric field on any dielectric causes a displacement of ions in the material and causes a strain in the material in the direction of the electric field. The strain presented by the dielectric materials is quadratic to the applied electric field (unlike the piezoelectric materials, where the strain is a linear effect). The strain and displacement of the ions cause a temporary asymmetric crystal structure in some dielectrics, resulting in an

inverse piezoelectric characteristic when an electric field is applied [36]. Thus, transducers designed with electrostrictive material are bias-sensitive, and they deliver a high coupling factor when they are biased. The coupling factor measures the efficiency of converting mechanical energy into electrical form and vice versa [37]. Higher coupling factors will lead to detecting weaker signals and eventually higher quality images. The bias-sensitivity of the electrostrictive relaxor arrays is a helpful characteristic that provides additional control, makes it possible to design 2D arrays with row-column addressing. Row-column transducers make it possible to create large 2D arrays for high-resolution 3D imaging. They are discussed in more detail in the section 2.6.4.

2.6.2 Capacitive micromachined ultrasound transducers (CMUTs)

CMUTs technology was first introduced in 1989 by Hohm and Hess [38] and started a new era of ultrasound imaging. CMUTs structure is shown in Fig. 5. As shown, CMUTs contain a flexible membrane with a conductive electrode suspended over a fixed bottom electrode with a gap space between. When a bias voltage is applied across the two electrodes, electrostatic force deflects the flexible membrane, which causes a change in the CMUTs capacitance. Also, when ultrasound waves hit the flexible membrane, it vibrates the membrane and modulates the capacitance of the CMUT device. The capacitance versus deflection for a circular clamped membrane can be modelled by [39]:

$$C(t) = \frac{\epsilon_0 \pi a^2 \tanh^{-1}\left(\sqrt{\frac{X_P(t)}{a}}\right)}{2\sqrt{t_{ge} X_p(t)}} \tag{3}$$

where C is the CMUT capacitance, a is the membrane radius, $x_p(t)$ is the peak membrane

deflection and t_{ge} is the effective membrane gap. The sensitivity of a CMUT is the derivation of the changes in the capacitance over the changes in the membrane deflection, which presents a nonlinear capacitance-deflection relationship and makes the CMUTs bias sensitive. Bias sensitivity of CMUTs is useful because it makes it possible to design 2D CMUTs with row-column addressing. The created force on the membrane with a bias voltage $V(t)$ can be calculated [39]:

$$F_{tot} = \frac{\epsilon a^2 \pi V(t)^2}{4t_{ge}^2} \left[\frac{t_{ge}}{t_{ge} - X_p(t)} + \frac{\tanh^{-1}\left(\sqrt{\frac{X_p(t)}{t_{ge}}}\right)}{\sqrt{\frac{X_p(t)}{t_{ge}}}} \right] \tag{4}$$

The main advantage of CMUTs over piezoelectric transducers is their lack of need for matching layers for acoustic impedance matching to the tissue. Therefore CMUTs can present a broader bandwidth and lead ultrasound images with higher axial resolution. Also, their higher electro-mechanical efficiency makes them more sensitive to detect weaker ultrasound signals and generate SNR images [40–43].

CMUT transducers are fabricated with MEMS technology with either surface micromachining or wafer bonding processes [44] where both methods have potential for massively

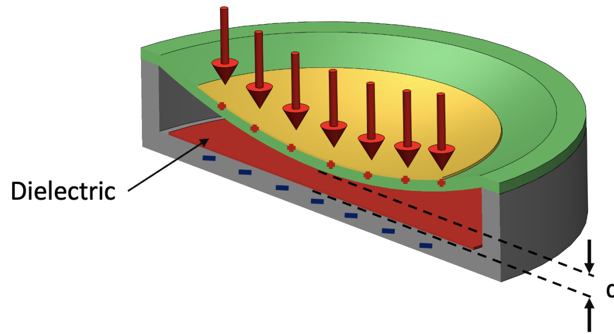

Fig. 5: A cross-sectional drawing a circular CMUT cell, where the membrane is deflected under ultrasonic pressures.

scalable fabrication and CMUT-on-CMOS combined chips for reduced manufacturing costs.

Surface micromachining involves a sacrificial release process where a sacrificial layer is deposited between the top and bottom electrode and selectively etched before sealing the gaps [45–47].

Wafer bonding processes use a donor wafer containing the thin membrane film to bond to a wafer containing the gap structures. Fusion, anodic and adhesive bondings are some of the bonding techniques used for making CMUTs. Fusion bonding has traditionally been limited to silicon, silicon nitride, and silicon dioxide materials [48–52]. Recently, K. Steenberg and E. Thomsen [53] introduced a new fabrication process based on silicon to silicon-dioxide fusion bonding process on top of insulating substrates and using silicide as a conductive base layer.

Another wafer bonding method is the adhesive wafer bonding technique which can accommodate a wide variety of materials [54,55]. Larger material selectability of the adhesive wafer bonding technique was the primary motivation behind our introduced fabrication process to fabricate transparent transducer arrays, discussed in Chapter Three.

2.6.3 Transparent transducers

The demand for transparent transducers started with the emergence of new imaging modalities such as photoacoustic imaging, where optical excitation generates ultrasound pressures in the tissue [12]. In addition, transparent transducers can also be used for multi-modality imaging applications where small footprint probes are needed with both optical and ultrasonic elements [16]. However, fabricating transparent transducers is not straightforward since most of the materials used to built transducers are not optically transparent. Therefore, to date, the fabrication of transparent transducers has been limited to only single element

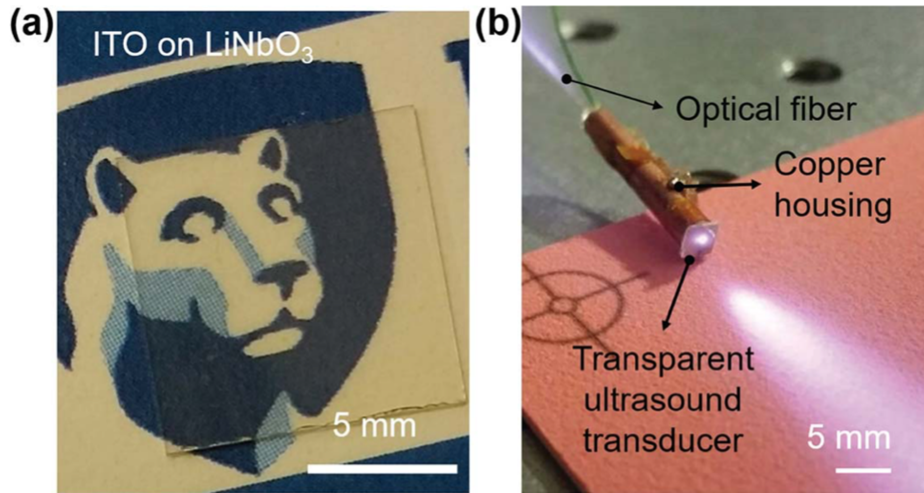

Fig. 6: (a) Single element LiNbO3 substrate-coated with ITO (b) LiNbO3 transparent transducer integrated with an optical fiber for PA imaging. Figure taken from [4]

transducers.

In recent years, several research groups have demonstrated designing transparent ultrasound transducers. A. Dangi et al. in [4] demonstrate the fabrication of a single element transducer using Lithium Niobite material sandwiched between two transparent Indium Tin Oxide (ITO) layers. The transducer displayed transparency of %75 for wavelengths longer than 350 nm and has an air operation frequency of 14.5 MHz. Fig. 6a illustrate the transparency of the transducer by showing a logo through the transducer and Fig. 6b illustrates the assembled transducer for PA imaging. By performing AR-PAM and passing laser pulses through the transducer, they demonstrated lateral resolution of 900 μm and a photoacoustic bandwidth of 70%.

In another study, polyvinylidene fluoride (PVDF) based transducers are designed, and ITO sued as a transparent conductor for the electrodes [5]. The transducers then mounted on a convex lens to focus the laser pulses in spot ≈ 4.3 μm for performing OR-PAM. The

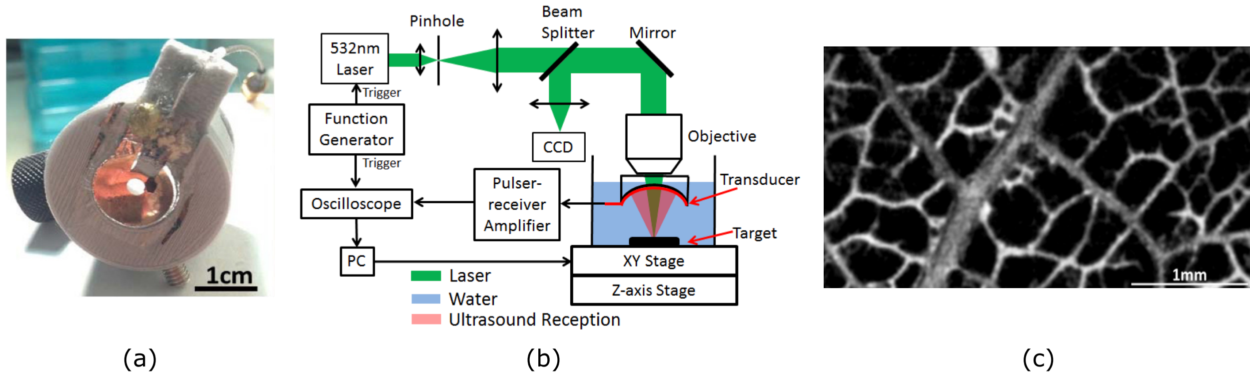

Fig. 7: (a) Front side of the fabricated focused transparent transducer mounted on a 3D-printed fixture (b) Test setup diagram (c) PA image of the black leaf skeleton. Figure taken from [5]

curved shape of the transducer is also provided with an acoustic focusing of 900 μm. The transducer and the lens assembly provide a smaller form factor and easier alignment between the optical and acoustic focuses, producing sharper images. Fig. 7a illustrate the assembled transducer, and Fig. 7b illustrates the diagram of the imaging systems. PA image of a black leaf skeleton phantom taken with the transducer is presented in Fig. 7c.

Transparent ultrasound transducers provide a unique opportunity for designing multi-modality imaging systems. For example, J. Park et al. in [6] designed a single element transparent ultrasound transducer for a combined quadruple imaging system. The transducer is manufactured with transparent piezoelectric layers, transparent electrodes, matching and backing layers, and an acoustic lens. The transducer presents peak transparency of 74% in visible wavelength and an air operation frequency range from 7.5 MHZ to 31.5 MHz. Fig. 8a & b demonstrate the transparent ultrasound transducer structure and its transparency. Combining the transparent transducer with an optical system resulted in a quadruple fusion imaging system capable of performing ultrasound imaging, photoacoustic imaging, optical coherence tomography (OCT), and fluorescence fusion (FL) imaging. In vivo capabilities of

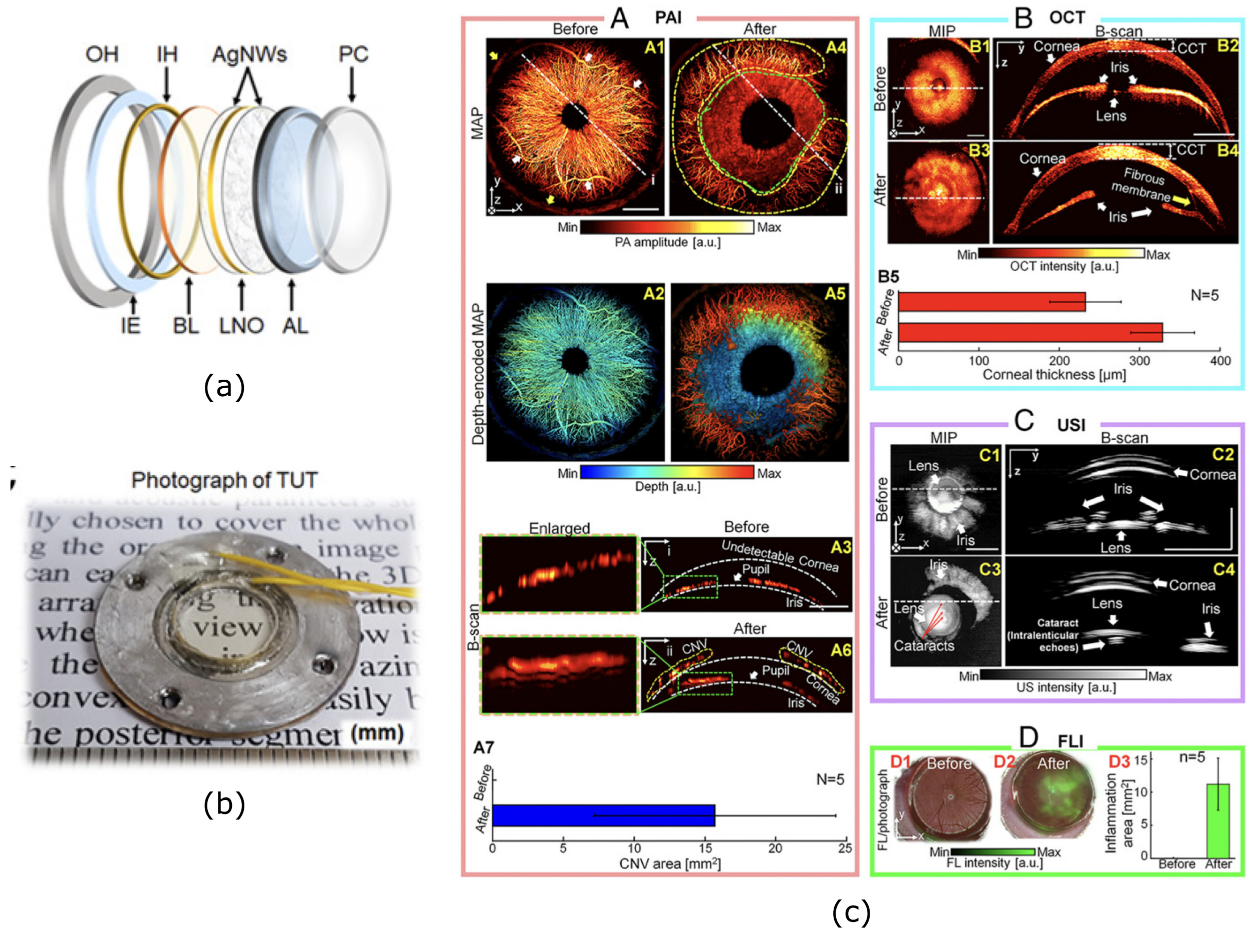

Fig. 8: (a) Layer strucutre of the transparent ultrasound transducer (b) Assembled transparent ultrasound transducer (c) Imaging results of the quadruple imging system. Figure taken from [6]

the system are investigated by imaging rat eyes before and after inflicting alkali burn and suture injuries. Fig. 8c illustrate the imaging results before and after suture injuries. The system also demonstrated advances in multimodality imaging of tumours with and without pigmentation. Thanks to the minimum effect of the transducer on the device through illuminated optical beams, high-quality images were acquired with PA, OCT and FL along with US images. The combination of imaging modalities makes the quadruple fusion system a suitable observation tool for various diagnoses.

Some other similar designs of transparent transducers with the piezoelectric material

are also investaged [56–60]. However, all of the transducers designed with the piezoelectric materials are single-elements, and they require mechanical scanning to form photoacoustic images.

Designing transparent transducers is not limited to piezoelectric materials, and MEMS-based transparent transducers have also been investigated. For example, X. Zhang et al. in [61] demonstrated a single element optically transparent CMUT transducer using SU-8 polymer. The polymer is used to create the vacuum gaps and bonding agent for the wafer bonding process, and the ITO layer is used as the transparent conductive film. Fabricated transparent CMUTs demonstrated %70 optical transparency with an air resonance frequency of 62 kHz.

Glass to silicon anodic bonding fabrication method is also investigated to design single element near-infrared transparent transducers for photoacoustic imaging in [62]. However, since the silicon is not transparent for optical wavelengths, the CMUT demonstrated reduced transparency for wavelengths shorter than 700 nm.

There also has been an attempt to design transparent transducer arrays. J. Cheng et al. [63] introduced a sacrifice layer release process for fabricating transparent transducer arrays for the far-infrared range. The array was fabricated on a 100 μm thick substrate to mitigate the poor transparency of the transducer. The array demonstrated a poor transparency less than %12 for wavelengths longer than 1 μm.

Up to date, there has not been any report of any transparent transducer arrays designed for visible optical wavelengths. Transparent transducer arrays with device-through illumination can enable compelling new opportunities for combined multi-modality ultra-fast imaging systems.

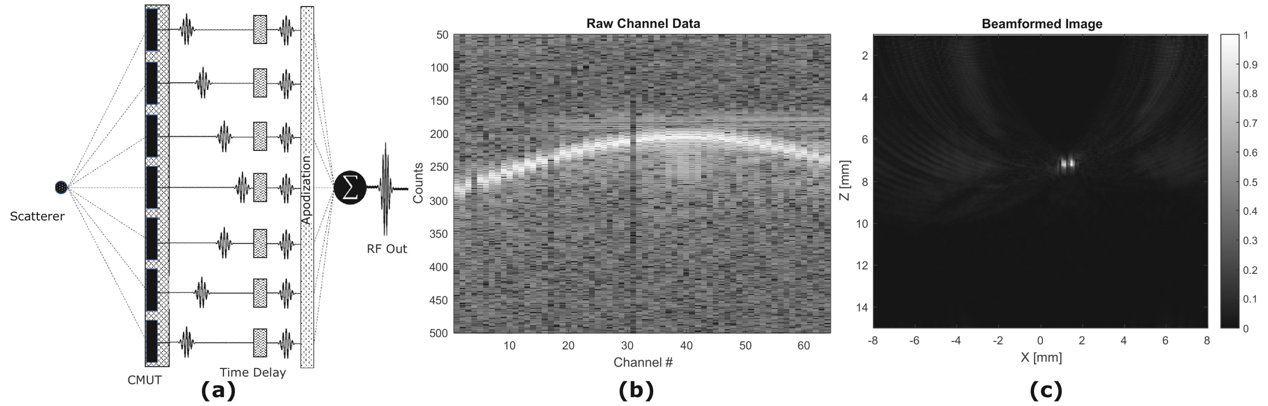

Fig. 9: (a) Receive beamforming used in ultrasound imaging scanners. The time delays applied are proportional to the distance between the region of interest (ROI) and the probe elements. An apodization can be used to reduce sidelobes or control energy. (b) PA raw channel data of a 20 μm gold wire illuminated by 532 nm laser (c) Beamformed image of the collected PA data.

2.6.4 2D transducers with TOBE wiring

2D ultrasound images are generated with 1D ultrasound arrays. This is possible by considering the time of the flight of the ultrasound pressures in the medium. For example, Fig. 9a illustrates a simplified 1D array receiving signals from a scatterer. Elements closer to the target receive the ultrasound pressures earlier than the elements placed on the edges of the transducer. The delay between received signals is demonstrated by plotting the received signals' intensity over time in Fig. 9b. The opposite also can be performed in transmit, where delayed signals can be fed into transducer elements to focus ultrasound pressures on any specific location in a 2D plane.

The dynamic receive beamforming (DRBF) technique [30] is then used to focus the received ultrasound signals. The DRBF technique applies a delay to each channel and sums the values from all the channels for every point on a 2D image. The time delay for each channel is proportional to the distance between the considered point in space and the receiving channel. Fig. 9c shows the beamformed image of the scatterer.

Based on the above assumption that 2D images only require a 1D ultrasound array, generating 3D images would be possible by 2D transducers. The most straightforward approach for creating a 2D array would be connecting every element of the array to a transmit & receive electronics channel and controlling every element individually. This is called a fully-wired 2D array. It would allow for complete control over every pixel of the transducer and make it possible to generate, steer, and focus ultrasound beams on any point of a 3D volume. However, the main limitation to this type of transducer is the requirement of a massive number of transmitting and receiving channels [64]. For example, an array with 32×32 elements would require 1024 transmit-receive channels to be operated, and slightly increasing the array size would increase the channels with N^2 relation, e.g. a 128×128 array would require 16384 channels. Therefore, fully-wired 2D arrays can only be made with a limited number of elements and a small aperture size. On the other hand, a typical 1D array can have a large aperture size, which helps achieve high numerical aperture and thus fine lateral resolution.

One method to address the channel count for larger 2D arrays is the use of micro-beamformers integrated into the transducer [65, 66]. In micro-beamforming, fine-delays are introduced to elements before summing in groups, and coarse delays are implemented in the mainframe. Micro-beamformers may implement tilt-only fine-delays as a linear approximation to a quadratic delay profile. This approach allows a larger aperture size, keeps all elements active and reduces the required channels to operate the transducer. Limitations to this approach are the chip heating problem and requiring expensive ASIC electronic designs.

An alternative method is to use a row-column wiring approach to address the 2D arrays [67]. In a row-column addressed array, top electrodes are in strips orthogonal to bottom

electrodes, and only rows and columns are addressed, sometimes referred to as top orthogonal to bottom electrode (TOBE) array [68]. Thanks to this approach, the number of channels required to operate the array is reduced from N^2 to $2N$.

2D row-column arrays can provide a meaningful larger aperture for 2D imaging than fully-wired 2D arrays, where in some cases, the active area can be 100 times larger, leading to high-resolution images. However, these transducers have some limitations when it comes to ultrasound images. One of the main drawbacks of TOBE arrays is their edge effect [69]. Since elements are connected into long channels, this leads to so-called edge-wave artifacts. To describe in more detail, it would be helpful to consider a scatterer back reflecting ultrasound pressures, which will propagate in an outward expanding spherical shape. When these pressures approach the active channels on the array, each point along the channel will receive signals at a different timing due to their relative distance to the scatterer, and when all received signals add up, the effect-wave artifact appears in the images.

The edge wave artifact can be minimized by the application of apodization on the array [70, 71]. Apodization can be applied physically on the array or electronically [69]. Physical apodization can be performed in several ways, e.g. placing sparse elements on the edge of the transducer and denser at the center of the array, also known as Hanning apodization. However, since physical apodization is hardwired on the transducer, it is impossible to control the apodization dynamically. Another method to apply apodization is to use bias voltages by taking advantage of the bias-sensitivity of the TOBE arrays and dynamically control their receive sensitivity.

Another problem with the row-column addressing (TOBE wiring) is the inability to read all the elements at once. One method to address the problem is to perform synthetic aperture

imaging by performing N number of the transmit/receive events for an N $\times$ N array and actively controlling the row/column for every frame by applying bias patterns [36]. Bias encoding with Hadamard or S-sequence can also be employed to achieve high SNR images. This approach will be explained in more detail in Chapter Six.

2.6.5 Bias sensitivity of ultrasound transducers

Bias sensitivity of CMUT and electrostrictive TOBE arrays is the cornerstone of new bias-encoded imaging schemes where bias voltages are used along with the transmit and receive events to achieve superior image quality. Bias sensitive transducers are sensitive to ultrasound pressure only when they are biased [36].

The sensitivity of a CMUT is defined as the change in capacitance experienced with a change in deflection [39]. Applying bias voltage on the membrane will cause pre-deflection and cause higher sensitivity in the biased CMUT cell compared to non-biased cells on an array. To calculate the deflection of the membrane under electrostatic pressures for CMUTs, A. Havreland and E. Thomsen presented an analytical calculation based on perturbation theory [72]. Change in the capacitance of a CMUT cell with the membrane deflection is non-linear and can be defined as follows [39]:

$$i_c(t) = (C(t) - C_0)\,\frac{dV(t)}{dt} \tag{5}$$

Where i_c is the electrical current passing through the CMUT cell, C_0 is the capacitance of a non-deflected membrane, $C(t)$ is the capacitance of the CMUT, which can be calculated with Eq. 3. A membrane with bias voltage presents more significant changes in $C(t)$ for the

same stimulus on the membrane. Bias sensitivity offers additional control over the activation of target elements in row-column addressing. To demonstrate the bias sensitivity of CMUT devices, we used a previously developed ADS model by Chris Ceroici, and Roger Zemp [73] and performed a simulation. The model is based on the lumped model presented in Fig. 14b. For example, a 5X5 TOBE array (3X3 membrane per cell) is simulated with a 1KPa pressure on the membranes. Columns are DC grounded, and the middle row is connected to a 100 VDC bias voltage. Fig. 10 illustrates a graphical plot of the generated current by each membrane. Simulation results show that the biased elements contribute to over 99% of the received signals on the columns. After scaling the results for a 128 $\times$ 128 TOBE array, the contribution of the dominant elements drops to 79%, which can be improved with higher bias voltages if necessary.

Bias sensitivity of electrostrictive materials is caused by the polarization of domains in the crystal lattice upon being exposed to an external electric field [36]. This polarization will accumulate throughout the bulk material and result in an overall strain (elongation) in the direction of the field. Insulating materials consisting of more than one type of atom will be ionic due to the difference of electronegativity of the atoms and therefore exhibit electrostriction. The resulting strain (ratio of deformation to the original dimension) is proportional to the square of the displacement of the electric field. In addition to bias sensitivity, these materials present bias polarity sensitivity, an important property that is required for bias-encoded imaging schemes with TOBE arrays. For example, in the FORCES imaging scheme, every receive channel is either biased with positive or negative voltages. Thus, the received signal is due to a pressure transient received with a positive bias voltage is effectively polarity inverted with a negative bias voltage. In particular, the response to

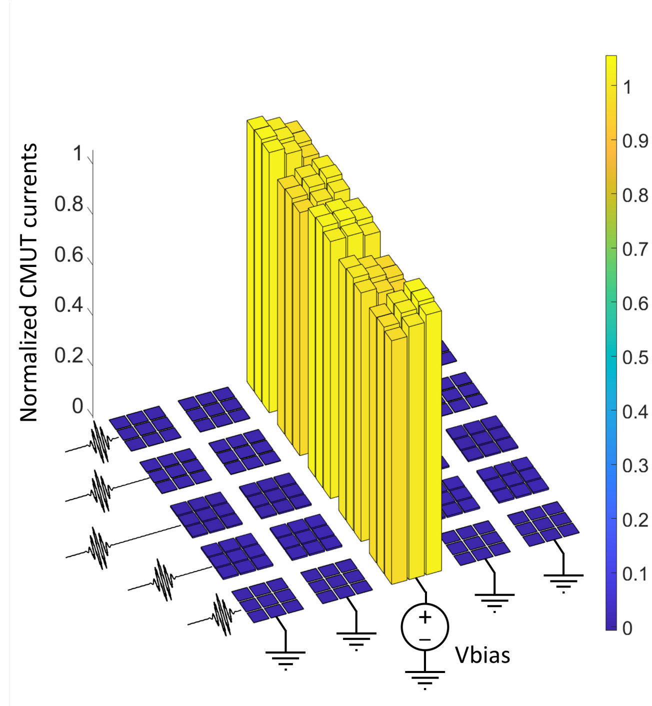

Fig. 10: ADS simulation results of the sensitivity of the channels with and without biasing. The graph illustrates the i_c of every single element normalized to 20 pA. The active channel is biased with 100 V biased and is contributing to the 99% of the received signal.

excitation with a positive bias may be the same as that of an amplitude-inverted excitation with a negative bias. Likewise, the received signal from a pressure transient δp received with a positive bias voltage is effectively polarity-inverted with a negative bias voltage.

We experimentally confirmed the bias polarity sensitivity of the electrostrictive arrays. Fig. 11a illustrates the test setup. For the experiment, a TOBE electrostrictive array was submerged in a water tank, and a single row of the transducer was connected to biasing and transmitting electronics. Four different scenarios were tested by applying positive and negative voltage and transmitting pulses with positive and negative polarities. Next, pressures created in the medium were recorded with a hydrophone. Based on our results, positive bias voltages inverted the pressures created in the medium compared to the polarity of the

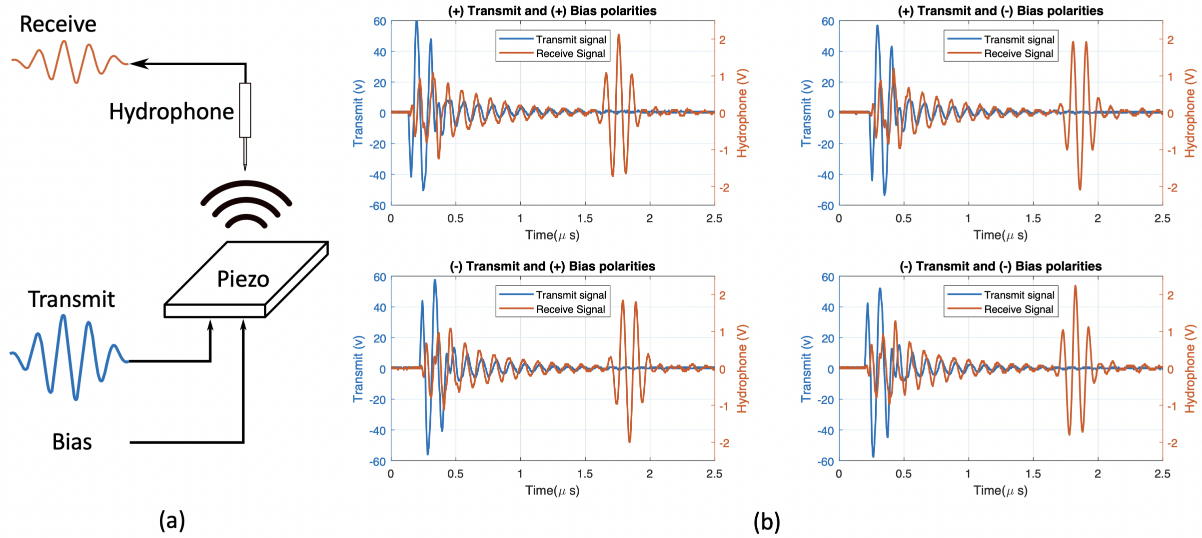

Fig. 11: Bias polarity sensitivity test of an electrostrictive relaxor array. (a) schematic of the test setup, where one channel of the transducer is connected to a biasing electronics and imaging system through a bias tee. The transducer is placed in a water tank, and a hydrophone is suspended over the transducer to record the generated ultrasound pressures. (b) illustrates the test results for positive and negative bias voltages with positive and negative transmit pulse polarity. Based on our results, pressures generated in the medium experienced 180-degree phase shit compared to transmit polarity when positive bias voltages are applied.

transmit signals and negative bias polarity generated pressures following the transmit signals polarity. The results are presented in the Fig. 11b.

Chapter 3: Design and fabrication of transparent CMUT transducers

Objective

Fabricating highly transparent CMUT arrays is beneficial for multi-modality imaging systems. However, fabricating such transducers is highly non-trivial, and most of the transparent ultrasound transducers designed today are single elements transducers. This chapter introduces a new fabrication process flow that will make it possible to reliably and cost-effectively fabricate 1D and 2D CMUT transducers with exceptionally high transparency. The results of the research is published in [12] and presented in IUS 2019, 2020 conferences [14, 18].

3.1 Introduction

Ultrasound transducers are mainly fabricated with piezoelectric materials, in which bulk material is diced into 1D or 2D arrays, and the space between the elements is filled with epoxy [74]. However, the majority of the piezoelectric materials are not optically transparent. On top of that, these materials have higher acoustic impedance than soft tissue, resulting in the back reflection of the ultrasound pressures into the tissue and not being detected with the transducers [22]. Acoustic mismatching is addressed by adding matching layers, posing another bottleneck for designing transparent arrays with piezoelectric materials.

CMUT technology, on the other hand, has naturally better acoustic matching properties to soft tissue, dropping the need for matching and backing layers [12]. Furthermore, the adaptability of the fabrication methods invented for CMUT transducer makes fabricating CMUTs with targeted properties more convenient [75]. For a long time, the main two fabrication processes developed for CMUT devices, wafer bonding and sacrificial release, essentially focused on improving the CMUTs imaging characteristics but not their optical transparency [44]. This chapter introduces a new fabrication process to fabricate highly transparent CMUT arrays.

3.2 One-dimensional transparent CMUT arrays with wafer bonding technique

The primary objective is to develop a new fabrication technique that would allow us to fabricate highly transparent CMUT devices into 1D arrays. The main challenge for designing such transducers is the poor electrical conductivity of the transparent conductive thin-films such as indium-tin-oxide (ITO) needed for electrodes wiring. Another challenge of creating transparent transducers is their light absorption which needs to be kept low to maintain CMUTs' transparency as high as possible. This is important for photoacoustic imaging applications, where high-power laser pulses need to be delivered through the transducer's body and having high absorptions can cause extensive heating and finally destroying the CMUT device.

Currently, none of the leading fabrication processes, including sacrificial release and fusion wafer bonding techniques, would satisfy the requirements for our targeted specifications. Therefore, we propose an innovative fabrication technique using a transparent polymer as a bonding agent and thin-metal strips to improve the channels' electrical conductivity.

3.2.1 Material selection and design considerations

To fabricate transparent ultrasound transducer arrays, we use fused silica substrates coated with a highly conductive indium-tin-oxide layer as a transparent conductive material. Benzocyclobutene (BCB) polymer [76] is used as a bonding agent. This polymer is light sensitive and can be directly exposed to UV light and pattered to create CMUT gaps. Silicon-nitride is used as a membrane material and bonded directly to the BCB polymer. Since all the

materials used in this fabrication process are optically transparent, CMUTs provided over %90 transparency in the visible optical range.

3.2.2 Fabrication overview for 1D transparent CMUTs

In our previous report [77], we demonstrated the design and fabrication of a single element transparent CMUT with the photo BCB wafer bonding technique. Here, we expand the process to fabricate 1D transparent CMUT arrays.

The challenge is the requirement for transparent electrical interconnects across the arrays, where only parenting ITO layers is insufficient as resistance losses along thin and long ITO layers are high (in the ranges of $M\Omega$). Also, the previous fabrication process flow required two layers of photo BCB polymer in the CMUT structure to make the bonding feasible, unnecessarily increasing the gap height and reducing the transducers' transparency and sensitivity. Here, the process flow requires only one photo BCB polymer, and the spacing between the top and bottom electrodes has reduced to 400 nm (previously was 1.3 μm). In addition, thin metal strips are implemented in the CMUT channels to compensate for the ohmic resistivity of the ITO layers. As a result, the CMUTs become more sensitive, requiring less or no bias voltage to operate. We used the proposed fabrication process below to fabricate CMUT arrays with 64 and 128 active elements.

Fig. 12 illustrates the fabrication process flow. The fabrication process involves two wafers: a prime silicon wafer with 1000 $\pm$ 50 nm LPCVD nitride and a glass wafer with a 300 nm high-conductive ITO layer. Nitride prime wafer cleaned in a Piranha solution (a 1:3 mixture of hydrogen peroxide and sulfuric acid) for about 15 minutes. Glass-ITO wafer cleaned with a two-step cleaning recipe to prepare them for a one-layer photo BCB

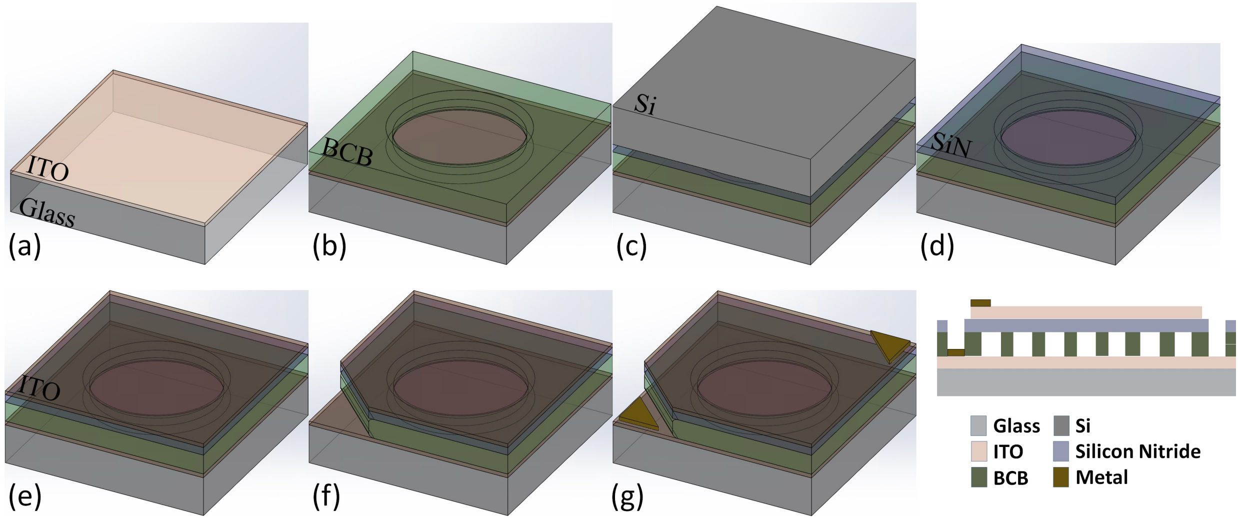

Fig. 12: Fabrication process flow of transparent CMUTs arrays.

bonding process. Initially, the glass wafer bathed in a solution mixture of 1:1:5 hydrogen peroxide, ammonium hydroxide and deionized water at 75 $°C$ for 15 minutes and rinsed with deionized water. Then, the wafer is sonicated in separate baths of acetone, isopropyl alcohol and deionized water, each for 15 minutes and spin-dried(Fig. 12a).

In the next step, adhesive promoter AP 3000 from Dow Chemical is spin-coated on both nitride and ITO wafers with 3000 RPM for 30 seconds, followed by a quick bake at 150 $°C$ for 1 minute. Then, 4 millilitres of photo BCB is spin-coated on the nitride wafer with 6500 RPM for 45 seconds followed by a soft-bake at 60 $°C$ for 90 seconds. Photo BCB exposed to UV light with 140 mJ/cm^2 with maks 1. After exposure, photo BCB is cured with post-exposure bake at 50 $°C$ for 1 minute and puddle-developed for 2 minutes with DS 2100 developer and spin-dried at 2000 RPM for 2 minutes. Fig. 12b presents the patterned BCB layer.

Wafers are bonded with a SUSS wafer bonder (ELAN CB6L) at 250 $°C$ for 1 hour at 5 $mTorr$ chamber pressure and 0.5 MPa compressive pressure. We investigated the bonding

on five wafers, and we had successful bonding on all wafers without any voids. Fig. 12c illustrates the two bonded wafers. Then, membranes are released by etching the handle layer of the prime wafer in 25% potassium hydroxide solution (Fig. 12d).

ITO is used as a transparent conductive coating and sputter-coated on the wafer. The sputtering process is done at room temperature with 50 sccm of Ar under chamber pressure of 6 mTorr. After depositing a 300 nm ITO layer, the ITO layer is patterned into electrode strips with a hydrochloric acid etching process. To improve the transparency and conductivity of the ITO film, a thermal treatment process at 250 $°C$ for 1 hour is performed [77]. Fig. 12e illustrates this step. After performing the third lithography, an access hole to the bottom electrode is created (Fig. 12f).

Then, a metal lift-off process is performed to form the contact pads and the thin metal strips on the channels. We used the AZ5214 image reversal photoresist and conducted an e-beam evaporation process to deposit the metal contacts. Finally, the lift-off process is carried

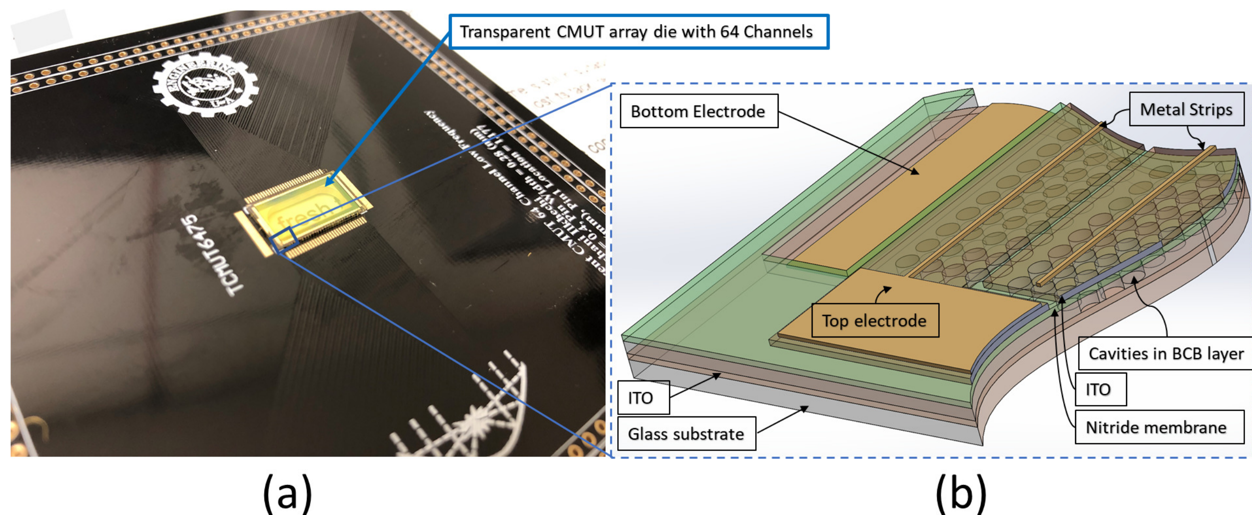

Fig. 13: Photos of the Fabricated CMUT. (a) Wire bonded 64 Channel transparent CMUT die on a PCB board for testing (b) A 3D drawing of a transparent CMUT Chip.

out in an acetone bath. Fig. 12g illustrates the fabricated CMUT with metal pads. We used a combination of chromium, copper and gold metals with 10/950/50 nm thicknesses.

Fig. 13a presents a fabricated die attached to a printed circuit board (PCB) board for a PA imaging test. Fig. 13b illustrates the metal strips fabricated on the channels.

The advantages of the fabricated transparent transducers in this chapter are investigated for device-through photoacoustic imaging and combined optical-ultrasound imaging systems in chapters four and five. Appendix E expands the fabrication of transparent transducers into 2D arrays with TOBE wiring.

Chapter 4: Transparent CMUT linear arrays for device-through illumination photoacoustic imaging

Objective

Photoacoustic imaging has shown great potential for non-invasive high-resolution deep-tissue imaging. Minimizing the optical and acoustic paths for excitation and detection could significantly increase the signal-to-noise ratio. This could be accomplished by transparent transducers permitting through-transducer illumination. Here, we introduce transparent CMUT linear arrays with high transparency in the visible and near-infrared ranges. To fabricate the devices, we used an adhesive wafer bonding technique. Fabricated devices have shown average transparency of 70% in the visible wavelength range, goes up to 90% in the near-infrared range. The result of the research is published in [12]. The published paper includes all the sections except section 4.2 which is original to this chapter.

4.1 Introduction

Photoacoustic (PA) imaging is an imaging modality that exploits the benefits of both optical and ultrasound imaging systems [77, 78]. Generally, in this technique, a laser pulse illuminates tissue. The targeted tissue experiences sudden localized heating and expands due to thermal expansion. The expansion generates acoustic pressure, which propagates and is detected by an ultrasound transducer. An image can be reconstructed based on the amplitude of the detected signals where time-of-flight encodes depth [79]. Pure optical imaging systems can produce high-resolution images with optical contrast, but light scattering in the tissue limits resolution and penetration depth. [80,81]. Achievable depth with the optically-focused resolution is limited to the optical transport mean free path. In biological tissues, the optical transport mean free path is on the order of 1 mm [74] for red to near-infrared light. On the other hand, ultrasound imaging techniques use an ultrasound beam for excitation and records the back-scattered acoustic waves to generate images with acoustic scattering contrast [79]. Ultrasound beams can penetrate tissues with low scattering losses and can achieve high depth penetration, and fine resolution limited by acoustic diffraction [22]. However, ultrasound imaging can only map the mechanical properties of the tissue, while optical imaging systems can monitor the biological states of the tissue, such as oxygenation of blood vessels [82]. PA imaging mixes the advantages of optical contrast and acoustic penetration to generate high-resolution images deep in the tissue. Since this technique relies on acoustic wave detection, it is tolerant of multiply-scattered photons. In comparison, PA imaging can produce images with depth to resolution ratios of few orders of magnitude compared to optical microscopy imaging systems [83, 84]. The lateral resolution of a PA imaging system

is mainly determined by the transducer's receive frequency and F-number and is typically hundreds of microns for diagnostic frequencies. Axial resolution is mainly determined by the reciprocal of the bandwidth of the transducer. A comprehensive comparison between PA imaging and ultrasound systems is provided in [23].

A key component of a PA imaging system is the ultrasound transducer. Transducer specifications such as central operation frequency, element pitch, and receive sensitivity play an important role in determining the characteristics of a PA imaging system. There are several possible detection platforms used for ultrasound detection. These include optical resonators [85–87], piezoelectric transducers [88–92], and capacitive transducers [68, 93]. Piezoelectric transducers are well developed and widely available but are, for the most part, non-transparent. Recently, single element transparent piezoelectric transducers were introduced that were primarily used in optically-scanned PA imaging systems [94]. Optical resonators have excellent sensitivity, but the image acquisition time is not efficient.

CMUTs utilize capacitive sensing to detect ultrasound waves [95, 96]. CMUTs have two parallel plates, one fixed as a bottom electrode and one clamped membrane suspended above the bottom electrode with a top electrode. When ultrasound waves hit the top electrode, it vibrates the membrane and modulates the capacitance of the CMUT device. Thus, ultrasound wave detection is done by monitoring the capacitance of the CMUT over time. As a result, CMUTs have several advantages over other transducers mentioned above, such as broader bandwidth, the potential for massively scalable fabrication, higher electro-mechanical efficiency and potential for CMUT-on-CMOS compatibility [40–43]. CMUTs, unlike piezoelectric transducers, do not need matching layers for acoustic impedance matching to the tissue.

Even though CMUTs have shown excellent potential for PA imaging, the majority of the CMUTs fabricated up to date are not optically transparent, or they present inadequate transparency in the visible range [62, 63]. In PA imaging, this leads to choosing different optical excitation and ultrasonic detection paths [97]. Transparent transducers have the advantage of delivering the laser beam through the device. This minimizes the optical path and acoustic paths, thus leading to less attenuation, improved uniform illumination, and improved SNR [77].

We recently introduced a transparent CMUT architecture fabricated using an adhesive wafer bonding process and demonstrated photoacoustic signal detection using single-element transducers containing many CMUT membranes [77]. The fabrication process involves a glass substrate, photo BCB polymer as a bonding agent, silicon nitride as a membrane material and Indium Tin Oxide (ITO) as a conductive coating. All of the mentioned materials have acceptable optical transparency, and the fabricated devices have transparency above 80% in the visible range. However, single-element transducers are not very useful for acoustic-resolution PA tomography, they can be mechanically scanned to acquire the image, but this is slow.

In this study, our primary objective is to design transparent CMUT arrays for PA imaging and fabricate them with the wafer bonding process introduced in Chapter three. Fabricated transducers have 64 and 128 channels with an operating frequency of 8 MHz and transparency of up to 90% in the visible range. To validate the operation of the CMUTs, we have performed PA imaging of a 20 μm gold phantom wire in oil immersion mode. Our PA imaging test recorded an SNR value of 40 dB and special lateral and axial resolutions (in the 3dB bandwidth) of 234 μm and 220 μm.

4.2 Design and simulation

Designing CMUT transducers requires an accurate model that can predict the corresponding frequency response, sensitivity, output pressure and snapdown voltage of the CMUT. Equivalent circuit models for CMUTs based on Mason's equivalent circuit [98] have shown a computational superiority to the FEM simulations. A large signal lumped circuit model is developed and verified with FEM simulations in [39]. We used the modified and improved ADS model by Chris Ceroici and Roger Zemp [73] to obtain the design parameters for the transparent CMUT arrays. Table 2 presents the parameters for the transparent CMUT arrays. Fig. 14 illustrates the simulation results for the frequency response of the transparent CMUT. Membranes present smaller deflections and lower resonance frequency when submerged in the water.

Transparent CMUTs introduced in this work contain nitride membranes that act as the dielectric between the top and bottom electrodes and prevent short-circuiting while a CMUT is in a collapsed state. With a membrane thickness of 1um, the nitride layer can withstand

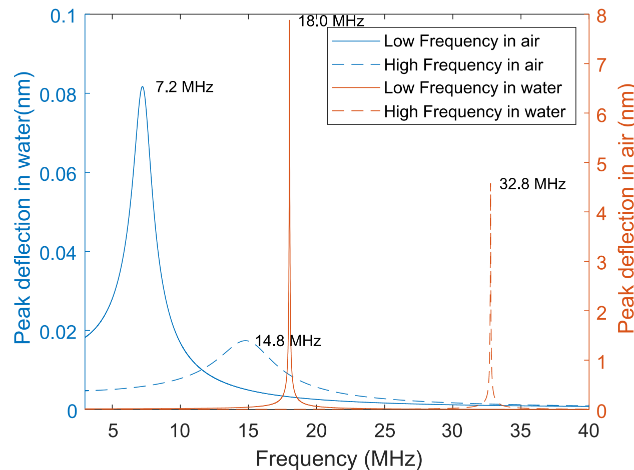

Fig. 14: ADS simulation of the frequency response of the proposed transparent CMUT arrays. Simulation parameters are presented in Table 2

Table 2: Design parameters of the transparent CMUT arrays

Device Parameter	Low Freq.	High Freq.
Membrane radius (μm)	17.75	13
Number of the membranes per element	656	675
Element pitch (μm)	204	102
Kerf (μm)	26	14
Membrane thickness (nm)	~950	~950
Number of the elements	64 & 128	64 & 128
Gap height (nm)	550	550

voltages up to 1100 V (nitride has breakdown voltages up to 1.1 MV/cm [99]). Snapdown voltages for the low and high-frequency CMUT are computed for a gap height of 550 nm. Our study shows the low and high-frequency arrays' snapdown voltages of 380 V and 740 V, respectively.

Length, width, and spacing between the channels are also essential and need to be precisely designed. The Pitch of the elements is related to the speed of sound in the medium and the central membrane frequency. Kerf, the spacing between the channels can be optimized with the lumped circuit model to minimize the membranes' cross-talk.

4.3 Characterization

4.3.1 Transducer structure and dimensions

Fig. 15 shows one of the fabricated transparent CMUT arrays. The die has 64 operational channels designed for 8 MHz operation in immersion mode and has a 7 mm by 13 mm active area. Fig. 15a shows a camera photo of the die on top of the University of Alberta logo where the logo is visible through the die. Fig. 15b illustrates a microscopic picture of the channels and the cells with their actual dimensions. The device contains 64 elements, each element consisting of 656 individual CMUT cells. In total, the device has nearly 42000 CMUT cells.

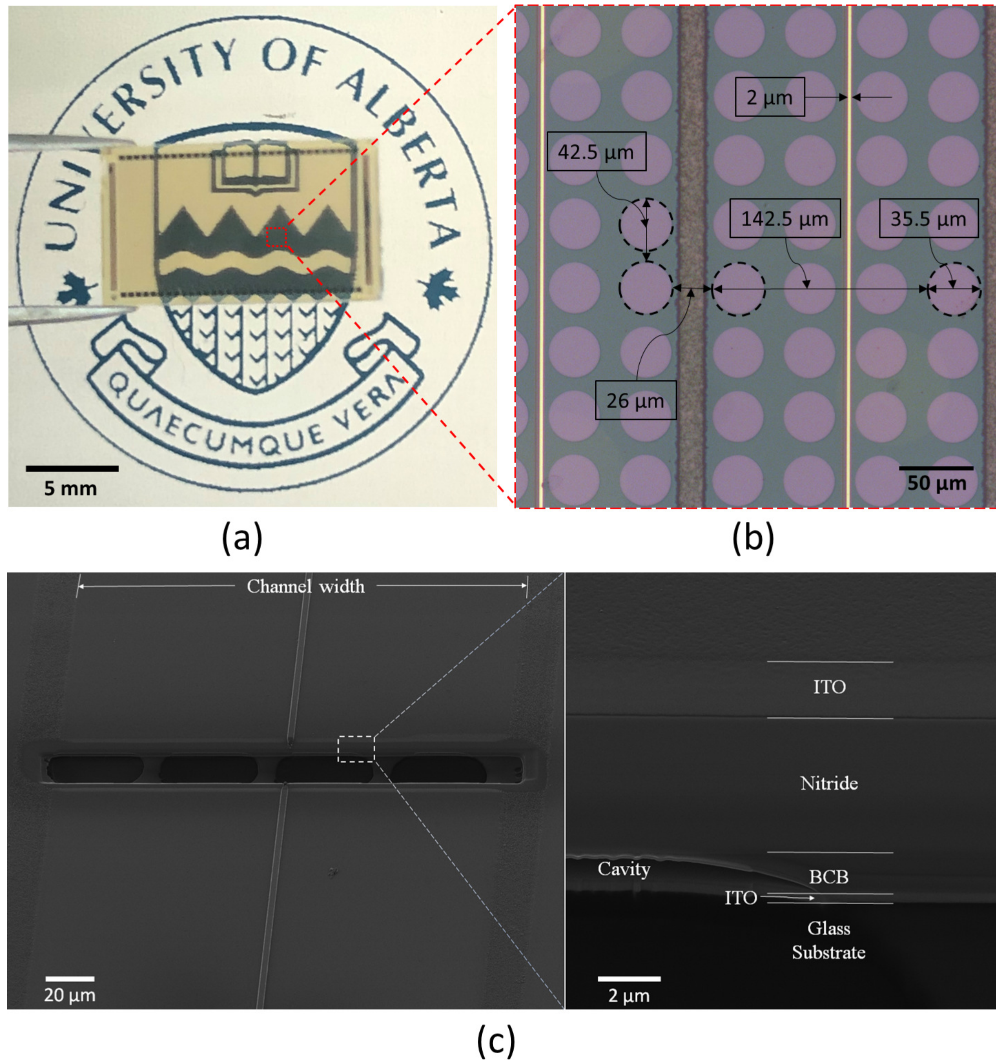

Fig. 15: Images of a fabricated transparent CMUT array with 64 channels (a) A photo of the array, where the University of Alberta's logo can be seen through the device. (b) Microscope image of the die showing membranes within elements, along with their associated dimensions. The die has a pitch of 204 μm and a kerf of 26 μm. The pitch is close to the center frequency wavelength. (c) Helium ion microscope image of the cross-sectional structure and the thicknesses of the layers.

A focused ion beam (FIB) is used to create a cut on the CMUT membrane and expose the cross-sectional structure. With the help of a helium ion microscope, the structure is inspected. Fig.15c. illustrates the cross-sectional image of the transducer taken by the helium ion microscope at 54 $^{\circ}$ degrees. The layers are visible in the picture, but thicknesses

Table 3: Transparent CMUT arrays' structural dimensions.

Metal strips thickness	1.5 μm
ITO (Top electrode)	300 nm
Silicon nitride	954 nm
Cavity depth	400 nm
ITO (Bottom electrode)	100 nm
Cell Diameter	35.5 μm
Number of the cells in each channel	656
Number of the channels	64 & 128
Pitch	204 μm
Kerf	26 μm

do not appear to scale because of the view angle. Actual thicknesses for each layer are calculated and presented in Table 3.

4.3.2 Transducer transparency

The transparent CMUT arrays fabricated in this work contain six layers. Layers are: glass substrate, ITO layer for bottom electrode, photo BCB, nitride, ITO as the top electrode, and metal strips. Five of the layers have good transparency in the visible wavelength, and their transparency measurement is presented in our previous publication [77]. Metal strips only cover less than 1% of the device area and have shown no significant impact on transparency. As a result, the fabricated CMUT arrays have excellent transparency ranging from UV to NIR. The transparency of the device is measured with a Perkin-Elmer NIR-UV Spectrophotometer. As shown in Fig. 16, the device has average transparency of more than 70% that goes up to 90% in the near-infrared range. We believe that the transparency of the device can be further improved if layers, such as ITO, get deposited in industry-rated deposition tools and if anti-reflection coatings are considered.

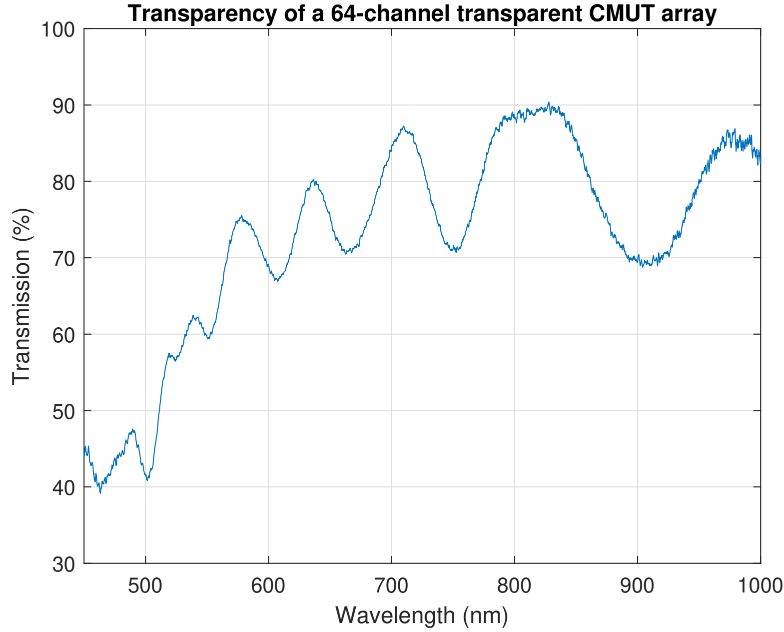

Fig. 16: Transparency measured by spectrophotometer of the fabricated transparent CMUT arrays with 64 channels

4.3.3 Device receive sensitivity

The sensitivity of a transducer plays an important role in determining the signal-to-noise ratio (SNR) of a PA imaging system. In order to determine the sensitivity of the transparent CMUT arrays, we used calibrated acoustic pressures generated with an external transducer and detected by the fabricated CMUTs. With a bias voltage of 40 V, a receive sensitivity of -251 $dB\ V/\mu Pa$, noise equivalent pressure (NEP) of 67 $mPa/\sqrt{Hz}$ and channel SNR of 37.7 dB was recorded. Sensitivity has a direct relation with the bias voltages where sensitivity reaches 10.4 $mPa/\sqrt{Hz}$ with a bias voltage of 250 V. Fig. 17a illustrates the sensitivity versus bias voltage of the fabricated CMUT array. Comparing our NEP results with previously published CMUT and piezoelectric transducers confirms that the transducer's transparency is not compromising the transducer's sensitivity. Previously reported transducers demonstrated NEPs ranging from 0.55 $mPa/\sqrt{Hz}$ up to hundreds of

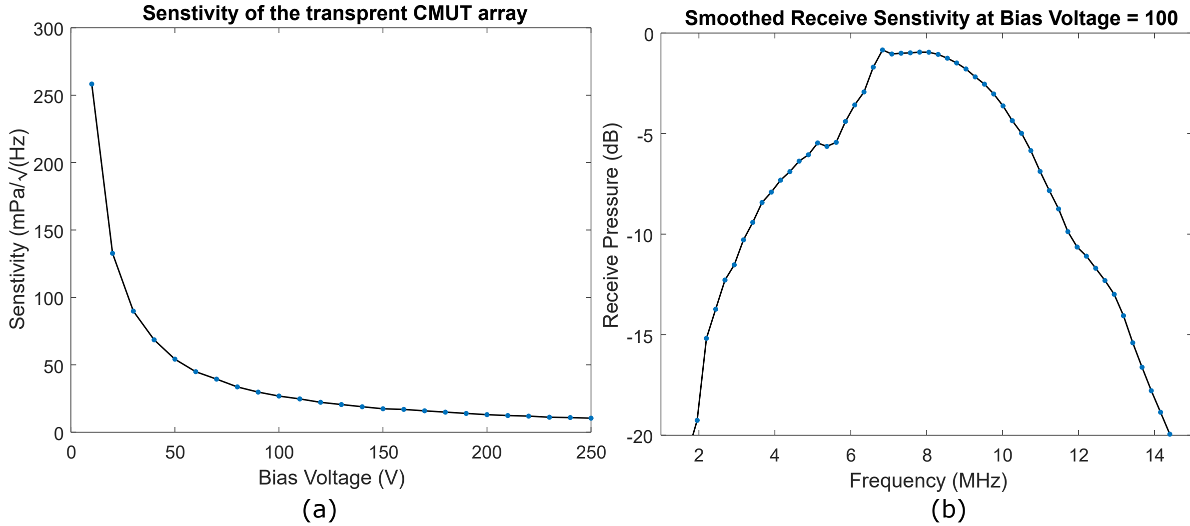

Fig. 17: Results of receive sensitivity test of the transparent CMUT array. (a) Receive Senstivity v.s. bias voltage of a single element of the array (b) Frequency response

$mPa/\sqrt{Hz}$ [68, 92, 97, 100–107].A comprehensive comparison between CMUT and piezoelectric transducer sensitivity is presented in [108].

The frequency response of the transducer is carried out by taking a fast Fourier transform (FFT) of the received signal. Fig. 17b illustrates the frequency response of the transducers. The graph shows that the CMUT signal had a central frequency of 8 MHz with a -6dB fractional bandwidth of 75 %.

Crosstalk between the elements can degrade the performance of the array. Previous literature indicates CMUT array crosstalk levels at -23dB or -39dB in collapse-mode operation, comparable with other piezoelectric arrays. A more thorough crosstalk analysis should be conducted in future work. [109].

4.3.4 B-scan PA imaging

The setup for the PA images is shown in Fig. 18a & b. The fabricated transducer is wire-bonded to a detachable PCB board that can plug into an interfacing board containing the

pre-amplifiers and the bias tees. The board then connected to a research ultrasound platform (Verasonics Vantage 256). The PCB contains a clear aperture to deliver the laser light through the transducer. A transparent tank is glued on the PCB and filled with vegetable oil, mimicking soft tissue. 20 μm gold wires as phantoms are submerged in the oil, having a perpendicular orientation with the transducer. A 532 nm pulsed Nd:YAG (Surelight III, Continuum SLIII-10) laser with a 10 Hz repetition rate is used to delivered light to the target phantom. Fig. 18c & d are photos of the explained setup. After transmitting the laser pulse to the target, photoacoustic waves are recorded, and B-scan images are generated. B-scan images are generated with the delay and sum receive beamforming (DBRF) technique [30, 110] but in current work no elevational focusing was used. This could be incorporated using a transparent acoustic lens in future work. Imaging is done in two different laser delivery modes: through the CMUT and through the transparent tank. Fig. 18e illustrates the beamformed image of two gold wires with laser delivery through the tank. Results presented lateral and axial resolutions of 483 μm and 207 μm, respectively (with an array of 64 channels). Fig. 18f illustrates the PA imaging test result for delivering the laser beam through the transparent CMUT array. The test is performed with both 64- and 128-element arrays. Resolution for through-array transmission remained the same as the through-tank transmission for the 64-channel array. For the array with 128-channels lateral and axial resolutions of 234 μm and 220 μm, respectively, were obtained. Table 4 presents the SNR values collected for each experiment. Laser fluence presented in the table is measured before passing through the transducer or the transparent tank, and fluence reaching the target may be smaller due to transmission losses.

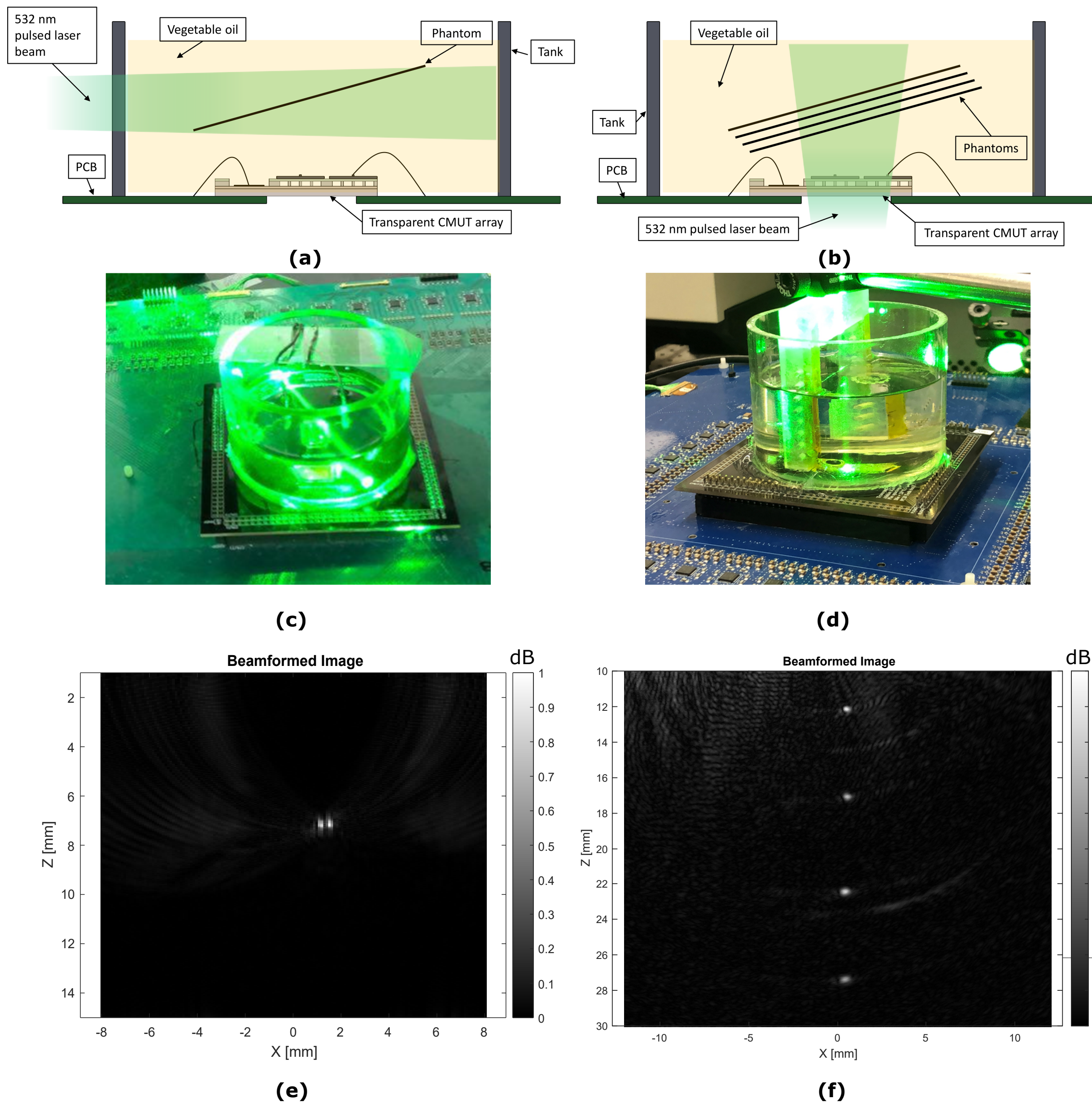

Fig. 18: (a) Drawing of the experimental PA setup with laser delivered through the transparent tank on a gold wire phantom. Wires are positioned orthogonal to the CMUT arrays and placed with 5 mm spacing in the Z-axis. (b) Drawing of the experimental PA setup with laser passing through the transparent CMUT array and 20 μm gold wire phantoms. (c) A camera image of the imaging setup with the transparent CMUTs with a laser passing through the tank. (d) A camera photo of the PA setup with a laser delivery to the targets by passing through the transparent CMUT arrays (e) Beamformed image of the PA test guiding laser through the tank. (f) Beamformed image of the collected PA data of laser-illuminated through the transducer. All four wires are detected with the transducer.

Table 4: B-scan results comparison for Transparent CMUT for various DC bias voltages and laser powers

Test	Laser delivery	DC Bias (V)	Intensity (mJ/cm^2)	SNR(dB)
1	Through Tank	30	10.7	28.5
2	Through Tank	50	21.8	32.25
3	Through CMUT 64 Ch	42.5	21.8	35.5
4	Through CMUT 64 Ch	65.5	14.93	35.5
5	Through CMUT 128 Ch	30	10.7	38.9
6	Through CMUT 128 Ch	30	13.5	40

4.3.5 Durability test

We have performed several PA tests with the same fabricated transducer in a period of a few months in pre-collapse mode operation. In each test, CMUTs were tested over a three-hour continuous test, and results remained the same. The same tests repeated several times over three months showed no degradation and exhibited reliable pre-collapse operation, good hermetic sealing and minimal charging.

Conclusion

In this chapter, we presented the design and characterization of the first 1D transparent ultrasound array and demonstrated its application for photoacoustic imaging applications. Transparent CMUT arrays were fabricated with a polymer adhesive bonding process where photo BCB was used as a bonding agent, ITO as a transparent conductive layer, and silicon nitride as a transparent membrane. The fabricated CMUT array has shown excellent transparency up to 90% in the visible and NIR range. The device has demonstrated an operational immersion frequency of 8 MHz and a receive sensitivity of 10.4 $mPa/\sqrt{Hz}$ with a bias voltage of 250V. B-scan PA imaging has shown an SNR of 40 dB for PSF imaging of a 20 μm gold phantom with an imaging lateral and axial resolutions of 234 μm and 220 μm,

respectively (with 128-channel transparent CMUT array).

Chapter 5:Transparent CMUTs for combined optical-ultrasound endoscopy systems

Objective

Transparent ultrasound transducers could enable many novel applications involving both ultrasonics and optics. Recently we reported transparent capacitive micromachined ultrasound transducers (CMUTs) and demonstrated through-illumination photoacoustic imaging. This work presents the feasibility of transparent CMUT transducers for combined ultrasound imaging and through-array white-light imaging with a miniature camera placed behind the array. Realtime plane-wave imaging is performed for ultrasound imaging, and lateral and axial resolutions of 234 and 338 μm are achieved. Transparent CMUT has demonstrated a high transmit sensitivity of 1.4 kPa/V per channel with a 100 VDC bias voltage. The signal-to-noise ratio for a beamformed image of wire targets is determined to be 28.4 dB. This is the first report of combined realtime optical and ultrasonic imaging with transparent arrays. This technology may enable one to visually see what is being scanned and scan what one sees without co-registration errors. The result of the research is published in [16] journal and presented in SPIE 2020 conference [17].

5.1 Introduction

Most ultrasound transducers are opaque, limiting their combined use with important optical methods. Transparent ultrasound transducers could enable emerging novel technologies. For example, transparent arrays could enable exact co-registration of optical- and ultrasonic imaging, enable through-illumination photoacoustic imaging, and may have novel applications to non-medical technologies such as smart ultrasonic touchscreens and biometrics such as transparent ultrasonic fingerprint scanners. Here we develop transparent ultrasound linear arrays for combined ultrasound- and white-light camera imaging with the objective of optical visualization of the scanning targets that are depth-imaged with ultrasound.

One motivating application for this technology is multi-modality endoscopy. Endoscopy makes it possible to inspect and diagnose the gastrointestinal tract [7] and is a tool for interventional and surgical procedures. Superficial visualization is a limitation of camera endoscopy, making it hard, and sometimes impossible, to detect deeper disorders. To address this, endoscopic ultrasound imaging technology can be used to reveal depth-related information beyond the surface [8]. This includes visualization of lungs, gal bladder, pancreas, and liver without the need for surgical exposure [9, 10]. High-frequency endoscopic ultrasound may also enable assessment of depth of invasion in gastrointestinal malignancies. However, gastro-enterologists and surgeons currently have endoscopic ultrasound technologies that are poorly co-registered with optical endoscopy [111–113]. Improved co-registration between optical and ultrasonic imaging methods could lead to reduced procedure times, miniaturized probes, more confident navigation and more accurate diagnosis. Such improved co-registration could be achieved with transparent ultrasound transducers. However,

development of transparent transducers is non-trivial.

Transparent piezoelectric transducers were recently fabricated with lithium niobate [4]. These transducers provided high transparency in the visible wavelength range, however, the investigators developed only single element transducers, not arrays. Difficulty achieving transparent backing and matching materials is another drawback of these transducers, resulting in unwanted ringing and poor transmission efficiency due to acoustic impedance mismatches. On the other hand, transparent CMUTs require no such layers and can be made highly transparent. Optical-based ultrasound transducers such as Fabry-Perot etalons [114, 115] can be made transparent, and while they possess high receive sensitivity, they, require long optical readouts, require non-transparent layers to achieve ultrasonic excitation, and can not achieve steerable ultrasound transmit focusing. CMUTs have also been shown to exhibit exquisite receive sensitivity, albeit with only modest transmit sensitivity. Previous works on transparent CMUTs include NIR-transparent CMUTs by Zhang et al. [62] and Chen et al. [63]. However, these provided poor visible-light transparency due to the use of silicon layers in the CMUT structure. Our group previously introduced highly transparent immersible CMUTs in the visible wavelength spectrum for the first time. Li et al. first introduced such transparent CMUTs by fabricating single element transducers using transparent Silicon Nitride membranes, transparent indium-tin-oxide (ITO) electrodes and a transparent adhesive bonding agent. We further improved the fabrication and introduced transparent linear arrays for photoacoustic imaging applications [12]. Here we introduce transparent CMUT linear arrays for combined ultrasound and white-light optical imaging using a miniature camera embedded behind the array.

One of the potential challenges in achieving high ultrasound image quality with such

transparent CMUTs could be acoustic reverberations in the glass substrate. Another challenge is to achieve sufficient optical transparency when using a large number of wired elements, since thin-strip ITO electrical conductivity is poor and requires augmenting the conductivity with metal strips. Finally, acoustic transmit- and receive performance of such devices must be validated.

5.2 Methods

Transparent CMUT arrays were fabricated using an adhesive wafer bonding process discussed in Chapter three. The device cross-section with a photo of a fabricated CMUT die is shown in Fig. 19. With this fabrication process, we developed 64- and 128-element lambda-pitch linear arrays targeting 7.5 MHz center frequency.

Fig. 20 shows a diagram of our ultrasound combined ultrasound-optical imaging system. Optical imaging is performed with a small 6×6 mm colour charge-coupled device (CCD) camera. The camera has a 5 MP resolution, and with the help of a high-speed driver board, the camera can captures high resolution videos at 60 frames per second. Ultrasound imaging is performed with a 128-element transparent CMUT transducer array. An application-specific

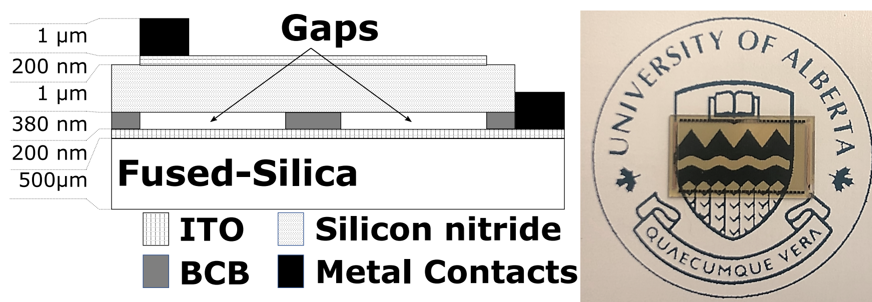

Fig. 19: (Left) Cross-sectional drawing of the CMUT structure (Right) A photo of transparent CMUT over University of Alberta logo demonstrating the device transparency.

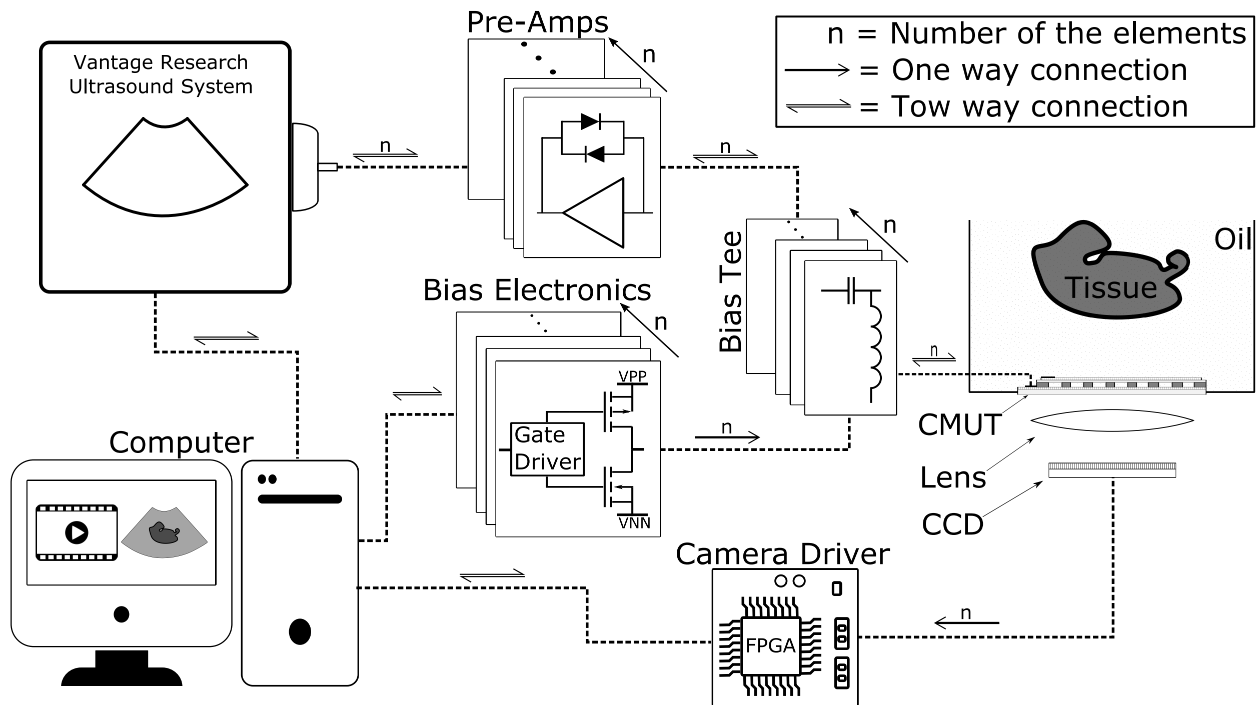

Fig. 20: Diagram of our combined ultrasound-optical imaging system using transparent linear array CMUT transducers .

printed circuit board (PCB) is designed to connect our programmable ultrasound system to the CMUT die. Each element of the transducer is connected to a bias-tee to bias the CMUT and transmit or receive the ultrasound signal.

For biasing the CMUT elements, we have developed a high voltage H-bridge MOSFET configuration that provides sub-microsecond switching time and bi-polar biasing up to ±250 VDC on each channel, independently. Fast switching is useful for bias encoded imaging schemes, which can provide opportunities for future high-quality 2D/3D imaging [92].

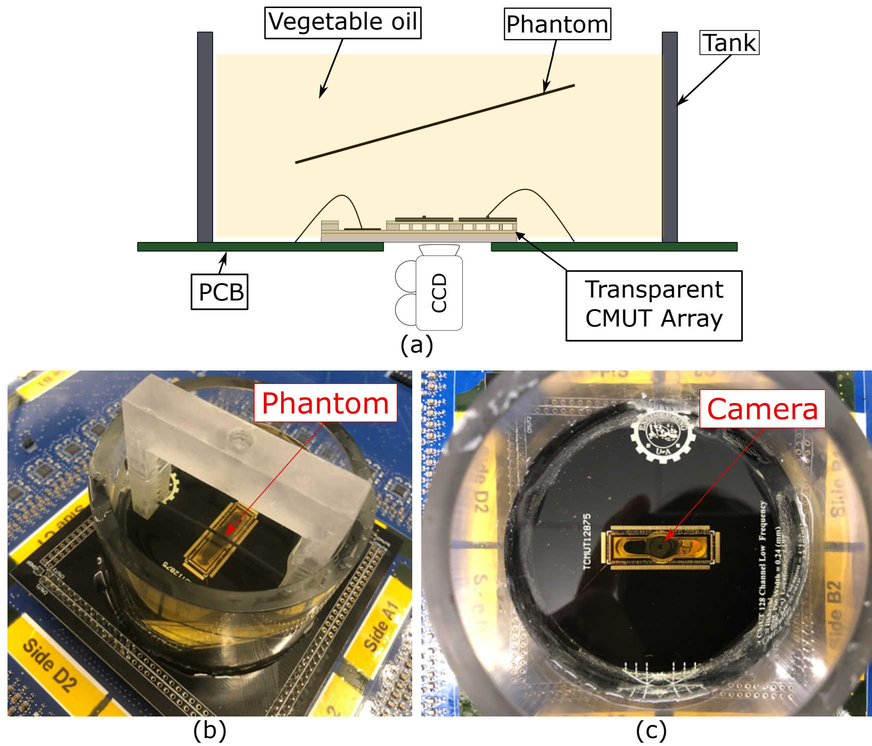

Fig. 21: Ultrasound transparent array evaluation setup. (a) A cross-sectional view of the setup, (b) Side photo of the setup illustrating the phantom wire targets and the ultrasound sensor, (c) Top view of the the setup, showing the camera position under the CMUT die.

5.3 Results

Ultrasound transmit-receive signals are recorded with a 256-channel Verasonics Vantage research ultrasound system. CMUT elements are operated with a central transmit frequency of 9 MHz. To minimize parasitic capacitance and improve the signal-to-noise (SNR) ratio of the received ultrasound signal, for each channel, a voltage-protected low-noise pre-amplifier (MAX4805A) is placed in the path between the CMUT and the ultrasound system. The breakout PCB board has an opening under the CMUT die for positioning the camera behind the transparent CMUT device. An acrylic tank is glued on the PCB and filled with vegetable oil to mimic the tissue. A wire phantom is suspended above the die as an imaging target. Fig. 21a illustrates the cross-sectional view of the setup, and Fig. 21b & c present a side

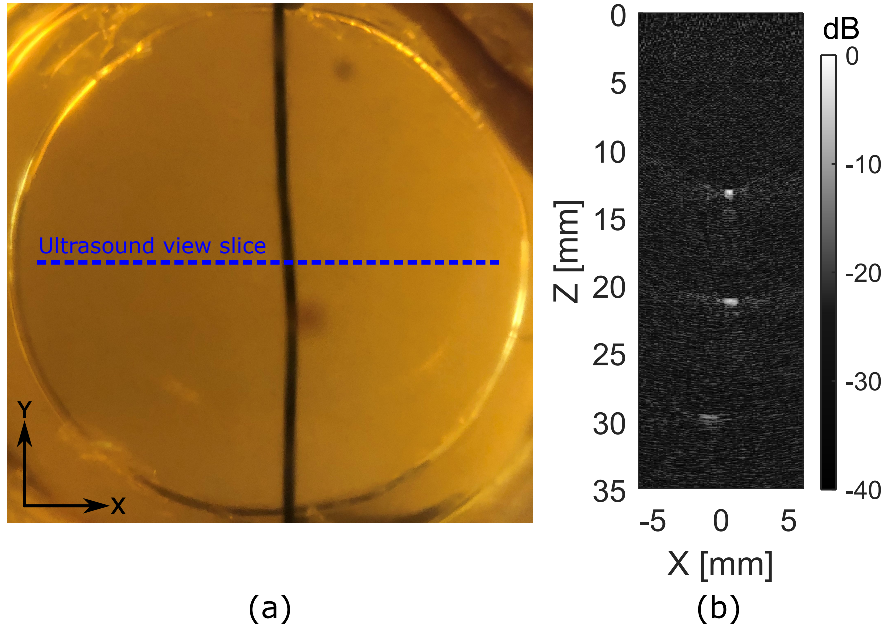

Fig. 22: Combined optical-ultrasound imaging test results. (a) Camera shot of the wire phantom through transducer, (b) Beamformed image of the wire phantom targets with 10 mm spacing. For ultrasound imaging, plane-wave imaging is performed with a bias voltage of 100 VDC on all elements, and transmit signal amplitude is set to 30 V_{pp}. A full-length video recording of realtime optical-ultrasound imaging is provided as supplementary material (see Visualization 1).

view and a top view of the die and the camera.

Plane-wave ultrasound imaging is performed with 100 VDC bias voltage and 30 V_{pp} transmit signal amplitude. After receiving the ultrasound signal, a CPU delay-and-sum beamforming technique [30, 110] is used to generate the beamformed images. Fig. 22a & b illustrate the optical and ultrasound images of the wire-phantom. Video capture of the moving phantom wire and realtime ultrasound beamforming is provided as supplementary material Due to computational limitations, ultrasound display is rendered with 47 frames per second.To demonstrate the ability of the array for ultrasound imaging of tissues, we imaged an ex-vivo rat heart with an inserted needle. A photo of the experimental setup, along with optical and ultrasound images is shown in Fig. 23. The needle location is apparent as the

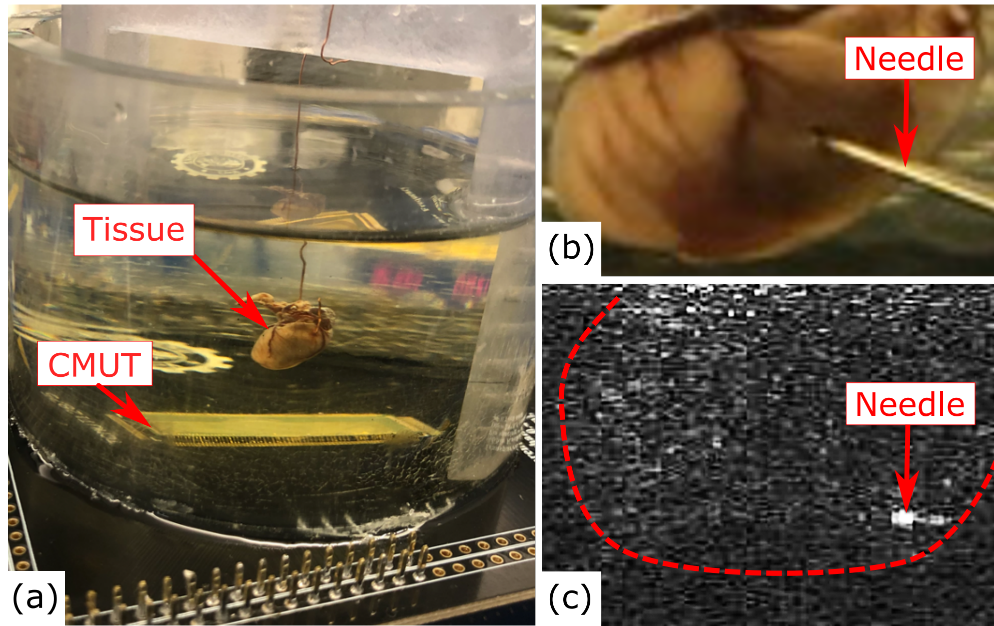

Fig. 23: a) Photo of ex-vivo experimental setup, b) Camera image of tissue with needle, c) ultrasound image using the transparent CMUT array.

bright spot in the ultrasound image.

Optical imaging through transparent CMUT may experience optical distortion and reduced image quality. To determine the image distortion caused by the CMUT, a USAF 1951 target is imaged. Two optical images are taken before and after installing the CMUT in front of the camera. Fig. 24a & b presents the photos. A negligible image distortion is recorded by comparing the results where the camera's resolution remained the same for both photos at 12.70 lp/mm (line pairs per millimetre).

Generating high SNR ultrasound images is highly dependent on transmit and receive sensitivity of the transducer. High-pressure ultrasound waves penetrate deeper in tissue and produce stronger back-reflected ultrasound pressures, resulting in high quality images. To determine the transducer's transmit sensitivity, a pulse with 100 μJ energy is applied (Olympus 5900PR Pulser Receiver) to a single element of the transducer and generated pressure

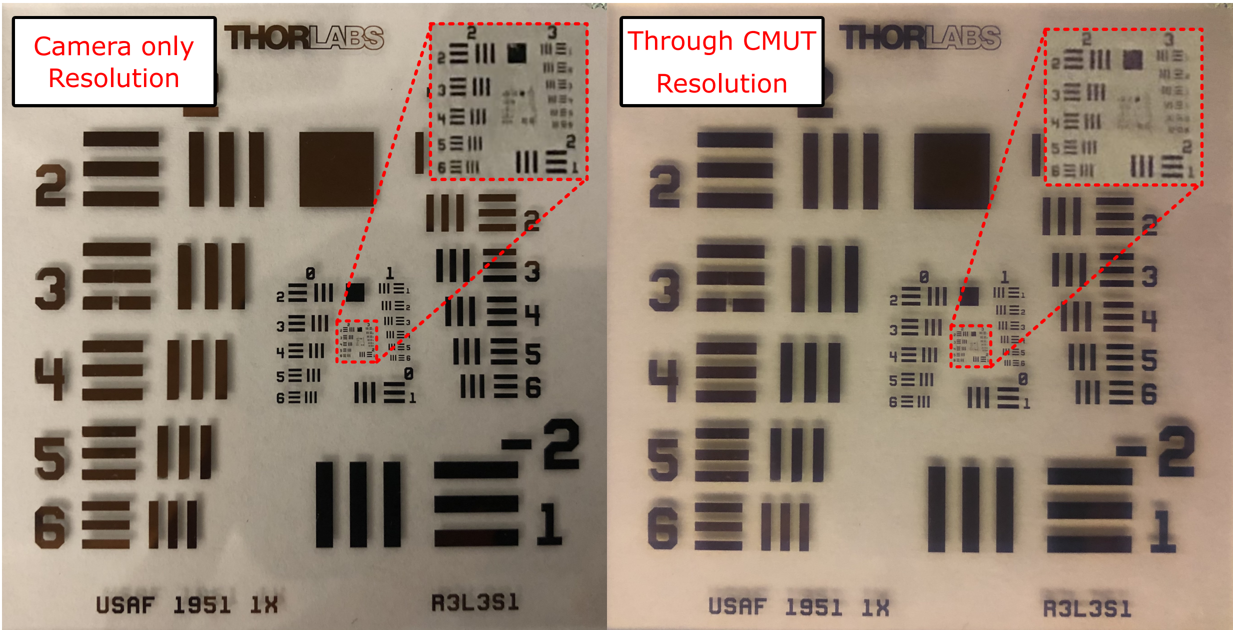

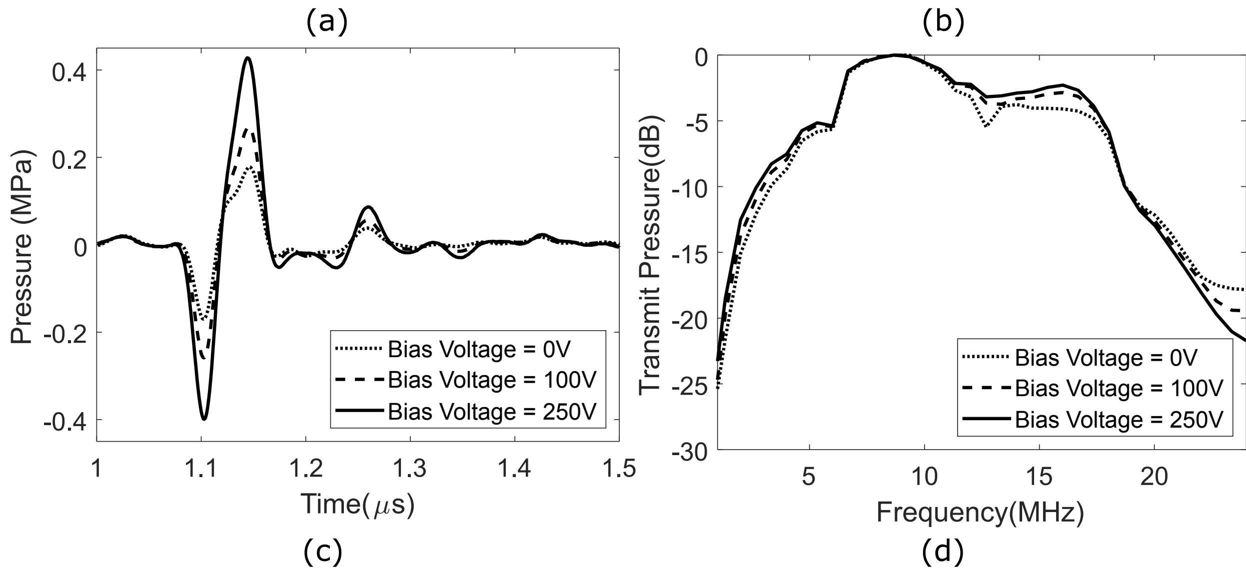

Fig. 24: Optical and ultrasound characterization of the setup (a) Camera resolution test with USAF 1951 target without attaching the transparent CMUT. (b) Camera resolution test through CMUT. (c) Time-varying acoustic pressure generated with a single element of the transparent CMUT due to a transmit pulse with 100 μJ energy under various bias voltages. (d) The frequency response of the transmit sensitivity. The central operating frequency is determined to be 9 MHz with a fractional bandwidth of 150%.

is recorded with a hydrophone (Onda NHP-0400). Without a bias voltage, each element generated ultrasound pressures over 0.2 MPa peak-to-peak, which could be further increased up to 0.8 MPa peak-to-peak with the presence of a 250 VDC bias voltage. Transmit pressure of elements across the array was measured to be similar to representative data shown here for one element, with less than 8% variability between elements. Also, transmitting with all elements and implementing elevational focusing may further improve the transmit sensitivity. The transducer has a central immersion frequency of 9 MHz with a -6-dB bandwidth of 150%. Fig. 24c & d show the transmit test results and frequency response of the transducer.

Receive sensitivity was quantified by measuring signals recorded due to a hydrophone-calibrated external transducer transmitting pressure transients. The transparent arrays presented a receive sensitivity of 37.5 $mPa/\sqrt{Hz}$ with a bias voltage of 100 VDC or 10.4 $mPa/\sqrt{Hz}$ with a bias voltage of 250 VDC. Ultrasound imaging of 25-micron bonding wire target provided lateral and axial resolutions of 234 μm and 338 μm, respectively. Axial and lateral resolutions were determined from a beamformed image of a gold wire phantom with a 25 μm diameter where a 50% drop in the intensity was observed. Compared to optical imaging (having resolution of 40 μm or 12.7 lp/mm) ultrasound has coarser resolution, but provides depth information. An SNR of 28.4 dB is recorded for the received ultrasound signals.

Conclusion and future work

To the best of our knowledge, this is the first time using a transparent transducer for through-array combined optical-ultrasound imaging. Transparent transducers provide unique opportunities over opaque transducers and may enable novel miniaturized multimodality endoscopic probes by placing a camera behind the transducer. Realtime co-registered optical and ultrasound imaging may open new doors for ultrasound-guided surgeries, could lead to reduced procedure times, more confident navigation and more accurate diagnosis. Transparent arrays could also enable next-generation neuroscience tools by enabling both optogenetic activation and ultrafast functional brain imaging.

A limitation of our work is the lack of an acoustic lens. Future work could include curved arrays, transparent acoustic lenses, or transparent 2D arrays for improved elevational and 3D imaging. Future work should also aim to further improve transmit and receive sensitivity, further improve optical transparency, and explore new applications. Ultrasound image quality can be further improved with the help of temporal codes, more advanced imaging sequences, and aperture encoding [92]. Tri-modality ultrasound-photoacoustic-optical imaging could enable exciting pre-clinical and clinical imaging opportunities [12] since photoacoustic imaging can provide biological and molecular information of the target tissue [116].

Chapter 6: High-speed bias switching electronics for fast 3D and 4D ultrasound imaging

Objective

TOBE array technology enables packing a large number of ultrasound transducer elements in a transducer while keeping the transmit and receive channels low and only requires 2N transmit/receive and/or bias channels for an N×N array. This makes it possible to design 2D arrays with a massive aperture for high-resolution, high-quality 3D imaging. However, with row-column addressing (TOBE wiring), it is not possible to read all the elements simultaneously. Thanks to the bias-sensitivity of the TOBE arrays, this problem can be addressed with the help of fast-biasing electronics to perform bias-encoded imaging. However, designing fast, reliable high voltage electronics with a large number of independent channels is nontrivial. This chapter introduces a novel approach for designing electronics that can switch bipolar high voltages in sub-microsecond switching times, allowing ultra-fast 3D and 4D ultrasound imaging. The results of the research were presented at SPIE 2021, and IUS 2021 conferences [17, 18].

6.1 Introduction

The majority of the ultrasound imaging systems can only perform 2D imaging. 3D ultrasound systems can provide volumetric visualization, leading to more accurate diagnostics [117]. A fast 3D imaging system can also be beneficial in intraoperative ultrasound examinations and ultrasound-guided surgeries [118]. However, hardware complexity and computational limitations limited the progress of 3D ultrasound imaging systems.

As previously discussed, 2D array transducers can perform 3D ultrasound imaging. With such 2D arrays, there is often an engineering trade-off between system complexity and achievable image quality. Large probes with high-element density would produce high-quality images but with a resulting large number of channels leading to significant interconnect and channel count difficulties.

As mentioned in Chapter Two, row-column arrays have been investigated to reduce interconnection complexity as they can be addressed using only row and column electrodes, which are sometimes referred to as TOBE arrays w [64]. TOBE arrays have been implemented with piezoelectrics, CMUTs, and more recently, electrostrictive realizations. Unlike piezoelectric implementations, CMUT- and electrostrictive implementations of TOBE arrays offer bias-sensitivity, which can be used advantageously for novel imaging schemes. These have included Simultaneous Azimuthal and Fresnel Elevational (SAFE) compounding, which exploits Fresnel-lens-based elevational focusing [119]. Importantly, each element of such a bias-sensitive TOBE array can be addressed by biasing a row and transmitting or receiving from a column. Hadamard or S-Matrix-encoded biasing schemes may also be used to improve signal-to-noise ratios.

Such Hadamard-encoding schemes have also been used for aperture-encoded synthetic aperture imaging using an imaging scheme referred to as Fast Orthogonal Row-Column Electronic Scanning (FORCES) [32]. briefly, FORCES involves biasing columns with a sequence of Hadamard biasing patterns while transmitting pulses along rows with focal delays to create a cylindrical elevational transmit focus. FORCES uses a new Hadamard column biasing pattern for each of N transmit events while receiving echoes from columns. After decoding by multiplying by an inverse Hadamard matrix, the decoded channel dataset represents a synthetic transmit-receive aperture dataset, consisting of a received signal from each element for each respective (elevationally-focused) transmitting column. FORCES may be used to produce elevationally-steerable B-scans with image quality superior to previous non-encoded row-column imaging schemes and significantly superior to Explososcan schemes constrained by a similar total channel count. C. Ceroici [92] demonstrates results comparing non-biased imaging to FORCES imaging. FORCES generates superior and higher quality images with even lower transmit-receive events compared to MATRIX probes. These contributions were significant because they demonstrated the potential advantages of using a bias-switchable row-column array. Unlike previous row-column imaging schemes with non-bias-sensitive arrays, it illustrated B-scan image quality comparable to a linear array [92]. Moreover, unlike a linear array, our methods provided electronic elevational focusing control, electronic scan-plane steering, and 3D imaging.

6.2 High voltage high speed biasing electronics requirements

The integration of fast bias-encoding electronics with TOBE arrays could lead to transformative new 3D/4D imaging schemes. Previous attempts to perform bias-encoding were implemented with relay boards and using bias switching solid-state integrated circuits.

Since mechanical relays are slow, a single bias-coded image can take several minutes to be taken, which is insufficient for future clinical applications. In addition, relays are noisy, and suddenly switching high voltages create sparks which can burn transducers, and significantly shorten the imaging systems' lifespan.

Solid-state integrated circuits (ICs) might also be used for switching the bias voltages. They can be fast and less noisy. However, most of the ICs available have a voltage limitation of 100 Volts, limiting the bias voltage and transmitting voltages to the transducer. Other problems associated with the ICs are their low current support, prone to malfunctions due to strong electric fields, and becoming damaged with a single short in the transducer. Shorting channels and current spikes while bias switching is common with the TOBE arrays, and electronics dealing with TOBE arrays must withstand the current spikes.

In this study, we are approaching the problem with a novel electronic design. Our goal is to design electronics with the following main specifications:

1. Every channel in the imaging system should be connected to biasing, pulsing, and receiving electronics simultaneously without a switch to provide flexibility for the imaging schemes executed using the row-column arrays. For example, while FORCES requires biasing on columns and pulsing on rows while receiving on columns to achieve a steerable depth-azimuthal imaging plane, the roles of rows and columns may be electronically reversed to

obtain imaging in the orthogonal depth-elevation imaging plane. Additionally, other schemes may require pulsing and biasing on columns while receiving on rows. Thus, not all imaging schemes will make use of pulsing, receiving, and biasing simultaneously for every column (and/or every row), but to achieve the maximum imaging flexibility, pulsing, receiving and biasing should be provided for each channel. This has not yet been achieved previously. Latham et al. [119] used TOBE arrays but used columns for biasing and rows were connected to pulsing and receiving electronics. Our previous work using FORCES and Hadamard readout of TOBE arrays for photoacoustic imaging lacked solid-state electronics for fast switching.

2. In order to permit certain imaging schemes, the electronics should be designed to accommodate a high bias voltage in combination with a high transmit pulse. For example, for some imaging schemes, high transmit pulses are needed to perform deep-tissue imaging. These transmit pulses can be as high as 300 volts peak-to-peak. Such high transmit voltages and associated large peak currents in combination with high bias voltages can damage many solid state components

3. Biasing electronics should provide enough current for the electrostrictive material (or CMUTs) to change their polarity. Imaging schemes that involve high transmit pulsing and fast bias switching may also produce transient peak current that may damage electronics if not properly designed.

4. Biasing electronics should perform fast bias switching. In order to achieve imaging depths useful for medical imaging purposes while using fast bias-voltage switching to increase image-capturing speeds, high bias-voltages with high switching frequencies are needed.

5. Biasing electronics should provide high bias voltages. As noted herein, bias-switchable

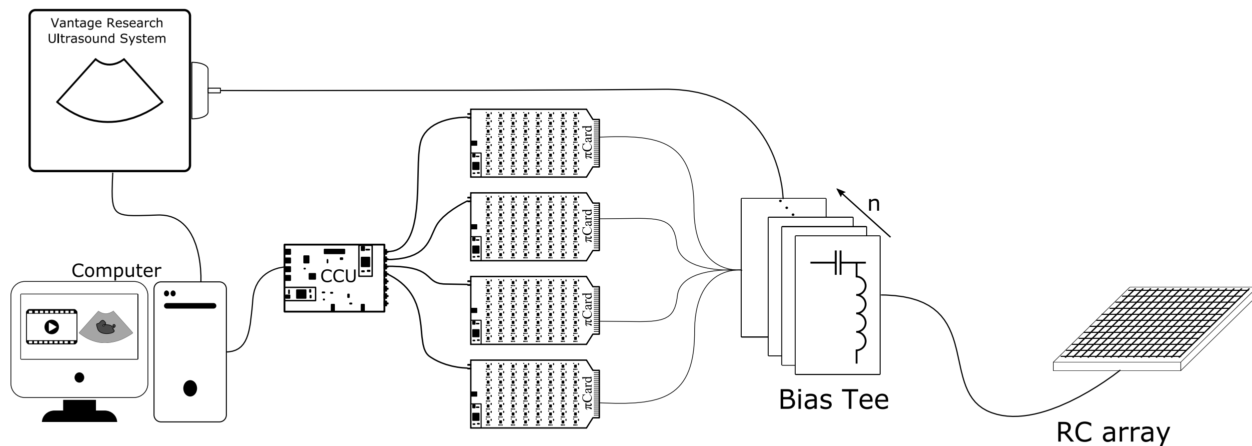

Fig. 25: Block diagram of bias controlled ultrasound imaging system

arrays intended for diagnostic frequencies (i.e. with center frequencies <20MHz) may be require high bias voltages for high electromechanical efficiency. As opposed to high-frequency arrays, which may use a thin electrostrictive layer, and thus require only moderate bias voltages to induce the needed polarization for efficient operation, lower diagnostic frequencies typically require a high bias-voltage operation to achieve the same electric fields in the material for needed polarization and electromechanical efficiency. In one example, a 10MHz array may require, for example, 50-60V bias voltages, while a 5MHz array may require at least 100V bias voltages, and a 2.5MHz array may require 200V bias voltage magnitudes.

6. Finally, the biasing system should have modular channels to accommodate various channel needs based on the transducer specifications. For example, in an imaging system utilizing TOBE arrays with 128 × 128 elements, biasing electronics must provide 256 independent programmable channels, while for a different transducer with 512 × 512 elements, the biasing electronics required to provide 1024 channels.

6.3 High voltage bias electronics design

Fig. 25 provides an overview of the proposed imaging system. The biasing system, which we call a πCard system, named for the H-bridge architecture, which looks like a pi-symbol, consists of three main units:

1) The interface board (IB) consisting of individual bias tees to combine AC and DC signals and deliver them to TOBE arrays.

2) The biasing boards (πCards), each consisting of 64 independent programmable high voltage channels. Every channel can be programmed to one of the four electrical states (VPP, VNN, GND, and high impedance) at any given time.

3) The central control unit (CCU), which is the main hub to communicate with the imaging system including the host computer, ultrasound imaging systems, πCards and high voltage power supplies.

In the following sub-sections, each unit is described in more detail.

6.3.1 Interface board

The interface board is a bridge between the ultrasound transducer arrays and the imaging system. The board makes it convenient to plug any ultrasound transducer arrays mounted on a separate PCB into the imaging system, and has individual bias-tee channels to combines AC ultrasound signals with DC bias voltages. Fig. 26a shows the interface board. The board has AC channel inputs through micro-coax connectors (APEX 40pin,...). A custom ZIF-connector was fabricated having 256 micro-coax cables bunched in groupings and terminated by the male counterparts to these micro-coax connectors. πCards can be connected to the

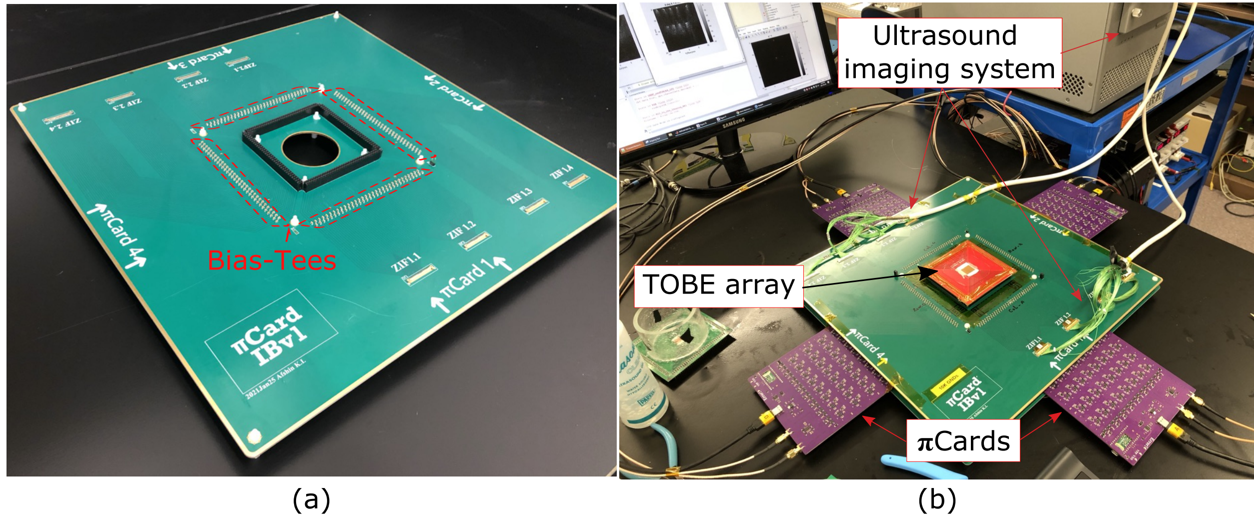

Fig. 26: Interface board to connect πCards and Verasonics. a) Interface board without the connection. The board has 256 individual bias-tees to support up to 256 imaging channels. b) Ultrasound imaging setup. A TOBE array with 128 $\times$ 128 attached to a separate PCB board is plugged into the designated area at the center of the interface board. Four πCards are plugged into the interface board for providing the bias voltages. Verasonics Vantage ultrasound imaging System is attached to the board through APEX connectors.

interface board through four board-to-board connectors positioned at the bottom side of the interface board as shown in Fig. 26b. Transducer PCB boards (which we call SURF boards) can be connected to the interface board through the header pins positioned at the center. Fig. 26b shows the interface board with all the connections.

The main restriction of the interface board is its size which is only suitable for characterizing ultrasound transducers and ex-vivo imaging. Therefore, another generation of interface board is designed for imaging on animals. The new board is called μIB due to its smaller form factor. Fig. 27a illustrates four μIBs, each consisting of 64 channels, Fig. 27b illustrates a πCard connecting μIB boards (through flexible cables) to the ultrasound system through micro-coax connectors. Fig. 27c illustrates a concept design of a handheld probe using four μIBs for interfacing to a TOBE transducers.

The bias tees designed for interface boards are a combination of a 10KOhm resistor and

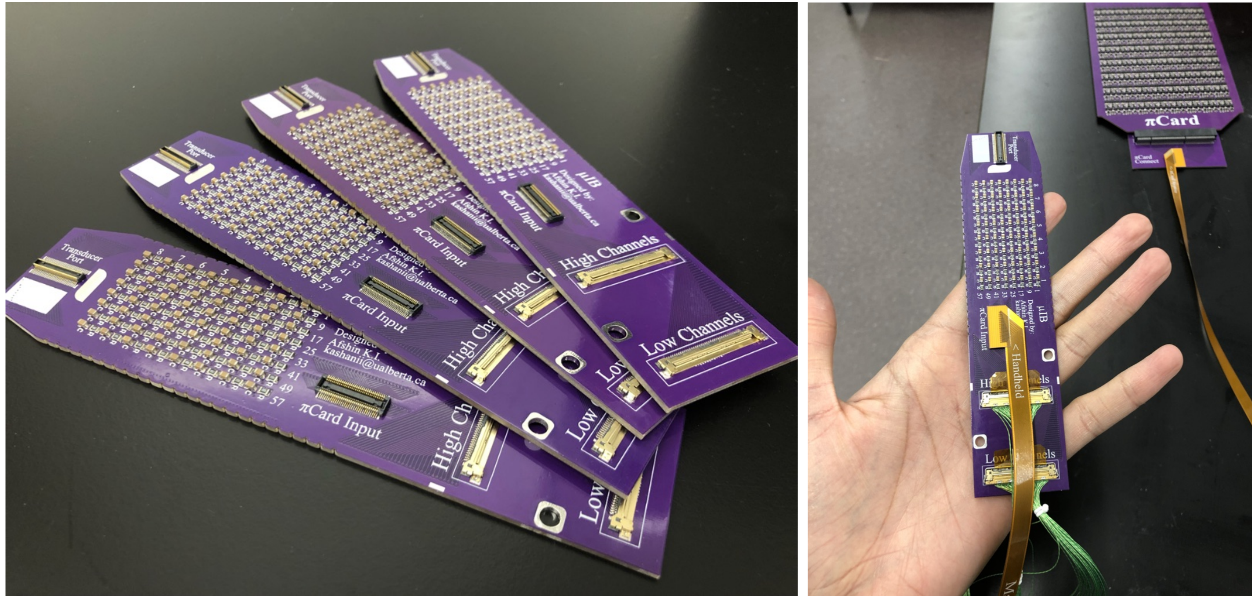

(a) (b)

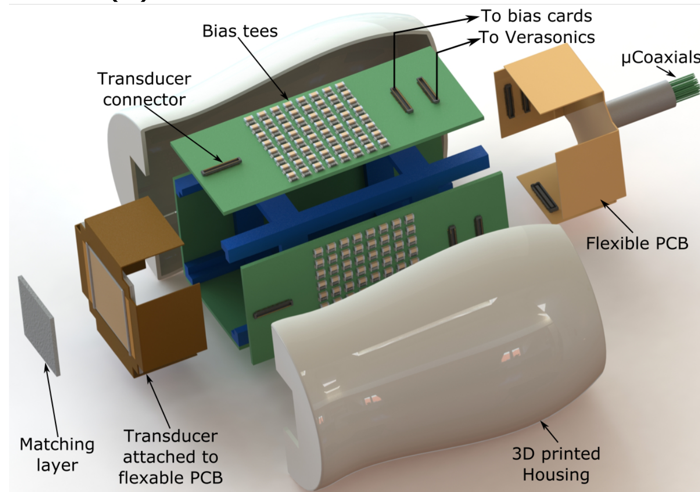

(c)

Fig. 27: μIBs for handheld scanner a) μIB PCBs, each consisting of 64 channels. b) A μIB board with the AC and DC connections, a πCard is connected through a flexPCB and Vantage Verasonics is connected through APEX connectors. c) Handheld design concept using four μIBs in a housing

a 5nF capacitor. The combination of the resistor and capacitor will act as a high pass filter. The main reason for using resistors instead of inductors is to archive high receive bandwidth. In addition, resistors are optimized to maximize the power delivered to the transducers independent of the pulsing frequency.

6.3.2 πCards

The heart of the biasing electronics is the πCard boards. These boards are designed to receive biasing instructions in advance and execute bias voltages switching patterns during an ultrasound or photoacoustic imaging pulse sequence. Every channel on a πCard can be independently controlled and programmed to one of the four supported states at any point in a pulse sequence. Posible state are:

1. VPP or DC high positive voltage with an internal resistance of $10K\Omega$. This depends on the VPP supplied by a power supply and can go up to 500V.

2. DC Ground (GND). Note that a separate ground is used for AC. The DC GND state still permits AC signals to be transmitted or received, but supplies 0V bias.

3. VNN or DC negative voltage with an internal resistance of $10K\Omega$. Similar to VPP this is determined by a power supply and can go down as low as -500V.

4. High impedance or High-z-state. This state will resemble an electrically floating connection by having electrical impedances $\geq 100G\Omega$

Fig. 29 illustrates a block diagram of a single channel of the πCard boards. Every channel has three separate blocks to generate VPP, GND, and VNN states. A head-to-head diode pair is used parallel with the output to provide a high impedance state when all three blocks are disabled. The high impedance state works based on the non-ideal operations of

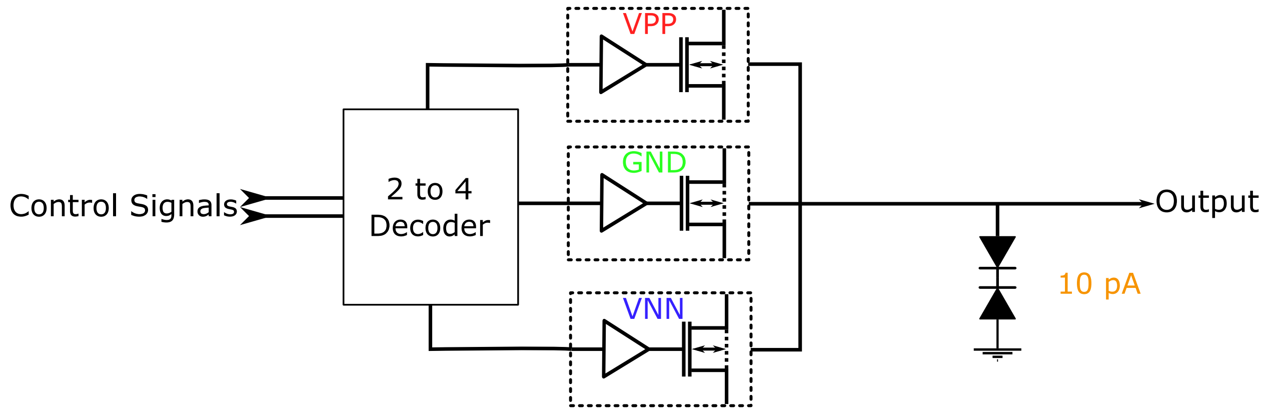

Fig. 28: Block Diagram of a single high-voltage high-speed switching channel

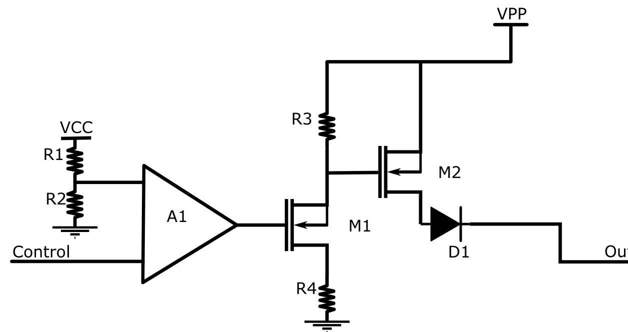

Fig. 29: Block Diagram of the VPP switching block

the diodes. Since diodes are placed head-to-head, at any point, one of the diodes will be in the reverse mode, allowing a minimal leakage current (in this case $\leq 1e^{-15}A$) to pass. Thus, diodes will allow a only a negligible constant current to pass, almost independent of the bias voltage.

The decoder which controls the state blocks has two benefits: reducing the digital control lines from 3 lines per channel to two lines and preventing simultaneous activation of the state blocks. For example, two power supplies might be shorted if VPP and VNN blocks are activated simultaneously due to a software glitch. However, since only one output of the decoder can be activated at any given time, the decoder will prevent this from happening by nature.

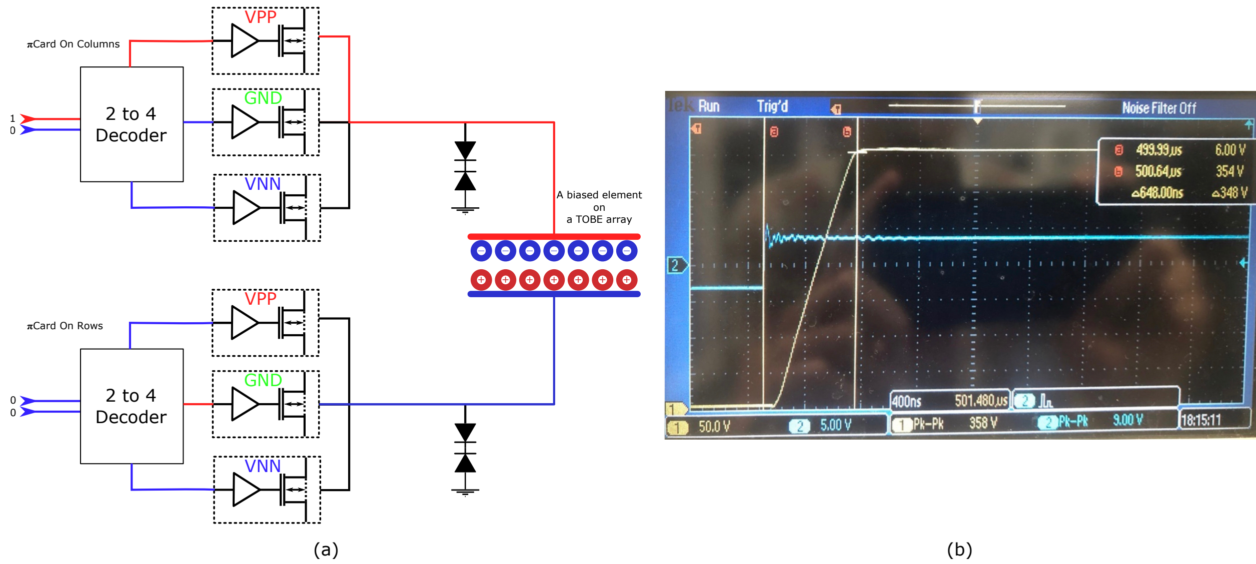

Fig. 30: a) Block diagram of a single element of TOBE array biased with πCards. In this example, an electrostrictive TOBE array is connected to πCards, where a column is biased with VPP and a row is biased GND. b) Transitioning the output of a single channel from VNN to VPP. Blue sginal is the traigger generated with the imaging system, and yellow line is the voltage transion at the output of the channel switching from -175V to +175V during a 648 nS time period.

Fig. 29 illustrates a simplified schematic drawing for the VPP block. The circuit can be divided into two sections, a gate driver and the main switching transistor. The combination of the comparator A1 with the high voltage MOSFET (M1) will act as a gate driver for the main MOSFET M2. The comparator A1 is used in the driving circuitry for differentially driving the gate circuit. Differential input is essential to prevent unwanted triggers caused by high electric fields and noise during the imaging. In contrast to switching electronics, where the gate driver is responsible for driving the MOSFET quickly to avoid any ohmic loss in the MOSFET, gate drivers in the πCards are designed in such ways a way that they prevent MOSFETs from switching instantly, and switch gradually with a controlled ramp transition from one state to another. Gradually changing the bias voltage provides enough time for the material to respond to the changing electric field without previously

experienced sparking problems. As discussed in Chapter Two, when electrostrictive arrays are connected to bias voltages, dipoles become polarized and electric charge separation is generated. When a charge is built upon a transducer electrode surface, and the bias polarity immediately switches to an opposite polarity, a large rush current will be generated, which can produce unwanted sparking in the array, leading to damage. Due to this, our previous attempts using relays and solid-state switching electronics failed. Fig. 30a illustrates a scenario where a single element of a TOBE array is biased with VPP voltages and charges are distributed on the material. Fig. 30b illustrated the voltage transition of a channel on a πCard. Initially, the channel was set to VNN, and when a trigger signal is generated, the πCard gradually transitions the channel's output toward VPP. The smooth transition between states is achieved by controlling gate current supplied to the MOSFETs. For instance, when a channel switches from VNN to VPP, the gate driver of the VNN block has a timed response causing the output of the VNN block to reduce toward GND gradually. Meanwhile, the VPP block is simultaneously turning on and pulling the output toward the VPP voltage. The voltage transition is further controlled by software by generating pulse-wave modulation (PWM) control signals (if needed). The slew rate is primarily determined by resistors R3 as well as R1 and R4. These resistor values are chosen to be 10, 47, and 470 $K\Omega$s, respectively. Fig. 31b shows an experiment with a 1MOhm load on the oscilloscope showing a slew rate of 0.5V/ns. With these slew rates, no sparking problems were observed in our array while the speed is fast enough for $\leq$5KHz switching rates suitable for KHz-rate ultrafast imaging applications. GND and VNN blocks have similar design considerations.

Fig. 31a & b shows the two sides of a fabricated πCard where every πCard has been designed with 64 channels. Fig. 31a illustrates the logic side, including all digital electronics

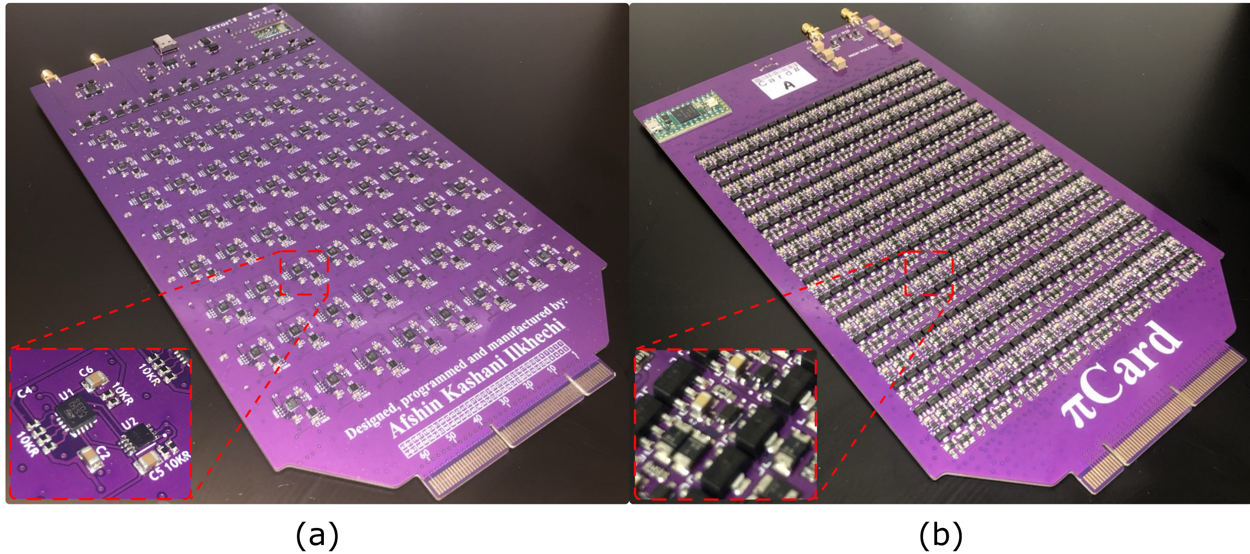

Fig. 31: Assembled πCards a) Logic side, consisting low voltage electronics and logic controls, b) High voltge side, consisting high voltage MOSFETs, and gate drivers.

and low voltage components, and Fig. 31b illustrates the high voltage side of the board. Designing the board with separated low- and high-voltage sides helps to shield the sensitive electronics from high voltage noises generated by the transistors.

6.3.3 Central control unit (CCU)

CCU is the main hub in our imaging system. CCU connects with the computer to receives the biasing instructions and transfer them to the πCards. CCU also synchronizes the πCards with the imaging system by generating trigger signals. Fig. 25 illustrates the CCU board with all the connections, and Fig. 32 shows a photo of the fabricated CCU unit.

The CCU has two main controllers, one handling the low-priority tasks such as communicating with the computer and the other controller to generate extremely precise control signals with jitter less than 1.6 ns to keep all the imaging units in sync. For example, performing bias-encoded photoacoustic imaging with a TOBE array would require generating at least eight trigger signals for controlling πCards, Vantage ultrasound system, lasers, and

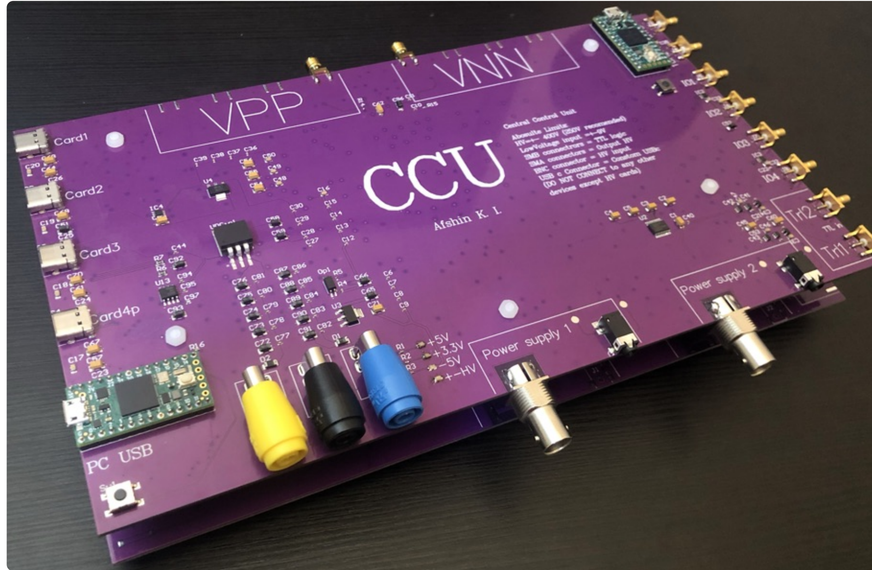

Fig. 32: Central Contol Unit (CCU), the main hub of the imaging system. CCU can connect to power supplies, ultrasound imaging system, πCards, lasers, photo-diodes, and a computer to synchronize all units for ultrasound and photoacoustic imaging.

photodiodes.

CCU is also responsible for regulating and supplying VPP and VNN voltages. CCU is equipped with two 1mF capacitor banks to store energy and provide it during the transition times. The capacitor banks have equivalent series resistance (ESR) of 10 $\mu\Omega$. Low ESR is crucial for keeping the VPP and VNN voltages steady during the transition times where πCards may require a large transient current. The current is driven by TOBE arrays and the gate drivers.

6.3.4 CCU app

CCU communicates with the computer by opening a virtual serial port through a USB connection. Every command sent and received by the CCU has 64 bytes and includes authentication codes along with biasing and control commands. All the necessary codes and

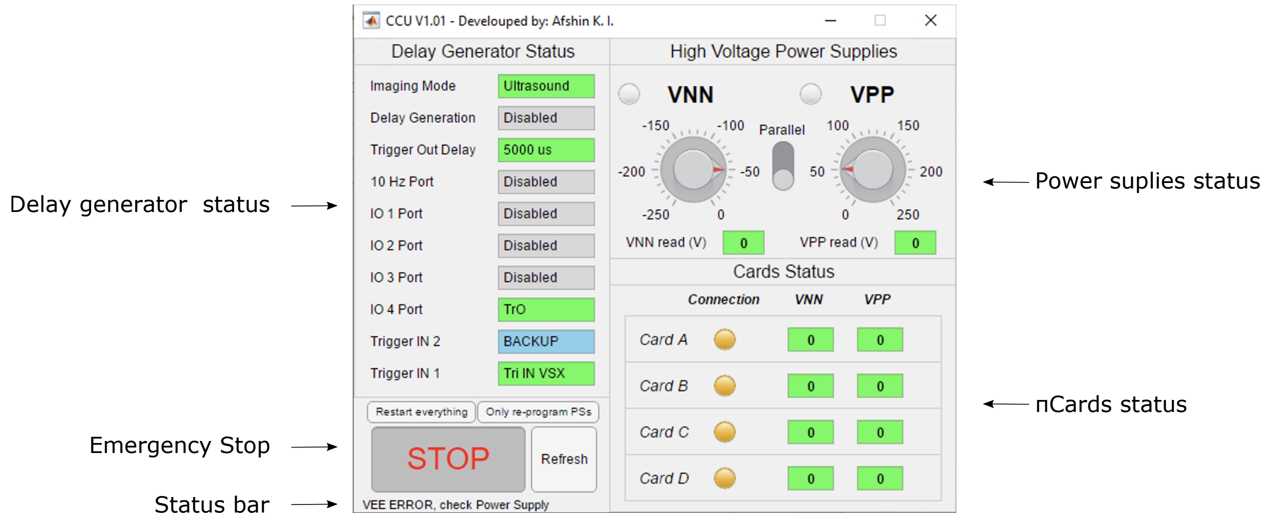

Fig. 33: Screenshot of CCU app. This software can program the CCU and πCards with a single matlab command and monitor them live during the imaging.

commands to communicate with the CCU are automatically generated with the CCU app, which is developed for Windows operating systems. CCU V1.01 is our latest app developed for the πCard system. The app monitors, programs, and controls the πCard system. Fig. 33 illustrates the graphical interface of the CCU app.

All command and biasing sequences are passed to the CCU app through a Matlab interface. For doing so, a structure variable must be constructed with the necessary parameters and passed it to the CCU app. The code below is an example of defining the CCU parameters:

```
1  input.COM='COM4';                 % CCU port
2  input.VNN=-50;                    % VNN to set
3  input.VPP=50;                     % VPP to set
4  input.VNNc=200;                   % VNN current Limit > 100
5  input.VPPc=200;                   % VPP current limit > 100
6  input.TrOd=TrOdCalc(input);       % Delay to send out trigger 0 to 65e3 us
7  input.TrOd=5000;    % Delay to send out trigger 0 to 65e3 us
8  input.ImgMode='US';               % imaging mode US or PA, in the future fPA
9  input.Qswitch=390;                % laser Qswitch 250 to 550, for PA ImgMode
10 input.TimerInterval=0.5;          % Refreshing GUI in seconds < 1 second
11 input.VoltageTolerance=5;         % Tolerance for voltage in Votls
12 input.BiasPatern=bits;            % biasing paternsn N*M (N=seq. (max 512), ...
       M=256)  -1=VNN, 0=GND, 1=VPP, 2=High impedance
```

Where COM is the virtual serial port name, VNN and VPP are the negative and positive

bias voltage values, VNNc and VPPc are the DC current limits for the negative and positive power supplies, TrOd is the delay per image to control the number of the frames taken per second, ImgMode is to set the imaging mode which can be US or PA for ultrasound and photoacustic imagings, respectively. Future vesrions of the sofware will also suport fPA and USfPA (ultrasound and functional PA) imaging modes. Q-switch controls the qswitch of pulsed lasers for PA and fPA imaging modes, and TimerInterval is the refreshing interval for the app with CCU boards. VoltageTolerance is the maximum allowed tolerance for the bias voltages, and beyond this voltage, CCU will generate a warning. BiasPatern is a two-dimensional variable containing biasing pattern for every channel and every sequence. The variable must have a column for every channel in the πCard system, and every row in the variable is a single imaging sequence.

For example, to program πCard system to perform two image sequences on a 64x64 die where columns are connected to channels 1 to 64, and rows are connected to channels 65 to 128, and the first frame has VPP on the columns and GND on the rows and the second frame has VNN on the rows and GND on the columns, and the rest of the channels are in high impedance mode, the code will look like as follow:

```
1 bits=ones(2,256); % create the matrix of ones
2 bits=bits*2;      % put all channels in high impedance mode
3 bits(1,1:64)=1;   % Apply VPP to channels 1 to 64 for the first sequence
4 bits(1,65:128)=0; % Apply GND to channels 65 to 128
5 bits(2,1:64)=0;   % Apply GNG to channels 1 to 64 for the second sequence
6 bits(2,65:128)=-1;% Apply VNN to channels 65 to 128 for the second sequence
7 input.BiasPatern=bits; %store the bits in the input structure for ...
      transferring into piCards
```

Here, at line 1, a 2D variable is created with 256 columns for 256 channels, and two rows for two image sequences. In line 2, all variable' values are set to 2, which means putting all channels at high impedance for both frames. In line 3, channels corresponding to columns

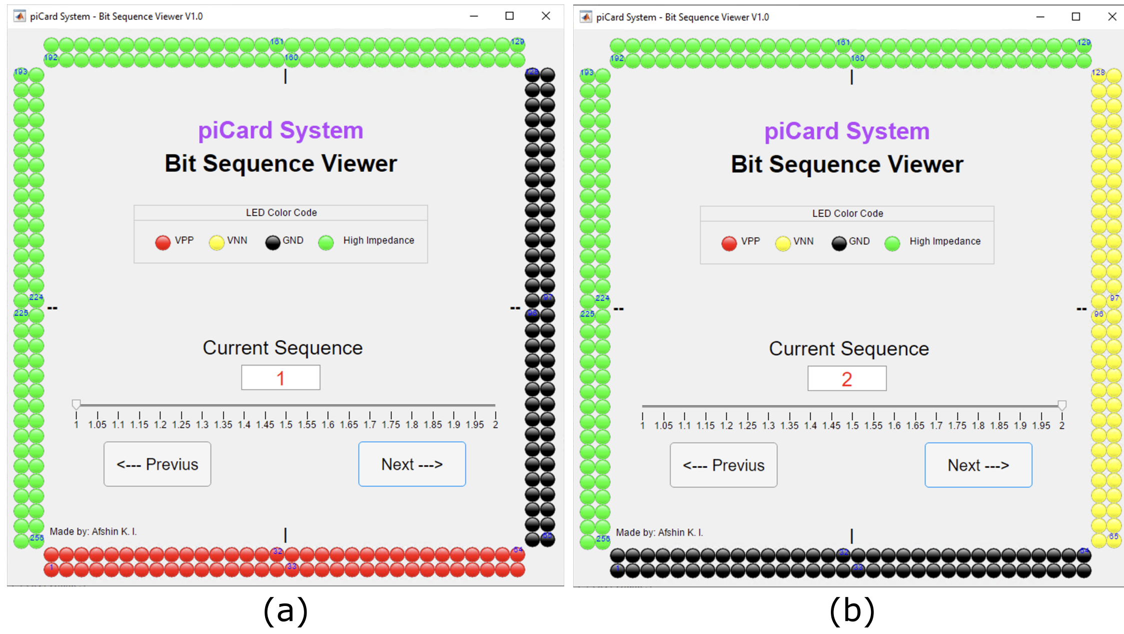

Fig. 34: Bit Sequence Viewer app. (a) sequence 1 of the biasing pattern mentioned in the text, (b) the second sequence

are set to 1, representing VPP on columns for frame 1. The following line puts channels connected to rows into GND mode by changing their values to zero. In lines 5 and 6, the second row of the variable is modified for the second frame by placing a -1 value for VNN on the rows and zero for GND on the columns. Finally, the constructed 2D variable is copied into the structure variable.

A sister app is also developed to visualize the bias voltages on the pins of the interface board called Bit Sequence Viewer. Fig. 34a & b illustrate the two bias sequences generated with the code above. Every output is colour-coded, where red is for VPP, yellow for VNN, Black for GND and green for High impedance states. After verifying the generated sequences, the CCU app can be called and programmed with the following command:

```
1 CCU(input);  %Runs CCU app and passes input structure variable
```

Sofware codes and schematics for the electronics are provided in the appendix.

6.4 Live cross-plane FORCES imaging

The combination of existing ultrasound systems with the πCard system can enable novel imaging schemes. One of the techniques to acquire high SNR images is to implement a FORCES imaging algorithm with TOBE arrays. Briefly, in the FORCES imaging scheme [32], a Hadamard bias pattern is applied on columns while a transmit pulse is applied to rows. Columns are used to receive the ultrasound signals. After every acquisition, an inverse Hadamard matrix is used to decode the received signals. Then delay and sum beamforming is performed to generate an ultrasound image for every sub-frame. Finally, a high-resolution image is formed by the summation of all the sub-frames. Cross-plane FORCES imaging performs the mentioned processes twice, once on rows and then on columns, by electronically switching the transmit, receive and biasing channels. Volumetric 3D imaging can be performed by electronically steering the imaging plane.

We used our in-house developed electrostrictive TOBE array with 128 $\times$ 128 elements to perform cross-plane FORCES on a wire target. The diagram of our imaging system is presented in Fig. 25. Every cross-plane FORCES image had 256 sub-frames, and thanks to our fast biasing electronics, we could perform cross-plane FORCES imaging at a rate of 20 fps and generate a movie of the target. Fig. 35a presents our imaging setup, and Fig. 35b to d illustrate ultrasound images of the wire target in various positions. The results are presented with a dynamic range of -40 dB with lateral, azimuthal, and axial resolution of 270 μm, 278, and 230 μm.

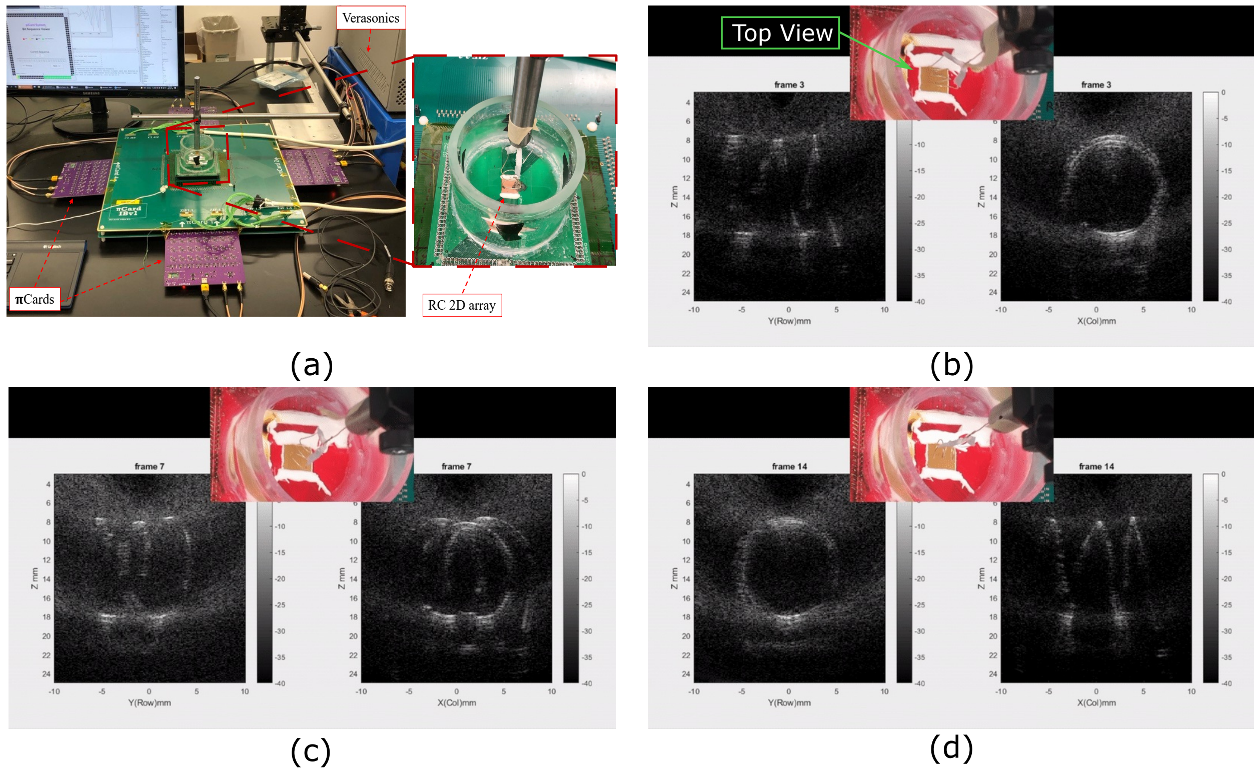

Fig. 35: Cross-plane live FORCES imaging. (a) Imaging setup, where an electrostrictive TOBE array is connected to the interfacing board and πCards and Verasonics Vantage Ultrasound System are connected to the interfacing board. A spring-shaped wire target is suspended in the water tack attached to the TOBE array as a target. The wire target is rotated clockwise for the cross-plane imaging, and a video file is generated of the moving target. (b) Frame 3 of the live cross-plane FORCES imaging video, illustrating cross-plane FORCES imaging the spring in a 90-degree orientation. (c) Frame 7 of the live cross-plane FORCES imaging video, illustrating cross-plane FORCES imaging the spring in a 45-degree orientation and (d) Frame 14 of the live cross-plane FORCES imaging video, illustrating cross-plane FORCES imaging a spring in a 0-degree orientation.

6.5 Cross-plane power Doppler imaging

Doppler ultrasound can estimate the blood flow passing through blood vessels in the body by bouncing high-frequency ultrasound pressures and monitoring echoes from moving blood. Our electronics enable Doppler ultrasound with TOBE arrays using bias encoding schemes. To test our electronics, we performed Power-Doppler ultrasound imaging [120] on a vessel miming target while applying the cross-plane FORCES imaging scheme. For a phantom, a corn starch solution (5 grams of cornstarch dissolved in 95 millilitres of deionized water) passed through a plastic tube with 0.5 mm diameter. Fig. 36a & b illustrate our setup. We used a 128 $\times$ 128 electrostrictive TOBE transducer with a central frequency of 10 MHz.

For every power-Doppler image, a total of 1280 B-scan frames are taken, and a frame rate of 5 fps is achieved. Every image is presented with a dynamic range -40 dB with lateral, azimuthal, and axial resolution of 269, 280, and 230 μm. Fig. 36c illustrates the beamformed power-Doppler images overlaid on cross-plane FORCES ultrasound images. Unfortunately, we experienced some difficulties performing the test due to shorted channels in our transducers, and we believe having a well-working transducer will result in much higher quality images.

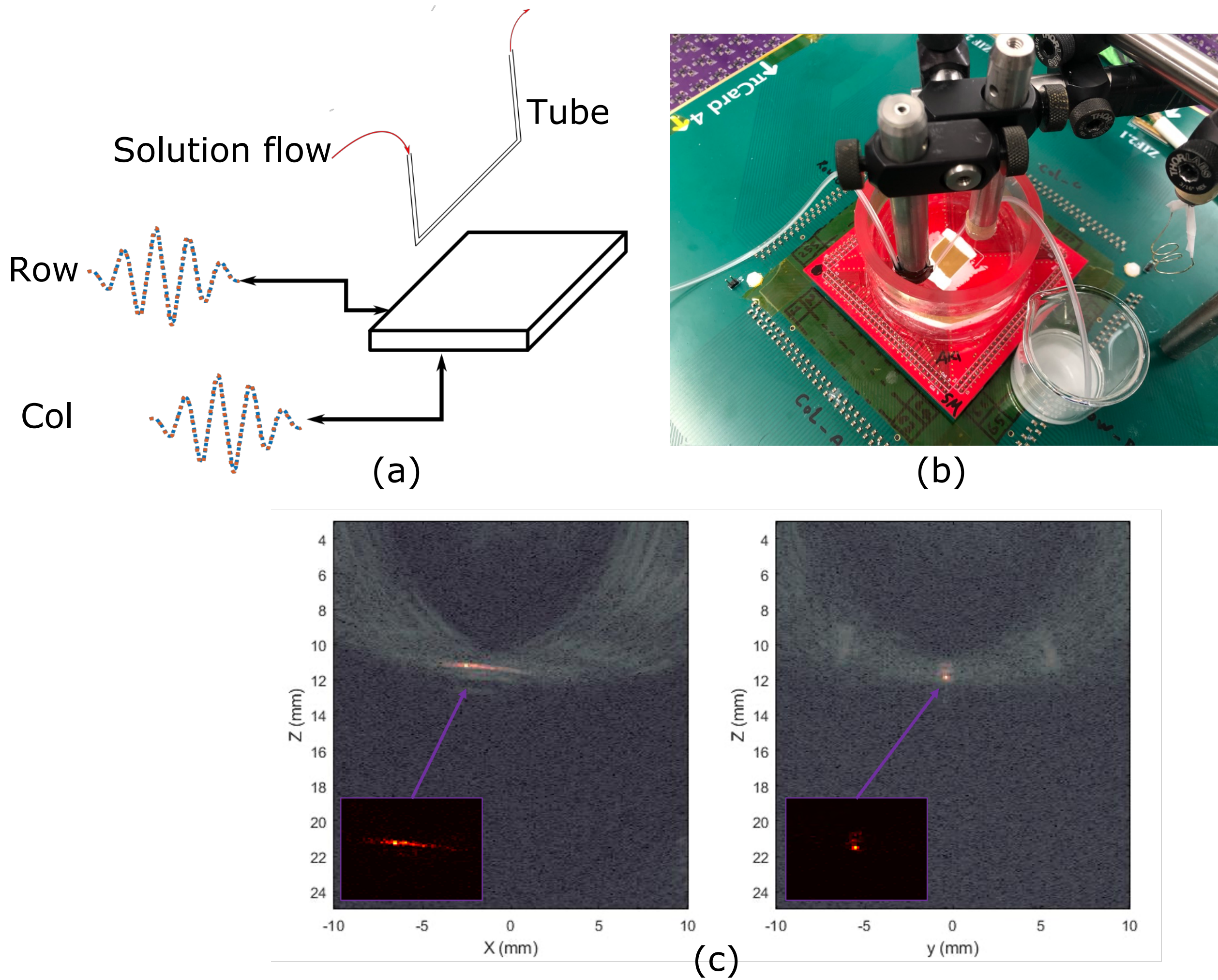

Fig. 36: Cross-plane Doppler imaging with electrostrictive TOBE array. (a) Schematic of the imaging setup, a tube with a flowing corn starch solution is used to mimic blood flow in a vessel (b) A picture of the setup with the tube and a 128x128 electrostrictive TOBE array connected to our bias-encoded ultrasound imaging setup (c) Cross-plane Doppler imaging with FORCES imaging scheme. To obtain cross-plane images, transmit, receive, and biasing channels are electronically switched between rows and columns.

Conclusion and future work

Here, a unique biasing electronics system is designed and developed for performing fast 3D ultrasound imaging with TOBE arrays. Our πCard system can provide any arbitrary biasing sequence to any TOBE array to perform high-quality cross-plane B-scan and Power Doppler imaging. The πCard system can provide bi-polar high voltage bias voltages up to $\pm$ 500V in a sub-microsecond range. Live cross-plane FORCES and power Doppler ultrasound imaging are performed to experimentally test the advantages of bias-encoded imaging using πCard System and TOBE arrays. Future work should optimize the fabrication of the TOBE arrays to prevent shorting and other problems. Future work should also explore improve imaging schemes for volumetric power Doppler and color Doppler imaging. Future work should also aim to improve B-scan imaging frame rates with sparse synthetic aperture schemes. Finally, we believe that our FORCES methods can outperform state-of-the art MATRIX probes with integrated micro-beamformers since our approach can achieve transmit and receive focusing everywhere in the scan plane, whereas MATRIX probes cannot. Future work should further explore these comparisons and experimentally demonstrate this hypothesis.

Chapter 7: Charging-free CMUT transducers

Objective

Dielectric charging is a major problem limiting the commercial and clinical applications of the CMUT devices. The problem arises from the presence of dielectric thin-films in the structure of the CMUTs. The charging affects the capacitance and the snapdown voltage of a CMUT, leading to permanent device failure. CMUTs that incorporate isolation posts have been shown immune to charging [121]. However, fabrication challenges, low yield, and lower sensitivity are some of the main drawbacks. Here, we replace the isolation layer with semiconductor materials that have high contact resistance and fabricate charging free CMUT transducers. Since the semiconductor materials have a low sheet resistance, the proposed CMUTs expected to dissipate the trapped/injected charges. The results of the research is presented at IUS 2019 conference [19].

7.1 Motivation

The majority of the ultrasound transducers designed today are based on the piezoelectric effect. The high sensitivity and reliability of the piezoelectric materials are some of the compelling properties that make them a good candidate for many transducer designs. On the other hand, CMUTs utilize capacitive sensing to detect ultrasound waves [12, 16, 95]. CMUT structure consists of two parallel plates, a clamped membrane with a top electrode and a fixed bottom electrode. When ultrasound pressures hit the suspended membrane, it causes a transient movement of the membrane and modulates the capacitance of the CMUTs. As a result, CMUTs can detect ultrasound pressures capacitively, which have several advantages over other transducers mentioned above, such as broader bandwidth, massively-scalable fabrication, higher electro-mechanical efficiency, and potential for CMUT-on-CMOS compatibility [40–43]. CMUTs, unlike piezoelectric transducers, do not need matching layers for acoustic impedance matching to the tissue.

A key drawback of CMUT devices is their dielectric charging problem. The dielectric layer charging is mainly attributed to the electron injection during the snapdown events [11]. However, other mechanisms such as operating temperature can also affect the charging process, which may accelerate or decelerate the charging independent from the actuation mechanism. To simplify the concept of trapping charge in a dielectric, here we consider that the trapped charges are either trapped at the surface (which can occur at the junction between any dielectric an another material, by Gauss's Law) or charges trapped in the dielectric, sometimes called bulk charge.

Charge injection happens through some processes such as Schottky injection [122], and

tunnelling [123], and the amount of the injected charges increases exponentially with the increase of the applied electric field.

Some of the well-known dielectrics are Silicon dioxide, Silicon nitride, Aluminum nitride,Aluminum oxide, Tantalum oxide and Hafnium oxide. Each of the mentioned materials presents different charging characteristics depending on the material structure. Generally, due to the fabrication limitations and material compatibility, CMUTs are fabricated either with Silicon dioxide or Silicon nitride. Charging characteristics of both materials have been intensively studied for years and well-characterized [124, 125].

In the CMUT community, there have been many investigations on the effect of charging on the CMUT operation. T. Zure and S. Chowdhury [126] studied the trapped charge's impact in the silicon oxide layer of a CMUT cell. Based on their analytical model and experimental results, as long as a CMUT is not biased, there is a good agreement between the analytical and experimental data. However, CMUT with a bias voltage tends to have a 4-10 times higher capacitance value than the analytical model prediction. This high mismatch is due to charge trapped in the silicon oxide layer, dipole polarization, and interfacial polarization.

Long term reliability of a CMUT with charging is addressed in [127]. Their study focuses on the effects of bias voltage on the transducer's lifetime, sensitivity, and ageing. The experimental data confirm that the trapped charge increases the capacitance in the short-term operation leading to higher sensitivity. However, in long-term operation, the sensitivity drops catastrophically. Also, the trapped charge limits the practical lifetime of a CMUT device. The experimental data shows a few orders of magnitude drop in a CMUT device's operational hours with only a 50% increase in the bias voltage.

There have been several attempts to address charging for CMUTs. One of the successful

methods introduced recently was to replace the isolation layer with isolation posts [121]. Unlike the isolating layer, the posts have a small transverse area where the trapped charge in the posts has a negligible effect on the operation of the CMUT. In a more robust design introduced in our group, isolated isolation posts (IIP) were implemented in the structure of a CMUT device [128]. Since the posts are also isolated, trapped charges in the posts are reduced to zero leading to a long-term reliable charging-free operation. However, the design suffers from additional fabrication complexity and increase likelihood of breakdown due to lack of insulation in non-post regions.

Here, we introduce a novel technique for fabricating CMUT transducers with high contact resistance, semi-conductor thin-films as an alternative to dielectric insulators. The hypothesis is that these films will not accumulate charge even when a CMUT membrane is in a collapsed state, since the high contact resistance will preclude tunneling currents and since the low sheet resistance should dissipate any such charge. Moreover, with the use of atomic layer deposition technology we should achieve nearly atomically smooth surfaces which should greatly minimize surface charging. A rough surface dieletric in contact with a top electrode can be modelled as a bulk dielectric with an intermediate dielectric thin layer having a dielectric constant which is an average of the volume fraction of dielectric in the rough layer. Because of Gauss's law, this will always result in surface charge trapping when an electric field is applied. By using an atomically smooth layer, such surface-trapping should be mitigated. We use ZnO and Ga_2O_3 thin films deposited with atomic layer deposition which achieved extremely high contact resistance and led to charging-free CMUT devices. Our fabrication process involves using Benzocyclobutene (BCB) material [76] as a bonding agent to fabricate CMUT devices with such a materials.

7.2 Alternative semiconducting isolation layers and their electrical properties

Metal-semiconductor contacts are an integral part of many microelectronic designs and have been studied for decades [129]. Contact resistance is dependent on several factors such as deposition parameters, material, doping, etc. and can vary considerably [129]. For decades, minimizing contact resistance was a key objective. In contrast, in our work, we desire high contact resistance.

We experimentally studied the contact resistance of semiconductor thin films in search of high-contact resistance materials as an alternative to dielectrics in CMUTs. Among many materials, we chose to study the contact resistance of ZnO and gallium oxide (Ga_2O_3) thin films, which are known to have poor contact resistance.

ZnO is an n-type semiconductor and is well known for its high electron mobility, high extinction binding energy, and wide and direct bandgap (3.37 eV at room temperature) [130]. Plasma enhanced atomic layer deposition (PEALD) is one of the effective methods of depositing ZnO thin films with the ability to control its electrical properties [131]. In this method, the conductivity of the ZnO thin film has a direct relation with the deposition temperature. Muneshwar et al. [131] studied the conductivity of the PEALD ZnO thin films based on the deposition temperature.

Contact resistivity of the ZnO thin-films is highly dependent on the contact materials which can range from $K\Omega$ for germanium/ZnO up to $10^{13}\Omega$ with indium tin oxide (ITO) using a gold interface. By choosing the right contact material and deposition temperature, it is possible to obtain the desirable characteristics mentioned above.

Table 5: Experimental data for contact and sheet resistances of ALD ZnO and Ga_2O_3 thin films

Contact Material	Thickness of Semiconductor (nm)	Optimal Annealing Temp. ($°C$)	Optimal Annealing Time (minutes)	Contact Resistance (Ω)	Specific Contact Resistance ($\Omega \times cm^2$)	ALD film Resistivity ($\Omega \times cm$)
Al/Au/ZnO	20/100/20	370	10	5.45E+08	4.36E-02	0.108
Al/Au/ZnO*	20/100/20	400	5	1.84E+08	1.47E-02	0.4712
Al/Ti/Au/ZnO	20/70/30/20	300	10	3.99E+11	3.19E+01	23.03
Ge/Au/ZnO	37/20/20	200	10	1942.5	3.13E-04	0.1558
ZrN/Cu/ZnO	3.47/20/10	300	10	1.61E+13	1.29E+03	1.88
ITO/Au/ZnO	20/80/20	200	15	5.95E+13	4.76E+03	0.96
Si^{**}/Ga_2O_3	20/40	200	90	2.90E+10	2.32	2.44E+5

*Al-doped ZnO **highly n-dopped silicon

Another robust candidate for the semiconductor insulating layer is Ga_2O_3 thin films deposited with the PEALD method. The material shows a $G\Omega$ range contact resistance in contact with silicon and sheet resistance of ~200 $K\Omega$. We have performed several characterization tests on the ZnO and Ga_2O_3 PEALD thin films. We used a Keithley 4200-Semiconductor Characterization System to perform 4-probe measurements of resistance in van der Pauw structures (vdP) [132]. The measurements were used to extract the contact resistance and sheet resistance of various metal-semiconductor vdP structures. The vdP structures were fabricated using a ALD-150LX (Kurt. J. Lesker) PEALD system for depositing semiconductors, Kurt J Lesker CSM-18 sputtering system for depositing metals, and contact lithography with lift-off for patterning the semiconducting thin films, but using metal etch for metal patterning. The vdP structures are designed with four circle-shaped contact points with radii of 250 μm and a square spacing of 1.5 mm. Results are presented in Table 5.

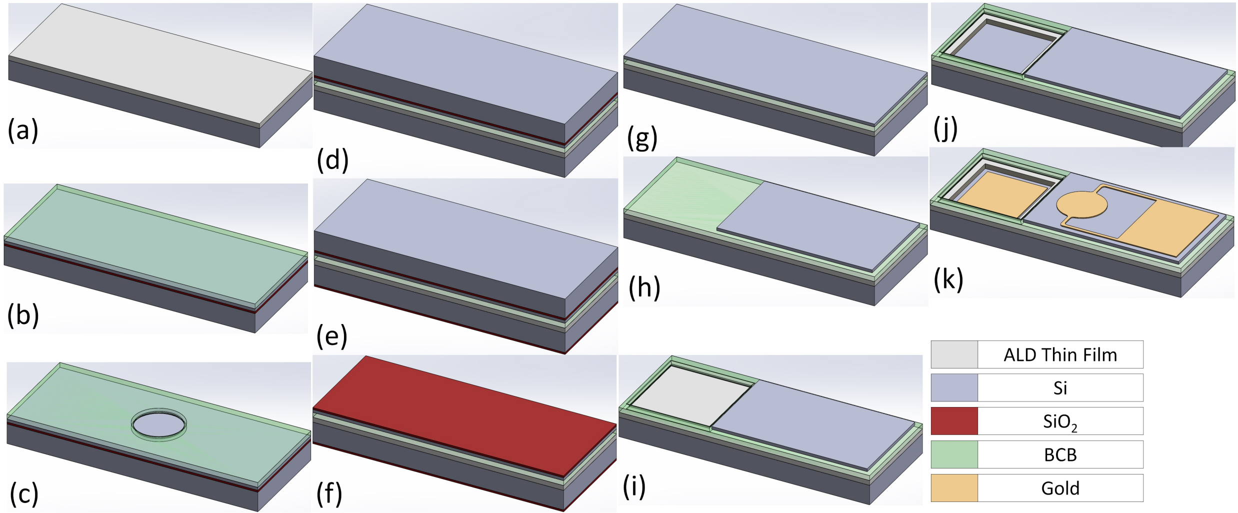

Fig. 37: Fabrication process flow of the charging free CMUT transducers.

7.3 Fabrication process

Unlike the compelling properties of the semiconductors, fabricating CMUTs with such materials is challenging. Recently, we developed an adhesive wafer bonding technique [77] which is suitable for adding proposed semiconducting thin film layers.

We fabricated the first generation of charging-free transducers with single element structures. Fabricated CMUTs consist of a gold layer for the top electrode, a 1 μm single-crystal silicon membrane, and a ∼500 nm gap on a low resistivity silicon prime wafer. The proposed fabrication process is presented in Fig. 37. The process starts by depositing a thin layer of the semiconductor layer on a highly Boron-doped silicon wafer to form the high contact resistance layer (Fig. 37.a). We developed CMUTs based on both PEALD ZnO and Ga_2O_3 thin films. For Ga_2O_3, a 40 nm thickness was deposited on top of a silicon wafer providing a contact resistance of $G\Omega$ and breakdown voltage up to 20 V. The deposited Ga_2O_3 presented a breakdown voltage of 5 MV/cm).

A separate SOI wafer is prepared by spin-coating a thin layer of BCB polymer. Fig. 37.b

illustrates BCB on an SOI wafer. After baking the BCB, the polymer is photosensitive and can be directly patterned with a lithography process. For this step, a first mask is used to pattern the cavities for CMUT cells (Fig. 37.c). In the next step, two wafers are bonded together (Fig. 37.d). Bonding is done in a vacuum chamber. Removing the SOI wafer's handle layer is done by the tetramethylammonium hydroxide (TMAH) solution, which has high selectivity between oxide and silicon. The prime wafer's backside is protected with a thin PECVD oxide layer (Fig. 37.e & f). The BOX layer is selectively etched, and the device layer is exposed. (Fig. 37.g). During this step, the protective PECVD oxide layer (on the backside of the prime wafer) is also removed. Next, a second lithography step along with ICP-RIE etching of the silicon was performed to isolate membranes between devices. Fig. 37.h illustrates the patterned membrane on top of the cavity. In the next two steps, BCB and semiconductor layers are selectively etched with dry and wet etching processes respectively to create the access holes for the bottom electrodes (Fig. 37.i & j). BCB dry etching is performed with RIE process and semiconductor thifilms are etched with hydrochloric (HCL) acid solution.

A thin Cr/Au layer (10 nm (Cr) and 100 nm (Au)) is then deposited on top of the membrane and patterned with the fourth lithography step to form the connection pads. Fig. 37.k illustrates the finished CMUT cell.

7.4 Device characterization

ZnO and Ga_2O_3 CMUT transducers are separately fabricated and characterized. Fig. 38.a shows the fabricated CMUTs. The wafer includes single cell and single element CMUT

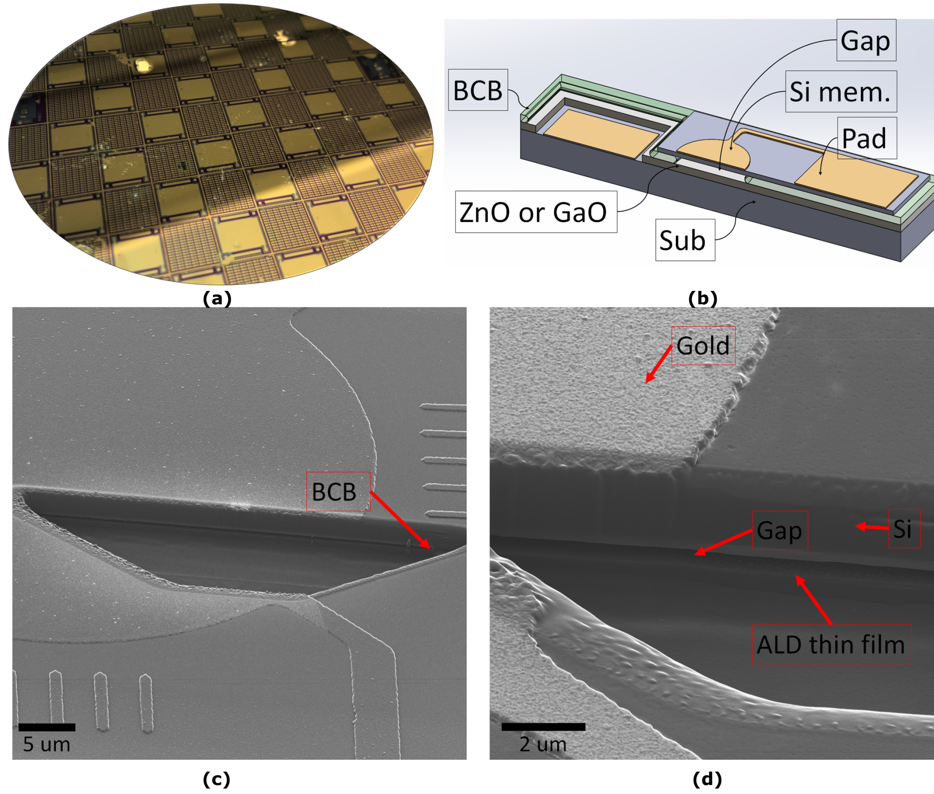

Fig. 38: (a) Fabricated CMUts (b) Cross-sectional view of the structure of a single CMUT cell (c) Helium ion microscopy image of the CMUTs. A cut is made with a FIB to reveal the CMUT structure (d) A close view of the layers with their relative thicknesses.

devices with membrane radii ranging from 30 to 100 μm. Fig. 38.b illustrates a cross-sectional drawing of the proposed CMUTs. The structure of the CMUT cell is imaged with helium ion microscopy, and with the help of Focused Ion Beam (FIB) milling, a cut on the membrane is created to expose the underlying layers. Fig. 38.c & d are representative microscopy images showing layers of the fabricated devices.

The charging effect is studied by monitoring the capacitance versus voltages graphs of CMUT cells over multiple snapdown events. In traditional CMUTs with a dielectric layer, trapped charges in the dielectric can alter the effective electric field of CMUT cells, and monitoring the capacitance versus voltage curve (CV curve) while CMUTs are experiencing

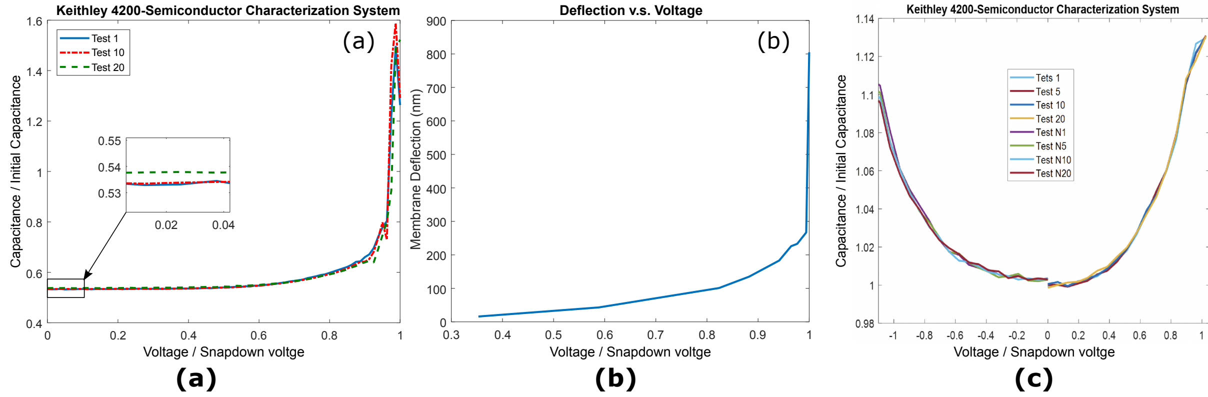

Fig. 39: (a) Capacitance versus voltage measured for ZnO CMUTs with a Keithley 4200-Semiconductor Characterization System. (b) Membrane deflection versus bias voltage measured by ZYGO optical profilometer (c) Capacitance versus voltage measured for Ga_2O_3 CMUTs with Keithley 4200-Semiconductor Characterization System.

snapdown events is a practical way to determine the charging effect as charging will be manifested as horizontal shifts of the CV curve after multiple collapse-snapback cycles. We have performed extensive CV tests on the fabricated ZnO CMUTs with a Keithley 4200-Semiconductor Characterization System. Fig. 39.a presents the acquired data for twenty consecutive actuation cycles using the ZnO CMUT devices. The figure shows that CMUTs did not trap any charges after several snapdowns. Also, to confirm that the membranes did snapdown, ZYGO Optical profilometer tests were conducted to measure the height profile of the membranes versus applied bias voltages (Fig. 39.b). The horizontal scale on both graphs is normalized to the snapdown voltage.

Similarly, charging is studied on the CMUTs fabricated with a gallium oxide layer. CMUTs are designed to accommodate the low breakdown voltage of the gallium oxide layer ($5MV/cm$) and have snapdown voltages less than the breakdown threshold of the gallium oxide layer. As expected, CMUTs did not trap any charges after several consecutive snapdown events. Fig. 39.c. presents the CV test results.

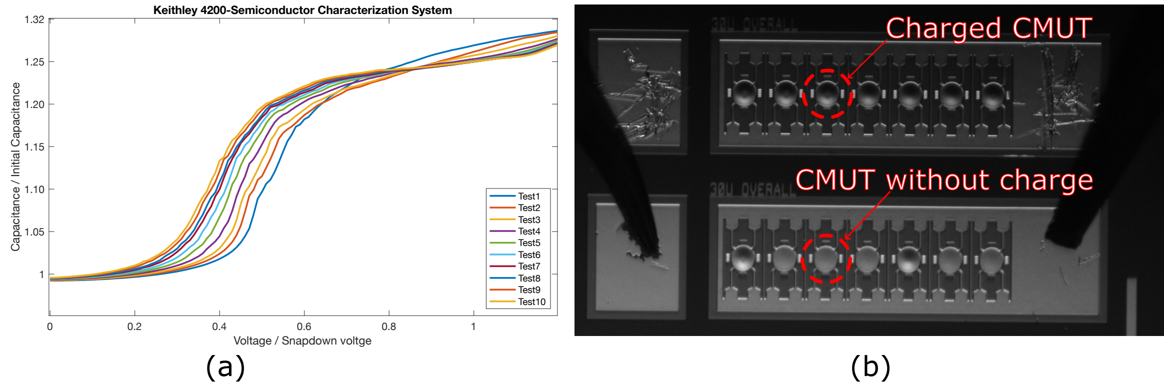

Fig. 40: (a) Capacitance versus voltage measured with a Keithley 4200-Semiconductor Characterization System of the CMUTs fabricated with a silicon dioxide layer. (b) Charging effect on the operation of the CMUT cells. Charged CMUT cells exhibit an unrestorable membrane snapdown due to the build up charge in the dielectric layer

To illustrate that charging is present in devices with a dielectric present, we fabricated CMUTs with a silicon dioxide insulation layer for comparison. Fig. 40.a illustrates the test results and the charging effect on the capacitance of a CMUT cell. Every colored curve in the Fig. 40.a illustrates a CV measurement right after a snapdown event. As seen in the figure, after every snapdown, more charges get trapped in the silicon dioxide layer, resulting in a change in the capacitance versus voltage and finally causing a complete collapse of the membrane. Fig. 40.b illustrates some membranes with unrestorable snapdown as the result of trapped charge.

In contrast, neither our ZnO nor our Ga_2O_3 based CMUT devices demonstrated charging even after several membrane collapse-actuation cycles.

7.5 Discussion

It was found that ZnO did not remain stable as it is hygroscopic which makes fabrication challenging since aqueous rinsing steps are needed in the fabrication. In contrast, the

Ga2O3 devices exhibited long-term stability over more than 1 month of operation. Current performance is limited by the maximum thickness practically achievable with the PEALD process. Future work could investigate other deposition methods, perhaps in combination with PEALD to achieve both a thicker semiconducting layer with low surface roughness and high contact resistance. This could potentially increase the tolerable bias voltage so as to avoid breakdown. Future work should develop these devices into arrays for ultrasound imaging applications.

Conclusion and future work

Here we presented the design and fabrication of CMUTs with semiconductor materials as a barrier between the top and bottom electrodes for the first time. Semiconductor materials with high contact resistance are selected for this purpose, where they can withstand high electric fields during snapdown events and dissipate trapped charges thanks to their low sheet resistance. The experimental results provided proof of principle, where the CMUTs presented a negligible charging behaviour after extended operation under snapdown events. Semiconductor material deposited with the PEALD process presented high contact resistance up to 5.95E+13 Ω in contact with silicon membranes.

Chapter 8: Conclusion

Ultrasound imaging is safe, affordable and capable of live monitoring internal organs of the body. Currently, most ultrasound imaging systems rely on piezoelectric transducers, where the majority of them are opaque. Transparent transducers can open new opportunities for the emergence of multi-modality imaging systems. However, designing a transparent transducer is challenging. This thesis introduced three new fabrication processes to fabricate transparent transducers with the CMUT technology.

The thesis mainly focuses on developing new fabrication processes that make it possible to fabricate transparent transducer arrays. The process relies on the wafer bonding technique employing a transparent epoxy as a bonding agent. All the materials and layers used for the process are optimized for maximum transparency in the optical wavelength. For this purpose, nitride is used as the membrane material due to its high transparency and dielectric constant, and ITO is used as a transparent conductive material for the electrodes. However, the low conductivity of ITO layers negatively affects the transducer's sensitivity. Thus, thin metal strips are introduced to the channels to improve the conductivity of the elements and keep the transparency intact. The optimized fabrication process makes it possible to fabricate large 1D transparent transducer arrays. After successfully fabricating the first generation of the transparent transducers arrays, a process is proposed to enable 2D arrays by introducing a modified fabrication process involving the wafer bonding technique. We

have not yet completed the fabrication of these 2D arrays, which should be a topic of future work. However, we have taken steps to ensure we have the right interfacing electronics and have tested these electronics with opaque electrostrictive TOBE arrays.

A major limitation of the adhesive wafer bonding technique is the lack of precise control over the gap of the CMUT transducers. On the other hand, fabricating high-frequency transparent transducers require perfectly controlled gap height. Therefore, this thesis introduced the third fabrication process, based on sacrificial release technique utilizing silicon oxide as a sacrificial layer to precisely control the CMUTs' gap height during the fabrication process.

The key advantage of transparent transducer arrays is their unique application for photoacoustic imaging. The laser pulses can be guided through the transducer, minimizing the optical and acoustic paths for excitation and detection mechanisms. This is not possible with the current opaque transducers. This thesis investigated the possibility of using transparent transducer arrays for the device through photoacoustic imaging. Transparent transducer arrays were fabricated in-house containing 64 and 128 elements. The advantage of the device through illumination for photoacoustic imaging is investigated by performing two sets of experiments where laser pulses are delivered through and around the side of the transducer. The comparison between the results illustrated a sharp improvement in the SNR values using through-illumination.

The application of transparent transducer arrays is not limited to photoacoustic imaging applications, and they can be utilized to combine ultrasound imaging with other imaging modalities such as optical, OCT, and fluorescence imaging. An excellent application of combined optical ultrasound modalities is endoscopy probes equipped with ultrasound transducers. Optical imaging with an endoscopy probe can only provide exterior visualization of the

target, where ultrasound imaging can reveal depth-related information beyond the surface. Transparent transducers can provide a unique opportunity to combine ultrasound with the existing endoscopy probes, where the transducer can be attached in front of the camera and provide co-registered ultrasound visualization with the camera view. This thesis demonstrated the use of a transparent transducer array for designing highly compact endoscopy ultrasound probes. The experimental tests are carried out by placing an optical camera behind our fabricated transparent transducer array and performing optical and ultrasound imaging simultaneously. Optical imaging through transparent CMUTs may experience optical distortion and reduced image quality. However, after studying the optical images taken by the camera, negligible image distortion was recorded.

3D ultrasound imaging provides more advantages over 2D images, especially for imaging tumours, ultrasound-guided needle biopsy, and cardiac studies. However, The majority of the ultrasound systems are only capable of producing 2D images the design of 3D imaging systems is fraught with technical challenges such as transducer design, electronic complexity and massive computational power.

3D imaging requires 2D arrays, packing N^2 elements for an N $\times$ N array. TOBE arrays make it possible to address all the elements in a 2D array with row-column addressing. However, the lack of individual wiring for each element poses some limitations, such as the inability to receive on individual elements for generating 3D imaging.

The bias-sensitivity of TOBE arrays makes it possible to individually activate any elements in the transducer by applying bias-voltage on the corresponding row and columns. It also offers the opportunity to use bias encoding algorithms such as Hadamard encoding with two-way azimuthal focusing to perform high resolution, high SNR 3D imaging. This

approach, however, requires N ransmit-receive events for an N $\times$ N array. Without fast electronics for apply bias voltages quickly, imaging a single 3D volume may take an unacceptably long time. This thesis investigates the possibility of making fast-switching electronics that can switch bipolar voltages up to $\pm$ 500 volts. Due to the unique requirements for the electronics, such as sub-microsecond switching time and bi-polar high voltage switching, it was not possible to use any existing voltage switching integrated circuits (ICs). Therefore, unique electronic circuits were designed using high voltage MOSFETs. With the help of the fast biasing electronics, live cross-plane FORCES imaging is performed, with a frame rate of 20 fps. Live cross-plane power Doppler imaging is also demonstrated using the biasing electronics on a tube target caring corn starch solution. This reaches an imaging speed of 5 frames/sec with potential to reach hundreds of frames per second.

CMUTs are gaining popularity in modern ultrasound systems. Their broad bandwidth, higher electro-mechanical efficiency and bias sensitivity make them an excellent candidate for fabricating TOBE arrays. The main drawback of CMUT devices is their dielectric charging problem. The problem arises from the presence of dielectric thin films in the structure of the CMUTs. This thesis addressed the issue by replacing the dielectric layer with non-isolating semiconductor materials presenting high contact resistances. The high contact resistance of semiconductor materials can prevent the short-circuiting in snapdown events, while their non-isolating nature can dissipate any trapped charges in the film. However, the main challenge of fabricating CMUTs with semiconductor materials is their incompatibility with the current fabrication processes. This thesis investigated a new fabrication process and introduced CMUT devices fabricated with zinc oxide and gallium oxide thin films as barriers between the top and bottom electrodes. Fabricated CMUT devices presented a charging-free

operation after extended snapdown events.

In future work, we anticipate large 2D transparent arrays which are charging-free, and which will enable volumetric ultrasound, Doppler ultrasound and photoacoustic imaging modes. This thesis represents important steps towards the realization of this objective.

References

[1] S. Hu, K. Maslov, and L. V. Wang, "Second-generation optical-resolution photoacoustic microscopy with improved sensitivity and speed," *Optics letters*, vol. 36, no. 7, pp. 1134–1136, 2011.

[2] E. W. Stein, K. Maslov, and L. V. Wang, "Noninvasive mapping of the electrically stimulated mouse brain using photoacoustic microscopy," in *Photons Plus Ultrasound: Imaging and Sensing 2008: The Ninth Conference on Biomedical Thermoacoustics, Optoacoustics, and Acousto-optics*, vol. 6856, p. 68561J, International Society for Optics and Photonics, 2008.

[3] J. A. Jensen, S. I. Nikolov, K. L. Gammelmark, and M. H. Pedersen, "Synthetic aperture ultrasound imaging," *Ultrasonics*, vol. 44, pp. e5–e15, 2006.

[4] A. Dangi, S. Agrawal, and S.-R. Kothapalli, "Lithium niobate-based transparent ultrasound transducers for photoacoustic imaging," *Optics letters*, vol. 44, no. 21, pp. 5326–5329, 2019.

[5] C. Fang, H. Hu, and J. Zou, "A focused optically transparent pvdf transducer for photoacoustic microscopy," *IEEE Sensors Journal*, vol. 20, no. 5, pp. 2313–2319, 2019.

[6] J. Park, B. Park, T. Y. Kim, S. Jung, W. J. Choi, J. Ahn, D. H. Yoon, J. Kim, S. Jeon, D. Lee, *et al.*, "Quadruple ultrasound, photoacoustic, optical coherence, and fluorescence fusion imaging with a transparent ultrasound transducer," *Proceedings of the National Academy of Sciences*, vol. 118, no. 11, 2021.

[7] J. Mannath and K. Ragunath, "Role of endoscopy in early oesophageal cancer," *Nature Reviews Gastroenterology & Hepatology*, vol. 13, no. 12, p. 720, 2016.

[8] Y. Li, Z. Zhu, J. C. Jing, J. J. Chen, A. E. Heidari, Y. He, J. Zhu, T. Ma, M. Yu, Q. Zhou, *et al.*, "High-speed integrated endoscopic photoacoustic and ultrasound imaging system," *IEEE Journal of Selected Topics in Quantum Electronics*, vol. 25, no. 1, pp. 1–5, 2018.

[9] J. T. Annema, M. Veseliç, and K. F. Rabe, "Eus-guided fna of centrally located lung tumours following a non-diagnostic bronchoscopy," *Lung cancer*, vol. 48, no. 3, pp. 357–361, 2005.

[10] P. Prasad, N. Schmulewitz, A. Patel, S. Varadarajulu, S. M. Wildi, S. Roberts, R. Tutuian, P. King, R. H. Hawes, B. J. Hoffman, *et al.*, "Detection of occult liver metastases during eus for staging of malignancies," *Gastrointestinal endoscopy*, vol. 59, no. 1, pp. 49–53, 2004.

[11] P. Zhang, G. Fitzpatrick, W. Moussa, and R. J. Zemp, "Cmuts with improved electrical safety & minimal dielectric surface charging," in *2010 IEEE International Ultrasonics Symposium*, pp. 1881–1885, IEEE, 2010.

[12] A. K. Ilkhechi, C. Ceroici, Z. Li, and R. Zemp, "Transparent capacitive micromachined ultrasonic transducer (cmut) arrays for real-time photoacoustic applications," *Optics express*, vol. 28, no. 9, pp. 13750–13760, 2020.

[13] A. K. Ilkhechi, Z. Li, C. Ceroici, and R. Zemp, "Transparent capacitive micromachined ultrasound transducer linear arrays for high-resolution photoacoustic imaging applications," *International Society for Optics and Photonics*, 2019.

[14] A. K. Ilkhechi, C. Ceroici, and R. Zemp, "Transparent capacitive micromachined ultrasound transducer arrays," *IEEE International Ultrasonics Symposium*, 2020.

[15] A. K. Ilkhechi and R. Zemp, "Transparent capacitive micromachined ultrasound transducer arrays for multimodal imaging systems," pp. EM2D–3, 2021.

[16] A. K. Ilkhechi, C. Ceroici, E. Dew, and R. Zemp, "Transparent capacitive micromachined ultrasound transducer linear arrays for combined realtime optical and ultrasonic imaging," *Optics Letters*, vol. 46, no. 7, pp. 1542–1545, 2021.

[17] A. K. Ilkhechi, C. Ceroici, and R. J. Zemp, "High sensitivity transparent capacitive micromachined ultrasound transducer linear arrays for optical, photoacoustic and ultrasound imaging," in *Photons Plus Ultrasound: Imaging and Sensing 2021*, vol. 11642, p. 116421Z, International Society for Optics and Photonics, 2021.

[18] A. K. Ilkhechi, M. R. Sobhani, C. Ceroici, K. Latham, J. Brown, and R. Zemp, "Fast bias-switching electronics for ultrafast volumetric imaging with bias-encoded row-column 2d arrays," *IEEE International Ultrasonics Symposium*, 2021.

[19] A. K. Ilkhechi, Z. Li, C. Ceroici, and R. Zemp, "Charging-free cmut transducers with high contact-resistance ald thin-films fabricated with an adhesive wafer bonding process," *IEEE International Ultrasonics Symposium*, 2019.

[20] P. N. Wells, "Ultrasound imaging," *Physics in Medicine & Biology*, vol. 51, no. 13, p. R83, 2006.

[21] R. W. Cootney, "Ultrasound imaging: principles and applications in rodent research," *Ilar Journal*, vol. 42, no. 3, pp. 233–247, 2001.

[22] R. S. Cobbold, *Foundations of biomedical ultrasound*. Oxford university press, 2006.

[23] J. Yao and L. V. Wang, "Photoacoustic microscopy," *Laser & photonics reviews*, vol. 7, no. 5, pp. 758–778, 2013.

[24] L. V. Wang and S. Hu, "Photoacoustic tomography: in vivo imaging from organelles to organs," *science*, vol. 335, no. 6075, pp. 1458–1462, 2012.

[25] R. G. Kolkman, E. Hondebrink, W. Steenbergen, and F. F. de Mul, "In vivo photoacoustic imaging of blood vessels using an extreme-narrow aperture sensor," *IEEE Journal of selected topics in quantum electronics*, vol. 9, no. 2, pp. 343–346, 2003.

[26] C. Zhang, K. Maslov, and L. V. Wang, "Subwavelength-resolution label-free photoacoustic microscopy of optical absorption in vivo," *Optics letters*, vol. 35, no. 19, pp. 3195–3197, 2010.

[27] C. Burckhardt, P.-A. Grandchamp, and H. Hoffmann, "An experimental 2 mhz synthetic aperture sonar system intended for medical use," *IEEE Transactions on Sonics and Ultrasonics*, vol. 21, no. 1, pp. 1–6, 1974.

[28] S. Bennett, D. Peterson, D. Corl, and G. S. Kino, "A real-time synthetic aperture digital acoustic imaging system," in *Acoustical Imaging*, pp. 669–692, Springer, 1982.

[29] K. E. Thomenius, "Evolution of ultrasound beamformers," in *1996 IEEE Ultrasonics Symposium. Proceedings*, vol. 2, pp. 1615–1622, IEEE, 1996.

[30] J. Kortbek, J. A. Jensen, and K. L. Gammelmark, "Synthetic aperture sequential beamforming," in *2008 IEEE Ultrasonics Symposium*, pp. 966–969, IEEE, 2008.

[31] C. Ceroici, T. Harrison, and R. J. Zemp, "Fast orthogonal row–column electronic scanning with top-orthogonal-to-bottom electrode arrays," *IEEE transactions on ultrasonics, ferroelectrics, and frequency control*, vol. 64, no. 6, pp. 1009–1014, 2017.

[32] C. Ceroici, K. Latham, B. A. Greenlay, J. A. Brown, and R. J. Zemp, "Fast orthogonal row–column electronic scanning experiments and comparisons," *IEEE transactions on ultrasonics, ferroelectrics, and frequency control*, vol. 66, no. 6, pp. 1093–1101, 2019.

[33] A. Arnau *et al.*, *Piezoelectric transducers and applications*, vol. 2004. Springer, 2004.

[34] K. Uchino, S. Nomura, L. E. Cross, R. E. Newnham, and S. J. Jang, "Electrostrictive effect in perovskites and its transducer applications," *Journal of Materials science*, vol. 16, no. 3, pp. 569–578, 1981.

[35] R. E. Davidsen and S. W. Smith, "Relaxor ferroelectric materials in two-dimensional transducer arrays," in *1995 IEEE Ultrasonics Symposium. Proceedings. An International Symposium*, vol. 2, pp. 1283–1286, IEEE, 1995.

[36] C. Ceroici, "Novel 3d ultrasound imaging techniques using top-orthogonal-to-bottom-electrode (tobe) arrays," 2019.

[37] P. C. Eccardt and K. Niederer, "Micromachined ultrasound transducers with improved coupling factors from a cmos compatible process," *Ultrasonics*, vol. 38, no. 1-8, pp. 774–780, 2000.

[38] D. Hohm and G. Hess, "A subminiature condenser microphone with silicon nitride membrane and silicon back plate," *The Journal of the Acoustical Society of America*, vol. 85, no. 1, pp. 476–480, 1989.

[39] H. Koymen, A. Atalar, E. Aydogdu, C. Kocabas, H. K. Oguz, S. Olcum, A. Ozgurluk, and A. Unlugedik, "An improved lumped element nonlinear circuit model for a circular cmut cell," *IEEE transactions on ultrasonics, ferroelectrics, and frequency control*, vol. 59, no. 8, 2012.

[40] M. Torndahl, M. Almqvist, L. Wallman, H. W. Persson, and K. Lindstrom, "Characterisation and comparison of a cmut versus a piezoelectric transducer for air applications," in *Ultrasonics Symposium, 2002. Proceedings. 2002 IEEE*, vol. 2, pp. 1023–1026, IEEE, 2002.

[41] J. Gelly and F. Lanteri, "Comparison of piezoelectric (thickness mode) and mems transducers," in *Ultrasonics, 2003 IEEE Symposium on*, vol. 2, pp. 1965–1974, IEEE, 2003.

[42] G. Gurun, C. Tekes, J. Zahorian, T. Xu, S. Satir, M. Karaman, J. Hasler, and F. L. Degertekin, "Single-chip cmut-on-cmos front-end system for real-time volumetric ivus and ice imaging," *IEEE transactions on ultrasonics, ferroelectrics, and frequency control*, vol. 61, no. 2, pp. 239–250, 2014.

[43] J. Zahorian, M. Hochman, T. Xu, S. Satir, G. Gurun, M. Karaman, and F. L. Degertekin, "Monolithic cmut-on-cmos integration for intravascular ultrasound applications," *IEEE transactions on ultrasonics, ferroelectrics, and frequency control*, vol. 58, no. 12, pp. 2659–2667, 2011.

[44] A. Erguri, Y. Huang, X. Zhuang, O. Oralkan, G. G. Yarahoglu, and B. T. Khuri-Yakub, "Capacitive micromachined ultrasonic transducers: Fabrication technology," *IEEE transactions on ultrasonics, ferroelectrics, and frequency control*, vol. 52, no. 12, pp. 2242–2258, 2005.

[45] R. K. Chee, P. Zhang, M. Maadi, and R. J. Zemp, “Multifrequency interlaced cmuts for photoacoustic imaging,” *IEEE transactions on ultrasonics, ferroelectrics, and frequency control*, vol. 64, no. 2, pp. 391–401, 2016.

[46] B. A. Greenlay and R. J. Zemp, “Fabrication of linear array and top-orthogonal-to-bottom electrode cmut arrays with a sacrificial release process,” *IEEE transactions on ultrasonics, ferroelectrics, and frequency control*, vol. 64, no. 1, pp. 93–107, 2016.

[47] Q. Zhang, P.-V. Cicek, K. Allidina, F. Nabki, and M. N. El-Gamal, “Surface-micromachined cmut using low-temperature deposited silicon carbide membranes for above-ic integration,” *Journal of microelectromechanical systems*, vol. 23, no. 2, pp. 482–493, 2013.

[48] A. S. Logan, L. L. Wong, and J. T. Yeow, “A 1-d capacitive micromachined ultrasonic transducer imaging array fabricated with a silicon-nitride-based fusion process,” *IEEE/ASME Transactions on Mechatronics*, vol. 16, no. 5, pp. 861–865, 2011.

[49] M. I. Haller and B. T. Khuri-Yakub, “A surface micromachined electrostatic ultrasonic air transducer,” *IEEE transactions on ultrasonics, ferroelectrics, and frequency control*, vol. 43, no. 1, pp. 1–6, 1996.

[50] F. Y. Yamaner, X. Zhang, and Ö. Oralkan, “A three-mask process for fabricating vacuum-sealed capacitive micromachined ultrasonic transducers using anodic bonding,” *IEEE transactions on ultrasonics, ferroelectrics, and frequency control*, vol. 62, no. 5, pp. 972–982, 2015.

[51] K. F. Pedersen, A. S. Havreland, and E. V. Thomsen, “Fabrication, characterization and modelling of delay line based cmuts,” in *2021 IEEE International Ultrasonics Symposium (IUS)*, pp. 1–4, IEEE, 2021.

[52] A. S. Havreland, O. Hansen, K. F. Pedersen, M. Engholm, and E. V. Thomsen, “Delay line separation of cmut elements,” in *2020 IEEE International Ultrasonics Symposium (IUS)*, pp. 1–4, IEEE, 2020.

[53] K. Steenberg and E. V. Thomsen, “Polysilicon on quartz substrate for silicide based row-column cmuts,” in *2021 IEEE International Ultrasonics Symposium (IUS)*, pp. 1–4, IEEE, 2021.

[54] Z. Li, L. L. Wong, A. I. Chen, S. Na, J. Sun, and J. T. Yeow, “Fabrication of capacitive micromachined ultrasonic transducers based on adhesive wafer bonding technique,” *Journal of Micromechanics and Microengineering*, vol. 26, no. 11, p. 115019, 2016.

[55] Y. Huang, A. S. Ergun, E. Haeggstrom, M. H. Badi, and B. T. Khuri-Yakub, “Fabricating capacitive micromachined ultrasonic transducers with wafer-bonding technology,” *Journal of microelectromechanical systems*, vol. 12, no. 2, pp. 128–137, 2003.

[56] D. Ren, Y. Sun, J. Shi, and R. Chen, “A review of transparent sensors for photoacoustic imaging applications,” in *Photonics*, vol. 8, p. 324, Multidisciplinary Digital Publishing Institute, 2021.

[57] R. Chen, Y. He, J. Shi, C. Yung, J. Hwang, L. V. Wang, and Q. Zhou, “Transparent high-frequency ultrasonic transducer for photoacoustic microscopy application,” *IEEE transactions on ultrasonics, ferroelectrics, and frequency control*, vol. 67, no. 9, pp. 1848–1853, 2020.

[58] H. Chen, S. Agrawal, A. Dangi, C. Wible, M. Osman, L. Abune, H. Jia, R. Rossi, Y. Wang, and S.-R. Kothapalli, "Optical-resolution photoacoustic microscopy using transparent ultrasound transducer," *Sensors*, vol. 19, no. 24, p. 5470, 2019.

[59] B. Park, M. Han, J. Park, T. Kim, H. Ryu, Y. Seo, W. J. Kim, H. H. Kim, and C. Kim, "A photoacoustic finder fully integrated with a solid-state dye laser and transparent ultrasound transducer," *Photoacoustics*, vol. 23, p. 100290, 2021.

[60] S. Park, S. Kang, and J. H. Chang, "Optically transparent focused transducers for combined photoacoustic and ultrasound microscopy," *Journal of Medical and Biological Engineering*, vol. 40, pp. 707–718, 2020.

[61] X. Zhang, O. Adelegan, F. Y. Yamaner, and Ö. Oralkan, "An optically transparent capacitive micromachined ultrasonic transducer (cmut) fabricated using su-8 or bcb adhesive wafer bonding," in *2017 IEEE International Ultrasonics Symposium (IUS)*, pp. 1–4, IEEE, 2017.

[62] X. Zhang, X. Wu, O. J. Adelegan, F. Y. Yamaner, and Ö. Oralkan, "Backward-mode photoacoustic imaging using illumination through a cmut with improved transparency," *IEEE transactions on ultrasonics, ferroelectrics, and frequency control*, vol. 65, no. 1, pp. 85–94, 2017.

[63] J. Chen, M. Wang, J.-C. Cheng, Y.-H. Wang, P.-C. Li, and X. Cheng, "A photoacoustic imager with light illumination through an infrared-transparent silicon cmut array," *IEEE transactions on ultrasonics, ferroelectrics, and frequency control*, vol. 59, no. 4, pp. 766–775, 2012.

[64] A. Sampaleanu and R. Zemp, "Synthetic aperture 3d ultrasound imaging schemes with s-sequence bias-encoded top-orthogonal-to-bottom-electrode 2d cmut arrays," in *2013 IEEE International Ultrasonics Symposium (IUS)*, pp. 1994–1997, IEEE, 2013.

[65] S. Blaak, Z. Yu, G. Meijer, C. Prins, C. Lancee, J. Bosch, and N. de Jong, "Design of a micro-beamformer for a 2d piezoelectric ultrasound transducer," in *2009 IEEE International Ultrasonics Symposium*, pp. 1338–1341, IEEE, 2009.

[66] T. Halvorsrod, W. Luzi, and T. S. Lande, "A log-domain/spl mu/beamformer for medical ultrasound imaging systems," *IEEE Transactions on Circuits and Systems I: Regular Papers*, vol. 52, no. 12, pp. 2563–2575, 2005.

[67] N. M. Daher and J. T. Yen, "2-d array for 3-d ultrasound imaging using synthetic aperture techniques," *IEEE transactions on ultrasonics, ferroelectrics, and frequency control*, vol. 53, no. 5, pp. 912–924, 2006.

[68] A. Sampaleanu, P. Zhang, A. Kshirsagar, W. Moussa, and R. J. Zemp, "Top-orthogonal-to-bottom-electrode (tobe) cmut arrays for 3-d ultrasound imaging," *IEEE transactions on ultrasonics, ferroelectrics, and frequency control*, vol. 61, no. 2, pp. 266–276, 2014.

[69] C. E. Demore, A. W. Joyce, K. Wall, and G. R. Lockwood, "Real-time volume imaging using a crossed electrode array," *IEEE transactions on ultrasonics, ferroelectrics, and frequency control*, vol. 56, no. 6, pp. 1252–1261, 2009.

[70] M. F. Rasmussen and J. A. Jensen, "3d ultrasound imaging performance of a row-column addressed 2d array transducer: a simulation study," in *Medical Imaging 2013: Ultrasonic Imaging, Tomography, and Therapy*, vol. 8675, p. 86750C, International Society for Optics and Photonics, 2013.

[71] M. F. Rasmussen, T. L. Christiansen, E. V. Thomsen, and J. A. Jensen, "3-d imaging using row-column-addressed arrays with integrated apodization-part i: apodization design and line element beamforming," *IEEE transactions on ultrasonics, ferroelectrics, and frequency control*, vol. 62, no. 5, pp. 947–958, 2015.

[72] A. S. Havreland and E. V. Thomsen, "Analytical deflection profiles and pull-in voltage calculations of prestressed electrostatic actuated mems structures," *Journal of Microelectromechanical Systems*, 2021.

[73] C. Ceroici and R. J. Zemp, "Large-scale nonlinear lumped and integrated field simulations of top-orthogonal-to-bottom-electrode cmut architectures," *IEEE transactions on ultrasonics, ferroelectrics, and frequency control*, vol. 64, no. 7, pp. 1087–1091, 2017.

[74] J. Chan, Z. Zheng, K. Bell, M. Le, P. H. Reza, and J. T. Yeow, "Photoacoustic imaging with capacitive micromachined ultrasound transducers: Principles and developments," *Sensors*, vol. 19, no. 16, p. 3617, 2019.

[75] O. Oralkan, A. S. Ergun, J. A. Johnson, M. Karaman, U. Demirci, K. Kaviani, T. H. Lee, and B. T. Khuri-Yakub, "Capacitive micromachined ultrasonic transducers: Next-generation arrays for acoustic imaging?," *IEEE transactions on ultrasonics, ferroelectrics, and frequency control*, vol. 49, no. 11, pp. 1596–1610, 2002.

[76] I. L. Klundt, "Benzocyclobutene and its derivatives," *Chemical Reviews*, vol. 70, no. 4, pp. 471–487, 1970.

[77] Z. Li, A. K. Ilkhechi, and R. Zemp, "Transparent capacitive micromachined ultrasonic transducers (cmuts) for photoacoustic applications," *Optics express*, vol. 27, no. 9, pp. 13204–13218, 2019.

[78] Y. Wang, Z. Guo, L. V. Wang, T. N. Erpelding, L. Jankovic, J.-L. Robert, and G. David, "In vivo three-dimensional photoacoustic imaging based on a clinical matrix array ultrasound probe," *Journal of Biomedical Optics*, vol. 17, no. 6, p. 061208, 2012.

[79] M. Xu and L. V. Wang, "Photoacoustic imaging in biomedicine," *Review of scientific instruments*, vol. 77, no. 4, p. 041101, 2006.

[80] P. Hajireza, W. Shi, K. Bell, R. J. Paproski, and R. J. Zemp, "Non-interferometric photoacoustic remote sensing microscopy," *Light: Science & Applications*, vol. 6, no. 6, p. e16278, 2017.

[81] P. H. Reza, K. Bell, W. Shi, J. Shapiro, and R. J. Zemp, "Deep non-contact photoacoustic initial pressure imaging," *Optica*, vol. 5, no. 7, pp. 814–820, 2018.

[82] Y. Wang, S. Hu, K. Maslov, Y. Zhang, Y. Xia, and L. V. Wang, "In vivo integrated photoacoustic and confocal microscopy of hemoglobin oxygen saturation and oxygen partial pressure," *Optics letters*, vol. 36, no. 7, pp. 1029–1031, 2011.

[83] L. V. Wang and L. Gao, "Photoacoustic microscopy and computed tomography: from bench to bedside," *Annual review of biomedical engineering*, vol. 16, pp. 155–185, 2014.

[84] J. Xia, J. Yao, and L. V. Wang, "Photoacoustic tomography: principles and advances," *Electromagnetic waves (Cambridge, Mass.)*, vol. 147, p. 1, 2014.

[85] J. Buchmann, J. Guggenheim, E. Zhang, C. Scharfenorth, B. Spannekrebs, C. Villringer, and J. Laufer, "Characterization and modeling of fabry–perot ultrasound sensors with hard dielectric mirrors for photoacoustic imaging," *Applied optics*, vol. 56, no. 17, pp. 5039–5046, 2017.

[86] P. Zarkos, O. Hsu, and V. Stojanović, "Ring resonator based ultrasound detection in a zero-change advanced cmos-soi process," in *CLEO: Applications and Technology*, pp. JW2A–78, Optical Society of America, 2019.

[87] W. X. Xin, J. Yuhao, L. Z. Yong, W. Wang, and Z. Li, "Sensitivity characteristics of microfiber fabry-perot interferometric photoacoustic sensors," *Journal of Lightwave Technology*, 2019.

[88] K. I. Maslov and L. V. Wang, "Photoacoustic imaging of biological tissue with intensity-modulated continuous-wave laser," *Journal of biomedical optics*, vol. 13, no. 2, p. 024006, 2008.

[89] G. Paltauf, P. Hartmair, G. Kovachev, and R. Nuster, "Piezoelectric line detector array for photoacoustic tomography," *Photoacoustics*, vol. 8, pp. 28–36, 2017.

[90] A. Dangi, S. Agrawal, S. Tiwari, S. Jadhav, C. Cheng, S. Trolier-McKinstry, R. Pratap, and S.-R. Kothapalli, "Evaluation of high frequency piezoelectric micromachined ultrasound transducers for photoacoustic imaging," in *2018 IEEE SENSORS*, pp. 1–4, IEEE, 2018.

[91] K. H. Martin, B. D. Lindsey, J. Ma, M. Lee, S. Li, F. S. Foster, X. Jiang, and P. A. Dayton, "Dual-frequency piezoelectric transducers for contrast enhanced ultrasound imaging," *Sensors*, vol. 14, no. 11, pp. 20825–20842, 2014.

[92] C. Ceroici, K. Latham, R. Chee, B. Greenlay, Q. Barber, J. A. Brown, and R. Zemp, "3d photoacoustic imaging using hadamard-bias encoding with a crossed electrode relaxor array," *Optics letters*, vol. 43, no. 14, pp. 3425–3428, 2018.

[93] P. Zhang, G. Fitzpatrick, T. Harrison, W. A. Moussa, and R. J. Zemp, "Double-soi wafer-bonded cmuts with improved electrical safety and minimal roughness of dielectric and electrode surfaces," *Journal of Microelectromechanical Systems*, vol. 21, no. 3, pp. 668–680, 2012.

[94] J. Park, B. Park, T. Kim, D. Lee, U. Yong, J. Jang, U. Jeong, H. H. Kim, and C. Kim, "Seamlessly integrated optical and acoustical imaging systems through transparent ultrasonic transducer," in *Photons Plus Ultrasound: Imaging and Sensing 2020*, vol. 11240, p. 112401P, International Society for Optics and Photonics, 2020.

[95] C. D. Gerardo, E. Cretu, and R. Rohling, "Fabrication and testing of polymer-based capacitive micromachined ultrasound transducers for medical imaging," *Microsystems & Nanoengineering*, vol. 4, no. 1, p. 19, 2018.

[96] Z. Li, S. Na, A. I. Chen, L. L. Wong, Z. Sun, P. Liu, and J. T. Yeow, "Optimization on benzocyclobutene-based cmut fabrication with an inverse structure," *Sensors and Actuators A: Physical*, vol. 281, pp. 1–8, 2018.

[97] S. Vaithilingam, T.-J. Ma, Y. Furukawa, I. O. Wygant, X. Zhuang, A. De La Zerda, O. Oralkan, A. Kamaya, R. B. Jeffrey, B. T. Khuri-yakub, *et al.*, "Three-dimensional photoacoustic imaging using a two-dimensional cmut array," *IEEE transactions on ultrasonics, ferroelectrics, and frequency control*, vol. 56, no. 11, pp. 2411–2419, 2009.

[98] W. P. Mason, *Electromechanical transducers and wave filters.* D. Van Nostrand Company, Inc., 1948.

[99] C. Ng, K. Chew, and S. Chu, "Characterization and comparison of pecvd silicon nitride and silicon oxynitride dielectric for mim capacitors," *IEEE Electron Device Letters*, vol. 24, no. 8, pp. 506–508, 2003.

[100] M. Sautto, D. Leone, A. Savoia, D. Ghisu, F. Quaglia, G. Caliano, and A. Mazzanti, "A cmut transceiver front-end with 100-v tx driver and 1-mw low-noise capacitive feedback rx amplifier in bcd-soi technology," in *ESSCIRC 2014-40th European Solid State Circuits Conference (ESSCIRC)*, pp. 407–410, IEEE, 2014.

[101] T. Takezaki, M. Kawano, H. Hasegawa, S. Machida, and D. Ryuzaki, "Ultra-narrow gap cmut cell structure for highly sensitive photoacoustic imaging," in *2017 IEEE International Ultrasonics Symposium (IUS)*, pp. 1–4, IEEE, 2017.

[102] S. J. Carey, C. Brox-Nilsen, H. M. Lewis, C. M. Gregory, and J. V. Hatfield, "Scanning head with 128-element 20-mhz pvdf linear array transducer," *IEEE transactions on ultrasonics, ferroelectrics, and frequency control*, vol. 56, no. 8, pp. 1769–1777, 2009.

[103] A. Hurrell and F. Duck, "A two-dimensional hydrophone array using piezoelectric pvdf," *ieee transactions on ultrasonics, ferroelectrics, and frequency control*, vol. 47, no. 6, pp. 1345–1353, 2000.

[104] K. Chen, H.-S. Lee, A. P. Chandrakasan, and C. G. Sodini, "Ultrasonic imaging transceiver design for cmut: A three-level 30-vpp pulse-shaping pulser with improved efficiency and a noise-optimized receiver," *IEEE Journal of Solid-State Circuits*, vol. 48, no. 11, pp. 2734–2745, 2013.

[105] G. Gurun, P. Hasler, and F. L. Degertekin, "Front-end receiver electronics for high-frequency monolithic cmut-on-cmos imaging arrays," *IEEE transactions on ultrasonics, ferroelectrics, and frequency control*, vol. 58, no. 8, pp. 1658–1668, 2011.

[106] I. O. Wygant, N. S. Jamal, H. J. Lee, A. Nikoozadeh, Ö. Oralkan, M. Karaman, and B. T. Khuri-Yakub, "An integrated circuit with transmit beamforming flip-chip bonded to a 2-d cmut array for 3-d ultrasound imaging," *IEEE transactions on ultrasonics, ferroelectrics, and frequency control*, vol. 56, no. 10, pp. 2145–2156, 2009.

[107] I. O. Wygant, X. Zhuang, D. T. Yeh, O. Oralkan, A. S. Ergun, M. Karaman, and B. T. Khuri-Yakub, "Integration of 2d cmut arrays with front-end electronics for volumetric ultrasound imaging," *IEEE transactions on ultrasonics, ferroelectrics, and frequency control*, vol. 55, no. 2, pp. 327–342, 2008.

[108] I. Wygant, "A comparison of cmuts and piezoelectric transducer elements for 2d medical imaging based on conventional simulation models," in *2011 IEEE International Ultrasonics Symposium*, pp. 100–103, IEEE, 2011.

[109] B. Khuri-Yakub, G. G. Yaralioglu, B. Bayram, and M. Kupnik, "5f-4 acoustic crosstalk reduction method for cmut arrays," in *2006 IEEE Ultrasonics Symposium*, pp. 590–593, IEEE, 2006.

[110] S. Park, A. B. Karpiouk, S. R. Aglyamov, and S. Y. Emelianov, "Adaptive beamforming for photoacoustic imaging using linear array transducer," in *2008 IEEE Ultrasonics Symposium*, pp. 1088–1091, IEEE, 2008.

[111] S. Yoshinaga, I. Oda, S. Nonaka, R. Kushima, and Y. Saito, "Endoscopic ultrasound using ultrasound probes for the diagnosis of early esophageal and gastric cancers," *World journal of gastrointestinal endoscopy*, vol. 4, no. 6, p. 218, 2012.

[112] J. Peng, X. Li, H. Tang, X. Peng, and S. Chen, "An optimized high resolution radial ultrasound endoscope for digestive tract imaging," in *2017 IEEE International Ultrasonics Symposium (IUS)*, pp. 1–4, IEEE, 2017.

[113] J. Peng, X. Peng, H. Tang, X. Li, R. Chen, Y. Li, T. Wang, S. Chen, K. K. Shung, and Q. Zhou, "Fabrication and performance of a miniaturized and integrated endoscope ultrasound convex array for digestive tract imaging," *IEEE Transactions on Biomedical Engineering*, vol. 65, no. 1, pp. 140–148, 2017.

[114] K. Pham, S. Noimark, N. Huynh, E. Zhang, F. Kuklis, J. Jaros, A. Desjardins, B. Cox, and P. Beard, "Broadband all-optical plane-wave ultrasound imaging system based on a fabry-perot scanner," *IEEE Transactions on Ultrasonics, Ferroelectrics, and Frequency Control*, 2020.

[115] P. Hajireza, K. Krause, M. Brett, and R. Zemp, "Glancing angle deposited nanostructured film fabry-perot etalons for optical detection of ultrasound," *Optics express*, vol. 21, no. 5, pp. 6391–6400, 2013.

[116] Y. Li, G. Lu, J. J. Chen, J. C. Jing, T. Huo, R. Chen, L. Jiang, Q. Zhou, and Z. Chen, "Pmn-pt/epoxy 1-3 composite based ultrasonic transducer for dual-modality photoacoustic and ultrasound endoscopy," *Photoacoustics*, vol. 15, p. 100138, 2019.

[117] Q. Huang and Z. Zeng, "A review on real-time 3d ultrasound imaging technology," *BioMed research international*, vol. 2017, 2017.

[118] A. Fenster, J. Bax, H. Neshat, D. Cool, N. Kakani, and C. Romagnoli, "3d ultrasound imaging in image-guided intervention," in *2014 36th Annual International Conference of the IEEE Engineering in Medicine and Biology Society*, pp. 6151–6154, IEEE, 2014.

[119] K. Latham, C. Ceroici, C. A. Samson, R. J. Zemp, and J. A. Brown, "Simultaneous azimuth and fresnel elevation compounding: A fast 3-d imaging technique for crossed-electrode arrays," *IEEE transactions on ultrasonics, ferroelectrics, and frequency control*, vol. 65, no. 9, pp. 1657–1668, 2018.

[120] H. F. Routh, "Doppler ultrasound," *IEEE Engineering in Medicine and Biology Magazine*, vol. 15, no. 6, pp. 31–40, 1996.

[121] Y. Huang, E. O. Hæggstrom, X. Zhuang, A. S. Ergun, and B. T. Khuri-Yakub, "A solution to the charging problems in capacitive micromachined ultrasonic transducers," *IEEE transactions on ultrasonics, ferroelectrics, and frequency control*, vol. 52, no. 4, pp. 578–580, 2005.

[122] K. Kao and W. Hwang, "Electrical transport in solids, international series in the science of the solid state," 1981.

[123] S. M. Sze and K. K. Ng, *Physics of semiconductor devices.* John wiley & sons, 2006.

[124] J. Wibbeler, G. Pfeifer, and M. Hietschold, "Parasitic charging of dielectric surfaces in capacitive microelectromechanical systems (mems)," *Sensors and Actuators A: Physical*, vol. 71, no. 1-2, pp. 74–80, 1998.

[125] X. Zhang and G. M. Sessler, "Charge dynamics in silicon nitride/silicon oxide double layers," *Applied Physics Letters*, vol. 78, no. 18, pp. 2757–2759, 2001.

[126] T. Zure and S. Chowdhury, "Effect of dielectric charging on capacitance change of an soi based cmut," *Micro and Nanosystems*, vol. 6, no. 1, pp. 55–60, 2014.

[127] D. Zhao, C. Simopoulos, and S. Zhuang, "Long term reliability test results of cmut," in *2017 IEEE International Ultrasonics Symposium (IUS)*, pp. 1–3, IEEE, 2017.

[128] B. A. Greenlay and R. J. Zemp, "Fabrication of linear array and top-orthogonal-to-bottom electrode cmut arrays with a sacrificial release process," *IEEE transactions on ultrasonics, ferroelectrics, and frequency control*, vol. 64, no. 1, pp. 93–107, 2017.

[129] R. S. Muller, T. I. Kamins, M. Chan, and P. K. Ko, *Device electronics for integrated circuits*. Wiley New York, 1986.

[130] A. Janotti and C. G. Van de Walle, "Fundamentals of zinc oxide as a semiconductor," *Reports on progress in physics*, vol. 72, no. 12, p. 126501, 2009.

[131] T. Muneshwar, G. Shoute, D. Barlage, and K. Cadien, "Plasma enhanced atomic layer deposition of zno with diethyl zinc and oxygen plasma: Effect of precursor decomposition," *Journal of Vacuum Science & Technology A: Vacuum, Surfaces, and Films*, vol. 34, no. 5, p. 050605, 2016.

[132] A. Ramadan, R. Gould, and A. Ashour, "On the van der pauw method of resistivity measurements," *Thin Solid Films*, vol. 239, no. 2, pp. 272–275, 1994.

[133] S. J. Lukes and D. L. Dickensheets, "Su-8 2002 surface micromachined deformable membrane mirrors," *Journal of Microelectromechanical Systems*, vol. 22, no. 1, pp. 94–106, 2013.

[134] P. A. Himmer, D. L. Dickensheets, and R. A. Friholm, "Micromachined silicon nitride deformable mirrors for focus control," *Optics Letters*, vol. 26, no. 16, pp. 1280–1282, 2001.

[135] M. J. Moghimi, B. J. Lutzenberger, B. M. Kaylor, and D. L. Dickensheets, "Moems deformable mirrors for focus control in vital microscopy," *Journal of Micro/Nanolithography, MEMS, and MOEMS*, vol. 10, no. 2, p. 023005, 2011.

[136] H. Yang, C.-Y. Yang, and M.-S. Yeh, "Miniaturized variable-focus lens fabrication using liquid filling technique," *Microsystem Technologies*, vol. 14, no. 7, pp. 1067–1072, 2008.

[137] S. Kuiper and B. Hendriks, "Variable-focus liquid lens for miniature cameras," *Applied physics letters*, vol. 85, no. 7, pp. 1128–1130, 2004.

[138] S. J. Lukes, P. A. Himmer, E. J. Moog, S. R. Shaw, and D. L. Dickensheets, "Feedback-stabilized deformable membrane mirrors for focus control," *Journal of Micro/Nanolithography, MEMS, and MOEMS*, vol. 8, no. 4, p. 043040, 2009.

[139] H.-T. Hsieh, H.-C. Wei, M.-H. Lin, W.-Y. Hsu, Y.-C. Cheng, and G.-D. J. Su, "Thin autofocus camera module by a large-stroke micromachined deformable mirror," *Optics express*, vol. 18, no. 11, pp. 11097–11104, 2010.

[140] J.-L. Wang, T.-Y. Chen, C. Liu, C.-W. E. Chiu, and G.-D. J. Su, "Polymer deformable mirror for optical auto focusing," *ETRI journal*, vol. 29, no. 6, pp. 817–819, 2007.

[141] H.-C. Wei, Y.-H. Chien, W.-Y. Hsu, Y.-C. Cheng, and G.-D. J. Su, "Controlling a mems deformable mirror in a miniature auto-focusing imaging system," *IEEE Transactions on Control Systems Technology*, vol. 20, no. 6, pp. 1592–1596, 2012.

[142] M.-J. Lin and K.-W. Wu, "Design and fabrication of an electrostatically actuated microdeformable focusing mirror," *Journal of Micro/Nanolithography, MEMS, and MOEMS*, vol. 10, no. 1, p. 011504, 2011.

[143] J.-L. Wang, T.-Y. Chen, Y.-H. Chien, and G.-D. J. Su, "Miniature optical autofocus camera by micromachined fluoropolymer deformable mirror," *Optics Express*, vol. 17, no. 8, pp. 6268–6274, 2009.

[144] V. X. Yang, Y. Mao, B. A. Standish, N. R. Munce, S. Chiu, D. Burnes, B. C. Wilson, I. A. Vitkin, P. A. Himmer, and D. L. Dickensheets, "Doppler optical coherence tomography with a micro-electro-mechanical membrane mirror for high-speed dynamic focus tracking," *Optics letters*, vol. 31, no. 9, pp. 1262–1264, 2006.

[145] R. J. Zemp, L. Song, R. Bitton, K. K. Shung, and L. V. Wang, "Realtime photoacoustic microscopy in vivo with a 30-mhz ultrasound array transducer," *Optics express*, vol. 16, no. 11, pp. 7915–7928, 2008.

[146] K. L. Bell, P. Hajireza, W. Shi, and R. J. Zemp, "Temporal evolution of low-coherence reflectrometry signals in photoacoustic remote sensing microscopy," *Applied optics*, vol. 56, no. 18, pp. 5172–5181, 2017.

[147] D. L. Dickensheets, "Requirements of mems membrane mirrors for focus adjustment and aberration correction in endoscopic confocal and optical coherence tomography imaging instruments," *Journal of Micro/Nanolithography, MEMS, and MOEMS*, vol. 7, no. 2, p. 021008, 2008.

[148] J. Sun, S. Guo, L. Wu, L. Liu, S.-W. Choe, B. S. Sorg, and H. Xie, "3d in vivo optical coherence tomography based on a low-voltage, large-scan-range 2d mems mirror," *Optics Express*, vol. 18, no. 12, pp. 12065–12075, 2010.

[149] M. F. la Cour, T. L. Christiansen, J. A. Jensen, and E. V. Thomsen, "Electrostatic and small-signal analysis of cmuts with circular and square anisotropic plates," *IEEE transactions on ultrasonics, ferroelectrics, and frequency control*, vol. 62, no. 8, pp. 1563–1579, 2015.

[150] S. A. Self, "Focusing of spherical gaussian beams," *Applied optics*, vol. 22, no. 5, pp. 658–661, 1983.

[151] K. Dupraz, K. Cassou, A. Martens, and F. Zomer, "The abcd matrix for parabolic reflectors and its application to astigmatism free four-mirror cavities," *Optics Communications*, vol. 353, pp. 178–183, 2015.

[152] B. Greenlay and R. Zemp, "Cmut isolated isolation posts," in *Ultrasonics Symposium (IUS), 2017 IEEE International*, pp. 1–1, IEEE, 2017.

[153] A. I. Chen, L. L. Wong, Z. Li, S. Na, and J. T. Yeow, "Practical cmut fabrication with a nitride-to-oxide-based wafer bonding process," *Journal of Microelectromechanical Systems*, vol. 26, no. 4, pp. 829–836, 2017.

[154] W. Kern, "The evolution of silicon wafer cleaning technology," *Journal of the Electrochemical Society*, vol. 137, no. 6, pp. 1887–1892, 1990.

[155] B. E. Saleh, M. C. Teich, and B. E. Saleh, *Fundamentals of photonics*, vol. 22. Wiley New York, 1991.

Appendix A: Ultra-fast deformable mirrors for laser pulse modulations

Objective

In recent decades, laser technology has been used in many industries, from 3D printers to diagnostic and therapeutic applications, which almost all are requiring a laser focusing. Current technology has limitations, and fast focusing is not possible, leading to slower machines. Here we introduce ultrafast tunable MEMS mirrors consisting of a miniature circular mirrored-membrane, which can be electrostatically actuated to change mirror curvature at unprecedented speeds. The central deflection zone is a close approximation to a parabolic mirror. The device is fabricated with minimal membrane mass to be only slightly larger than a tightly focused optical spot. These devices used for fast tuning of the focal wavefront of laser beams at $\approx$ MHz tuning rates, two to three orders of magnitude faster than current optical focusing technologies. Fabricated devices have a silicon membrane with 30 μm radius and 300 nm gap spacing between top and bottom electrodes. These devices can change the focal position of a tightly focused beam by ≈ 1 mm at rates up to 4.9 MHz and with response times smaller than 5 μs. The results of the research is presented at SPIE 2017 conference.

A.1 Introduction

Optical focus control is used in a vast verity of optical systems from imaging devices (such as camera modules) to medical diagnostic and therapeutic instruments. Fast microscopy methods such as optical coherence tomography and nonlinear microscopy require optical focusing, but performance is limited by the slow response of the focusing components. In most designs focusing is achieved with a lens-motor combinations, but the need for compact and faster components requires new techniques.

Deformable focus control components are an acceptable alternative for the traditional lens-motor techniques [133–135]. Examples include liquid-filled lenses [136], electro-wetting lenses [137,138], and deformable mirrors [138–143]. MEMS-based variable focal-length lenses use electrostatic forces or pressures to change the focal length of membranes or polymers. Liquid-deformable lens systems additionally use electro-wetting or other principles for actuation. These devices, compared to mechanical lenses, have shorter response times and require smaller spaces to operate. However, sensitivity to environmental shocks and ambient temperature limit their potential for many applications.

Aside from such deformable-lenses, MEMS mirrors with central deformation have several compelling properties. Sub-millisecond response time, parabolic membrane deformation capable of providing aberration-free focusing, and minimization of moving parts qualify them for numerous applications [144]. For instance, camera modules utilizing deformable mirrors for controlling the focus are small, fast and are less power-hungry than competing voice-coil focusing systems.

Himmer et al. [134] designed and fabricated a silicon nitride deformable mirror with a

spherical aberration adjustment for controlling focus. The mirror had a 1 mm diameter with a maximum $\approx$800 nm stable central deflection. The deflection effectively changes the focal length of the mirror from 36 to 360 mm. The mirror is fabricated by depositing a low-pressure chemical vapour deposition (LPCVD) nitride thin-film as a membrane on a thin phosphorous silicate glass (PSG) sacrificial layer then selectively etching the PSG and extra etching the substrate with Tetramethylammonium hydroxide (TMAH) to form a gap. A simple fabrication process and high optical power are some advantages of this design. However, LPCVD nitride has a high surface roughness, which can increase the scattering of the reflected light. Other groups have fabricated similar devices but still exhibit non-ideal surface roughness.

Polymer-based materials have been considered as an alternative to nitride membranes. These materials have several advantages, such as the possibility to form large membranes, smoother surface, simpler fabricating process, and larger membrane strokes [134]. Lukes et al. [133] developed two different fabrication techniques for fabricating deformable mirrors with a polymer membrane. Using SU-8 as the membrane material and silicon as the sacrificial layer, they achieved an acceptable membrane surface roughness. The mirrors had a central deflection of 16.7μm (in stable range) and frequency response up to 1 KHz. Sacrificial etch holes occupied 3% of the membrane and increased the scattering of the reflected rays.

Hsieh et al. [139] presented a deformable mirror for an auto-focusing camera module by using a polymer-based bonding technique. This technique eliminated the need for placing etch holes on the membrane and improved the surface quality of the mirror. The fabricated mirror had a 32μm gap, capable of providing stable membrane deformation up to 20 diopters.

Most fast-focusing systems have been limited to KHz focusing rates. However, many

emerging technologies could benefit from even faster focusing. These applications may include laser modulation systems, optical switches, laser printing and marking systems, projection systems, and microscopy systems.

Some microscopy methods use tunable optics for improved depth-scanning [144]. Microscopy techniques such as photoacoustic imaging [80,81,145,146], confocal microscopy and optical coherence tomography (OCT) [147,148] may benefit from faster deformable mirrors. These systems scan light in tissue and record the backscattered light or acoustic waves to generate images. Deformable mirrors can control the focus of the light and improve the depth-of-focus. Yang et al [144] introduced a silicon nitride deformable mirror with 8 KHz axial scan rate for a Doppler optical coherence tomography (DOCT) system to dynamically adjust the optical beam focus. The DOCT images were taken at one frame/sec. Significantly greater frame rates are currently possible with OCT but not yet using fast focusing systems to improve depth of focus. Similar resolution and image capturing improvements may be possible with other forms of optical microscopy when using fast-focusing optics, but current dynamic-focusing optics are too slow for many such applications.

Most previous deformable optics used collimated beams and relied on membrane deformation to optically focus incidence parallel rays. The use of collimated beams necessitated large membranes resulting in slow speeds. In contrast, our approach instead uses ultra-miniature membranes to change the focal wavefront-curvature of tightly focused beams to steer the downstream optical focus. This is done in a way that cannot be described using optical ray-tracing in the sense that focused rays converging to a point will experience a locally-flat surface regardless of the curvature. However, a diffraction-based view of light offers a different story. Wavefronts of a Gaussian beam at the focus are flat and will follow

the curvature of a reflecting surface. We use small reflective membranes to introduce near-parabolic focal curvature modulation. Because this can be done with very small membranes, very fast focusing speeds are possible. This represents a new approach for laser-beam focusing. Note that if existing mm-cm scale deformable optics were used with tightly focused laser spots, they would be ineffective at changing the focus since the curvature on these devices is locally almost flat. In contrast, our devices can achieve a tight radius of curvatures as small as 3mm, leading to fast focal-wavefront shaping.

We call our micro-scale deformable mirrors Capacitive Micromachined Optical-Focusing MEMS (CMOF-MEMS). The presented CMOF-MEMS have a radius of 30 μm and are capable of operating up to 4.9 MHz. The mirror has surface roughness less than 0.39 nm minimizing light scattering to a negligible level. The presented mirror has a 100 nm central deflection capable of providing optical power up to ≈900 diopters. In order to show the effectiveness of our design, we fabricated the mirrors with a silicon-on-insulating wafer-bonding technique and tested devices in an optical setup to observe the focal length shifts provided with the mirrors. With an optical relay system, we could successfully change the focus of a laser beam up to 8 mm with only 100 nm deflection of the membranes. With tighter optical focusing, we can achieve 1.3μm spot sizes and achieve a 300μm focal-length shift.

A.2 Principle of operation and simulations

Presented CMOF mirrors in this paper have a thin membrane which can be electrostatically actuated to deform the mirrored-membrane, changing the optical power of the device. A

simple optical setup to change the focus of a laser beam is illustrated in Fig. 41.

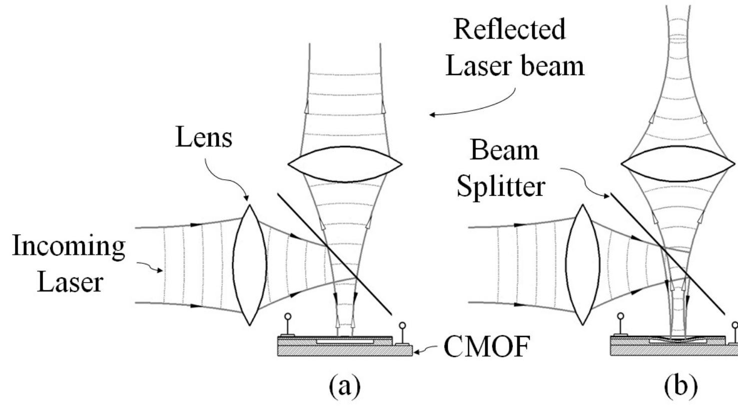

Fig. 41: Illustration showing the principle of fast optical focusing with a Capacitive Micromachined Optical Focusing (CMOF) deformable MEMS mirror (a) non deflected CMOF mirror (b) deflected CMOF mirror.

As shown in Fig. 41, a laser beam is focused on a CMOF mirror through a beam splitter. When electrostatic force is applied, the membrane's inward deflection forms a parabolic profile, affecting the reflected laser beam wavefront radius-of-curvature. The surface profile of a CMOF mirror is given from clamped-deformable plate theory as [149]:

$$h(r) = h_0 \left(1 - \left(\frac{r}{a}\right)^2\right)^2 \tag{6}$$

where r is the radial distance from the center of the mirror and a is the radius of the mirror. The radius-of-curvature given a height function $h(r)$ is given as:

$$ROC(r) = \left| \frac{(1 + h'^2)^{3/2}}{h''} \right| \tag{7}$$

where a prime denotes a derivative with respect to r.

Thus, radius-of-curvature (ROC) of the mirror at its center is given by:

$$ROC = \frac{a^2}{4h_0} \tag{8}$$

Where h_0 is the central deflection of the membrane for a given voltage. The focal length of this mirror is given as $f_M = ROC/2$. The Optical Power (OP) of the mirror is:

$$OP = \frac{1}{f_M} \tag{9}$$

Typically reported in Diopters $[1/m]$.

Figure 42a shows the OP of a CMOF for different membrane sizes and central deflections. As illustrated, the OP for a 30 μm membrane with 100 nm maximum central deflection is ≈900 diopters Thus such a membrane is capable of changing the focus from infinity to mm-range. This OP is substantially higher than the conventional deformable mirrors fabricated with MEMS technology which is up to 20 diopters for polymer membranes [139].

To describe the focusing of a laser beam using our proposed devices, we consider a Gaussian beam with waist w_0 focused on a CMOF mirror. The position of the refocused beam is given by [150]:

$$\frac{1}{(s + (z_R/M^2)^2/(s - f_M))} + \frac{1}{s'} = \frac{1}{f_M} \tag{10}$$

Where $z_R = \pi w_0^2/\lambda$ is the Rayleigh range, M^2 is the beam quality factor, $f_M = ROC/2$ is the focal length of the mirror, and s and s' are object and image distances, respectively. Fig. 42b and Fig. 42c are illustrating the focal length shift, and spot size change of a laser beam for membrane radii ranging from 20 to 50 μm with central deflection from zero to 100

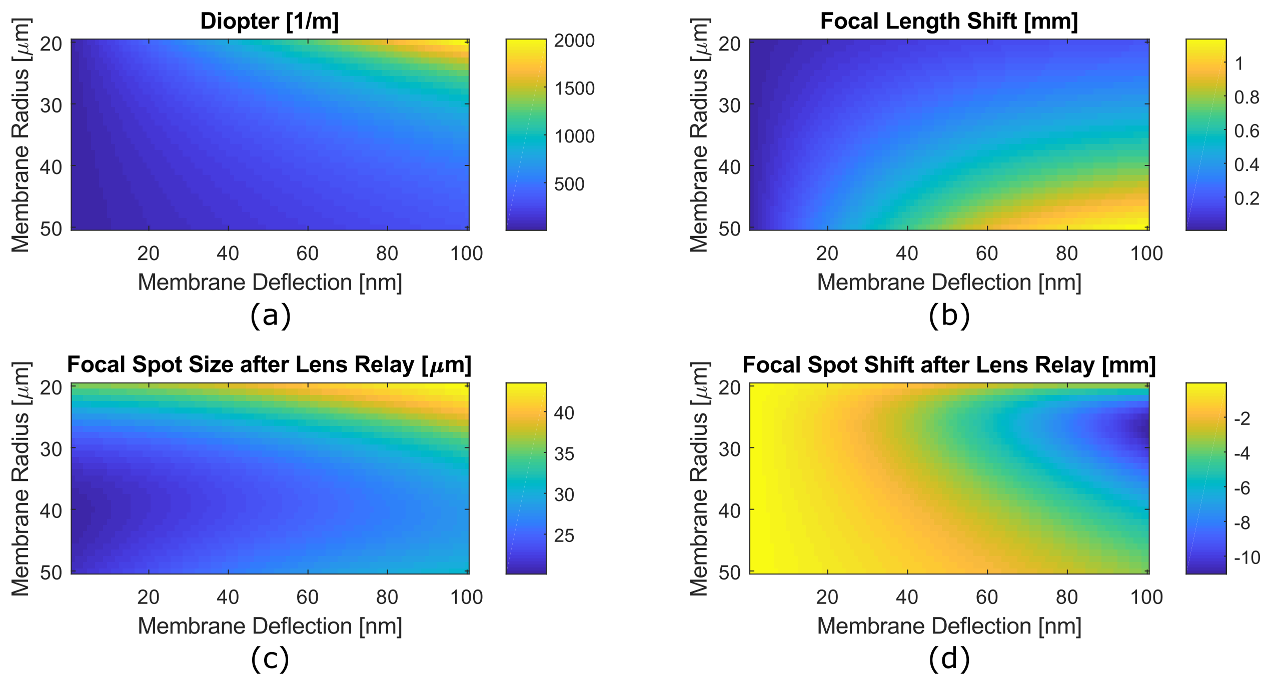

Fig. 42: MATLAB Calculations (a) Optical power of a CMOF for various membrane sizes and deflection (b) focal length shift of a laser beam after refocusing with a CMOF for various membrane sizes and deflections (c) focal spot size change of a laser beam after refocusing with a CMOF for various membrane sizes and deflections (d) focal spot shift of a laser beam after a lens relay with $f = 3\ mm$.

nm. These simulations were done for the beam focused onto the membrane with $s = 0$ and a $w_0 = 0.4a$. As we can see, the change of the laser beam focal position for a perfect Gaussian beam with $M^2 = 1$ is ≈ 1 mm. This change can be further magnified with an optical relay system. Fig. 42d illustrates the focal length shift after implementing a re-focusing lens with $f = 3$ mm, positioned 3.3 mm away from the CMOF-mirror. This magnifies the focal length shift up to 10 mm.The calculations are done without considering the aberration introduced by mirror. They hold up well with the experimental data, but more accurate modeling is possible by defining an ABCD matrix for parabolic deformable mirrors [151].

A.3 Device fabrication

Numerous fabrication processes have been published for fabricating deformable mirrors [133, 134]. Silicon nitride deformable membranes have a simple fabrication process, but the membrane size and roughness are limited. Polymer based deformable mirrors normally have sizes in the range of a few millimeters and exhibit slower speeds compared to rigid membranes such as silicon and silicon nitride. However, they provide a smoother surface finish resulting in less scattering.

Wafer bonding techniques are extensively used in micro-systems technology [44]. In this process, two wafers are bonded to form the membrane. There have been several bonding techniques introduced for fabricating micromachined capacitive ultrasound transducers (CMUTs) [44,152,153]. Fusion bonding provides a vacuum cavity with a single crystal silicon membrane which has atomic level roughness. Presented devices in this paper are fabricated with this technique to minimize the surface roughness and form membranes only tens of mi-

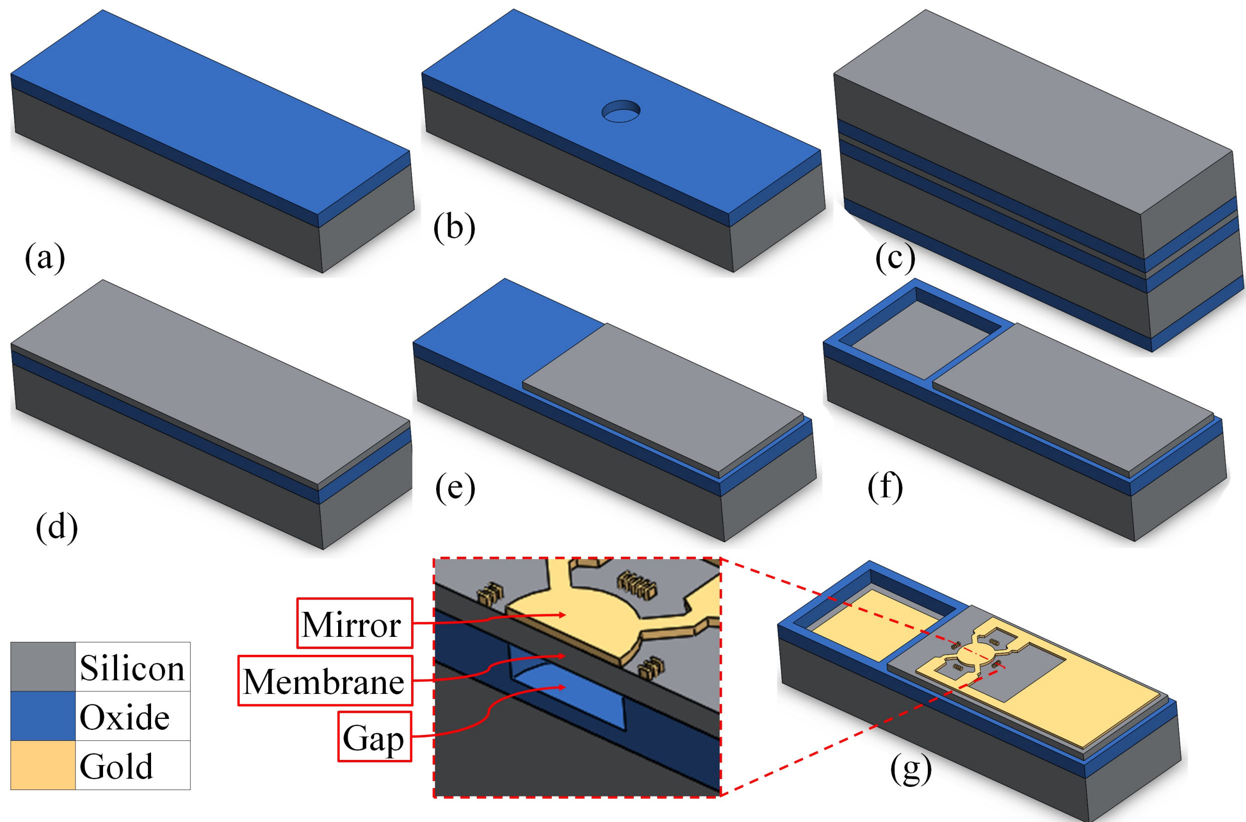

Fig. 43: Fabrication process flow (a) dry thermal oxidation to grow 340 nm oxide, (b) etching the gap spacing with BOE (c) bonded a SOI wafer on the prime wafer, the backside of the prime wafer is protected with PECVD Oxide (d) Handle and BOX layers of the silicon wafer are selectively etched and the device layer is exposed (e) the membrane of the deformable mirror is formed by selectively etching the silicon layer (f) the bottom pad is exposed by selectively etching the oxide layer and (g) the metal coating is deposited and etched to form the reflective coating and the electrical pads.

crons in size. To the best of our knowledge this is the first report of using SOI-wafer-bonding to fabricate such MEMS deformable mirror devices.

The mirror consists of 10 and 100 nm of Cr and Au, respectively, for the reflective coating and top electrode and a $1\mu m$ single crystal silicon membrane with a 300 nm oxide gap on a $< 100 >$ low resistivity silicon prime wafer. The process begins by thermally dry oxidizing a prime wafer to grow 340 nm of high quality silicon oxide (Fig. 43a). This layer is used as an electrical isolation between the top and bottom electrodes and also to form the mirror's cavity. This layer is important to withstand large electrical fields during un-intended snapdown events of the membrane. Dry oxidation has better oxide quality compared to other methods such as Plasma-enhanced chemical vapor deposition (PECVD) oxide and wet oxidation. Also, thermally grown oxide has a flat surface profile, resulting in high yield fusion bonding. A cavity is formed into the oxide layer in such a way that a thin oxide layer is left in the bottom of the cavity. Fig. 43b illustrates this step. This is done by performing the first lithography process with a positive photoresist (HPR 504) followed by an oxide wet etching process with buffered oxide etch (BOE). The timing of the process is critical to control the etch height of the oxide.

Fabrication followed with a cleaning process for both the processed prime wafer and a new SOI wafer (which will be bonded on the prime wafer). RCA cleaning is a standard cleaning process for preparing wafers for fusion bonding [154]. The device layer of the SOI wafer is bonded on the prime wafers by using pressure and heat followed with a 1100 degrees Celsius annealing process. In order to remove the handle layer of the bonded SOI wafer and expose the device layer, a silicon wet etching process is performed with a TMAH solution while the backside of the prime wafer is protected with a thin PECVD deposited silicon

oxide layer. Fig. 43c illustrates the bonded wafer before removing the handle layer. After removing the handle layer of the SOI wafer, the buried oxide (BOX) layer is also removed with a wet etching process with a BOE solution (Fig. 43d). During this step, the protective PECVD oxide layer on the backside of the prime wafer is also removed. The device layer of the SOI wafers acts as an etch stop. This is followed by the second lithography step to form the silicon membrane on the cavity. The excess silicon is etched with an inductively coupled plasma - reactive ion etching (ICP-RIE) process (Fig. 43e). A third lithography step is followed by a BOE process to create access holes for the bottom electrodes (Fig. 43f). Chromium/Gold layers are sputter deposited on the wafer and patterned with a fourth lithography step in order to form the mirror's surface along with the metalization for the connection pads. Fig. 43g shows a fabricated CMOF mirror with two electrodes.

A.4 Device characterization

In order to determine the mirrors optical quality, cut-off frequency, surface profile and capacitance change, several characterization measurements are performed. In the following subsections, the results are presented.

A.4.1 Surface quality

Surface roughness of an optical component is a key characteristic to minimize the scattering of the reflected/refracted light. In many optical devices, roughness is required to be less than $\lambda/20$ where λ is the optical wavelength. [140], However, given that our membranes are deflecting only tens of nm in our application, a smoother surface may be required owing to potential wavefront-scattering-effects of our tightly focused beam spot.

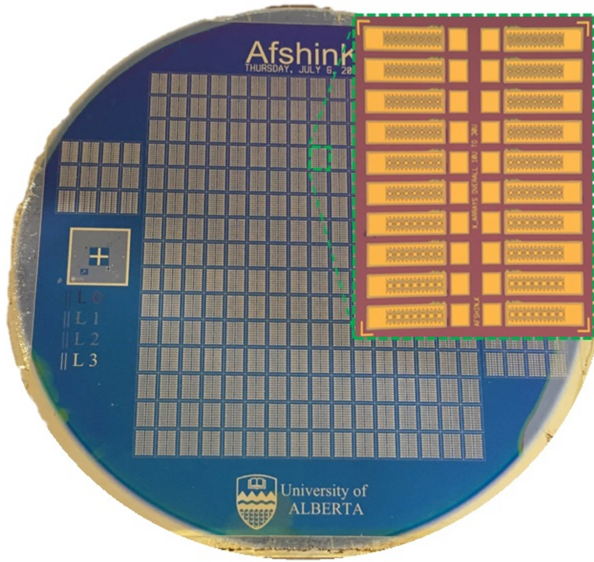

(a)

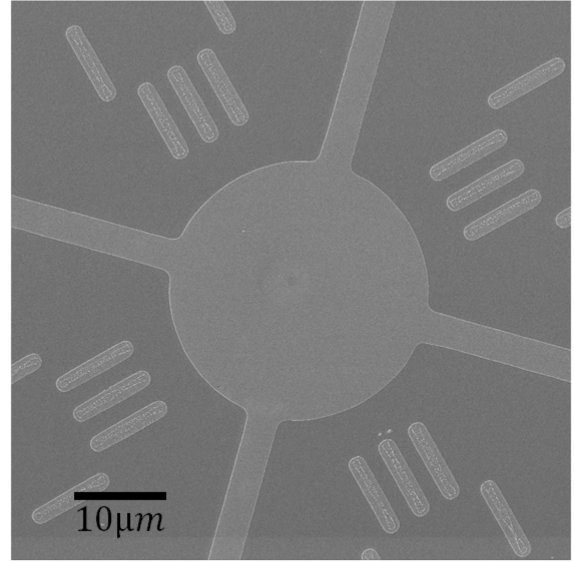

(b)

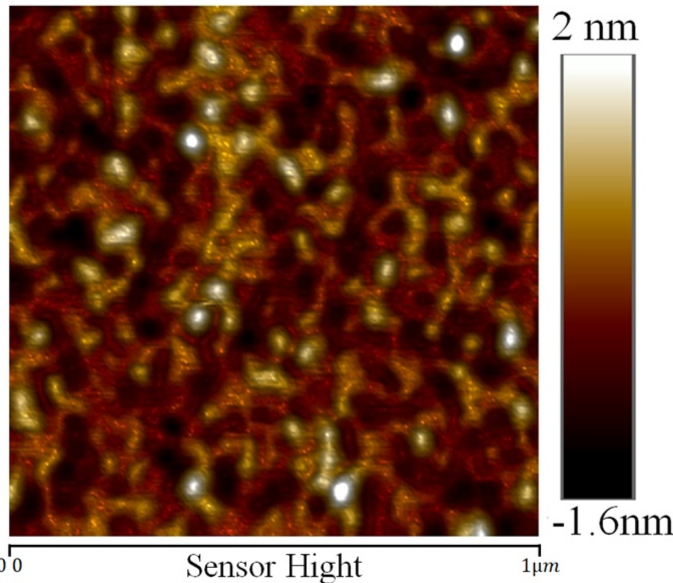

(c)

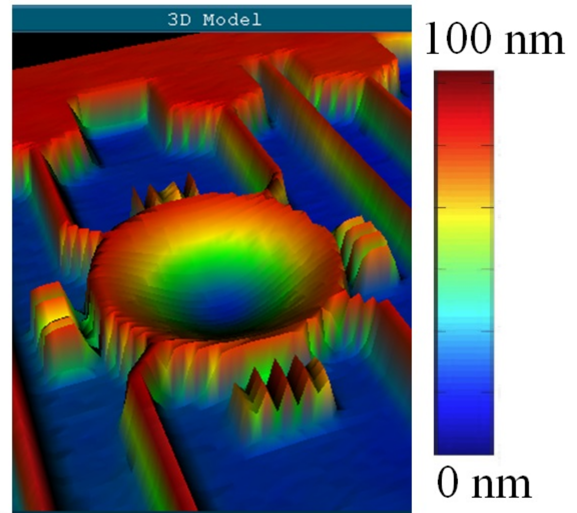

(d)

Fig. 44: Fabricated CMOF-MEMS deformable mirrors. (a) a full wafer view of the fabricated dies (b) Helium Ion Microscopy image of a CMOF-MEMS cell with 20 μm radius (c) AFM surface profile of a CMOF-MEMS mirror at the center of the mirror (d) 3D reconstructed image taken by ZYGO optical profilometer of a CMOF cell with 30 μm radius and 100 nm central deflection.

Fig. 44a shows the fabricated wafer and the dies of CMOF cells and Fig. 44b illustrates a Helium Ion microscope image of a single CMOF membrane. Atomic Force Microscopy (AFM)(Dimension Edge, Bruker Inc.) was used to provide the surface roughness measurements. Fig. 44c illustrates the results of a test on a 1 μm square area of the membrane. The surface roughness R_a is less than 0.39 nm. The peak to peak roughness is also limited to less than 3.6 nm. This low level of roughness is achieved by using a single crystal silicon membrane and carefully controlling deposition of the metal materials for the reflective coating. The membrane surface itself has roughness less than 10 angstroms.

To investigate the optimal metal-deposition recipe to achieve minimum possible roughness we performed at set of experiments. We deposited aluminum, chromium and chromium-gold materials with e-beam (custom built by Kurt J. Lesker Company) and sputtering techniques (CMS-18, Kurt J. Lesker Company) in various depositing conditions and measured the roughness of each material. In general gold deposited on the chromium layer had minimum surface roughness and adhesion to the silicon. The best depositions were found to be using a 10/100 Cr/Au layer deposited with sputtering under a 7 $mTorr$ chamber pressure, with 300-Watt forward power having a deposition rate of 230 pm/sec for both chromium and gold layers. These settings were equipment-specific and may vary on other machines.

A.4.2 Static characterization

Surface deflection profiles were obtained with an optical profilometer (ZYGO Optical Profilometer) during application of static actuation voltages. The largest stable deflection was recorded to be 106 nm for a 30-μm radius membrane with an actuation voltage of 29.6 volts. Fig. 44d illustrates a 3D profilometer image of a 30 μm radius membrane with a 100 nm

central deflection. The maximum deflection is limited by the snapdown voltage. In this design the effective gap is the combination of a 290 nm empty gap spacing and a 50nm oxide layer on the bottom. The oxide layer in the gap spacing acts as an isolation layer between the top and bottom electrodes and can withstand up to 50 volts before breaking down. The low actuation voltage minimizes dielectric charging in the gap isolation material which may impact device performance and lead to permanent electrostatic collapse. We tested our fabricated devices hundreds of times in pre-collapse mode and observed minimal dielectric charging. Fig. 45a illustrates the central deflection of a 30 μm membrane with different applied voltages.

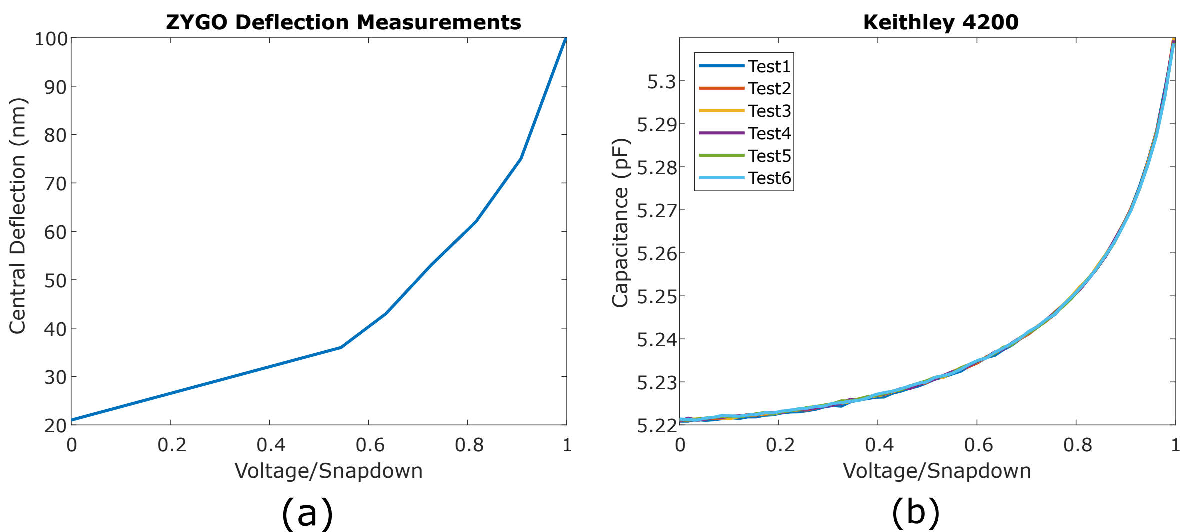

Fig. 45: Static tests (a) Deflection versus voltage changes measured by an optical profilometer (b) Capacitive versus voltage changes measured with a Semiconductor Characterization System. Both graphs are normalized to the snapdown voltage of the CMOF mirror which is 29.6 V

The corresponding capacitance change is measured to investigate the charging in the oxide layer. By using a Keithley 4200-Semiconductor Characterization System the capacitance is measured over hundreds of actuation cycles. Fig. 45b presents the acquired data for six such representative consecutive actuations up to the snapdown voltage (the maximum voltage

applied was 100 mV less than the snapdown voltage). All the measured tests produced very similar capacitance-voltage curves indicating that dielectric charging is negligible. Both graphs in the Fig. 45 are normalized to the snapdown voltage which is 29.6 V.

A.4.3 Dynamic characterization

Size, thickness and the material composition of the membrane are the main parameters influencing the frequency response of the CMOF mirrors. Previously published mirrors have a response time down to milliseconds [133]. The response time is limited because of membrane size which is normally in the mm-range. The frequency response of a deformable mirror is inversely related to the membrane size. In this design we fabricated the smallest deformable membrane reported to date and used a vacuum cavity to avoid squeeze-film damping effects. We carried out the resonance-frequency analysis of our designed membranes by performing ANSYS modal simulations, expecting to see the fundamental frequency near 4.56 MHz. In order to validate our simulation data, we measured the resonance frequency with a scanning laser Doppler vibrometer (Polytec MS5000) and a pseudo-random excitation. We recorded the resonance frequency as 4.94 MHz. The small difference between the simulation and the experimental data may be due to fabrication tolerances and membrane thickness variations. Vibrometer results are illustrated in Fig. 46a and Fig. 46b.

In order to determine the response time of the CMOF mirrors, a step voltage is applied and the membrane deflection is recorded over time with the scanning laser Doppler vibrometer. Fig. 46c shows the time response of a 30 μm-radius CMOF mirror to a step-function with 22V amplitude. The mirror shows a response time less than 20 μs and settling times less than 5 μs which is several orders of magnitude faster than previously published deformable

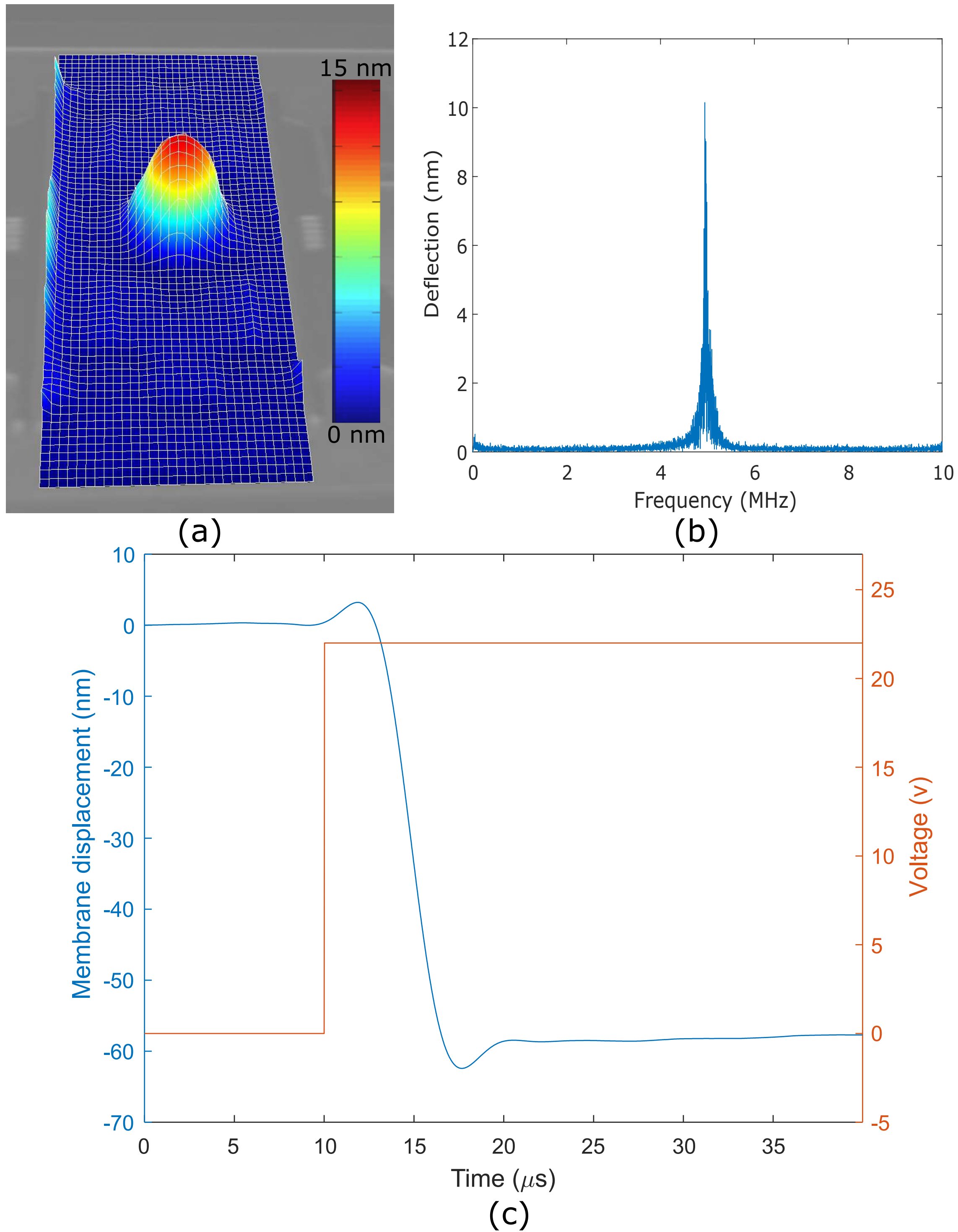

Fig. 46: Sample laser Doppler vibrometry measurements. (a) 2-D scan showing the membrane displacement for a given frequency. (b) Single point measurement using an 8 V AC signal. The peak shows the first fundamental frequency of the membrane. (c) Single point time domain measurement of the membrane displacement for a step-function input with 22V amplitude.

mirrors. The response time may be even faster than this but current measurements were limited by non-ideal voltage steps produced by the function generator, exhibiting overshoot at the beginning and end of each step lasting about one microsecond.

A.5 Focus control demonstration

We built a simple optical setup to investigate the focal point shift and Gaussian beam quality degradation with a CMOF mirror. Fig. 47 illustrates a drawing of the optical setup. In this setup we used a diode laser (QPHOTONICS QFBGLD-633-30PM) with wavelength λ=632.8 nm coupled to a single mode optical fiber. The single mode fiber ensures a TEM00 Gaussian beam mode with $M^2 \approx 1$. The Output of the fiber is collimated and telescoped to a desired beam waist size with a FC/PC-connectorized zoom fiber collimator (Thorlabs ZC618FC-A). Then the beam is focused on a CMOF deformable mirror with a long working distance objective lens with 20X magnification power and numerical aperture of 0.4. Fig. 47 is showing a camera image of the focused beam on a 30 μm radius CMOF device.

The beam focus size is important while the center of the CMOF MEMS mirror is closer to a parabolic deformation than the edges, therefore the beam is aligned to have $w_0 = 8\ \mu m$. The reflected beam is focused in front of a Shack-Hartmann Wavefront (SWF) (Thorlabs WFS30-7AR) sensor with another objective lens (10X, NA= 0.28, MY10X-803). The SWF sensor is used to measure the spot size and ROC changes (R_G) of the laser beam. The ROC of the beam as measured by the SWF indicates desired focal-length shifts. To see this, consider that the wavefront curvature of a Gaussian beam is a function of distance z form the focus point as given by [155]:

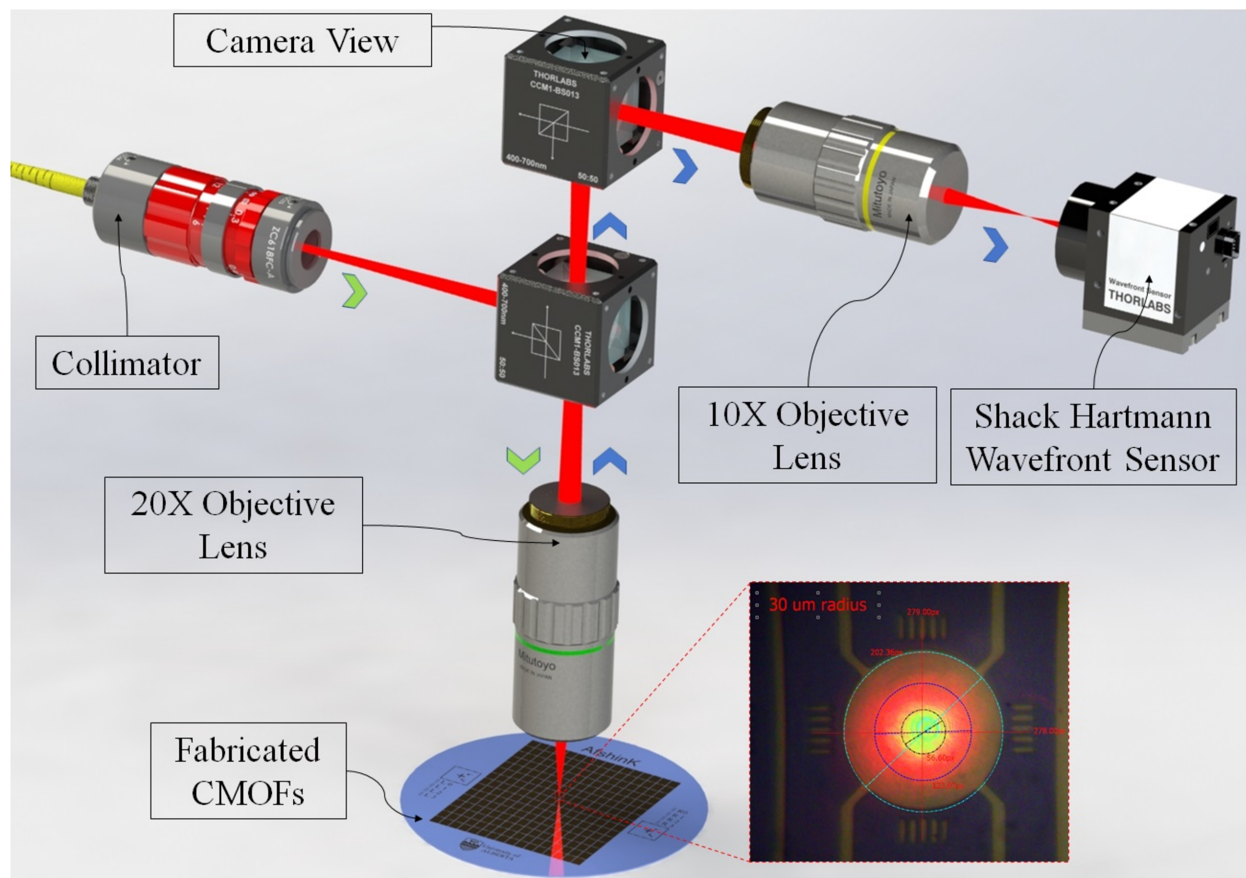

Fig. 47: 3D drawing of the optical setup for testing the CMOFs. Camera taken picture of the focused laser on a CMOF is showing a 16 μm laser spot on a 30 μm radius CMOF.

$$R_G(z) = z\left(1 + \left(\frac{z_R}{z}\right)^2\right) \tag{11}$$

If the observation point z is far compared to the Rayleigh range z_R then it is safe to approximate the measured R_G value as an exact distance of the focus point form the SWF sensor. We have recorded 40% lager beam size on the SWF sensor for 100 nm deflections on the CMOF-MEMS membrane compared to its non-actuated state.

To measure the R_G value, we used a signal generator with a square waveform to synchronize the actuations of the CMOF mirror with the camera's trigger. For each bias voltage, SWF sensor is used to recorded the ROC value where they are presented in Fig. 48a. The x-axis is normalized to the snapdown voltage and the membrane deflection for this measurement is between 18 and $\approx$ 45 nm. (The membrane has 18nm deflection without any actuation voltage due to the pressure differences between ambient environment and the cavity). By implementing another lens in the system and aligning it to have a 7X magnification, we could shift the beam focus by $\approx$8 mm with 100 nm deflection of the membrane Fig. 48b illustrates the recorded results with a normalized X axis to the snapdown voltage.

CMOF mirrors presented in this work provide parabolic deflection, which can give aberration-free focusing and focal shifts. Recorded profile intensity of the Gaussian beam on the SWF sensor for membrane deflection up to 100 nm presents us a high-quality Gaussian beam.. Fig. 48c illustrates the beam intensity profile at the output of the discussed optical system.

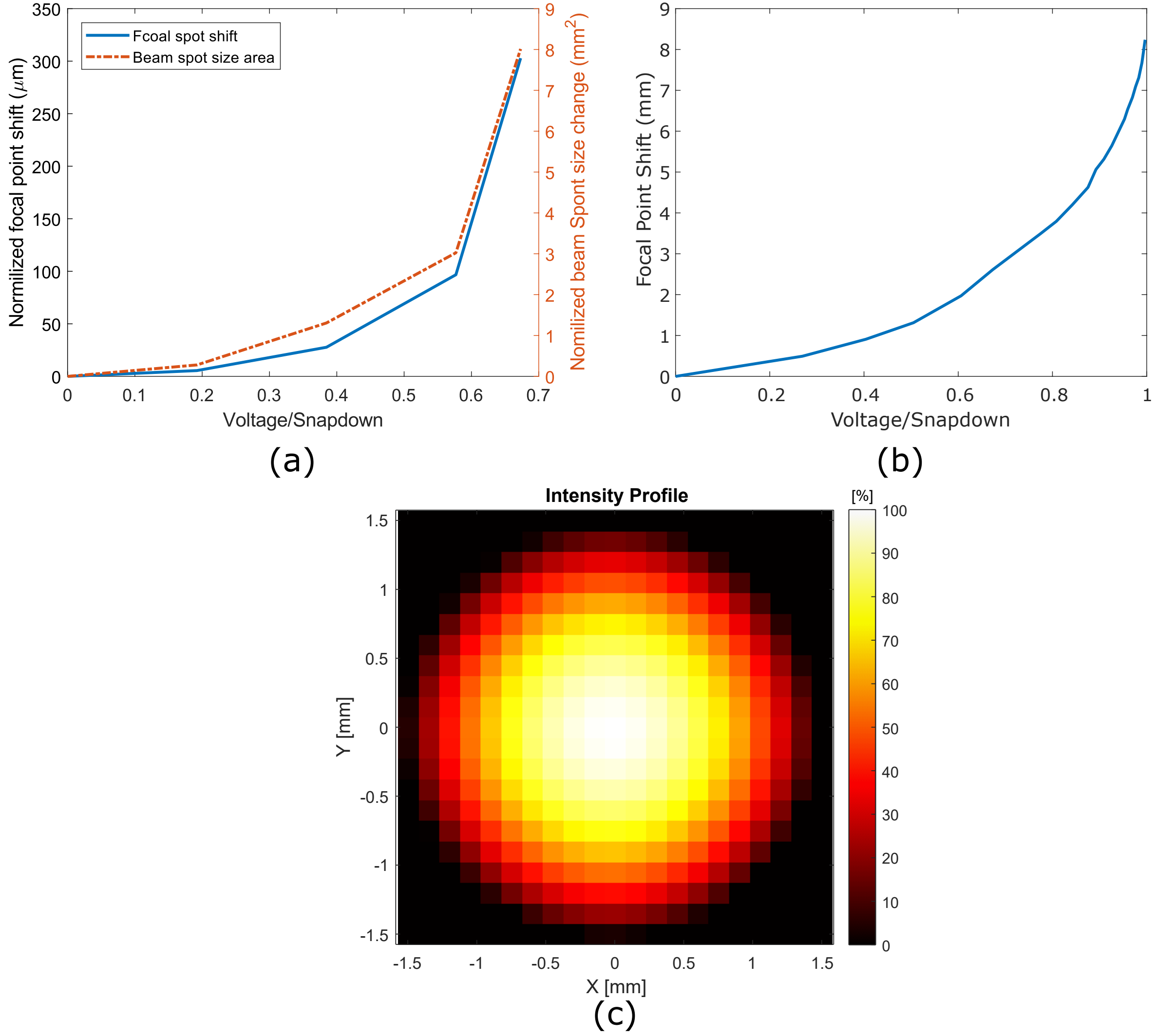

Fig. 48: Focal Point shifts recorded for a laser beam in the presented optical setup. The measurements are performed with a Shack-Hartman wavefront sensor and the distance between the focus point and camera CCD is removed in the graphs. (a) The graph shows measurements for a 30 μm radius membrane (b) Magnified focal point shift with a $f = 50$ mm lens for 30 μm membrane size. (c) Beam profile intensity recorded with the SWF sensor for membrane at 100 nm deflection. Pixelation of the figure is due to the lens array of the SWF sensor.

A.6 Discussion

The new design for deformable mirrors presented in this work enables for ultra-fast laser modulations in the ranges of ≈MHz range. This is done by controlling the wavefront curvature of the laser beam. Utilizing aberration-free lenses in the optical path enables diffraction-limited spot sizes. Currently our optical system achieves a focal spot size of 1.3 microns and a focal shift of more that $300\mu m$. A large focal shift, along with tight optical focusing will be crucial to achieving new applications in microscopy, etc. One of the limitations of using the proposed deformable mirror is their proportional change of depth-of-focus (DOF) to the focal length, where DOF becomes larger in longer focal lengths. This can impose some restrictions, especially in the applications, require tight DOFs. However, its ultra-fast operation, high OP, along with high-quality Gaussian beam profile capabilities introduced here, may offer new opportunities for improved fast-projection and imaging systems, improved optical holography applications.

Importantly, the MEMS systems discussed here may open up new opportunities to achieve high lateral- and axial resolution imaging over significant depths, above and beyond current systems. Some microscopy systems quickly scan with tight depth-of-focus to achieve optical sectioning within a plane, but then require mechanical scanning to probe depth. An emerging microscopy modality, Photoacoustic Remote Sensing Microscopy (PARS) [80] enables non-contact optical-absorption imaging in scattering tissue using an all-optical approach. Our introduced MEMS based deformable mirrors may likewise enable fast high-resolution depth- and volumetric scanning for emerging micron- and even sub-micron-resolution imaging applications.

The fabrication technique introduced for CMOFs reduces the surface roughness of the mirrors to few angstroms, mitigating surface scattering important for diffraction-scale wavefront shaping. However, based on our calculations and experiments, having a very tight focus will drastically reduce the capacity of the mirrors to affect the focal shifts, and will result in negligible laser modulations. For example, using the theory above, focusing light to a spot size of $w_0 = 3\ \mu m$ on a 30 μm-radius membrane results in only a 2.5 μm focal length shift.

Conclusions

In this paper we introduced a new generation of deformable mirrors called Capacitive Micromachined Optical Focusing (CMOF) MEMS mirrors which have several advantages over previous deformable optical systems. We used a wafer bonding technique to fabricate ultra-flat mirror surfaces having a single crystal silicon membrane. For the reflective coating of the membrane we used thin-films of chromium and gold with 10 and 100 nm respectively. Based on AFM tests, the surface roughness is measured to be 0.39 nm. This level of roughness has negligible scattering effects on the reflected light and is required for our constructed membranes due to their miniaturized size and diffraction-level effects of the focused laser beams. Temporal step response times are observed to be less than $5\mu s$.

The optical power calculated to be up to ≈900 diopters (with 30 um radius membranes) which is 45 times more than polymer based deformable mirrors fabricated to this date [141]. Recorded results show a ≈8 mm focus shift for only 100 nm deflection of the CMOF's membrane.

With the unprecedented focusing speeds demonstrated here, new applications to high-speed microscopy, holography, display-technology, and laser-marking can be envisioned.

Appendix B: CCU code

This appendix provides the Matlab code for the CCU app.

```
classdef PCUapp_exported < matlab.apps.AppBase

    % Properties that correspond to app components
    properties (Access = public)
        UIFigure                       matlab.ui.Figure
        CCUV11DesignedbyAfshinKashaniIlkhechiPanel  matlab.ui.container.Panel
        DelayGeneratorstatusPanel      matlab.ui.container.Panel
        ImagingModeEditFieldLabel      matlab.ui.control.Label
        ImagingModeEditField           matlab.ui.control.EditField
        TriggerIn1EditFieldLabel       matlab.ui.control.Label
        TriggerIn1EditField            matlab.ui.control.EditField
        TriggerIn2EditFieldLabel       matlab.ui.control.Label
        TriggerIn2EditField            matlab.ui.control.EditField
        TrOutDlyusEditFieldLabel       matlab.ui.control.Label
        TrOutDlyusEditField            matlab.ui.control.EditField
        Delay1EditFieldLabel           matlab.ui.control.Label
        Delay1EditField                matlab.ui.control.EditField
        Delay2EditFieldLabel           matlab.ui.control.Label
        Delay2EditField                matlab.ui.control.EditField
        Delay2EditField_2Label         matlab.ui.control.Label
        Delay2EditField_2              matlab.ui.control.EditField
        Delay3EditFieldLabel           matlab.ui.control.Label
        Delay3EditField                matlab.ui.control.EditField
        Delay4EditFieldLabel           matlab.ui.control.Label
        Delay4EditField                matlab.ui.control.EditField
        WaveGenEditFieldLabel          matlab.ui.control.Label
        WaveGenEditField               matlab.ui.control.EditField
        PowersupplysettingsandstatusPanel  matlab.ui.container.Panel
        Knob_2                         matlab.ui.control.Knob
        Knob                           matlab.ui.control.Knob
        VNNreadVEditFieldLabel         matlab.ui.control.Label
        VNNreadVEditField              matlab.ui.control.EditField
        VPPreadVEditField_2Label       matlab.ui.control.Label
        VPPreadVEditField_2            matlab.ui.control.EditField
        VNNLabel                       matlab.ui.control.Label
        VPPLabel                       matlab.ui.control.Label
        Lamp_13                        matlab.ui.control.Lamp
        Lamp_14                        matlab.ui.control.Lamp
        HVcardsstatusPanel             matlab.ui.container.Panel
        Card1Button                    matlab.ui.control.StateButton
        Card2Button                    matlab.ui.control.StateButton
        Card3Button                    matlab.ui.control.StateButton
        Card4Button                    matlab.ui.control.StateButton
        Lamp                           matlab.ui.control.Lamp
        Lamp_2                         matlab.ui.control.Lamp
        Lamp_3                         matlab.ui.control.Lamp
        Lamp_4                         matlab.ui.control.Lamp
        Lamp_5                         matlab.ui.control.Lamp
        Lamp_6                         matlab.ui.control.Lamp
        Lamp_7                         matlab.ui.control.Lamp
        Lamp_8                         matlab.ui.control.Lamp
        Lamp_9                         matlab.ui.control.Lamp
        Lamp_10                        matlab.ui.control.Lamp
        Lamp_11                        matlab.ui.control.Lamp
        Lamp_12                        matlab.ui.control.Lamp
        ConnectionLabel                matlab.ui.control.Label
        VNNLabel_2                     matlab.ui.control.Label
        VPPLabel_3                     matlab.ui.control.Label
        STOPButton                     matlab.ui.control.StateButton
        ChannelbiasingsettingsPanel    matlab.ui.container.Panel
        ImagingsequenceEditFieldLabel  matlab.ui.control.Label
        ImagingsequenceEditField       matlab.ui.control.EditField
        ActiveChannelsEditFieldLabel   matlab.ui.control.Label
        ActiveChannelsEditField        matlab.ui.control.EditField
        TriggersEditFieldLabel         matlab.ui.control.Label
```

```
66          TriggersEditField               matlab.ui.control.EditField
67          FPSEditFieldLabel               matlab.ui.control.Label
68          FPSEditField                    matlab.ui.control.EditField
69          PCUconnectionstatusLabel        matlab.ui.control.Label
70          PCUconnectionstatusLamp         matlab.ui.control.Lamp
71          COMportEditFieldLabel           matlab.ui.control.Label
72          COMportEditField                matlab.ui.control.EditField
73      end
74
75
76      properties (Access = private)
77          SerialPort='';
78          opendSerial='';
79          inputvariables=0;
80          timr;
81
82          %input Parameters
83          input;
84
85      end
86
87
88
89      methods (Access = private)
90
91            % Code that executes after component creation
92            function repeatingTimer(app)
93                app.timr = timer('StartDelay', 0, 'Period', ...
                      0.1,'ExecutionMode', 'fixedRate');
94                app.timr.TimerFcn = @(obj,event)toggleled(app);
95                    start(app.timr);
96            end
97
98            % called by timer and we can put any command to be excuted
99            % repeatedly
100           function toggleled(app)
101               app.PCUconnectionstatusLamp.Enable=¬app.PCUconnectionstatusLamp.Enable;
102             %  app.Card1Button.Value=¬app.PCUconnectionstatusLamp.Enable;
103             %  app.Card2Button.Value=¬app.PCUconnectionstatusLamp.Enable;
104             %  app.Card3Button.Value=¬app.PCUconnectionstatusLamp.Enable;
105             % app.Card4Button.Value=¬app.PCUconnectionstatusLamp.Enable;
106
107              app.PCUconnectionstatusLabel.Text="Coneection Pending...";
108               app.updateDisplay;
109           end
110
111           function updateDisplay(app)
112               if app.input.ImgMode =='US'
113                   app.ImagingModeEditField.Value='Ultrasound';
114                   app.WaveGenEditField.Value="Dsiabled";
115               elseif app.input.ImgMode =='PA'
116                   app.ImagingModeEditField.Value='Photoacoustic';
117                   app.ImagingModeEditField.FontColor='r';
118                   app.WaveGenEditField.Value="Enabled";
119                   app.WaveGenEditField.FontColor='r';
120
121                   if app.input.Qswitch>310 & app.input.Qswitch < 550
122                       app.Delay1EditField.Value="Enabled";
123                       app.Delay1EditField.FontColor='r';
124
125                   else
126                   app.stopApp("Wrong Qwitch");
127                   end
128
129               else
130                   app.stopApp("Wrong Imaging Mode");
131               end
132
133               if app.input.VNN ≤ 0
134                   app.Knob_2.Value=app.input.VNN;
135               else
136                   app.stopApp("Wrong VNN input");
137               end
138               if app.input.VPP ≥ 0
139                   app.Knob.Value=app.input.VPP;
140               else
141                   app.stopApp("Wrong VPP input");
142               end
143
144               if abs(app.input.VNNc) > 375
```

```
145                 app.stopApp("Wrong VNNc input");
146             end
147             if abs(app.input.VPP) >375
148                 app.stopApp("Wrong VPPc input");
149             end
150
151
152             if app.input.Trigger1==0
153                 app.TriggerIn1EditField.Value="Disabled";
154             elseif app.input.Trigger1==1
155                 app.TriggerIn1EditField.Value="Enabled";
156                 app.TriggerIn1EditField.FontColor='r';
157             else
158                 app.stopApp("Wrong Trigger1 settings");
159             end
160
161             if app.input.Trigger2==0
162                 app.TriggerIn2EditField.Value="Dsiabled";
163             elseif app.input.Trigger2==1
164                 app.TriggerIn2EditField.Value="Enabled";
165                 app.TriggerIn2EditField.FontColor='r';
166             else
167                 app.stopApp("Wrong Trigger2 settings");
168             end
169
170             if app.input.TrOd≥0
171                 app.TrOutDlyusEditField.Value=num2str(app.input.TrOd);
172             else
173                 app.stopApp("Wrong TrOd settings");
174             end
175
176             if size(app.input.BiasPatern,1)==256
177                 app.ActiveChannelsEditField.Value=num2str(size(app.input.BiasPatern,1));
178             else
179               app.stopApp("All channels must be programmed 256xN bias ...
                    patern is only acceptable");
180             end
181
182             if size(app.input.BiasPatern,2)>0
183                 app.ImagingsequenceEditField.Value=num2str(size(app.input.BiasPatern,2))
184             else
185               app.stopApp("At least one frame must be programmed for ...
                    biasing sequence");
186             end
187
188             app.COMportEditField.Value= app.input.COM;
189
190
191         end
192         function stopApp(app,Error)
193             display(Error);
194             stop(app.timr);
195             delete(app);
196         end
197     end
198
199
200
201     % Callbacks that handle component events
202     methods (Access = private)
203
204         % Code that executes after component creation
205         function startupFcn(app, iInput)
206             app.input = iInput;
207
208 %               app.input.COM
209 %               app.input.VNN
210 %               app.input.VPP
211 %               app.input.BiasPatern  <<<
212 %               app.input.VNNc
213 %               app.input.VPPc
214 %               app.input.Trigger1
215 %               app.input.Trigger2
216 %               app.input.TrOd
217 %               app.input.ImgMode
218 %               app.input.Qswitch
219 %               app.input.delay2.En
220 %               app.input.delay2.IniD
221 %               app.input.delay2.lengthD
```

```
222 %               app.input.delay2.Inv
223 %               app.input.delay3.En
224 %               app.input.delay3.IniD
225 %               app.input.delay3.lengthD
226 %               app.input.delay3.Inv
227 %               app.input.delay4.En
228 %               app.input.delay4.IniD
229 %               app.input.delay4.lengthD
230 %               app.input.delay4.Inv
231
232            %  display(app.input.delay4.BiasPatern);
233             app.UIFigure.Name="CCU V1.1";
234
235
236           app.repeatingTimer;     % starts timer at startup
237         end
238
239         % Callback function
240         function SearchPCUButtonPushed(app, event)
241          n = seriallist("all");
242
243         app.SerialPort=n;
244         if ¬isempty(n)
245         app.COMPortDropDown.Visible=1;
246         app.COMPortDropDown.Items=n;
247         app.COMPortDropDown.Value=n(1);
248         app.SerialPort=n(1);
249         app.ConnectButton.Visible=1;
250         app.repeatingTimer;
251         app.PressSearchPCULabel.Text='Ports found select one and press ...
                connect';
252         else
253             app.PressSearchPCULabel.Text='Search for COM ports ...
                    unsuccessful, check USB connections';
254         end
255
256         end
257
258         % Callback function
259         function DropDownValueChanged(app, event)
260             value = app.COMPortDropDown.Value;
261             app.SerialPort=app.COMPortDropDown.Value;
262         end
263
264         % Callback function
265         function ConnectButtonPushed(app, event)
266             newobjs = instrfind;
267          fclose(newobjs)
268          app.opendSerial= serial(app.SerialPort);
269          app.opendSerial.BaudRate = 9600;
270          fopen(app.opendSerial);
271          fwrite(app.opendSerial,'g');
272          data=fread(app.opendSerial,1);
273          display(data);
274          app.PressSearchPCULabel.Text=strcat('Connected to ',' ' ...
                ,app.SerialPort);
275         end
276
277         % Close request function: UIFigure
278         function UIFigureCloseRequest(app, event)
279             stop(app.timr);
280             delete(app)
281         end
282
283         % Value changed function: STOPButton
284         function STOPButtonValueChanged(app, event)
285             value = app.STOPButton.Value;
286             if value==0;
287                 start(app.timr);
288                 app.STOPButton.Text="STOP";
289                 app.STOPButton.FontSize=60;
290                 app.STOPButton.FontColor='r';
291             else
292                 stop(app.timr);
293                 app.STOPButton.Text="Resume";
294                 app.STOPButton.FontSize=50;
295                 app.STOPButton.FontColor='g';
```

```
296             end
297         end
298     end
299
300     % Component initialization
301     methods (Access = private)
302
303         % Create UIFigure and components
304         function createComponents(app)
305
306             % Create UIFigure and hide until all components are created
307             app.UIFigure = uifigure('Visible', 'off');
308             app.UIFigure.Position = [100 100 640 480];
309             app.UIFigure.Name = 'MATLAB App';
310             app.UIFigure.CloseRequestFcn = createCallbackFcn(app, ...
                    @UIFigureCloseRequest, true);
311
312             % Create CCUV11DesignedbyAfshinKashaniIlkhechiPanel
313             app.CCUV11DesignedbyAfshinKashaniIlkhechiPanel = ...
                    uipanel(app.UIFigure);
314             app.CCUV11DesignedbyAfshinKashaniIlkhechiPanel.TitlePosition = ...
                    'righttop';
315             app.CCUV11DesignedbyAfshinKashaniIlkhechiPanel.Title = 'CCU ...
                    V1.1                              Designed by: Afshin Kashani ...
                    Ilkhechi ';
316             app.CCUV11DesignedbyAfshinKashaniIlkhechiPanel.Position = [10 ...
                    10 623 461];
317
318             % Create DelayGeneratorstatusPanel
319             app.DelayGeneratorstatusPanel = ...
                    uipanel(app.CCUV11DesignedbyAfshinKashaniIlkhechiPanel);
320             app.DelayGeneratorstatusPanel.TitlePosition = 'centertop';
321             app.DelayGeneratorstatusPanel.Title = 'Delay Generator status';
322             app.DelayGeneratorstatusPanel.FontWeight = 'bold';
323             app.DelayGeneratorstatusPanel.Position = [5 89 214 346];
324
325             % Create ImagingModeEditFieldLabel
326             app.ImagingModeEditFieldLabel = ...
                    uilabel(app.DelayGeneratorstatusPanel);
327             app.ImagingModeEditFieldLabel.Position = [10 295 82 22];
328             app.ImagingModeEditFieldLabel.Text = 'Imaging Mode';
329
330             % Create ImagingModeEditField
331             app.ImagingModeEditField = ...
                    uieditfield(app.DelayGeneratorstatusPanel, 'text');
332             app.ImagingModeEditField.Editable = 'off';
333             app.ImagingModeEditField.Position = [102 295 93 22];
334             app.ImagingModeEditField.Value = 'Ultrasound';
335
336             % Create TriggerIn1EditFieldLabel
337             app.TriggerIn1EditFieldLabel = ...
                    uilabel(app.DelayGeneratorstatusPanel);
338             app.TriggerIn1EditFieldLabel.Position = [11 263 63 22];
339             app.TriggerIn1EditFieldLabel.Text = 'Trigger In1';
340
341             % Create TriggerIn1EditField
342             app.TriggerIn1EditField = ...
                    uieditfield(app.DelayGeneratorstatusPanel, 'text');
343             app.TriggerIn1EditField.Editable = 'off';
344             app.TriggerIn1EditField.Position = [102 263 93 22];
345             app.TriggerIn1EditField.Value = 'Disabled';
346
347             % Create TriggerIn2EditFieldLabel
348             app.TriggerIn2EditFieldLabel = ...
                    uilabel(app.DelayGeneratorstatusPanel);
349             app.TriggerIn2EditFieldLabel.Position = [11 231 107 22];
350             app.TriggerIn2EditFieldLabel.Text = 'Trigger In2';
351
352             % Create TriggerIn2EditField
353             app.TriggerIn2EditField = ...
                    uieditfield(app.DelayGeneratorstatusPanel, 'text');
354             app.TriggerIn2EditField.Editable = 'off';
355             app.TriggerIn2EditField.Position = [102 231 93 22];
356             app.TriggerIn2EditField.Value = 'Disabled';
357
358             % Create TrOutDlyusEditFieldLabel
```

```
359             app.TrOutDlyusEditFieldLabel = ...
                    uilabel(app.DelayGeneratorstatusPanel);
360             app.TrOutDlyusEditFieldLabel.Position = [10 199 84 22];
361             app.TrOutDlyusEditFieldLabel.Text = 'Tr Out Dly (us)';
362
363             % Create TrOutDlyusEditField
364             app.TrOutDlyusEditField = ...
                    uieditfield(app.DelayGeneratorstatusPanel, 'text');
365             app.TrOutDlyusEditField.Editable = 'off';
366             app.TrOutDlyusEditField.Position = [102 199 94 22];
367             app.TrOutDlyusEditField.Value = '0';
368
369             % Create Delay1EditFieldLabel
370             app.Delay1EditFieldLabel = uilabel(app.DelayGeneratorstatusPanel);
371             app.Delay1EditFieldLabel.Position = [10 135 46 22];
372             app.Delay1EditFieldLabel.Text = 'Delay 1';
373
374             % Create Delay1EditField
375             app.Delay1EditField = ...
                    uieditfield(app.DelayGeneratorstatusPanel, 'text');
376             app.Delay1EditField.Editable = 'off';
377             app.Delay1EditField.Position = [102 135 94 22];
378             app.Delay1EditField.Value = 'Disabled';
379
380             % Create Delay2EditFieldLabel
381             app.Delay2EditFieldLabel = uilabel(app.DelayGeneratorstatusPanel);
382             app.Delay2EditFieldLabel.Position = [10 103 46 22];
383             app.Delay2EditFieldLabel.Text = 'Delay 2';
384
385             % Create Delay2EditField
386             app.Delay2EditField = ...
                    uieditfield(app.DelayGeneratorstatusPanel, 'text');
387             app.Delay2EditField.Editable = 'off';
388             app.Delay2EditField.Position = [102 103 94 22];
389             app.Delay2EditField.Value = 'Disabled';
390
391             % Create Delay2EditField_2Label
392             app.Delay2EditField_2Label = ...
                    uilabel(app.DelayGeneratorstatusPanel);
393             app.Delay2EditField_2Label.Position = [10 71 46 22];
394             app.Delay2EditField_2Label.Text = 'Delay 2';
395
396             % Create Delay2EditField_2
397             app.Delay2EditField_2 = ...
                    uieditfield(app.DelayGeneratorstatusPanel, 'text');
398             app.Delay2EditField_2.Editable = 'off';
399             app.Delay2EditField_2.Position = [102 71 94 22];
400             app.Delay2EditField_2.Value = 'Disabled';
401
402             % Create Delay3EditFieldLabel
403             app.Delay3EditFieldLabel = uilabel(app.DelayGeneratorstatusPanel);
404             app.Delay3EditFieldLabel.Position = [10 39 46 22];
405             app.Delay3EditFieldLabel.Text = 'Delay 3';
406
407             % Create Delay3EditField
408             app.Delay3EditField = ...
                    uieditfield(app.DelayGeneratorstatusPanel, 'text');
409             app.Delay3EditField.Editable = 'off';
410             app.Delay3EditField.Position = [102 39 94 22];
411             app.Delay3EditField.Value = 'Disabled';
412
413             % Create Delay4EditFieldLabel
414             app.Delay4EditFieldLabel = uilabel(app.DelayGeneratorstatusPanel);
415             app.Delay4EditFieldLabel.Position = [10 8 46 22];
416             app.Delay4EditFieldLabel.Text = 'Delay 4';
417
418             % Create Delay4EditField
419             app.Delay4EditField = ...
                    uieditfield(app.DelayGeneratorstatusPanel, 'text');
420             app.Delay4EditField.Editable = 'off';
421             app.Delay4EditField.Position = [102 8 94 22];
422             app.Delay4EditField.Value = 'Disabled';
423
424             % Create WaveGenEditFieldLabel
425             app.WaveGenEditFieldLabel = ...
                    uilabel(app.DelayGeneratorstatusPanel);
```

```
426             app.WaveGenEditFieldLabel.Position = [10 167 58 22];
427             app.WaveGenEditFieldLabel.Text = 'WaveGen';
428
429             % Create WaveGenEditField
430             app.WaveGenEditField = ...
                   uieditfield(app.DelayGeneratorstatusPanel, 'text');
431             app.WaveGenEditField.Editable = 'off';
432             app.WaveGenEditField.Position = [102 167 94 22];
433             app.WaveGenEditField.Value = 'Disabled';
434
435             % Create PowersupplysettingsandstatusPanel
436             app.PowersupplysettingsandstatusPanel = ...
                   uipanel(app.CCUV11DesignedbyAfshinKashaniIlkhechiPanel);
437             app.PowersupplysettingsandstatusPanel.TitlePosition = 'centertop';
438             app.PowersupplysettingsandstatusPanel.Title = 'Power supply ...
                   settings and status';
439             app.PowersupplysettingsandstatusPanel.FontWeight = 'bold';
440             app.PowersupplysettingsandstatusPanel.Position = [218 237 401 ...
                   198];
441
442             % Create Knob_2
443             app.Knob_2 = uiknob(app.PowersupplysettingsandstatusPanel, ...
                   'continuous');
444             app.Knob_2.Limits = [-250 0];
445             app.Knob_2.Position = [60 56 60 60];
446
447             % Create Knob
448             app.Knob = uiknob(app.PowersupplysettingsandstatusPanel, ...
                   'continuous');
449             app.Knob.Limits = [0 250];
450             app.Knob.Position = [259 56 60 60];
451
452             % Create VNNreadVEditFieldLabel
453             app.VNNreadVEditFieldLabel = ...
                   uilabel(app.PowersupplysettingsandstatusPanel);
454             app.VNNreadVEditFieldLabel.Position = [34 14 78 22];
455             app.VNNreadVEditFieldLabel.Text = 'VNN read (V)';
456
457             % Create VNNreadVEditField
458             app.VNNreadVEditField = ...
                   uieditfield(app.PowersupplysettingsandstatusPanel, 'text');
459             app.VNNreadVEditField.Editable = 'off';
460             app.VNNreadVEditField.Position = [113 14 35 22];
461             app.VNNreadVEditField.Value = '0';
462
463             % Create VPPreadVEditField_2Label
464             app.VPPreadVEditField_2Label = ...
                   uilabel(app.PowersupplysettingsandstatusPanel);
465             app.VPPreadVEditField_2Label.Position = [228 14 76 22];
466             app.VPPreadVEditField_2Label.Text = 'VPP read (V)';
467
468             % Create VPPreadVEditField_2
469             app.VPPreadVEditField_2 = ...
                   uieditfield(app.PowersupplysettingsandstatusPanel, 'text');
470             app.VPPreadVEditField_2.Editable = 'off';
471             app.VPPreadVEditField_2.Position = [307 14 35 22];
472             app.VPPreadVEditField_2.Value = '0';
473
474             % Create VNNLabel
475             app.VNNLabel = uilabel(app.PowersupplysettingsandstatusPanel);
476             app.VNNLabel.FontSize = 24;
477             app.VNNLabel.FontColor = [0.149 0.149 0.149];
478             app.VNNLabel.Position = [62 139 56 30];
479             app.VNNLabel.Text = 'VNN';
480
481             % Create VPPLabel
482             app.VPPLabel = uilabel(app.PowersupplysettingsandstatusPanel);
483             app.VPPLabel.FontSize = 24;
484             app.VPPLabel.FontColor = [0.149 0.149 0.149];
485             app.VPPLabel.Position = [261 139 54 30];
486             app.VPPLabel.Text = 'VPP';
487
488             % Create Lamp_13
489             app.Lamp_13 = uilamp(app.PowersupplysettingsandstatusPanel);
490             app.Lamp_13.Position = [9 120 20 20];
491             app.Lamp_13.Color = [0.502 0.502 0.502];
492
493             % Create Lamp_14
```

```
494             app.Lamp_14 = uilamp(app.PowersupplysettingsandstatusPanel);
495             app.Lamp_14.Position = [205 120 20 20];
496             app.Lamp_14.Color = [0.502 0.502 0.502];
497
498             % Create HVcardsstatusPanel
499             app.HVcardsstatusPanel = ...
                   uipanel(app.CCUV11DesignedbyAfshinKashaniIlkhechiPanel);
500             app.HVcardsstatusPanel.TitlePosition = 'centertop';
501             app.HVcardsstatusPanel.Title = 'HV cards status';
502             app.HVcardsstatusPanel.FontWeight = 'bold';
503             app.HVcardsstatusPanel.Position = [414 5 205 233];
504
505             % Create Card1Button
506             app.Card1Button = uibutton(app.HVcardsstatusPanel, 'state');
507             app.Card1Button.Text = 'Card1';
508             app.Card1Button.Position = [8.5 155 48 38];
509
510             % Create Card2Button
511             app.Card2Button = uibutton(app.HVcardsstatusPanel, 'state');
512             app.Card2Button.Text = 'Card2';
513             app.Card2Button.Position = [8.5 105 48 38];
514
515             % Create Card3Button
516             app.Card3Button = uibutton(app.HVcardsstatusPanel, 'state');
517             app.Card3Button.Text = 'Card3';
518             app.Card3Button.Position = [8.5 56 48 38];
519
520             % Create Card4Button
521             app.Card4Button = uibutton(app.HVcardsstatusPanel, 'state');
522             app.Card4Button.Text = 'Card4';
523             app.Card4Button.Position = [8.5 7 48 38];
524
525             % Create Lamp
526             app.Lamp = uilamp(app.HVcardsstatusPanel);
527             app.Lamp.Position = [84 162 17 17];
528             app.Lamp.Color = [0.9294 0.6941 0.1255];
529
530             % Create Lamp_2
531             app.Lamp_2 = uilamp(app.HVcardsstatusPanel);
532             app.Lamp_2.Position = [84 114 17 17];
533             app.Lamp_2.Color = [0.9294 0.6941 0.1255];
534
535             % Create Lamp_3
536             app.Lamp_3 = uilamp(app.HVcardsstatusPanel);
537             app.Lamp_3.Position = [84 66 17 17];
538             app.Lamp_3.Color = [0.9294 0.6941 0.1255];
539
540             % Create Lamp_4
541             app.Lamp_4 = uilamp(app.HVcardsstatusPanel);
542             app.Lamp_4.Position = [84 18 17 17];
543             app.Lamp_4.Color = [0.9294 0.6941 0.1255];
544
545             % Create Lamp_5
546             app.Lamp_5 = uilamp(app.HVcardsstatusPanel);
547             app.Lamp_5.Position = [134 162 17 17];
548             app.Lamp_5.Color = [0.9294 0.6941 0.1255];
549
550             % Create Lamp_6
551             app.Lamp_6 = uilamp(app.HVcardsstatusPanel);
552             app.Lamp_6.Position = [134 114 17 17];
553             app.Lamp_6.Color = [0.9294 0.6941 0.1255];
554
555             % Create Lamp_7
556             app.Lamp_7 = uilamp(app.HVcardsstatusPanel);
557             app.Lamp_7.Position = [134 66 17 17];
558             app.Lamp_7.Color = [0.9294 0.6941 0.1255];
559
560             % Create Lamp_8
561             app.Lamp_8 = uilamp(app.HVcardsstatusPanel);
562             app.Lamp_8.Position = [134 18 17 17];
563             app.Lamp_8.Color = [0.9294 0.6941 0.1255];
564
565             % Create Lamp_9
566             app.Lamp_9 = uilamp(app.HVcardsstatusPanel);
567             app.Lamp_9.Position = [165 162 17 17];
568             app.Lamp_9.Color = [0.9294 0.6941 0.1255];
569
570             % Create Lamp_10
571             app.Lamp_10 = uilamp(app.HVcardsstatusPanel);
```

```
572            app.Lamp_10.Position = [165 114 17 17];
573            app.Lamp_10.Color = [0.9294 0.6941 0.1255];
574
575            % Create Lamp_11
576            app.Lamp_11 = uilamp(app.HVcardsstatusPanel);
577            app.Lamp_11.Position = [165 66 17 17];
578            app.Lamp_11.Color = [0.9294 0.6941 0.1255];
579
580            % Create Lamp_12
581            app.Lamp_12 = uilamp(app.HVcardsstatusPanel);
582            app.Lamp_12.Position = [165 18 17 17];
583            app.Lamp_12.Color = [0.9294 0.6941 0.1255];
584
585            % Create ConnectionLabel
586            app.ConnectionLabel = uilabel(app.HVcardsstatusPanel);
587            app.ConnectionLabel.Position = [59 180 66 22];
588            app.ConnectionLabel.Text = 'Connection';
589
590            % Create VNNLabel_2
591            app.VNNLabel_2 = uilabel(app.HVcardsstatusPanel);
592            app.VNNLabel_2.Position = [129 180 31 22];
593            app.VNNLabel_2.Text = 'VNN';
594
595            % Create VPPLabel_3
596            app.VPPLabel_3 = uilabel(app.HVcardsstatusPanel);
597            app.VPPLabel_3.Position = [162 180 30 22];
598            app.VPPLabel_3.Text = 'VPP';
599
600            % Create STOPButton
601            app.STOPButton = ...
                   uibutton(app.CCUV11DesignedbyAfshinKashaniIlkhechiPanel, ...
                   'state');
602            app.STOPButton.ValueChangedFcn = createCallbackFcn(app, ...
                   @STOPButtonValueChanged, true);
603            app.STOPButton.Text = 'STOP';
604            app.STOPButton.BackgroundColor = [1 1 1];
605            app.STOPButton.FontSize = 60;
606            app.STOPButton.FontColor = [1 0 0];
607            app.STOPButton.Position = [8 5 211 81];
608
609            % Create ChannelbiasingsettingsPanel
610            app.ChannelbiasingsettingsPanel = ...
                   uipanel(app.CCUV11DesignedbyAfshinKashaniIlkhechiPanel);
611            app.ChannelbiasingsettingsPanel.TitlePosition = 'centertop';
612            app.ChannelbiasingsettingsPanel.Title = 'Channel biasing ...
                   settings';
613            app.ChannelbiasingsettingsPanel.FontWeight = 'bold';
614            app.ChannelbiasingsettingsPanel.Position = [218 89 197 149];
615
616            % Create ImagingsequenceEditFieldLabel
617            app.ImagingsequenceEditFieldLabel = ...
                   uilabel(app.ChannelbiasingsettingsPanel);
618            app.ImagingsequenceEditFieldLabel.Position = [14 96 104 22];
619            app.ImagingsequenceEditFieldLabel.Text = 'Imaging sequence';
620
621            % Create ImagingsequenceEditField
622            app.ImagingsequenceEditField = ...
                   uieditfield(app.ChannelbiasingsettingsPanel, 'text');
623            app.ImagingsequenceEditField.Editable = 'off';
624            app.ImagingsequenceEditField.Position = [117 96 62 22];
625            app.ImagingsequenceEditField.Value = '0';
626
627            % Create ActiveChannelsEditFieldLabel
628            app.ActiveChannelsEditFieldLabel = ...
                   uilabel(app.ChannelbiasingsettingsPanel);
629            app.ActiveChannelsEditFieldLabel.Position = [14 66 92 22];
630            app.ActiveChannelsEditFieldLabel.Text = 'Active Channels';
631
632            % Create ActiveChannelsEditField
633            app.ActiveChannelsEditField = ...
                   uieditfield(app.ChannelbiasingsettingsPanel, 'text');
634            app.ActiveChannelsEditField.Editable = 'off';
635            app.ActiveChannelsEditField.Position = [117 66 62 22];
636            app.ActiveChannelsEditField.Value = '0';
637
638            % Create TriggersEditFieldLabel
```

```
639             app.TriggersEditFieldLabel = ...
                    uilabel(app.ChannelbiasingsettingsPanel);
640             app.TriggersEditFieldLabel.Position = [14 37 59 22];
641             app.TriggersEditFieldLabel.Text = '# Triggers';
642
643             % Create TriggersEditField
644             app.TriggersEditField = ...
                    uieditfield(app.ChannelbiasingsettingsPanel, 'text');
645             app.TriggersEditField.Editable = 'off';
646             app.TriggersEditField.Position = [117 37 62 22];
647             app.TriggersEditField.Value = '0';
648
649             % Create FPSEditFieldLabel
650             app.FPSEditFieldLabel = uilabel(app.ChannelbiasingsettingsPanel);
651             app.FPSEditFieldLabel.Position = [14 8 29 22];
652             app.FPSEditFieldLabel.Text = 'FPS';
653
654             % Create FPSEditField
655             app.FPSEditField = ...
                    uieditfield(app.ChannelbiasingsettingsPanel, 'text');
656             app.FPSEditField.Editable = 'off';
657             app.FPSEditField.Position = [117 8 62 22];
658             app.FPSEditField.Value = '0';
659
660             % Create PCUconnectionstatusLabel
661             app.PCUconnectionstatusLabel = ...
                    uilabel(app.CCUV11DesignedbyAfshinKashaniIlkhechiPanel);
662             app.PCUconnectionstatusLabel.Position = [274 24 128 22];
663             app.PCUconnectionstatusLabel.Text = 'PCU connection status';
664
665             % Create PCUconnectionstatusLamp
666             app.PCUconnectionstatusLamp = ...
                    uilamp(app.CCUV11DesignedbyAfshinKashaniIlkhechiPanel);
667             app.PCUconnectionstatusLamp.Position = [235 23 25 25];
668             app.PCUconnectionstatusLamp.Color = [0.9294 0.6941 0.1255];
669
670             % Create COMportEditFieldLabel
671             app.COMportEditFieldLabel = ...
                    uilabel(app.CCUV11DesignedbyAfshinKashaniIlkhechiPanel);
672             app.COMportEditFieldLabel.Position = [232 61 58 22];
673             app.COMportEditFieldLabel.Text = 'COM port';
674
675             % Create COMportEditField
676             app.COMportEditField = ...
                    uieditfield(app.CCUV11DesignedbyAfshinKashaniIlkhechiPanel, ...
                    'text');
677             app.COMportEditField.Editable = 'off';
678             app.COMportEditField.Position = [324 61 73 22];
679
680             % Show the figure after all components are created
681             app.UIFigure.Visible = 'on';
682         end
683     end
684
685     % App creation and deletion
686     methods (Access = public)
687
688         % Construct app
689         function app = PCUapp_exported(varargin)
690
691             % Create UIFigure and components
692             createComponents(app)
693
694             % Register the app with App Designer
695             registerApp(app, app.UIFigure)
696
697             % Execute the startup function
698             runStartupFcn(app, @(app)startupFcn(app, varargin{:}))
699
700             if nargout == 0
701                 clear app
702             end
703         end
704
705         % Code that executes before app deletion
706         function delete(app)
707
708             % Delete UIFigure when app is deleted
709             delete(app.UIFigure)
```

```
710             end
711         end
712     end
```

Appendix C: Matlab script for imaging with CCU

This appendix provides the Matlab script for performing any sorts of ultrasound and photoacoustic imaging using πCard system.

```
1  %% All In One Imaging Script.
2  %This script can perform US and PA imaging, all in one, it can perform
3  %sequenced imaging, complicated biasing algorithms, frame avaraging, angle
4  %steering and ultrasound focuing on multiple locations. Numeber of the
5  %frames and imaging speed is highly dependet on the various setting and it
6  %can go up to 24000 fps. This code requires an active CCU unit connected to
7  %Verasonics and piCards. WITHOUT THE CCU, THE CODE WILL NOT FUNCTION.
8  %
9  % Made by: Afshin Kashani Ilkhechi
10 % kashanii@ualberta.ca
11 %-----------------------------------------------------------------------
12 %% Main Settings and add-ones
13 close all force;
14 clear all;clc;        % Clear everything
15 %supported SURF boards(define new ones here -> DieDefiner.m):
16
17 % smx2_10Mhz_48x48
18 % Relaxor_64x64_2A
19 % Relaxor_64x64_D3
20 % Relaxor_64x64_Yellow_AKI
21 % Relaxor_128x128_SM3
22 % SM_128x128_AKI
23 % SM_128x128_Half_AKI
24 % AllChannels
25 % Relaxor_64x64_Yellow_AKI
26 % Bulk_PMN38_128x128_Mehmet_1
27 % Composite_PMN38_128x128_Mehmet_1
28 %smartX-
29
30
31 % Tx/Rx and Bias Settings
32 ArrayCode = 'Relaxor_64x64_Yellow_AKI';  % call the correct mapping for ...
       the surf board
33 PatternCode='FORCES';              % Flash, FORCES, uFORCES, S_Sequence
34 patternLocation='Cross';           % Cross Col Row CrossTx
35 TranmitPattern='Cross';            % Cross Col Row CrossTx
36 input.VNN=-50;                     % VNN Voltage
37 input.VPP=50;                      % VPP Voltage
38 input.TrOd=1000; %300                     % Delay to send out trigger 0 to ...
       9999 us
39 input.Qswitch=390;                 % laser Qswitch 250 to 550, for PA ImgMode
40 HighVoltageStartValue=2;           % Tx Voltage, can be overwritten elsewhere
41
42 % Frame acquisition setting (Imaging prority based on order below)
43 FrameAvaraging   = 1;              % Number of the frames per bias 1 to inf, ...
       NO ZERO
44 steeringAngle    = 0;              % longitudinal steering angle (1D array)
45 focal_point      = [20e-3];               % focal depth [m] (1D array)
46
47 % Bias Pattern Viewer and programmer
48 ViewBiasPattern=false;             % shows the bias pattern, false for run
49 pauseForpatternView=false;       % Will stop the process for viewing patterns
50 programPiCards=true;             % Program piCards
51
52 % Data Probing and saving
53 ShowChannelData  = true;           % Plot channel data
54 DRBFwhileImaging = false;           % Beamforming while imaging
55 SaveAfterAcuire  = false;          % Save data after receving all the frames
56 AskToSave        = false;           % Ask to save before saving, will pause
57 PauseAfterAcuire = false;           % Pause the imaging process after one run
58 VideoSave        = false;          % Video Save?other options maybe over written
59 LoopCountForVideo= 10;           % number of the frames for the video capture
60
61
62 %DRBF Settings
63 c_mod=1;                           % Modified Speed of sound, can be overwrtten
64 x_span = 10e-3;
65 y_span = 10e-3;
```

```
66  zmin = 12e-3;
67  zmax = 32e-3;  % if you get syrface, it will wash the point out
68  no_lines = 201;
69  Tmax = 1700;
70
71  % CCU Extra settings, can be left as is
72  input.COM='COM4';                 % CCU port
73  input.ImgMode='US';               % Imaging mode US or PA
74  input.VNNc=375;                   % VNN current Limit > 100 & <375 mA
75  input.VPPc=375;                   % VPP current limit > 100 & <375 mA
76  %input.TrOd=TrOdCalc(input);      % Delay to send out trigger 0 to 65e3 us
77  input.TimerInterval=0.5;          % Refreshing GUI in seconds < 1 second
78  input.VoltageTolerance=5;         % Tolerance for voltage in Votls
79  WaitforTrigger = true;            % if CCU is involved this MUST be true
80  DieDefiner;                       % Array definner
81  MakeBiasPattern;
82  piCardtoSURFmapper;               % Bias pattern generator
83  input.BiasPatern=bits;            % biasing patersn Sequence*Channels (-2¬1)
84
85  %% Beamform Script selector
86  GPUdecode=0;
87  switch PatternCode
88
89      case 'Flash'
90           BeamFormScript='DRBFaveFlash';
91      case 'FORCES'
92          GPUdecode=1;
93          BeamFormScript='DRBF_aveFORCES_GPU';
94      case 'uFORCES'
95          % BeamFormScript='uFORCES_BF';
96          disp ('PatternCode is not defined!')
97          return;
98      case 'S_Sequence'
99          % BeamFormScript='sSequence_BF';
100         disp ('BF script is not defined!')
101         return;
102     otherwise
103         disp ('PatternCode is not defined!')
104         return;
105
106 end
107 %% Safety Check before run
108 cd 'C:\Users\Verasonics\Desktop\Vantage-4.0.0-1812011200\Afshin'
109 %Stop if TX voltage is higher than safety limit
110 if (HighVoltageStartValue>specialmaxHighVoltage)
111     clc;
112     disp('Err 201: Transmit Voltage is higher than the safe voltage');
113     disp('HighVoltageStartValue > specialmaxHighVoltage');
114     close all force
115     return
116 end
117
118 % if FrameAvaraging is 0 set it to 1
119 if FrameAvaraging==0
120     FrameAvaraging=1;
121 end
122 % if focal_point is 0 set it to 1
123 if focal_point==0
124     focal_point=1;
125 end
126 maxFrameCount = biasPatternCount* ...
        max(size(focal_point))*max(size(steeringAngle))*FrameAvaraging;
127 FramesToshow = maxFrameCount/FrameAvaraging;
128 ChToshow = maxFrameCount/FrameAvaraging;
129 if VideoSave == true
130     maxFrameCount=maxFrameCount*LoopCountForVideo;
131      maxFrameCount=maxFrameCount/FrameAvaraging;
132     %do not change the following
133     ShowChannelData  = false;
134     DRBFwhileImaging = false;
135     SaveAfterAcuire  = true;
136     AskToSave        = true;
137     PauseAfterAcuire = true;
138     FrameAvaraging   = 1;
139     GPUdecode        = false;
```

```
140     disp('Video Mode is ON, Plot and DRBF mode is disbaled. Averaging is ...
            disabled!');
141 else
142     LoopCountForVideo=1;
143 end
144 switch PatternCode
145     case 'FORCES'
146      FramesToshow=FramesToshow/Nele;
147     case 'uFORCES'
148      FramesToshow=FramesToshow/8;
149     case 'S-Sequence'
150      FramesToshow=FramesToshow/(Nele-1);
151 end
152 if maxFrameCount≠1 & rem(maxFrameCount,2)≠0
153     clc;
154     disp('Error:');
155     disp('Frame count must be 1 or an even integer');
156     disp('Change number of the frames and re-run the script!');
157     close all force;
158     return
159 end
160 disp(['Total frame count is ' num2str(maxFrameCount) ' and ' ...
       num2str(biasPatternCount) ' biasing sequences with +' ...
       num2str(input.VPP) ' & ' num2str(input.VNN) ' Votls & ' ...
       num2str(FramesToshow) ' images frames .']);
161 if (FramesToshow>12 & DRBFwhileImaging==true)
162 answer = questdlg('DRBF plot count is high!', ...
163     'Frame Warning', ...
164     'Show them!','Disable DRBF','Disable DRBF');
165 % Handle response
166 switch answer
167     case 'Disable DRBF'
168         DRBFwhileImaging=false;
169 end
170 end
171
172 if (ChToshow>12 & ShowChannelData==true)
173 answer = questdlg('Channel plots are too high!', ...
174     'Frame Warning', ...
175     'Show them!','Disable Plot','Disable Plot');
176 % Handle response
177 switch answer
178
179     case 'Disable Plot'
180         ShowChannelData=false;
181 end
182 end
183 % If GPU is going to be used, make sure memory is free
184 if GPUdecode==1
185     disp('Checking GPU Memory Status...');
186             MemoryStatus=gpuDevice();
187             if MemoryStatus.AvailableMemory<2.1475e+09
188                 disp('GPU memory is almost full, Memory clean up is ...
                    initiated, may take few minutes...');
189                 gpuDevice(1);
190             end
191            addpath('C:\Users\Verasonics\Desktop\Vantage-4.0.0-1812011200\Afshin\GPU\FORCES
192 end
193 %% CCU
194 addpath('C:\Users\Verasonics\Desktop\Vantage-4.0.0-1812011200\Afshin\CCU');
195 if (ViewBiasPattern==true)
196     SeqView(bits);                 % If view requested
197     if pauseForpatternView==true
198         disp('Make "pauseForpatternView=false" to run the script');
199     return
200     end
201 end
202 if(programPiCards)
203 CCU(input);                        % program and monitor the CCU
204 end
205 %% Verasonics Settup
206 % Resorces
207 Resource.Parameters.numTransmit = 256;        % number of transmit channels.
208 Resource.Parameters.numRcvChannels = 256;     % number of receive channels. ...
       could be changed to 256
```

```
209 Resource.Parameters.speedOfSound = 1540;      % set speed of sound in ...
        m/sec before calling computeTrans
210 Resource.Parameters.simulateMode = 0;
211 Trans.Connector = (1:1:Resource.Parameters.numTransmit)'; %this is used ...
        for verasonics beamforming which we don't use
212
213
214 %Tx and Rx Channels
215 TXvec = ch_mapping_Tx;                  %pin mapping for transmit
216 RXvec = ch_mapping_Rx;                    %pin mapping for receive
217
218 Trans.name = 'custom';
219 Trans.frequency = dieFrequency;      % Frequency of the transducer MHz
220 lambda = Resource.Parameters.speedOfSound/Trans.frequency/1e6; % wavelength
221 Trans.type = 0;                         %  Linear (flat) array
222 Trans.numelements = 256;              %  Number of the elements of the Tx
223 Trans.units = 'wavelengths';
224 Trans.impedance = 50;
225 Trans.spacing = pitch/lambda;        % pitch of the array
226 Trans.elementWidth = (pitch-kerf)/lambda;
227 Trans.connType = 1;
228 Trans.Bandwidth = [0.6*dieFrequency, 1.6*dieFrequency];         % This ...
        will be based on %60 of Trans.frequency
229 Trans.id = 0;
230 Trans.ElementPos = ...
        [((0:pitch:pitch*(Trans.numelements-1))-pitch*Trans.numelements/2)/lambda; ...
        zeros(1,Trans.numelements); zeros(1,Trans.numelements); ...
        zeros(1,Trans.numelements)]';
231 Theta = (-pi/2:pi/100:pi/2);
232 X = Trans.elementWidth*pi*sin(Theta);
233 Trans.ElementSens = abs(cos(Theta).*(sin(X)./X));
234 Trans.maxHighVoltage = specialmaxHighVoltage;  % set maximum high voltage ...
        limit for pulser supply.
235 wavelength = 1540/(Trans.frequency*1e6);
236 TPC.hv = HighVoltageStartValue;
237 hvScale = 50.0/Trans.maxHighVoltage;
238 freq = Trans.frequency*1e6;
239 %%
240 % Specify SFormat structure array. Not used wih VSX
241 SFormat(1).transducer = 'custom';     % 128 element linear array with 1.0 ...
        lambda spacing
242 SFormat(1).scanFormat = 'RLIN';      % rectangular linear array scan
243 SFormat(1).radius = 0;               % ROC for curved lin. or dist. to ...
        virt. apex
244 SFormat(1).theta = 0;
245 SFormat(1).numRays = 1;      % no. of Rays (1 for Flat Focus)
246 SFormat(1).FirstRayLoc = [0,0,0];   % x,y,z
247 SFormat(1).rayDelta = 128*Trans.spacing;  % spacing in radians(sector) or ...
        dist. between rays (wvlnghts)
248 SFormat(1).startDepth = 0;   % Acquisition depth in wavelengths
249 SFormat(1).endDepth = 192;   % This should preferrably be a multiple of ...
        128 samples.
250
251 % Specify PData structure array. Only for recon by VSX
252 PData.sFormat = 1;      % use first SFormat structure.
253 PData.p∆X = Trans.spacing;
254 PData.p∆Z = 0.5;
255 PData.Size(1) = ceil((SFormat.endDepth-SFormat.startDepth)/PData.p∆Z); % ...
        startDepth, endDepth and p∆ set PData.Size.
256 PData.Size(2) = ceil((Trans.numelements*Trans.spacing)/PData.p∆X);
257 PData.Size(3) = 1;      % single image page
258 PData.Origin = ...
        [-Trans.spacing*(Trans.numelements-1)/2,0,SFormat.startDepth]; % x,y,z ...
        of upper lft crnr.
259
260 % Specify Media object. 'pt1.m' script defines array of point targets.
261 pt1;
262 Media.function = 'movePoints';
263
264 % Specify Resources.
265 Resource.RcvBuffer(1).datatype = 'int16';    % Only type
266 Resource.RcvBuffer(1).rowsPerFrame = 8192;   % <<<<<<
267 Resource.RcvBuffer(1).colsPerFrame = Resource.Parameters.numRcvChannels;
268 Resource.RcvBuffer(1).numFrames = maxFrameCount;       % m frames used for ...
        RF cineloop.
```

```
269 % Might not be needed!
270 Resource.InterBuffer(1).datatype = 'complex';
271 Resource.InterBuffer(1).rowsPerFrame = 1024; % <<<<<<<
272 Resource.InterBuffer(1).colsPerFrame = PData.Size(2);
273 Resource.InterBuffer(1).numFrames = 1;          % <<<<<
274 Resource.ImageBuffer(1).datatype = 'double';
275 Resource.ImageBuffer(1).rowsPerFrame = 1024;
276 Resource.ImageBuffer(1).colsPerFrame = PData.Size(2); %
277 Resource.Parameters.connector = 0;
278 %Tx Definition
279 TX = repmat(struct('waveform', 1, ...       % only this parameter we use in ...
        transmit
280     'Origin', Trans.ElementPos(1,1:3), ... %if we use internal beamforming ...
            matters
281     'focus', 0, ...                        %if we use internal ...
            beamforming matters
282     'Steer', [0.0,0.0], ...                %if we use internal ...
            beamforming matters
283     'Apod', zeros(1,Trans.numelements), ... %important to our custom transmit
284     'Delay', zeros(1,Trans.numelements)), 1, 1); %important to our custom ...
            transmit
285 i=1;
286 %for every bias pattern, all focal point will be scanned with all angles
287 %and avarged framed for each
288 for Loop9 = 1:LoopCountForVideo
289 for Loop1=1:biasPatternCount
290     for Loop2 = 1:length(focal_point)
291         for Loop3 = 1:length(steeringAngle)
292             [delay_times, T0] = ...
                    calcDT(Nele,kerf,width,Trans.frequency*1e6,focal_point(Loop2),steeringAngle
293             for Loop4 = 1:FrameAvaraging
294                 TW(i).type = 'parametric';   %this is the waveform structure
295                 if (TxPolaritySenstivity)
296                     clear TxWavePolarity;
297                     for k=1:Trans.numelements
298                        if bits(Loop1,k)==-1
299                        TxWavePolarity(k,:)=[Trans.frequency,0.67,number_cycles,bits(Loop1,
300                        else
301                        TxWavePolarity(k,:)=[Trans.frequency,0.67,number_cycles,1];
302                        end
303                     end
304                     TW(i).Parameters=TxWavePolarity;
305                 else
306                 TW(i).Parameters = [Trans.frequency,0.67,number_cycles,1];
307                 end
308                 TX(i).waveform = 1;              % use 1st TW structure.
309                 TX(i).Origin = [0.0,0.0,0.0];   % flash transmit origin at ...
                        (0,0,0).
310                 TX(i).focus = 0;
311                 TX(i).Steer = [0,0];        % theta, alpha = 0.
312                 TX(i).Apod = zeros(1,Trans.numelements);
313                 TX(i).Apod(TXvec(Loop1,:)) = 1;  %enables the coonected ...
                        channels for trqansmitting ONLY
314                 TX(i).Delay(1:256) = 0;
315                 if (length(TXvec)==Nele)
316                     for j=1:Nele
317                         TX(i).Delay(TXvec(j)) = delay_times(j);
318                     end
319                 end
320              %for decoding reference
321              FrameDecodeValues(i).biasPattern=Loop1;
322              FrameDecodeValues(i).focalPoint=focal_point(Loop2);
323              FrameDecodeValues(i).steeringAngle=steeringAngle(Loop3);
324              FrameDecodeValues(i).FrameAvaragingFrame=Loop4;
325              FrameDecodeValues(i).delay_times=delay_times;
326              FrameDecodeValues(i).ch_mapping_Tx=TXvec(Loop1,:);
327              FrameDecodeValues(i).TxLoc=TxRx(Loop1).Tx;
328              i=i+1;
329             end
330         end
331     end
332 end
333 end
334
```

```
335 TGC.CntrlPts = [0,500,500,500,500,500,500,500];
336 TGC.rangeMax = SFormat.endDepth;
337 TGC.Waveform = computeTGCWaveform(TGC);
338
339 % Specify Receive structure arrays -
340 %   endDepth - add additional acquisition depth to account for some channels
341 %              having longer path lengths.
342 %   InputFilter - The same coefficients are used for all channels. The
343 %              coefficients below give a broad bandwidth bandpass filter.
344 maxAcqLength = sqrt(SFormat.endDepth^2 + ...
       (Trans.numelements*Trans.spacing)^2) - SFormat.startDepth;
345 wlsPer128 = 128/(4*2); % wavelengths in 128 samples for 4 samplesPerWave
346 Receive = repmat(struct('Apod', zeros(1,Trans.numelements), ...
347     'startDepth', SFormat.startDepth, ...
348     'endDepth', SFormat.startDepth + ...
         wlsPer128*ceil(maxAcqLength/wlsPer128), ...
349     'TGC', 1, ...
350     'bufnum', 1, ...
351     'framenum', 1, ...
352     'acqNum', 1, ...           %here can be also used for avaraging
353     'samplesPerWave', 4, ...
354     'mode', 0, ...
355     'InputFilter',[0.0036,0.0127,0.0066,-0.0881,-0.2595,0.6494], ...
356     'callMediaFunc', 0),1,Resource.RcvBuffer(1).numFrames);
357 nn=maxFrameCount/biasPatternCount/LoopCountForVideo;
358 for loop9=1:LoopCountForVideo
359     j = loop9*biasPatternCount-biasPatternCount;
360 for k = 1:Resource.RcvBuffer(1).numFrames/LoopCountForVideo
361     i=j+k;
362     Receive(i).Apod(1:Resource.Parameters.numRcvChannels) = 0.0;
363     Receive(i).Apod(RXvec(ceil(k/nn),:)) = 1;
364
365     %diasabling specific channel for receive, Not recomended
366     %Receive(i).Apod(RXvec(20)) = 0;
367
368     Receive(i).framenum = i;
369     Receive(i).acqNum = 1;
370     Receive(i).callMediaFunc = 1;
371     FrameDecodeValues(i).ch_mapping_Rx=RXvec(ceil(k/nn),:);
372     FrameDecodeValues(i).RxLoc=TxRx(ceil(k/nn)).Rx;
373 end
374 end
375 save('ImagingSettings.mat');
376 % Specify Recon structure arrays.
377 Recon = struct('senscutoff', 0.6, ...
378     'pdatanum', 1, ...
379     'rcvBufFrame', -1, ...     % use most recently transferred frame
380     'IntBufDest', [1,1], ...
381     'ImgBufDest', [1,-1], ...  % auto-increment ImageBuffer each recon
382     'RINums', [1;2]);
383
384 % Define ReconInfo structures.
385 ReconInfo = repmat(struct('mode', 3, ...  % replace IQ data.
386     'txnum', 1, ...
387     'rcvnum', 1, ...
388     'regionnum', 0), 1, 2);
389 % - Set specific ReconInfo attributes.
390 ReconInfo(1).mode = 3;
391 ReconInfo(1).rcvnum = 1;
392
393 % Specify Process structure array.
394 pers = 40;
395 Process(1).classname = 'Image';
396 Process(1).method = 'imageDisplay';
397 Process(1).Parameters = {'imgbufnum',1,...   % number of buffer to process.
398     'framenum',-1,...   % (-1 => lastFrame)
399     'pdatanum',1,...    % number of PData structure to use
400     'norm',1,...        % normalization method(1 means fixed)
401     'pgain',8.0,...             % pgain is image processing gain
402     'persistMethod','simple',...
403     'persistLevel',pers,...
404     'interp',1,...      % method of interpolation (1=4pt interp)
405     'compression',0.5,...      % X^0.5 normalized to output word size
406     'reject',5,...      % reject level
```

```
407     'mappingMode','full',...
408     'display',1,...       % display image after processing
409     'displayWindow',1};
410 Process(2).classname = 'External';   %We use this later in the aquzation ...
        for ploting data
411 Process(2).method = 'PlotaveChannelData';
412 Process(2).Parameters = {'srcbuffer','receive',... % buffer to process.
413     'srcbufnum',1,...
414     };
415
416
417 Process(3).classname = 'External';
418 Process(3).method = BeamFormScript;
419 Process(3).Parameters = {'srcbuffer','receive',... % buffer to process.
420     'srcbufnum',1,...
421     'dstbuffer','none'}; % no output buffer
422
423 Process(4).classname = 'External';
424 if VideoSave==false
425 Process(4).method = 'SaveAveFrames';
426 else
427 Process(4).method = 'SaveMotion';
428 end
429
430 Process(4).Parameters = {'srcbuffer','receive',... % buffer to process.
431     'srcbufnum',1,...
432     'dstbuffer','none'}; % no output buffer
433
434 % Specify SeqControl structure arrays.
435 SeqControl(1).command = 'jump'; % jump back to start.
436 SeqControl(1).argument = 1;
437 SeqControl(2).command = 'timeToNextAcq';  % time between synthetic ...
        aperture acquisitions
438 SeqControl(2).argument = 200;  % 200 usec
439 SeqControl(3).command = 'timeToNextAcq';  % time between frames
440 SeqControl(3).argument = 100000;  % 10 msec
441 SeqControl(4).command = 'returnToMatlab';
442 SeqControl(5).command = 'pause';
443 SeqControl(5).condition = 'extTrigger';
444 SeqControl(5).argument = 2; % 18
445 SeqControl(6).command = 'triggerOut';
446 SeqControl(7).command = 'sync';
447 SeqControl(8).command = 'noop';  % this is a pause and the value ...
        determined with the argument
448 % SeqControl(8).argument = 524287;
449 % SeqControl(8).argument = 20000;
450 SeqControl(8).argument = 20000;
451 SeqControl(9).command = 'stop';
452 SeqControl(10).command = 'pause';
453 SeqControl(10).condition = 'extTrigger';
454 SeqControl(10).argument = 1;
455 nsc = 11; % nsc is count of SeqControl objects
456 TrGen=maxFrameCount/biasPatternCount/LoopCountForVideo;
457 TrCount=1;
458 n = 1; % n is count of Events
459     for i = 1:maxFrameCount  %if I need specific number of the frames, we ...
            define here, e.g. FORCES require 64 frame only
460
461         if floor(i/TrCount)
462             TrCount=TrCount+TrGen;
463             Event(n).info = 'Trig out';
464             Event(n).tx = 0;         % no transmit
465             Event(n).rcv = 0;        % no rcv
466             Event(n).recon = 0;      % reconstruction
467             Event(n).process = 0;    % processing
468             Event(n).seqControl = 6;
469             n = n+1;
470         if(WaitforTrigger)
471             Event(n).info = 'pause';
472             Event(n).tx = 0;         % no transmit
473             Event(n).rcv = 0;        % no rcv
474             Event(n).recon = 0;      % reconstruction
475             Event(n).process = 0;    % processing
```

```
476             Event(n).seqControl = 10; %Trigger input 1 enable with rising ...
                    edge. Page 120 VantageSequenceProgrammingManual.pdf
477             n = n+1;
478         end
479         end
480 if(input.ImgMode=='US')       %Ultrasound Imaging
481     Event(n).info = 'Acquire Data.';
482     Event(n).tx = i;          % use 1st TX structure.
483     Event(n).rcv = i;       % use 2nd Rcv structure.
484     Event(n).recon = 0;       % no reconstruction.
485     Event(n).process = 0;     % no processing
486     Event(n).seqControl = [nsc]; % time between frames, SeqControl struct ...
        defined below.
487     SeqControl(nsc).command = 'transferToHost';
488     nsc = nsc + 1;
489     n = n+1;
490 else                         %Photoacoustic
491     Event(n).info = 'Acquire Data.';
492     Event(n).tx = 0;          % No transmit for photoacoustic
493     Event(n).rcv = i;       % use 2nd Rcv structure.
494     Event(n).recon = 0;       % no reconstruction.
495     Event(n).process = 0;     % no processing
496     Event(n).seqControl = [nsc]; % time between frames, SeqControl struct ...
        defined below.
497     SeqControl(nsc).command = 'transferToHost';
498     nsc = nsc + 1;
499     n = n+1;
500 end
501      Event(n).info = 'Reconstruct';
502     Event(n).tx = 0;          % no transmit
503     Event(n).rcv = 0;         % no rcv
504     Event(n).recon = 0;       % reconstruction
505     Event(n).process = 0;     % processing
506     if floor(i/5) == i/1      % Exit to Matlab every 5th frame
507         Event(n).seqControl = 4; % return to Matlab
508     else
509         Event(n).seqControl = 0;
510     end
511     n = n+1;
512     end
513  if(ShowChannelData==true)
514     Event(n).tx = 0;          % no transmit --------  Show Channel Data
515     Event(n).rcv = 0;         % no rcv
516     Event(n).recon = 0;       % reconstruction
517     Event(n).process = 2;     % processing  Ploting the data from ...
        PlotChannelData_Afshin.m
518     Event(n).seqControl = 7; % =4: return to MATLAB, =7: sync
519     n = n+1;
520  end
521 if(DRBFwhileImaging==true)
522     Event(n).tx = 0;          % no transmit --------  Beamform
523     Event(n).rcv = 0;         % no rcv
524     Event(n).recon = 0;       % reconstruction
525     Event(n).process = 3;     % processing  Ploting the data from ...
        PlotChannelData_Afshin.m
526     Event(n).seqControl = 7; % =4: return to MATLAB, =7: sync
527     n = n+1;
528 end
529 if(SaveAfterAcuire==true)
530     Event(n).tx = 0;          % no transmit --------  Beamform
531     Event(n).rcv = 0;         % no rcv
532     Event(n).recon = 0;       % reconstruction
533     Event(n).process = 4;     % save the channel datainto today folder ...
        "SaveAveFrames.m"
534     Event(n).seqControl = 7; % =4: return to MATLAB, =7: sync
535     n = n+1;
536 end
537     if(PauseAfterAcuire==false)
538     % Comment this out for single acquisition
539     Event(n).info = 'Jump back to first event';
540     Event(n).tx = 0;         % no TX
541     Event(n).rcv = 0;        % no Rcv
542     Event(n).recon = 0;      % no Recon
543     Event(n).process = 0;
544     Event(n).seqControl = 1; % jump command
```

```
545     end
546
547 % User specified UI Control Elements
548 % - Sensitivity Cutoff
549 UI(1).Control =  {'UserB7','Style','VsSlider','Label','Sens. Cutoff',...
550     'SliderMinMaxVal',[0,1.0,Recon(1).senscutoff],...
551     'SliderStep',[0.025,0.1],'ValueFormat','%1.3f'};
552 UI(1).Callback = text2cell('%-SensCutoffCallback');
553
554 % - Range Change
555 UI(2).Control = {'UserA1','Style','VsSlider','Label','Range',...
556     'SliderMinMaxVal',[64,320,SFormat.endDepth],'SliderStep',[0.1,0.2],'ValueFormat','%3.0
557 UI(2).Callback = text2cell('%-RangeChangeCallback');
558
559 % Specify factor for converting sequenceRate to frameRate.
560 frameRateFactor = 5;
561
562 % Save all the structures to a .mat file.
563 save(ArrayCode);
564 %HERE we can program the biasing and next line will strart imaging
565 filename = ArrayCode;VSX;
566 return
567
568 % **** Callback routines to be converted by text2cell function. ****
569 %-SensCutoffCallback
570 ReconL = evalin('base', 'Recon');
571 for i = 1:size(ReconL,2)
572     ReconL(i).senscutoff = UIValue;
573 end
574 assignin('base','Recon',ReconL);
575 Control = evalin('base','Control');
576 Control.Command = 'update&Run';
577 Control.Parameters = {'Recon'};
578 assignin('base','Control', Control);
579 return
580 %-SensCutoffCallback
581
582 %-RangeChangeCallback
583 simMode = evalin('base','Resource.Parameters.simulateMode');
584 % No range change if in simulate mode 2.
585 if simMode == 2
586     set(hObject,'Value',evalin('base','SFormat.endDepth'));
587     return
588 end
589 range = UIValue;
590 assignin('base','range',range);
591 SFormat = evalin('base','SFormat');
592 SFormat.endDepth = range;
593 assignin('base','SFormat',SFormat);
594 evalin('base','PData.Size(1) = ...
        ceil((SFormat.endDepth-SFormat.startDepth)/PData.pΔZ);');
595 evalin('base','[PData.Region,PData.numRegions] = createRegions(PData);');
596 evalin('base','Resource.DisplayWindow(1).Position(4) = ...
        ceil(PData.Size(1)*PData.pΔZ/Resource.DisplayWindow(1).pΔ);');
597 Receive = evalin('base', 'Receive');
598 Trans = evalin('base', 'Trans');
599 maxAcqLength = sqrt(range^2 + ...
        (Trans.numelements*Trans.spacing)^2)-SFormat.startDepth;
600 wlsPer128 = 128/(4*2);
601 for i = 1:size(Receive,2)
602     Receive(i).endDepth = SFormat.startDepth + ...
            wlsPer128*ceil(maxAcqLength/wlsPer128);
603 end
604 assignin('base','Receive',Receive);
605 evalin('base','TGC.rangeMax = SFormat.endDepth;');
606 evalin('base','TGC.Waveform = computeTGCWaveform(TGC);');
607 Control = evalin('base','Control');
608 Control.Command = 'update&Run';
609 Control.Parameters = ...
        {'SFormat','PData','Receive','Recon','DisplayWindow','ImageBuffer'};
610 assignin('base','Control', Control);
611 assignin('base', 'action', 'displayChange');
612
613
614 return
615 %-RangeChangeCallback
```

The following codes are a helper functions to translate IBv1 channel maping to πCard System.

```
%% piCard and Verasonics to die channel mapping
%by usign this script piCards can be programmed for every transdcuer
% Copyright Afshin Kashani Ilkhechi

%%
if ¬...
    exist('PinCol')|¬exist('PinRow')|¬exist('pattern')|¬exist('patternLocation')|¬exist('Tr
    disp('Variables are missing');
    return
end
TxPolaritySenstivity=false;
sequence=size(pattern,1);
pins=size(pattern,2);

bits=ones(sequence,256);
bits=bits*2;

switch patternLocation
    case 'Cross'
        bits=ones(sequence*2,256);
        bits=bits*2;
        for i=1:sequence
        bits(i,PinRow)=pattern(i,:);
        bits(i,PinCol)=0;
        if DeadChnnelRow≠0;
        bits(i,DeadChnnelRow)=2;
        end
        if DeadChnnelCol≠0;
        bits(i,DeadChnnelCol)=2;
        end
        end
        n=1;
        for i=sequence+1:sequence*2
        bits(i,PinCol)=pattern(n,:);
        bits(i,PinRow)=0;
        if DeadChnnelCol≠0;
        bits(i,DeadChnnelCol)=2;
        end
        if DeadChnnelRow≠0;
        bits(i,DeadChnnelRow)=2;
        end
        n=n+1;
        end
    case 'Col'
        for i=1:sequence
        bits(i,PinCol)=pattern(i,:);
        bits(i,PinRow)=0;
        if DeadChnnelCol≠0;
        bits(i,DeadChnnelCol)=2;
        end
        if DeadChnnelRow≠0;
        bits(i,DeadChnnelRow)=2;
        end
        end
    case 'Row'
        for i=1:sequence
        bits(i,PinRow)=pattern(i,:);
        bits(i,PinCol)=0;
        if DeadChnnelRow≠0;
        bits(i,DeadChnnelRow)=2;
        end
        if DeadChnnelCol≠0;
        bits(i,DeadChnnelCol)=2;
        end
        end

    case 'CrossTx'
bits=ones(sequence*2,256);
        bits=bits*2;
        for i=1:sequence
        bits(i,PinCol)=pattern(i,:);
        bits(i,PinRow)=0;
        if DeadChnnelCol≠0;
        bits(i,DeadChnnelCol)=2;
        end
```

```
75          if DeadChnnelRow≠0;
76          bits(i,DeadChnnelRow)=2;
77          end
78          end
79          n=1;
80          for i=sequence+1:sequence*2
81          bits(i,PinRow)=pattern(n,:);
82          bits(i,PinCol)=0;
83          if DeadChnnelCol≠0;
84          bits(i,DeadChnnelCol)=2;
85          end
86          if DeadChnnelRow≠0;
87          bits(i,DeadChnnelRow)=2;
88          end
89          n=n+1;
90          end
91
92      otherwise
93          disp('Wrong patternlocation');
94          return
95  end
96  piCardIBv1_Ch_Mapping=zeros(1,256);
97  piCardIBv1_Ch_Mapping(2:2:256)=1:2:255;
98  piCardIBv1_Ch_Mapping(1:2:255)=2:2:256;
99
100 switch TranmitPattern
101     case 'CrossTx'
102         TxPolaritySenstivity=true;
103     for i=1:sequence
104     ch_mapping_Rx(i,:) = piCardIBv1_Ch_Mapping(PinRow);
105     ch_mapping_Tx(i,:) = piCardIBv1_Ch_Mapping(PinCol);
106     TxRx(i).Tx='X(Col)';
107     TxRx(i).Rx='Y(Row)';
108     end
109     for i=sequence+1:sequence*2
110     ch_mapping_Rx(i,:) = piCardIBv1_Ch_Mapping(PinCol);
111     ch_mapping_Tx(i,:) = piCardIBv1_Ch_Mapping(PinRow);
112     TxRx(i).Tx='Y(Row)';
113     TxRx(i).Rx='X(Col)';
114     end
115     case 'Cross'
116     for i=1:sequence
117     ch_mapping_Rx(i,:) = piCardIBv1_Ch_Mapping(PinRow);
118     ch_mapping_Tx(i,:) = piCardIBv1_Ch_Mapping(PinCol);
119     TxRx(i).Tx='X(Col)';
120     TxRx(i).Rx='Y(Row)';
121     end
122     for i=sequence+1:sequence*2
123     ch_mapping_Rx(i,:) = piCardIBv1_Ch_Mapping(PinCol);
124     ch_mapping_Tx(i,:) = piCardIBv1_Ch_Mapping(PinRow);
125     TxRx(i).Tx='Y(Row)';
126     TxRx(i).Rx='X(Col)';
127     end
128     case 'Col'
129     for i=1:sequence
130     ch_mapping_Rx(i,:) = piCardIBv1_Ch_Mapping(PinRow);
131     ch_mapping_Tx(i,:) = piCardIBv1_Ch_Mapping(PinCol);
132     TxRx(i).Tx='X(Col)';
133     TxRx(i).Rx='Y(Row)';
134     end
135     case 'Row'
136     for i=1:sequence
137     ch_mapping_Rx(i,:) = piCardIBv1_Ch_Mapping(PinCol);
138     ch_mapping_Tx(i,:) = piCardIBv1_Ch_Mapping(PinRow);
139     TxRx(i).Tx='Y(Row)';
140     TxRx(i).Rx='X(Col)';
141     end
142 end
143
144 biasPatternCount=size(bits,1);
145 FreqList = (6:197)'; TxFreq = 250 ./ (2.*FreqList);
146 dieFrequency=TxFreq(find(TxFreq<dieFrequency,1));
147 disp(['Tx Frequency is set to ' num2str(dieFrequency) ' MHz']);
```

```
1  %% Verasonics to die channel mapping using piCard System
2  %by usign this script verasonics can be programmed for every transdcuer, 1D
3  %and 2D
4
5  %% Template
6  %    case 'Template'
7  %          Nele = 0;                       % Number of the elements
8  %          width = 145e-6;                 % Width of the elements
9  %          kerf = 20e-6;                   % Kerf of the elements
10 %          pitch = width + kerf;           % Pitch of the elements
11 %          dieFrequency = 10;              % Centeral frequency of the transducer
12 %          specialmaxHighVoltage = 30;     % Maximum transmit voltage allowed
13 %
14 %                                          % Pin maping oh the elements
15 %                                          % Here Columns and Rows must be
16 %                                          % defined
17 %          PinCol(1:4:61)=130:2:160;
18 %          PinCol(3:4:63)=129:2:159;
19 %          PinCol(2:4:62)=31:-2:1;
20 %          PinCol(4:4:64)=32:-2:2;
21 %
22 %          PinRow(1:4:61)=194:2:224;
23 %          PinRow(3:4:63)=193:2:223;
24 %          PinRow(2:4:62)=95:-2:65;
25 %          PinRow(4:4:64)=96:-2:66;
26 %
27 %          switch TranmitPattern          % where transmit and Receive should be
28 %              case 'Row'                 %if Row is selected as transmit location
29 %       for i=1:NumFramesToSave
30 %       ch_mapping_Rx(i,:) = piCardIBv1_Ch_Mapping(PinCol);
31 %       ch_mapping_Tx(i,:) = piCardIBv1_Ch_Mapping(PinRow);
32 %       end
33 %              case 'Col'                 % if Col is selected and transmit ...
       locatino
34 %       for i=1:NumFramesToSave
35 %       ch_mapping_Rx(i,:) = piCardIBv1_Ch_Mapping(PinRow);
36 %       ch_mapping_Tx(i,:) = piCardIBv1_Ch_Mapping(PinCol);
37 %       end
38 %              case 'Xflash'              % Cross-plain flash imagin
39 %       NumFramesToSave=2;
40 %       ch_mapping_Rx(1,:)=piCardIBv1_Ch_Mapping(PinCol);
41 %       ch_mapping_Tx(1,:)=piCardIBv1_Ch_Mapping(PinRow);
42 %       ch_mapping_Rx(2,:)=piCardIBv1_Ch_Mapping(PinRow);
43 %       ch_mapping_Tx(2,:)=piCardIBv1_Ch_Mapping(PinCol);
44 %              otherwise
45 %               disp('Pattern location is not defined properly');
46 %           return;
47 %       end
48
49 %% Actual Code
50 TxCycles=2;  % if not determind, it will be 2, as suggested by the Verasonics
51 NumFramesToSave=size(pattern,1); %if nut determind, number of the frames ...
       will be based on the bias pattern
52 DeadChnnelCol=[];
53 DeadChnnelRow=[];
54 piCardIBv1_Ch_Mapping=zeros(1,256);
55 piCardIBv1_Ch_Mapping(2:2:256)=1:2:255;
56 piCardIBv1_Ch_Mapping(1:2:255)=2:2:256;
57 switch ArrayCode
58
59     case 'Relaxor_64x64_D3'
60         Nele=64;
61 %          pitch = 153e-6;
62 %          kerf = 30e-6;
63         width = 133e-6;
64         kerf = 20e-6;
65         pitch = width + kerf;
66         dieFrequency = 10;
67         specialmaxHighVoltage = 30;
68         number_cycles=2;
69         HighVoltageStartValue=20; % sets the high voltage value
70
71         DeadChnnelCol=[12 16 18];    %remove shorting channels from bias ...
           and receive
72         DeadChnnelRow=[];
73
74         PinCol(1:2:63)=33:1:64;
```

```
75          PinCol(2:2:64)=192:-1:161;
76
77          PinRow(1:2:63)=97:1:128;
78          PinRow(2:2:64)=256:-1:225;
79          switch TranmitPattern
80              case 'Row'
81       for i=1:NumFramesToSave
82       ch_mapping_Rx(i,:) = piCardIBv1_Ch_Mapping(PinCol);
83       ch_mapping_Tx(i,:) = piCardIBv1_Ch_Mapping(PinRow);
84       end
85              case 'Col'
86       for i=1:NumFramesToSave
87       ch_mapping_Rx(i,:) = piCardIBv1_Ch_Mapping(PinRow);
88       ch_mapping_Tx(i,:) = piCardIBv1_Ch_Mapping(PinCol);
89       end
90              case 'Xflash'
91       NumFramesToSave=2;
92       ch_mapping_Rx(1,:)=piCardIBv1_Ch_Mapping(PinCol);
93       ch_mapping_Tx(1,:)=piCardIBv1_Ch_Mapping(PinRow);
94       ch_mapping_Rx(2,:)=piCardIBv1_Ch_Mapping(PinRow);
95       ch_mapping_Tx(2,:)=piCardIBv1_Ch_Mapping(PinCol);
96
97              case 'XBiasCoded'
98          NumFramesToSave=size(pattern,1)*2;
99       for i=1:size(pattern,1)
100      ch_mapping_Rx(i,:) = piCardIBv1_Ch_Mapping(PinCol);
101      ch_mapping_Tx(i,:) = piCardIBv1_Ch_Mapping(PinRow);
102      end
103      for i=size(pattern,1)+1:NumFramesToSave
104      ch_mapping_Rx(i,:) = piCardIBv1_Ch_Mapping(PinRow);
105      ch_mapping_Tx(i,:) = piCardIBv1_Ch_Mapping(PinCol);
106      end
107          otherwise
108          return;
109      end
110
111
112     case 'Relaxor_64x64_2A'
113         Nele=64;
114 %         pitch = 153e-6;
115 %         kerf = 30e-6;
116         width = 133e-6;
117         kerf = 20e-6;
118         pitch = width + kerf;
119         dieFrequency = 10;
120         specialmaxHighVoltage = 30;
121         number_cycles=2;
122         HighVoltageStartValue=20; % sets the high voltage value
123
124         DeadChnnelCol=[4 14 22 23];     %remove shorting channels from bias ...
            and receive
125         DeadChnnelRow=[];
126
127         PinCol(1:4:61)=130:2:160;
128         PinCol(3:4:63)=129:2:159;
129         PinCol(2:4:62)=31:-2:1;
130         PinCol(4:4:64)=32:-2:2;
131
132         PinRow(1:4:61)=194:2:224;
133         PinRow(3:4:63)=193:2:223;
134         PinRow(2:4:62)=95:-2:65;
135         PinRow(4:4:64)=96:-2:66;
136         switch TranmitPattern
137             case 'Row'
138
139      for i=1:NumFramesToSave
140      ch_mapping_Rx(i,:) = piCardIBv1_Ch_Mapping(PinCol);
141      ch_mapping_Tx(i,:) = piCardIBv1_Ch_Mapping(PinRow);
142      end
143             case 'Col'
144
145      for i=1:NumFramesToSave
146      ch_mapping_Rx(i,:) = piCardIBv1_Ch_Mapping(PinRow);
147      ch_mapping_Tx(i,:) = piCardIBv1_Ch_Mapping(PinCol);
148      end
149             case 'Xflash'
150      NumFramesToSave=2;
151      ch_mapping_Rx(1,:)=piCardIBv1_Ch_Mapping(PinCol);
152      ch_mapping_Tx(1,:)=piCardIBv1_Ch_Mapping(PinRow);
153      ch_mapping_Rx(2,:)=piCardIBv1_Ch_Mapping(PinRow);
```

```
154       ch_mapping_Tx(2,:)=piCardIBv1_Ch_Mapping(PinCol);
155
156               case 'XBiasCoded'
157          NumFramesToSave=size(pattern,1)*2;
158       for i=1:size(pattern,1)
159       ch_mapping_Rx(i,:) = piCardIBv1_Ch_Mapping(PinCol);
160       ch_mapping_Tx(i,:) = piCardIBv1_Ch_Mapping(PinRow);
161       end
162       for i=size(pattern,1)+1:NumFramesToSave
163       ch_mapping_Rx(i,:) = piCardIBv1_Ch_Mapping(PinRow);
164       ch_mapping_Tx(i,:) = piCardIBv1_Ch_Mapping(PinCol);
165       end
166           otherwise
167           return;
168       end
169
170
171
172  case 'smx2_10Mhz_48x48'
173          Nele = 48;
174          width = 107e-6;
175          kerf = 16e-6;
176          pitch = width + kerf;
177          dieFrequency = 10;
178          specialmaxHighVoltage = 30;
179       PinRow = zeros(1,48);
180       PinCol = zeros(1,48);
181       PinCol(1:2:47)=56:-2:10;
182       PinCol(2:2:48)=138:2:184;
183       PinRow(1:2:47)=74:2:120;
184       PinRow(2:2:48)=248:-2:202;
185       load('piCardIBv1_Ch_Map.mat'); %Channle mapping from Verasonics to ...
             interfaceboard
186       switch TranmitPattern
187           case 'Row'
188       for i=1:NumFramesToSave
189       ch_mapping_Rx(i,:) = piCardIBv1_Ch_Mapping(PinCol);
190       ch_mapping_Tx(i,:) = piCardIBv1_Ch_Mapping(PinRow);
191       end
192
193           case 'Col'
194       for i=1:NumFramesToSave
195       ch_mapping_Rx(i,:) = piCardIBv1_Ch_Mapping(PinRow);
196       ch_mapping_Tx(i,:) = piCardIBv1_Ch_Mapping(PinCol);
197       end
198           case 'Xflash'
199        NumFramesToSave=2;
200       ch_mapping_Rx(1,:)=piCardIBv1_Ch_Mapping(PinCol);
201       ch_mapping_Tx(1,:)=piCardIBv1_Ch_Mapping(PinRow);
202       ch_mapping_Rx(2,:)=piCardIBv1_Ch_Mapping(PinRow);
203       ch_mapping_Tx(2,:)=piCardIBv1_Ch_Mapping(PinCol);
204
205       case 'XBiasCoded'
206          NumFramesToSave=size(pattern,1)*2;
207       for i=1:size(pattern,1)
208       ch_mapping_Rx(i,:) = piCardIBv1_Ch_Mapping(PinCol);
209       ch_mapping_Tx(i,:) = piCardIBv1_Ch_Mapping(PinRow);
210       end
211       for i=size(pattern,1)+1:NumFramesToSave
212       ch_mapping_Rx(i,:) = piCardIBv1_Ch_Mapping(PinRow);
213       ch_mapping_Tx(i,:) = piCardIBv1_Ch_Mapping(PinCol);
214       end
215           otherwise
216           return;
217       end
218
219
220      otherwise,
221          error('invalid die code (InterfaceToSURFmapper.m)');
222
223  end
224  FreqList = (6:197)'; TxFreq = 250 ./ (2.*FreqList);
225  dieFrequency=TxFreq(find(TxFreq<dieFrequency,1));
226  disp(['Tx Frequency is set to ' num2str(dieFrequency) ' MHz']);
227  save('channelMapping_temp.mat','TxCycles','DeadChnnelRow','DeadChnnelCol','ch_mapping_Tx',
228  %Made by: Afshin
```

```
1   %% Die Definer
2   % this script will define various pinout for SURFs. Every SURF has an
3   % unique name and its all properties will be defined here.
4   %%
5   TxCycles=2;  % if not determind, it will be 2, as suggested by the Verasonics
6   DeadChnnelCol=[];
7   DeadChnnelRow=[];
8   switch ArrayCode
9
10          case 'Composite_PMN38_128x128_Mehmet_1'
11
12          Nele=128;
13          width = 130e-6;
14          kerf = 20e-6;
15          pitch = width + kerf;
16          dieFrequency = 10;
17          specialmaxHighVoltage = 30;
18          number_cycles=2;
19          HighVoltageStartValue=25;        % sets the high voltage value
20          input.VNN=-50;                   % VNN Voltage
21          input.VPP=50;                    % VPP Voltage
22          DeadChnnelCol=[3 4 6 8 10 11 12 13 14 15 16 17 18 19 23 24 25 26 ...
                27 28 29 30 31 32 34 35 41 42 43 44 47 48 49 51 52 53 54 57 58 ...
                63 129 130 131 132 133 135 136 139 140 141:147 151 153 154 ...
                162:165 167:171 173 174 177:179 181 182 184:187];    %remove ...
                shorting channels from bias and receive
23          DeadChnnelRow=[97 100:102 105 106  109 110 115 116 118 125:128 ...
                193:196 198 200:206 208 211:213 215:227 230 232 236 245 248 ...
                250 252 254 256];
24
25          PinCol(1:4:125)=2:2:64;
26          PinCol(3:4:127)=1:2:63;
27          PinCol(2:4:126)=192:-2:130;
28          PinCol(4:4:128)=191:-2:129;
29
30          PinRow(1:4:125)=256:-2:194;
31          PinRow(3:4:127)=255:-2:193;
32          PinRow(2:4:126)=66:2:128;
33          PinRow(4:4:128)=65:2:127;
34
35      case 'Bulk_PMN38_128x128_Mehmet_1'
36
37          Nele=128;
38          width = 130e-6;
39          kerf = 20e-6;
40          pitch = width + kerf;
41          dieFrequency = 10;
42          specialmaxHighVoltage = 30;
43          number_cycles = 1;
44          HighVoltageStartValue=25;        % sets the high voltage value
45          input.VNN=-50;                   % VNN Voltage
46          input.VPP=50;                    % VPP Voltage
47          DeadChnnelCol=[];    %remove shorting channels from bias and receive
48          DeadChnnelRow=[];
49
50          PinCol(1:4:125)=2:2:64;
51          PinCol(3:4:127)=1:2:63;
52          PinCol(2:4:126)=192:-2:130;
53          PinCol(4:4:128)=191:-2:129;
54
55          PinRow(1:4:125)=256:-2:194;
56          PinRow(3:4:127)=255:-2:193;
57          PinRow(2:4:126)=66:2:128;
58          PinRow(4:4:128)=65:2:127;
59
60
61      case 'Relaxor_64x64_Yellow_AKI'
62
63          Nele=64;
64          width = 133e-6;
65          kerf = 20e-6;
66          pitch = width + kerf;
67          dieFrequency = 10;
68          specialmaxHighVoltage = 30;
69          number_cycles=4;
70          HighVoltageStartValue=15;        % sets the high voltage value
71          input.VNN=-60;                   % VNN Voltage
72          input.VPP=60;                    % VPP Voltage
73          DeadChnnelCol=[130 134 142 144 146 152 156 158 166 168 174 176 178 ...
```

```
            180 182 186 188 204 206 208 210 254];    %remove shorting ...
            channels from bias and receive
74          DeadChnnelRow=[66 78 108 116 120 122 124 126];
75
76          PinCol(1:2:63)=2:2:64;
77          PinCol(2:2:64)=192:-2:130;
78
79          PinRow(1:2:63)=256:-2:194;
80          PinRow(2:2:64)=66:2:128;
81
82      case 'Wearable64x64SM1'
83          Nele=64;
84          Type='TOBE';                        %TOBE, LNRE  , LNRE= 1D arrays
85          width = 91e-6*2+20e-6;
86          kerf = 20e-6;
87          pitch = width + kerf;
88          dieFrequency = 10;
89          specialmaxHighVoltage = 30;
90          number_cycles=2;
91          HighVoltageStartValue=20; % sets the high voltage value
92
93          DeadChnnelCol=[];    %remove shorting channels from bias and receive
94          DeadChnnelRow=[];
95
96          PinCol(1:2:63)=2:2:64;
97          PinCol(2:2:64)=130:2:192;
98          PinRow(1:2:63)=256:-2:194;
99          PinRow(2:2:64)=128:-2:66;
100
101
102
103
104     case 'TransmitSingleChannel'
105         Nele=1;
106         Type='TOBE';                        %TOBE, LNRE  , LNRE= 1D arrays
107         width = 500e-6;
108         kerf = 20e-6;
109         pitch = width + kerf;
110         dieFrequency = 10;
111         specialmaxHighVoltage = 30;
112         number_cycles=2;
113         HighVoltageStartValue=30; % sets the high voltage value
114
115         DeadChnnelCol=[];    %remove shorting channels from bias and receive
116         DeadChnnelRow=[];
117         clear PinCol PinRow
118         PinCol(1:2)=1:2;
119         %PinCol(6:10)=28:32;
120         PinRow(1:2)=1:2;
121
122     case 'SM_128x128_Half_AKI'
123         Nele=64;
124         Type='TOBE';                        %TOBE, LNRE  , LNRE= 1D arrays
125         width = 91e-6*2+20e-6;
126         kerf = 20e-6;
127         pitch = width + kerf;
128         dieFrequency = 10;
129         specialmaxHighVoltage = 30;
130         number_cycles=2;
131         HighVoltageStartValue=20; % sets the high voltage value
132
133         DeadChnnelCol=[6 7 ];    %remove shorting channels from bias and ...
            receive
134         DeadChnnelRow=[];
135
136         PinCol(1:64)=1:64;
137
138         PinRow(1:64)=65:128;
139
140
141
142     case 'SM_128x128_AKI'
143         Nele=128;
144         Type='TOBE';                        %TOBE, LNRE  , LNRE= 1D arrays
145         width = 91e-6;
146         kerf = 20e-6;
147         pitch = width + kerf;
148         dieFrequency = 12;
149         specialmaxHighVoltage = 30;
150         number_cycles=4;
151         HighVoltageStartValue=30; % sets the high voltage value
```

```
152
153         DeadChnnelCol=[];     %remove shorting channels from bias and receive
154         DeadChnnelRow=[];
155
156         PinCol(1:2:127)=1:64;
157         PinCol(2:4:126)=192:-2:130;
158         PinCol(4:4:128)=191:-2:129;
159
160         PinRow(1:4:125)=255:-2:193;
161         PinRow(3:4:127)=256:-2:194;
162         PinRow(2:2:128)=65:128;
163
164
165     case 'AllChannels'
166         Nele=256;
167         Type='TOBE';                          %TOBE, LNRE  , LNRE= 1D arrays
168         width = 500e-6;
169         kerf = 20e-6;
170         pitch = width + kerf;
171         dieFrequency = 3.54;
172         specialmaxHighVoltage = 30;
173         number_cycles=2;
174         HighVoltageStartValue=5; % sets the high voltage value
175
176         DeadChnnelCol=[];     %remove shorting channels from bias and receive
177         DeadChnnelRow=[];
178
179         PinCol(1:256)=1:256;
180         PinRow(1:256)=1:256;
181
182         case 'Relaxor_128x128_SM3_half'
183
184         Nele=64;
185         Type='TOBE';                          %TOBE, LNRE  , LNRE= 1D arrays
186         width = (91e-6*2)+20e-6;
187         kerf = 20e-6;
188         pitch = width + kerf;
189         dieFrequency = 12;
190         specialmaxHighVoltage = 30;
191         number_cycles=2;
192         HighVoltageStartValue=30; % sets the high voltage value
193
194         DeadChnnelCol=[48 ];     %remove shorting channels from bias and ...
            receive
195         DeadChnnelRow=[];
196
197         PinCol(1:64)=192:-1:129;
198
199
200
201         PinRow(1:64)=65:128;
202
203
204         case 'Relaxor_128x128_SM3'
205
206         Nele=128;
207         Type='TOBE';                          %TOBE, LNRE  , LNRE= 1D arrays
208         width = 91e-6;
209         kerf = 20e-6;
210         pitch = width + kerf;
211         dieFrequency = 12;
212         specialmaxHighVoltage = 30;
213         number_cycles=4;
214         HighVoltageStartValue=25; % sets the high voltage value
215
216         DeadChnnelCol=[48 ];     %remove shorting channels from bias and ...
            receive
217         DeadChnnelRow=[];
218
219         PinCol(1:4:125)=255:-2:193;
220         PinCol(3:4:127)=256:-2:194;
221         PinCol(2:2:128)=65:1:128;
222
223
224         PinRow(2:2:128)=1:1:64;
225
226         PinRow(1:2:127)=192:-1:129;
227
228         case 'Relaxor_128x128_SM3_lessBias'
229
230         Nele=128;
231         Type='TOBE';                          %TOBE, LNRE  , LNRE= 1D arrays
232         width = 91e-6;
233         kerf = 20e-6;
```

```
234         pitch = width + kerf;
235         dieFrequency = 12;
236         specialmaxHighVoltage = 30;
237         number_cycles=2;
238         HighVoltageStartValue=30; % sets the high voltage value
239 
240         DeadChnnelCol=[18  48 50 52 56 58 62 76 88 90 92 98 102 108 112 ...
                114 126];    %remove shorting channels from bias and receive
241         DeadChnnelRow=[4 8 18 20 22 24 26 28 34 42 46 50  54 72 78 88 96 ...
                100 102 104 110 112 116 118 120 126];
242 
243         PinCol(1:4:125)=255:-2:193;
244         PinCol(3:4:127)=256:-2:194;
245         PinCol(2:2:128)=65:1:128;
246 
247 
248         PinRow(2:2:128)=1:1:64;
249 
250         PinRow(1:2:127)=192:-1:129;
251 
252     case 'Relaxor_64x64_D3'
253 
254         Nele=64;
255         width = 133e-6;
256         kerf = 20e-6;
257         pitch = width + kerf;
258         dieFrequency = 10;
259         specialmaxHighVoltage = 30;
260         number_cycles=2;
261         HighVoltageStartValue=20; % sets the high voltage value
262 
263         DeadChnnelCol=[12 16 18];    %remove shorting channels from bias ...
                and receive
264         DeadChnnelRow=[];
265 
266         PinCol(1:2:63)=33:1:64;
267         PinCol(2:2:64)=192:-1:161;
268 
269         PinRow(1:2:63)=97:1:128;
270         PinRow(2:2:64)=256:-1:225;
271 
272     case 'Relaxor_64x64_2A'
273         Nele=64;
274         width = 133e-6;
275         kerf = 20e-6;
276         pitch = width + kerf;
277         dieFrequency = 10;
278         specialmaxHighVoltage = 30;
279         number_cycles=2;
280         HighVoltageStartValue=20; % sets the high voltage value
281 
282         DeadChnnelCol=[4 14 22 23];    %remove shorting channels from bias ...
                and receive
283         DeadChnnelRow=[];
284 
285         PinCol(1:4:61)=130:2:160;
286         PinCol(3:4:63)=129:2:159;
287         PinCol(2:4:62)=31:-2:1;
288         PinCol(4:4:64)=32:-2:2;
289 
290         PinRow(1:4:61)=194:2:224;
291         PinRow(3:4:63)=193:2:223;
292         PinRow(2:4:62)=95:-2:65;
293         PinRow(4:4:64)=96:-2:66;
294 
295 case 'smx2_10Mhz_48x48'
296         Nele = 48;
297         width = 107e-6;
298         kerf = 16e-6;
299         pitch = width + kerf;
300         dieFrequency = 10;
301         specialmaxHighVoltage = 30;
302         number_cycles=2;
303         HighVoltageStartValue=20; % sets the high voltage value
304 
305         DeadChnnelCol=[];    %remove shorting channels from bias and receive
306         DeadChnnelRow=[];
307 
308      PinRow = zeros(1,48);
309      PinCol = zeros(1,48);
310      PinCol(1:2:47)=56:-2:10;
```

```
311       PinCol(2:2:48)=138:2:184;
312       PinRow(1:2:47)=74:2:120;
313       PinRow(2:2:48)=248:-2:202;
314   end
```

Appendix D: Schematics

All designs files are publicly available in Afshin Kashani Ilkhechi's GitHub account (https://github.com/AfshinKI/piCards).

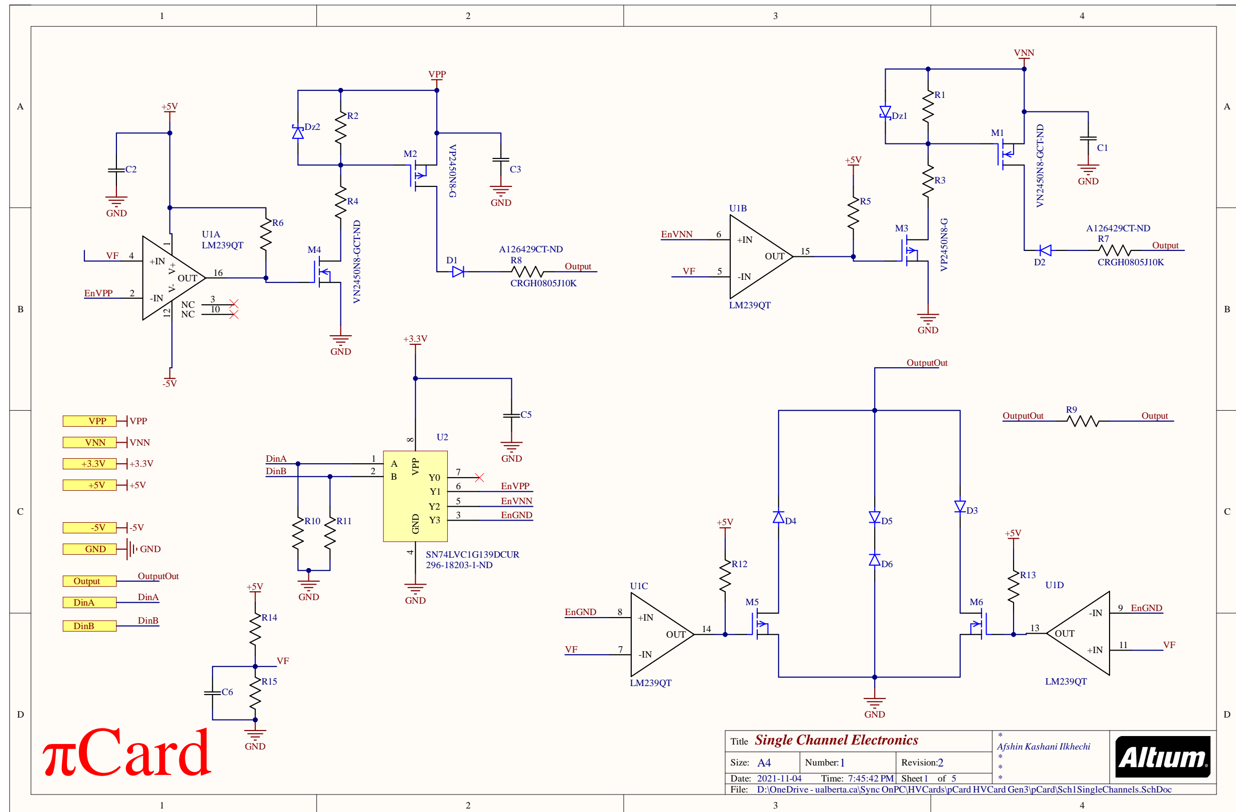

Fig. 49: πCards' single channel schematic

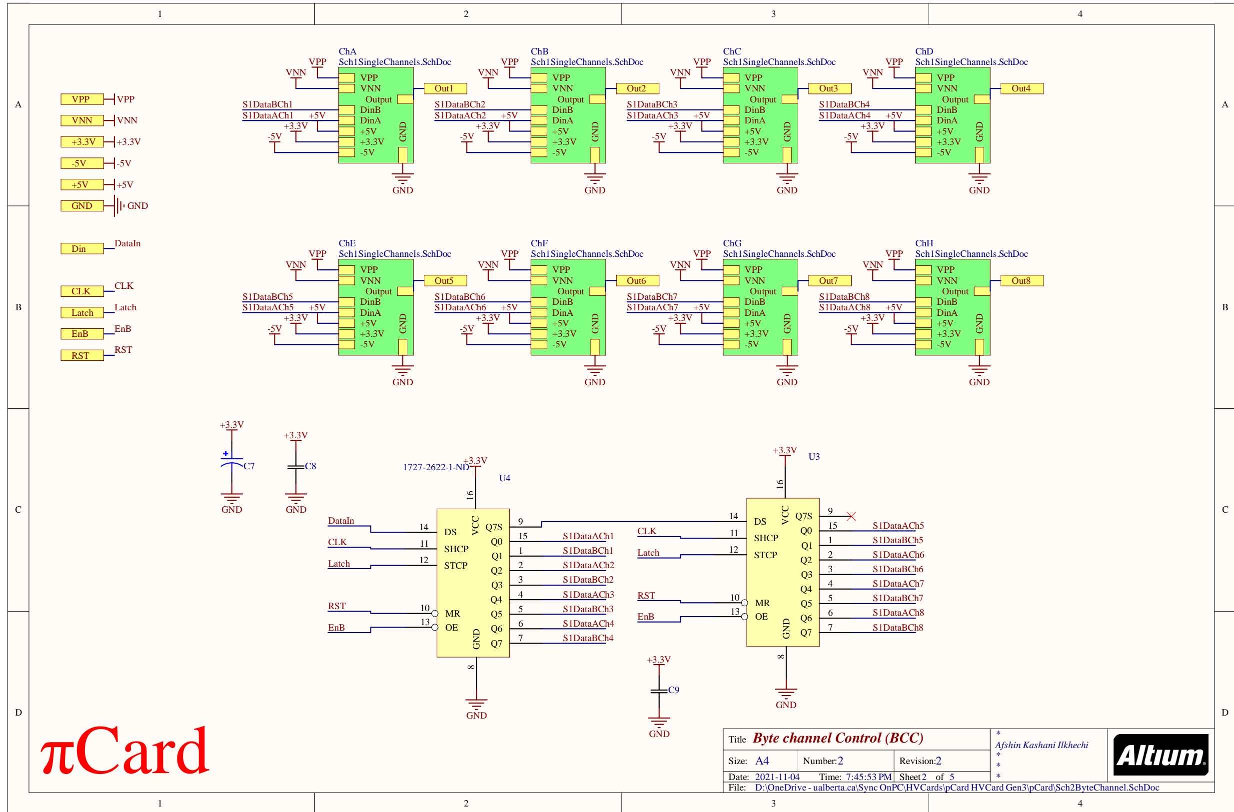

Fig. 50: πCards' eight channels with shift registers

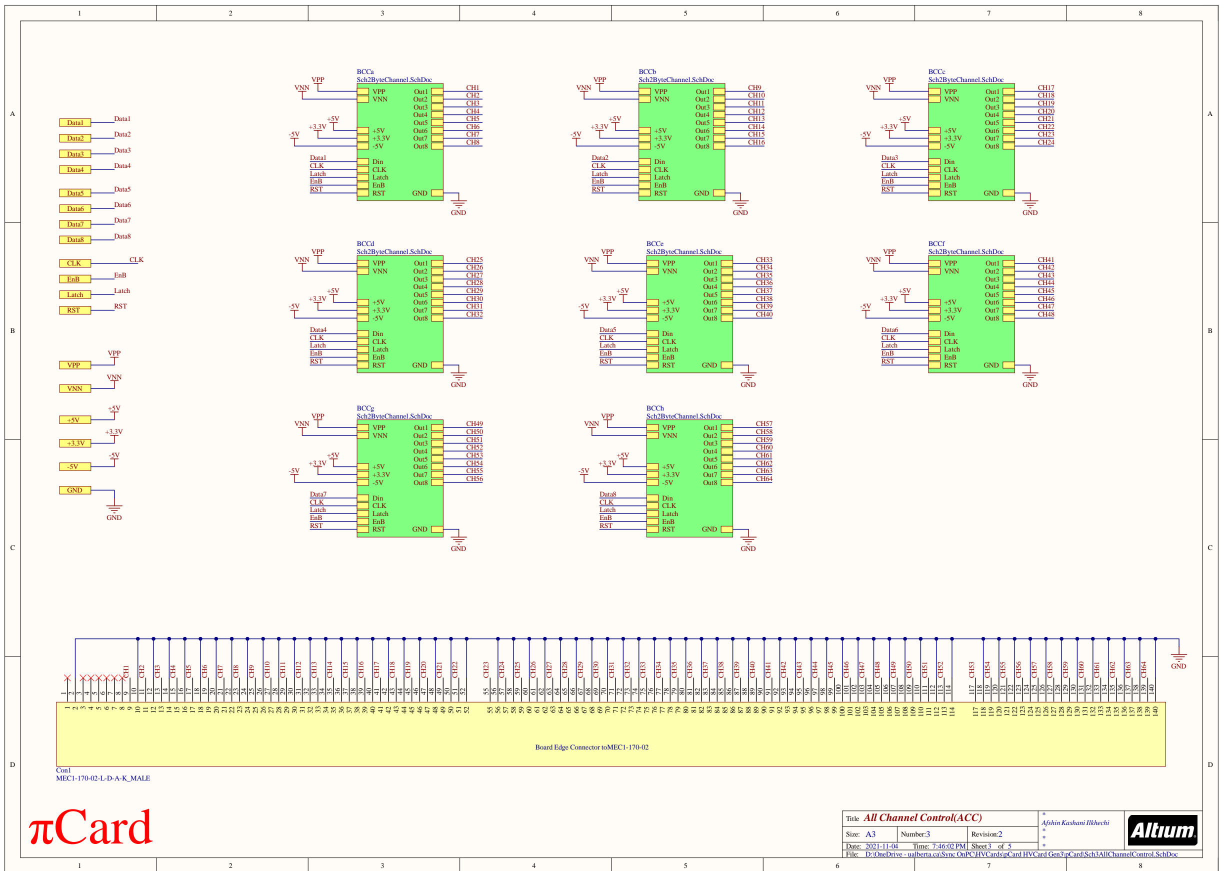

Fig. 51: πCards' all channels' connections

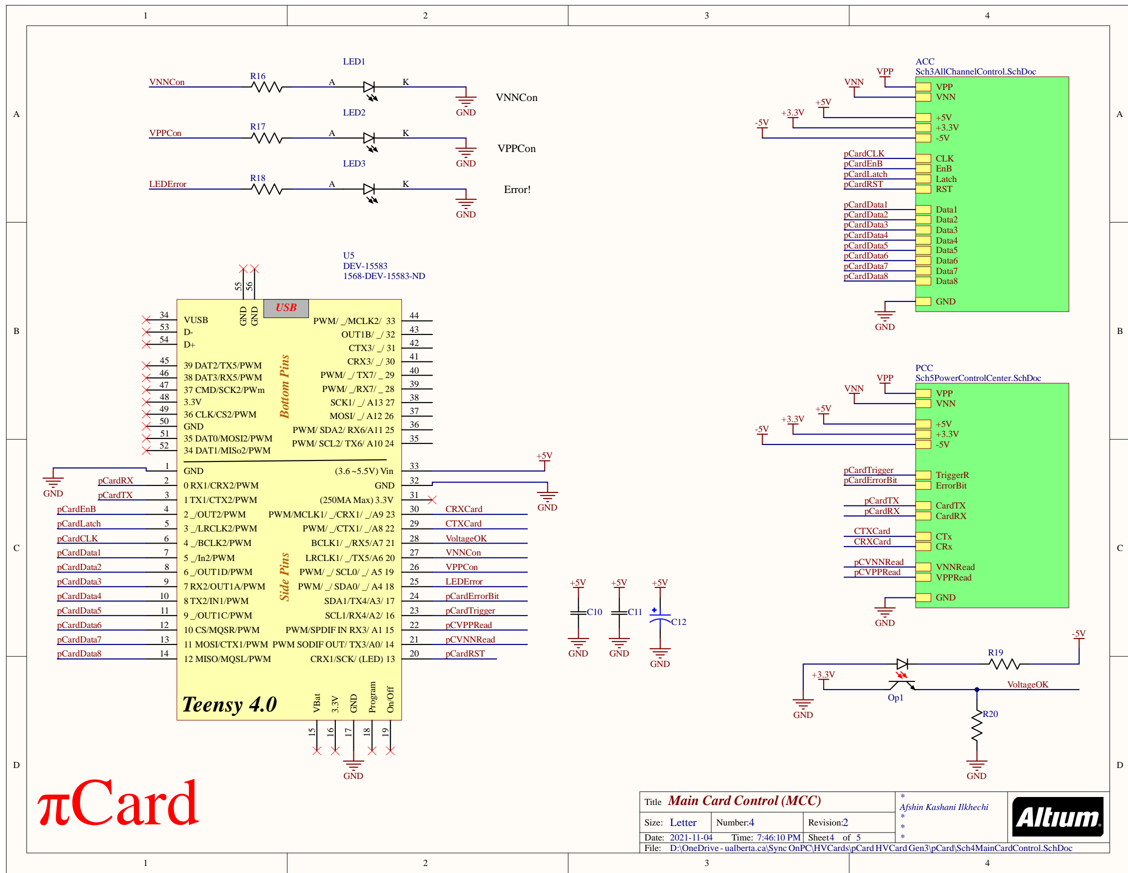

Fig. 52: πCards' main card controller

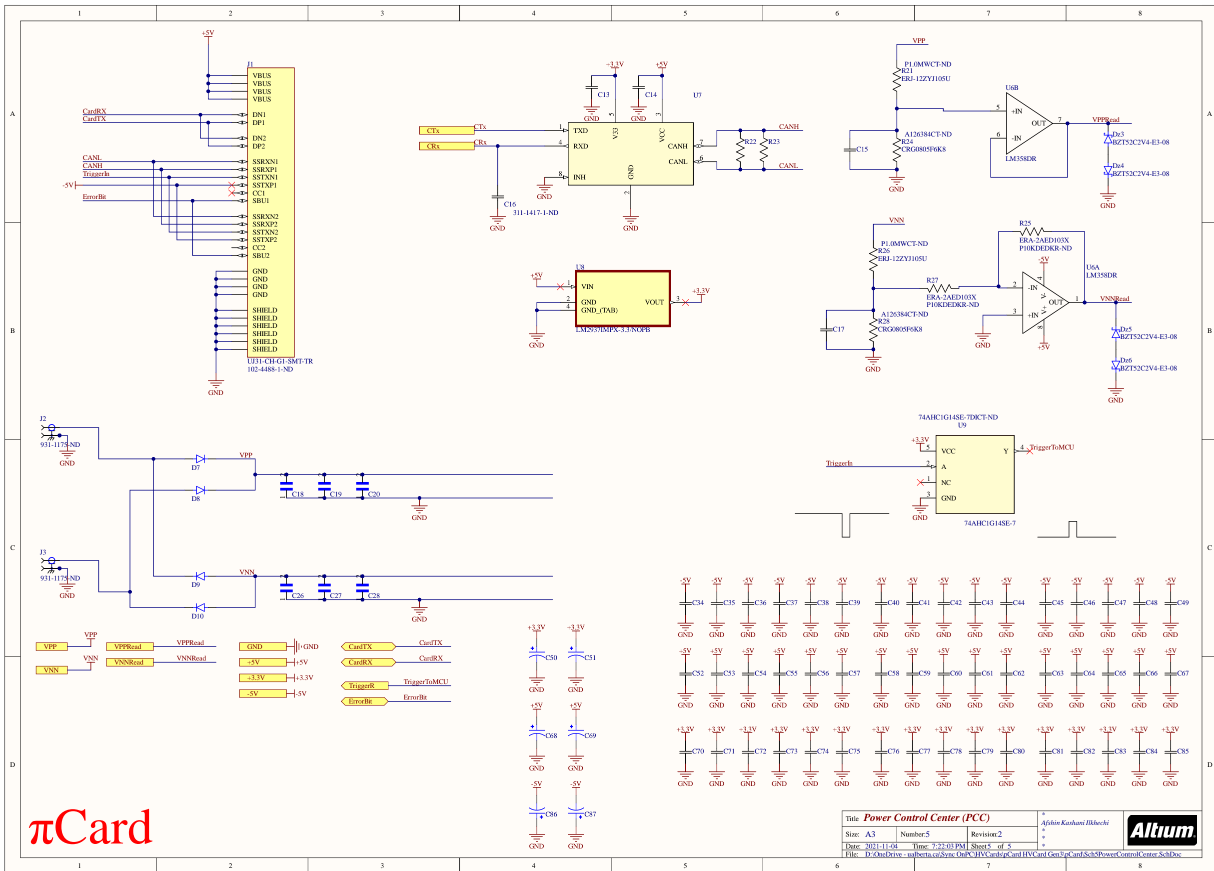

Fig. 53: πCards' power control schematic

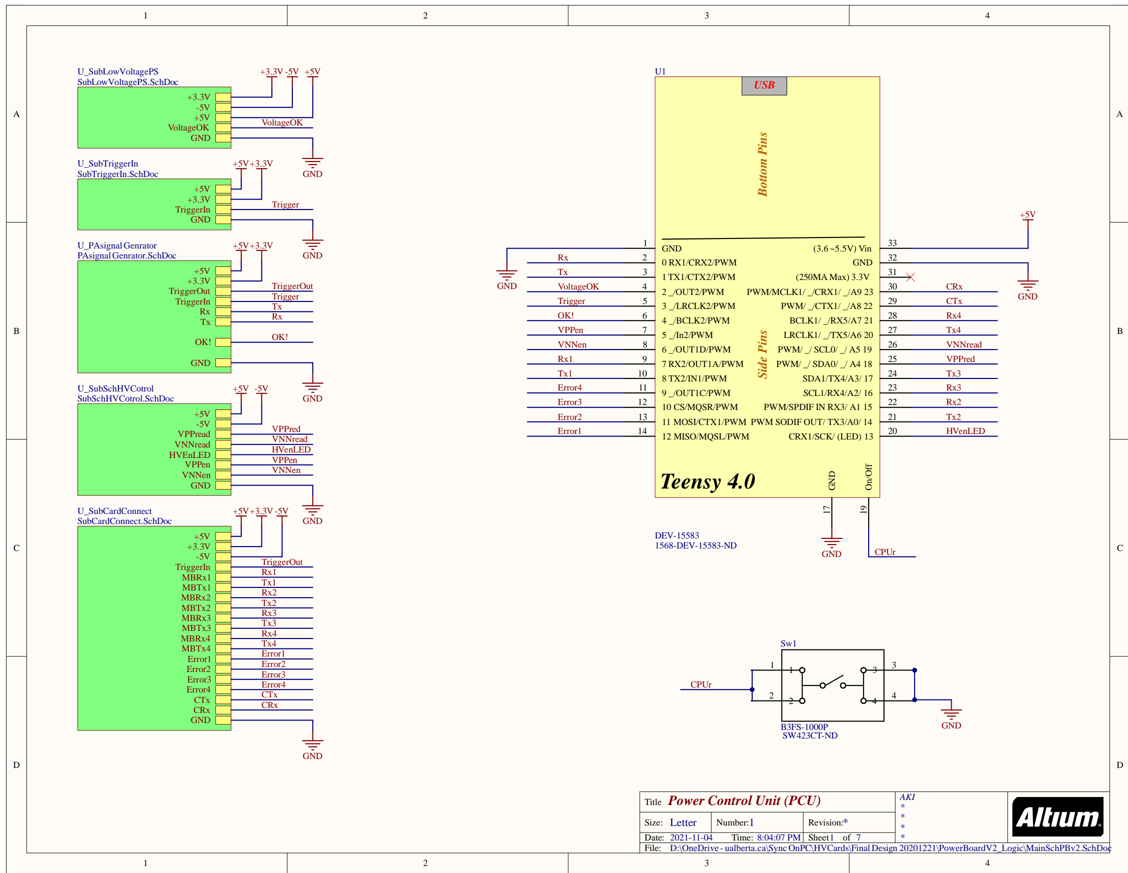

Fig. 54: CCUs' main controller

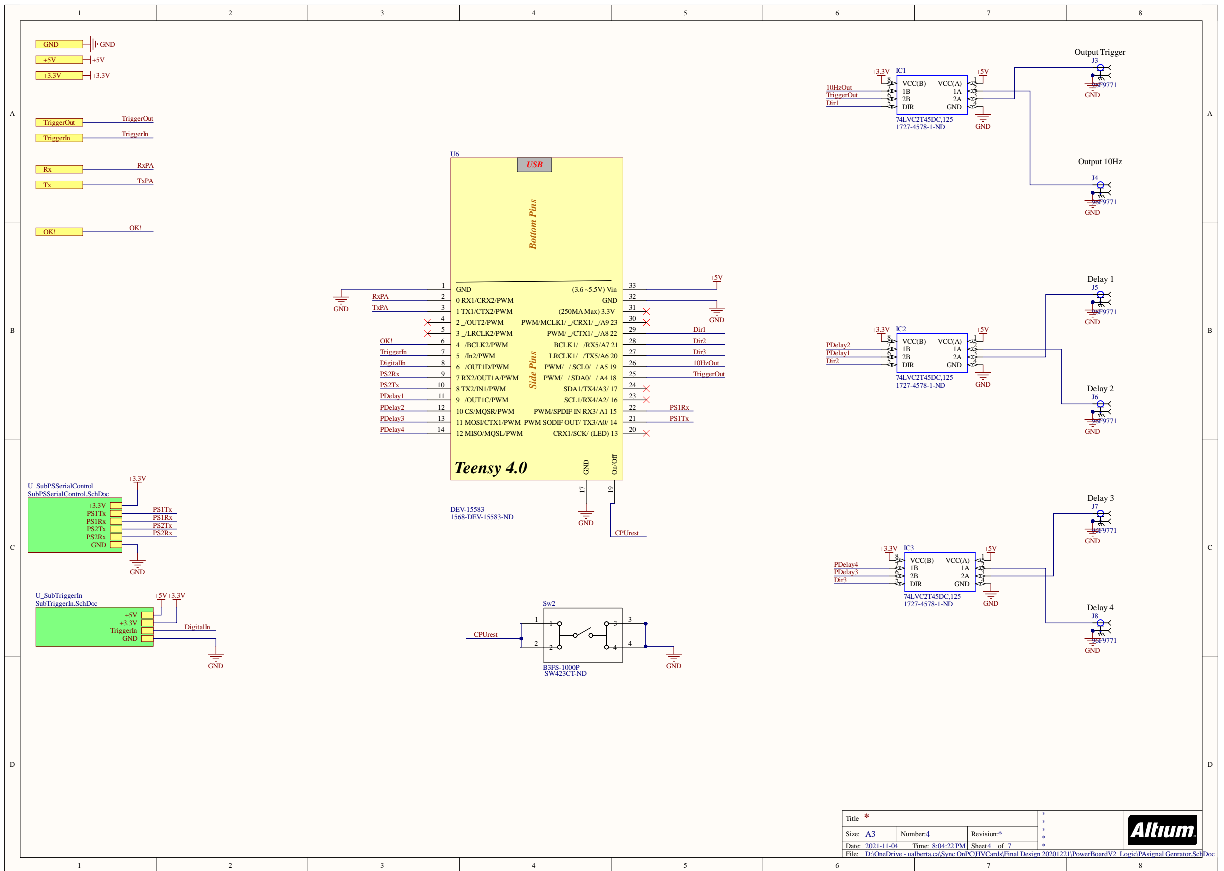

Fig. 55: CCUs' delay generator

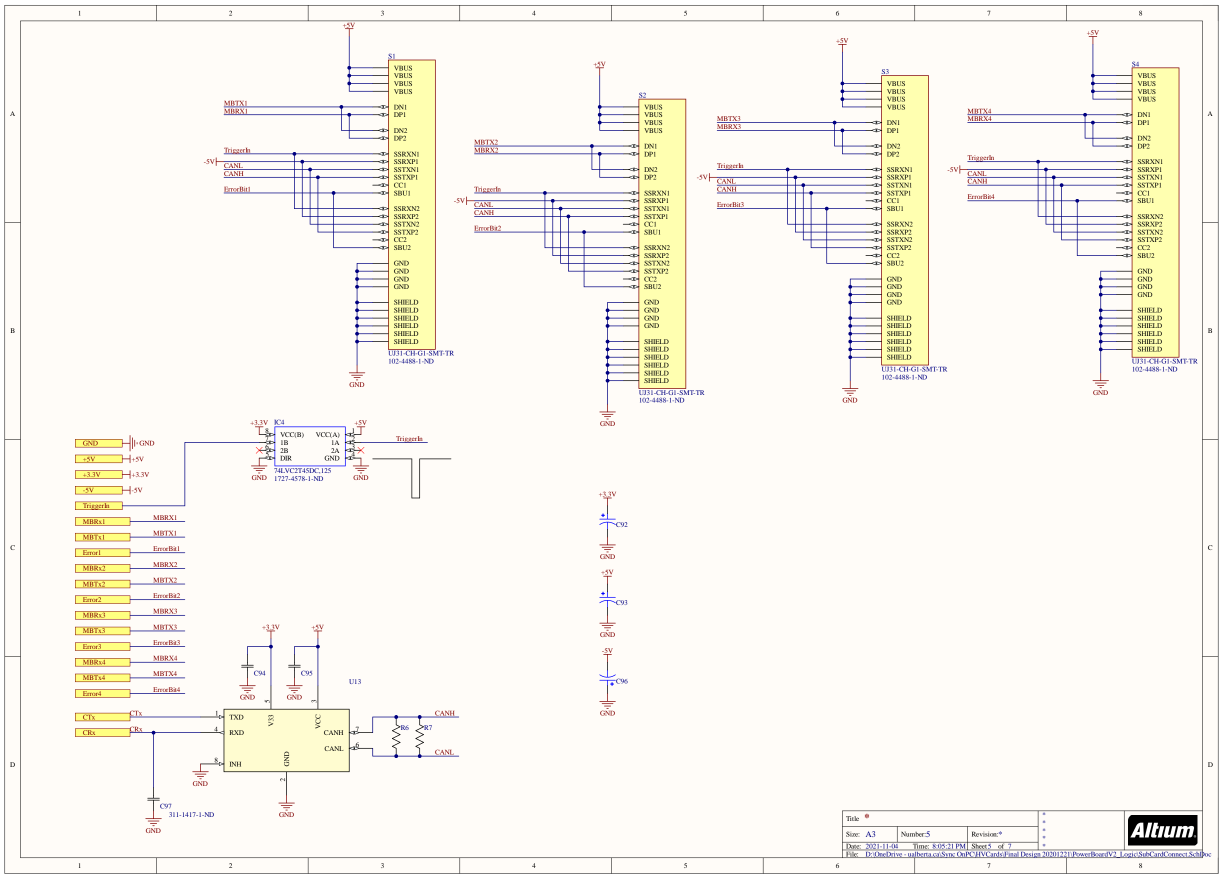

Fig. 56: CCUs' πCard interface

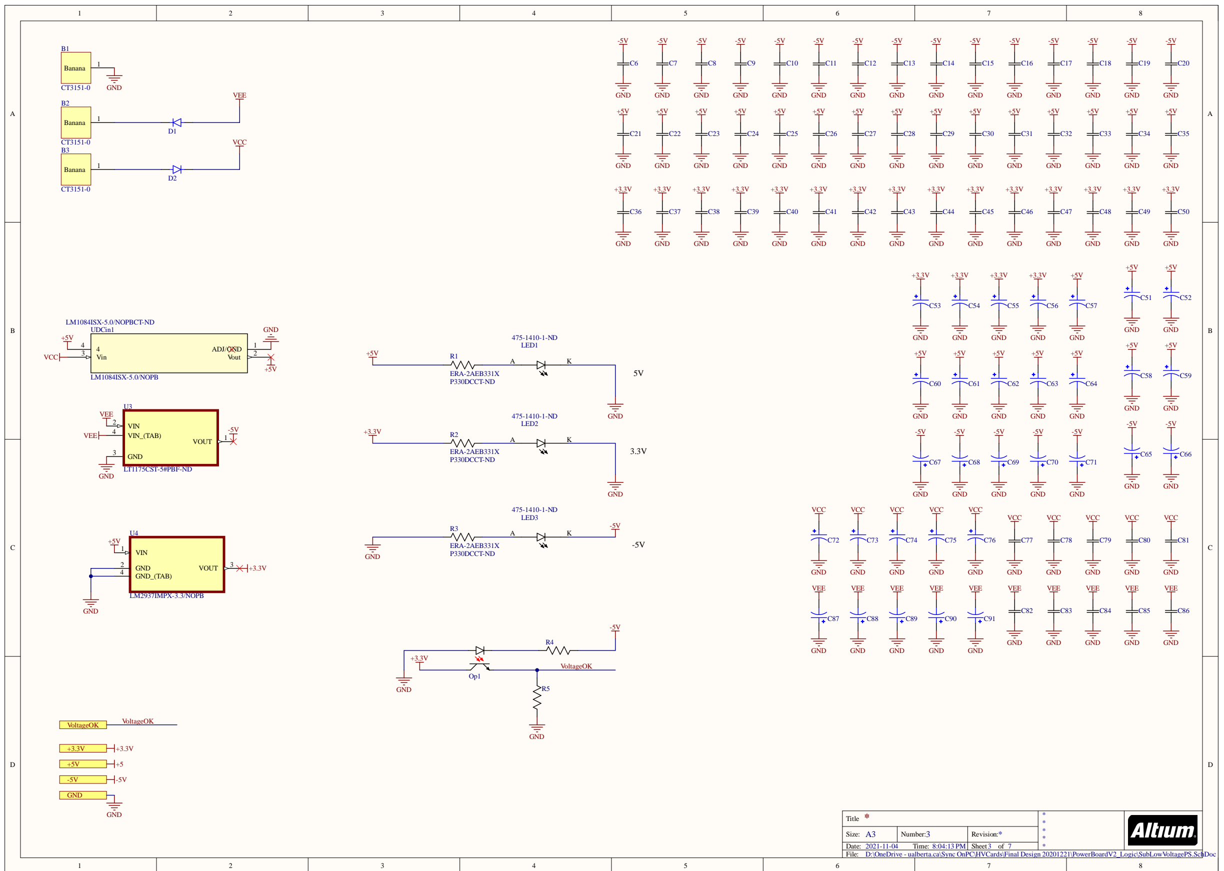

Fig. 57: CCUs' power controller

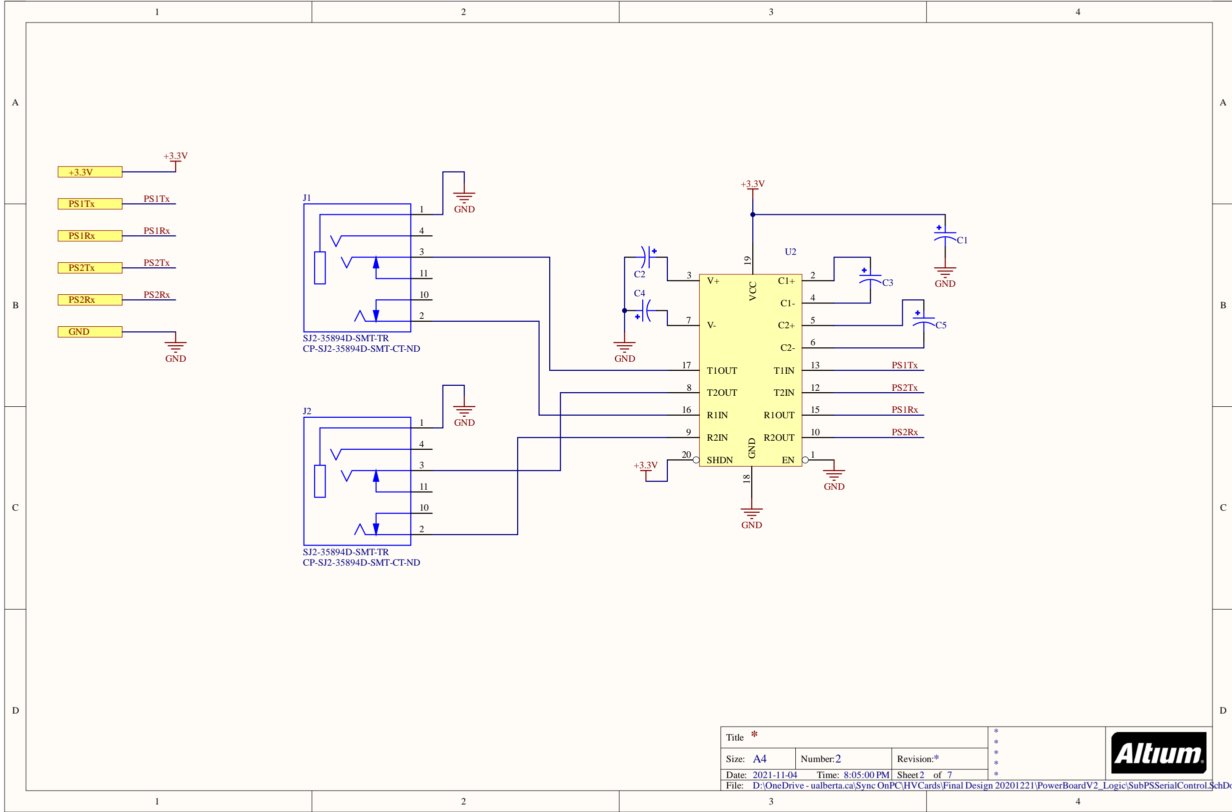

Fig. 58: CCUs' power supply port

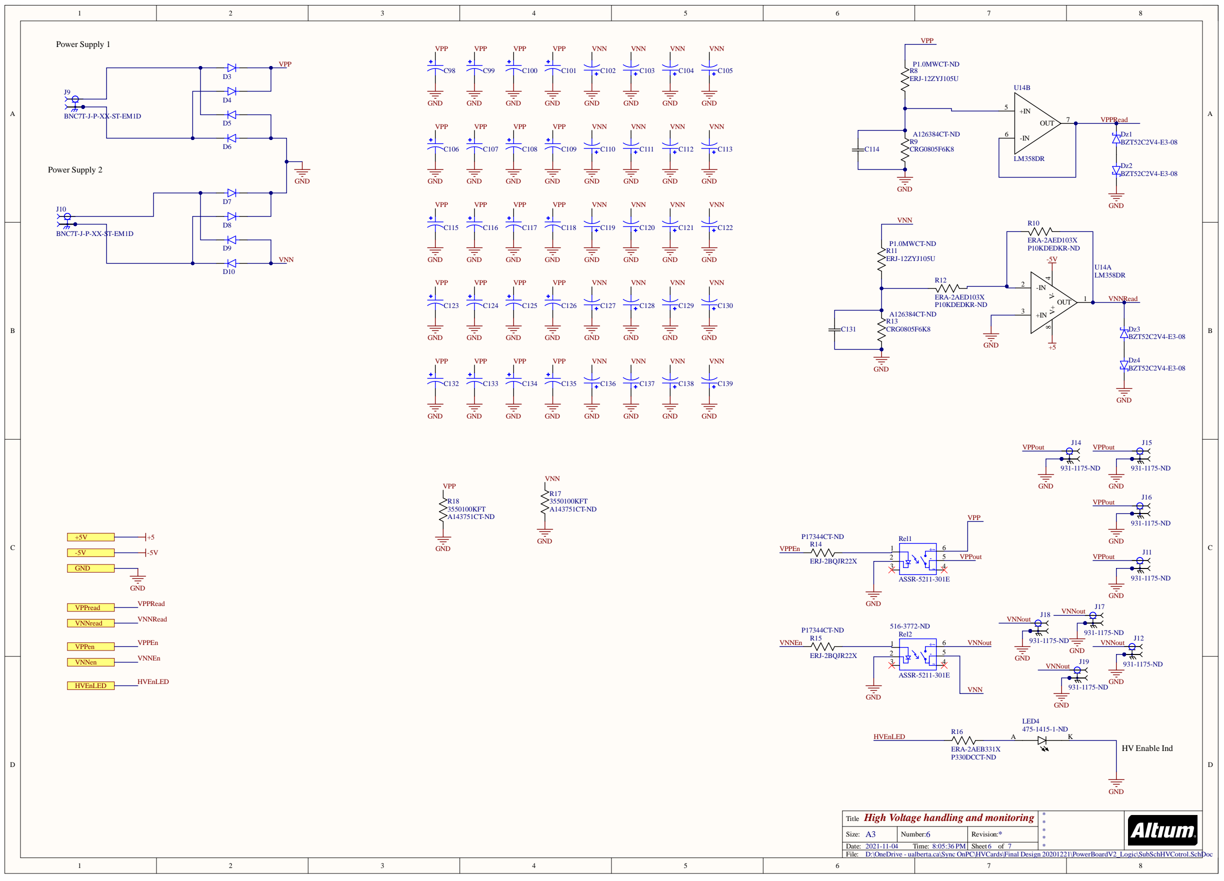

Fig. 59: CCUs' high voltage sampler

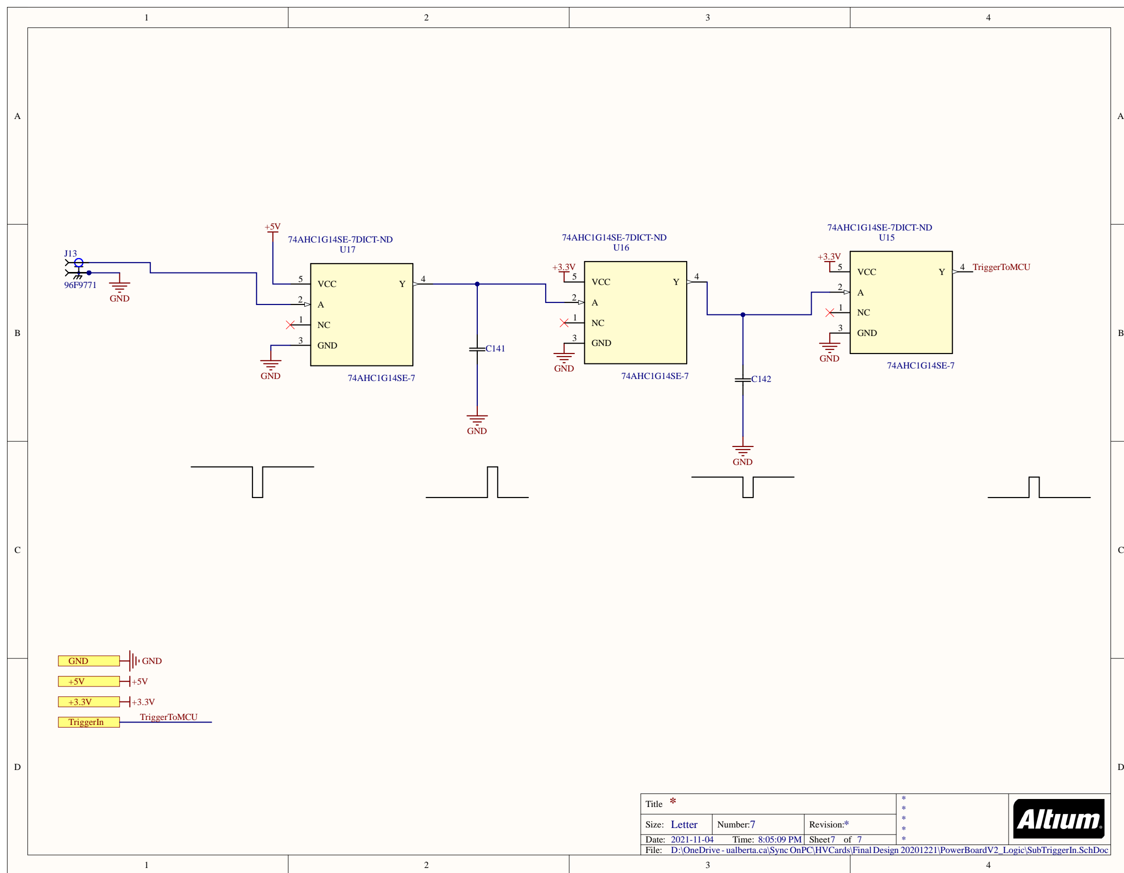

Fig. 60: CCUs' trigger receiving electronics

Appendix E: Fabrication processes for fabricating transparent TOBE arrays

E.1 Fabrication process for 2D transparent CMUT transducers

Described fabrication process in the previous section can be modified to fabricate transparent 2D arrays with top-orthogonal-bottom-electrode (TOBE) wiring scheme. The majority of the process flow remains the same, with some extra steps to form the bottom electrodes. In TOBE wiring scheme, bottom electrodes are formed on the glass substrate with an orthogonal orientation to the top electrodes.

Electrodes are made with ITO layer for high transparency along with metal strips for better conductivity of the channels. However, the thickness of the metal strips is over 1 μm, which can cause an uneven bonding surface. This problem is addressed by first etching trenches into the glass substrate and then filling them by depositing metal layers.

Fig. 61 illustrate the fabrication process flow. The process flow starts with a wafer cleaning step. Fused silica wafers are cleaned with Acetone and IPA to remove any residual contaminations. Wafer cleaning continues by 15 minutes piranha etching (1:3 hydrogen peroxide: sulfuric acid). Piranha cleaning step is highly recommended to remove any particles and contaminations. Next, ITO trenches are etched into the glass substrate. For this purpose, photoresist AZ1512 is spin-coated and baked on the fused silica wafer and patterned. Next, Glass etching is performed with ICP-RIE etching for about 200 nm. Fig. 61a illustrates this step.

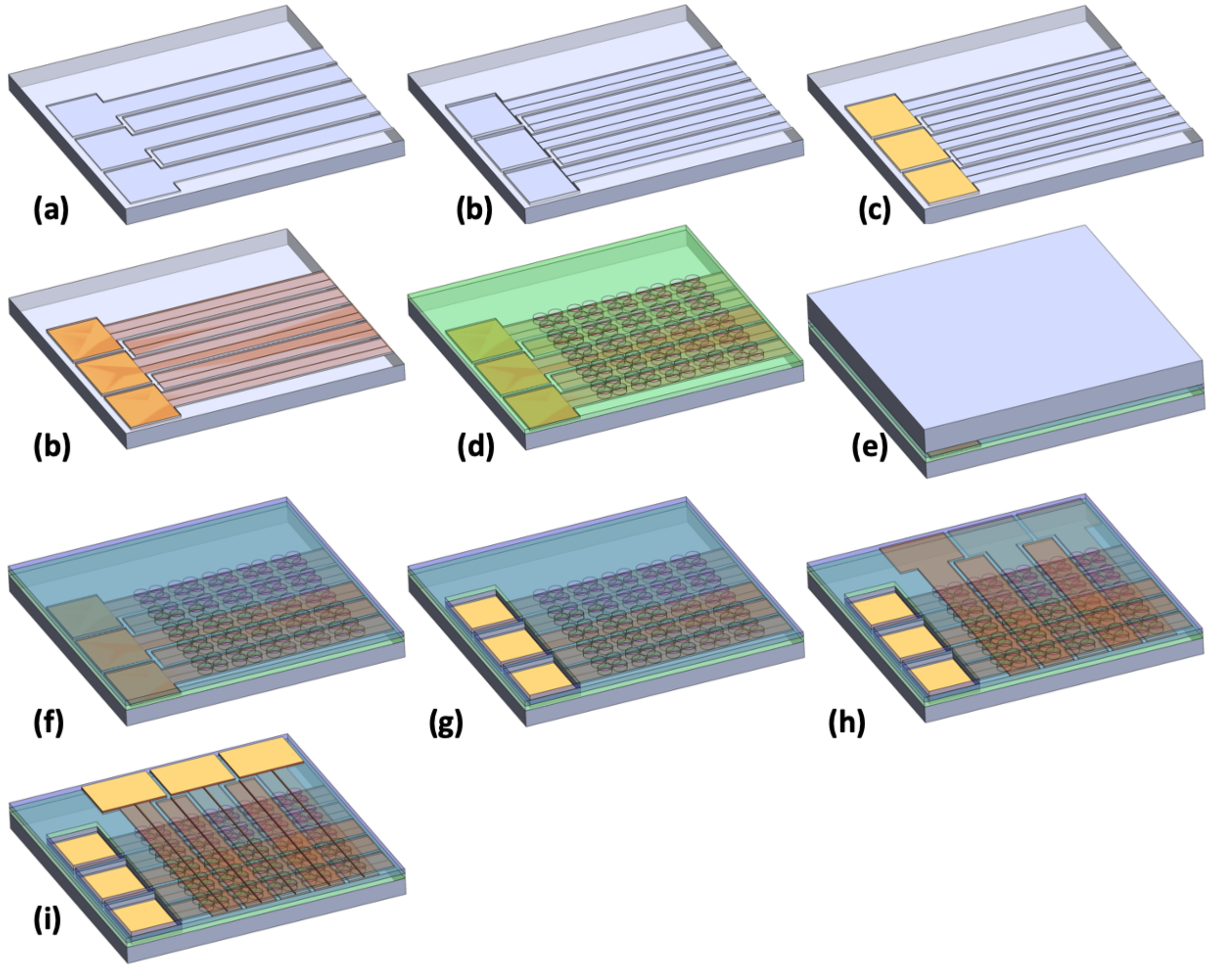

Fig. 61: Fabrication process flow for TOBE CMUT arrays with BCB wafer bonding technique.

Next, trenches for metal strips are etched. The main challenge is using a single lithography step for both etching the trenches and patterning the metals strips. Considering the 2 μm width of the metal strips, performing separate lithography steps would require high precision mask alignment. Therefore, a combination of LOR 5B and AZ1529 resists is recommended for performing the lithography. LOR 5B can provide under mask etching for the lift-off process, and AZ1529 provides a thick resist layer to withstand the glass etching process. Undercut etching is done by developing the LOR5B resist in the MF-319 developer. Fig. 62 presents the wafer before the undercut process; only AZ1529 photoresist is devel-

oped. Fig. 62b illustrates a proper undercut etching. Fig. 62c illustrates extra undercut where LOR5B is completely removed underneath the photoresist.

After performing the under-cut lithography of the LOR5B, ICP-RIE is performed to etch the trenches into the glass substrate, and 1.5 μm etching into the glass is performed.

Next, metal deposition is performed, and e-beam evaporation is used to deposit metal combinations. For the metal layer, a combination of the metal layers of Cr/Cu/Cr/Au with thicknesses of 10 nm/1.4 μm/10 nm/80 nm is deposited on the substrate in a single deposition process. Metal lift-off process is carried out by placing the wafer into an acetone bath. Fig. 61b&c are illustrating these steps. Next, ITO is deposited and etched using mask 3 (Fig. 61d).

The fabrication process is followed by spin-coating the BCB layer and exposing it to UV light for patterning the gaps (Fig. 61e). Then, a wafer containing a thin LPCVD nitride is bonded on the BCB layer and etched using KOH solution (Fig. 61f&g). After releasing the membranes, access to the bottom electrode is created with RIE etching, where the bottom ITO layer acts as an etch stop (Fig. 61h). The process flow continues by depositing and

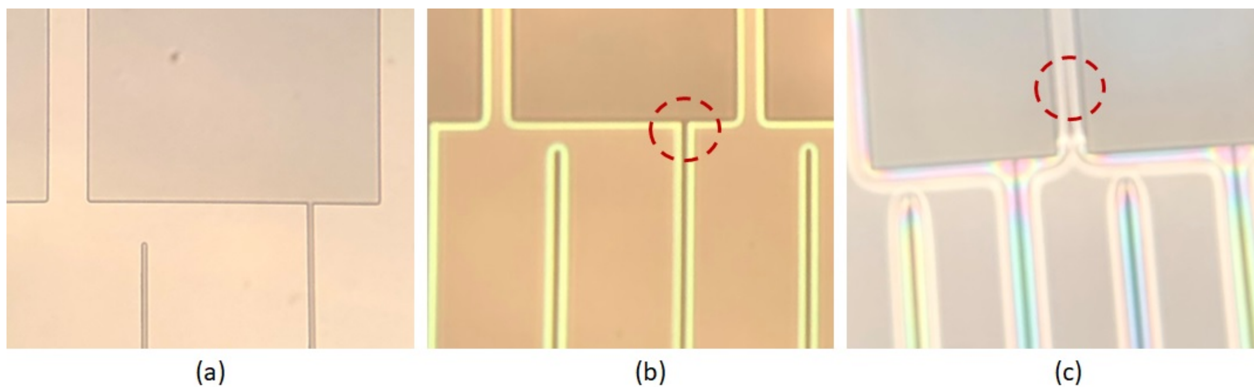

Fig. 62: (a) Before performing the undercut (b) Proper undercut (c) Excess undercut.

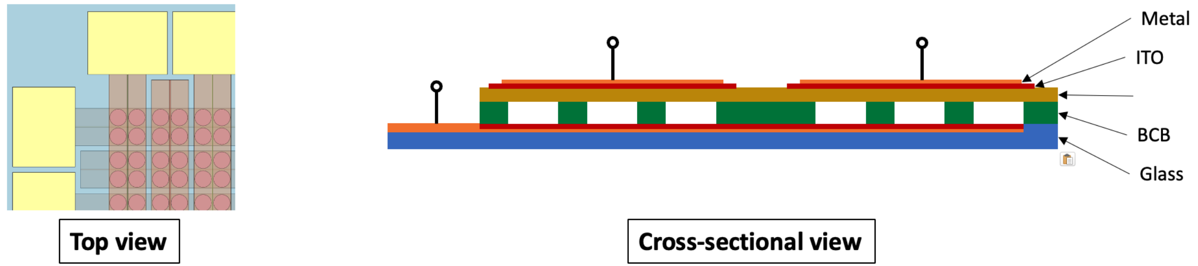

Fig. 63: Top view and cross-sectional views of the transparent CMUTs with BCB bonding technique.

forming the ITO layer into the TOP electrodes. A metal layer is deposited and formed into thin metal traces using the lift-off process. Fig. 61i&j illustrate these steps. The top view and the cross-sectional view of the proposed fabrication process flew are presented in Fig. 63.

E.2 Transparent TOBE CMUT transducers with sacrificial release process

The gap height of a CMUT cell plays an essential role in determining the characteristics of ultrasound transducers, such as snapdown voltage and transmit and receive sensitivity. Also, designing high-frequency CMUTs requires a precise, controlled gap height typically thinner than 400 nm. However, the BCB bonding process introduced in the previous section is limited in controlling the gap height and reaching film thickness below 400 nm.

Here, we will address this problem by introducing a modified sacrificial release process flow for fabricating high-frequency, high-sensitive transparent TOBE arrays. In our novel process, a Plasma Enhanced Chemical Vapor Deposition (PECVD) oxide layer is used as a sacrificial layer to obtain films with high uniformity and accuracy. The fabrication process contains eight lithography steps. Similar to the former fabrication process, a combination of ITO and metal strips are used to make conductive transparent electrodes.

The process starts by spin-coating a combination of LOR 5B and AZ1529 resists on a glass wafer and exposing it to the first mask to form the thin metal trenches. Then, an ICP-RIE glass etching process is performed to etch the metal trenches into the glass substrate (Fig. 64a), and immediately, an e-beam metal evaporation process is performed to fill the trenches. Fig. 64b illustrates the wafer with metal trenches etched into the glass substrate. Buried metal traces into the glass substrate will introduce less metal contamination for the upcoming PECVD and low pressure chemical vapor deposition (LPCVD) deposition processes.

Next, an ITO layer is sputtered on the substrate and etched with HCl solution to form the transparent bottom electrodes (Fig. 64c).

In the next step, a thin PECVD silicon nitride layer is deposited on the wafer to protect the ITO layer from future etching processes (Fig. 64d). Then, a 100-nm PECVD silicon dioxide film is deposited and patterned into the gaps as a sacrificial layer. Later in the process, this layer is selectively etched with the help of a vapour hydrofluoric acid (VHF) etching process (Fig. 64e).

To form the membranes, a low-stress $1\mu m$ LPCVD nitride layer is deposited on the wafer (Fig. 64f).

The process continues by etching the access holes into the silicon nitride layer with an RIE etching process (Fig. 64g). The sacrificial layer is removed by placing the wafer into a VHF chamber. The VHF process provides a stiction-free membrane release (Fig. 64h).

The fabrication process continues by depositing a PECVD silicon dioxide layer in order to seal the etch holes and form vacuum gaps. The excess dioxide layer is etched with BOE solution to form them into plugs (Fig. 64i).

A combination of lithography and RIE etching steps is performed to open access holes to the bottom electrodes. Next, the top ITO layer is deposited with magnetron sputtering process and formed into the top electrodes (Fig. 64j). Finally, with the last lithography step, a metal layer is deposited and formed into thin metal strips to improve the channels' electrical conductivity. Fig. 64k presents the metal strips.

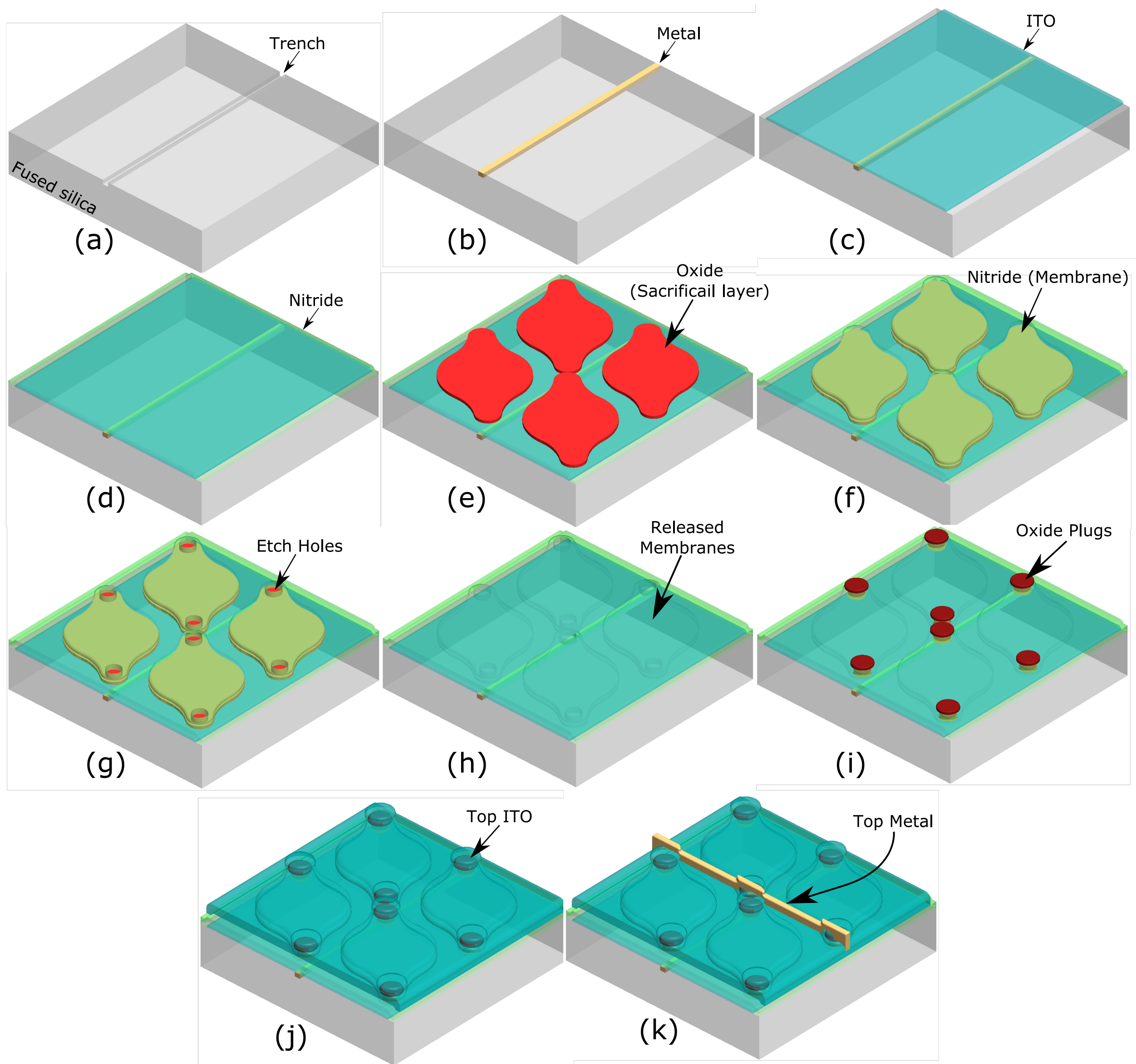

Fig. 64: Sacrificial release fabrication process flow for fabricating high-frequency transparent TOBE arrays. The process involves a silicon dioxide layer as a sacrificial layer and a silicon nitride layer as the membrane materials. (a) Etching thin trenches in the fused silica substrate. (b) Metal deposited in the trenches (c) ITO deposition and formation into the channels for the bottom electrodes. (d) Deposition of PECVD nitride for protecting the ITO layer. (e) Silicon dioxide deposition and formation as a sacrificial release layer. (f) LPCVD nitride deposition as a membrane material. (g) RIE nitride etching to open the etch holes for releasing the membrane. (h) Vapour HF etching the sacrificial layer. (i) PECVD dioxide deposition to seal the etch holes and formation into the plugs. (j) ITO deposition and formation into top electrodes (k) Metal strip deposition to improve the channel conductivity.